Energy Efficient Optical Wireless Communications based on Frequency-Shift Keying Modulations.

Muhammad Jehangir Khan

THÈSE

Pour obtenir le grade de

DOCTEUR DE L'UNIVERSITÉ GRENOBLE ALPES

École doctorale : EEATS - Electronique, Electrotechnique, Automatique, Traitement du Signal (EEATS)
Spécialité : Signal Image Parole Télécoms
Unité de recherche : Grenoble Images Parole Signal Automatique

Communications Optiques sans-fil à Haute Efficacité Energétique basées sur les Modulations de Fréquence .

Energy Efficient Optical Wireless Communications based on Frequency-Shift Keying Modulations.

Présentée par :

Muhammad Jehangir KHAN

Direction de thèse :

Yannis LE GUENNEC MAITRE DE CONFERENCES, Grenoble-INP	Directeur de thèse
Laurent ROS PROFESSEUR DES UNIVERSITES, Grenoble-INP	Co-directeur de thèse
Ghislaine MAURY MAITRE DE CONFERENCES, Grenoble-INP	Co-encadrante de thèse

Rapporteurs :

Stéphane AZOU
PROFESSEUR DES UNIVERSITES, École Nationale d'Ingénieurs de Brest
Mohammad-Ali KHALIGHI
MAITRE DE CONFERENCES HDR, École Centrale Marseille

Thèse soutenue publiquement le13 mars 2023, devant le jury composé de :

Emil NOVAKOV PROFESSEUR DES UNIVERSITES, Université Grenoble Alpes	Président
Stéphane AZOU PROFESSEUR DES UNIVERSITES, École Nationale d'Ingénieurs de Brest	Rapporteur
Mohammad-Ali KHALIGHI MAITRE DE CONFERENCES HDR, École Centrale Marseille	Rapporteur
Kosaï RAOOF PROFESSEUR DES UNIVERSITES, Université du Mans	Examinateur
Stéphanie SAHUGUEDE MAITRE DE CONFERENCES, Université de Limoges	Examinatrice

Invités :

Cyrille SICLET
MAITRE DE CONFERENCES, Grenoble-INP
Ali Waqar AZIM
PROFESSEUR ASSISTANT, University of Engineering and Technology, Taxila, Pakistan

Abstract

Optical wireless communications (OWC) is an appropriate technology to alleviate the scarcity issue of the radio-frequency (RF) spectrum. For OWC technology, the transmitted signals should be real-valued and unipolar to satisfy the constraints of the intensity modulation and direct detection (IM-DD). OWC have been extensively investigated for pervasive applications in high data rate communications which is based on pulse-amplitude modulation (PAM), optical-orthogonal frequency-division multiplexing (O-OFDM), etc. Recent research has confirmed the interest of OWC low data rate (100 kbps to 1 Mbps) applications, requiring high energy efficiency. In this context, frequency-shift keying (FSK) raised considerable interest for OWC technology. For IM-DD OWC systems, the conventional M-ary FSK is not compatible because of the bipolar nature of the FSK waveforms, but two compatible variants of FSK modulation have been introduced in the literature for OWC systems, i.e., direct current (DC)-FSK and unipolar (U)-FSK.

The current PhD work focuses on high energy-efficient modulation approaches for OWC, which are based on extensions/adaptations of the conventional M-ary FSK modulations. After the review of the state-of-the-art, a new modulation scheme called M-ary asymmetrically clipped (AC)-FSK is presented for high energy-efficient/low data rate OWC, which is based on the conventional bipolar M-ary FSK. Traditional receivers such as optimal time-domain (TD) receiver (based on maximum likelihood (ML) detection), and sub-optimal receiver (based on 1-tap DCT-based detection) exhibit the trade-off between the energy efficiency and the receiver complexity. A new frequency-domain (FD) low complexity receiver called L-tap harmonic receiver is proposed for the proposed M-ary AC-FSK and state-of-the-art M-ary U-FSK, that alleviates the energy-efficiency and the receiver complexity trade-off. Simulation results confirm that the bit error rate (BER) performance of the proposed M-ary AC-FSK is far better than the state-of-the-art M-ary DC-FSK, and its BER performance is slightly improved as compared to the state-of-the-art M-ary U-FSK. Moreover, simulation results also confirm that the proposed L-tap harmonic receiver for both M-ary AC-FSK and M-ary U-FSK approaches the optimal TD ML receiver performance with a benefit of the drastic reduction in the receiver complexity.

Secondly, a new modulation approach, i.e., Asymmetrically Clipped Frequency and Phase Shift Keying (AC-FPSK) is proposed for IM-DD OWC applications that is based on the amalgamation of M-ary AC-FSK and phase-shift keying (PSK). It is highlighted that AC-FPSK shows improved energy efficiency and spectral efficiency as compared to M-ary AC-FSK.

Finally, an experimental demonstration of the proposed M-ary AC-FSK and the proposed L-tap harmonic receiver is presented and compared with the state-of-the-art FSK-based modulations. The

experimental setup is based on commercial off-the-shelf components and a software defined radio (SDR) test bench. The experimental results confirm the validity of the proposed schemes in the thesis.

Keywords: Optical wireless communications, digital modulations, intensity modulation and direct detection, energy efficient modulation, frequency-shift keying, signal processing, LEDs, software defined radio, discrete cosine transform, harmonic receiver, Internet-of-Things.

Résumé

Les communications optiques sans fil (OWC) sont prometteuses pour pallier au problème de la saturation du spectre radiofréquence (RF). Dans la technologie OWC, les signaux transmis doivent être à valeur réelle et unipolaires pour satisfaire aux contraintes de la modulation d'intensité et de la détection directe (IM-DD). Les OWC ont fait l'objet de nombreuses études pour les applications haut débit, basées sur la modulation d'impulsion en amplitude (PAM), le multiplexage par répartition en fréquences orthogonales optique (O-OFDM), etc. Des recherches récentes ont confirmé l'intérêt des OWC pour des applications bas débit (100 kbps à 1 Mbps), nécessitant une grande efficacité énergétique. Dans ce contexte, la modulation par déplacement de fréquence (FSK) a suscité un intérêt considérable. Pour les systèmes OWC IM-DD, la modulation M-aire FSK classique n'est pas compatible en raison de la nature bipolaire des formes d'ondes FSK, mais 2 variantes compatibles ont été introduites dans la littérature et nous serviront de référence: la modulation à courant direct (DC)-FSK et la modulation unipolaire (U)-FSK.

Ce travail de thèse se concentre ainsi sur les approches de modulation à haute efficacité énergétique pour les OWC, basées sur des extensions/adaptations de la modulation conventionnelle M-aire FSK. Après un examen de l'état de l'art, un nouveau schéma de modulation appelé M-aire asymmetrically clipped (AC)-FSK est présenté pour les OWC à haute efficacité énergétique et bas débit. Les récepteurs traditionnels tels que le récepteur optimal dans le domaine temporel (basé sur la détection par maximum de vraisemblance (ML)) et le récepteur sous-optimal (basé sur la détection par DCT à 1 coefficient) présentent un compromis entre l'efficacité énergétique et la complexité du récepteur. Un nouveau récepteur à faible complexité opérant dans le domaine des fréquences (FD), appelé récepteur harmonique à L coefficients, est proposé pour les modulations M-aire AC-FSK (proposée) et M-aire U-FSK (littérature). Ce dernier améliore le compromis entre l'efficacité énergétique et la complexité du récepteur. Les résultats de simulation confirment que la performance en taux d'erreur binaire (BER) de la M-aire AC-FSK proposée est bien meilleure que celle de la M-aire DC-FSK de l'état de l'art, et qu'elle est légèrement améliorée par rapport à celle de la modulation M-aire U-FSK de la littérature. De plus, les résultats de simulation confirment également que le récepteur harmonique à L-coefficients pour la M-aire AC-FSK et la M-aire U-FSK approchent les performances du récepteur optimal ML, avec l'avantage d'une réduction importante de la complexité du récepteur.

Deuxièmement, une nouvelle approche de modulation, appelée Asymmetrically Clipped Frequency and Phase Shift Keying (AC-FPSK) est proposée pour les applications OWC IM-DD. Elle est basée sur

l'amalgame de la modulation M-aire AC-FSK et de la modulation par déplacement de phase (PSK). Il est mis en évidence que la modulation AC-FPSK présente une amélioration du compromis entre efficacités énergétique et spectrale par rapport à la modulation M-aire AC-FSK.

Enfin, une démonstration expérimentale de la modulation M-aire AC-FSK proposée et du récepteur harmonique à L coefficients proposé est présentée et les résultats sont comparés aux modulations de type FSK de la littérature. Le dispositif expérimental est basé sur des composants disponibles dans le commerce et un banc d'essai radio logicielle (SDR). Les résultats expérimentaux permettent de confirmer le bien fondé des schémas proposés dans la thèse.

Mots clés: Communications optiques sans fil, modulations numériques, modulation d'intensité et détection directe, modulation efficace en énergie, modulation par déplacement de fréquence, traitement du signal, LEDs, Radio-Logicielle, transformée discrète en cosinus, récepteur d'harmoniques, Internet des objets.

Résumé Étendu

Avec l'introduction de l'Internet des objets (IdO), un grand nombre de connexions sans fil vers des plateformes d'hébergement de données via Internet sont attendues pour un large éventail de dispositifs. Actuellement, les dispositifs IdO utilisent les ondes radiofréquences (RF) pour leurs communications, ce qui consomme une quantité importante de fréquences. Il en résulte un problème de rareté du spectre RF. Par conséquent, une solution alternative peut être d'un grand intérêt. À cet égard, l'intégration des communications optiques sans fil (OWC) avec l'IdO est un candidat crédible pour résoudre le problème de la rareté du spectre RF. En outre, les communications optiques sans fil offrent certains avantages potentiels, comme un spectre libre sans licence, la sécurité de la transmission des données, une faible complexité, l'absence d'interférence avec les communications RF et une communication potentiellement écologique à faible empreinte carbone (CO_2). Il convient cependant de noter qu'une contrainte des systèmes OWC à modulation d'intensité et détection directe (IM-DD) est que les signaux transmis doivent avoir une amplitude à valeur réelle et unipolaire.

De nombreuses recherches ont déjà été menées sur les applications IdO à haut débit, qui utilisent généralement des schémas de modulation à haut rendement spectral, tels que la modulation par impulsions (PAM) ou multiplexage par répartition en fréquences orthogonales optique (O-OFDM). Les modulations linéaires, telles que la M-aire PAM, sont plus simples à mettre en œuvre pour les systèmes OWC. Leur efficacité spectrale augmente avec la cardinalité de l'alphabet, mais en même temps, l'énergie électrique (ou optique) requise par bit, $E_{\mathrm{b(elec)}}$ (ou $E_{\mathrm{b(opt)}}$), augmente également pour atteindre un taux d'erreur binaire (BER) ciblé. Autrement dit, la modulation M-aire PAM est donc moins efficace sur le plan énergétique lorsque le nombre d'états M augmente, la meilleure efficacité énergétique étant déjà obtenue dans le cas binaire ($M = 2$).

Des recherches récentes ont confirmé que l'OWC peut également être utilisé pour des applications IdO bas débit (jusqu'à 1 Mbps maximum) et à haute efficacité énergétique. À cet égard, les modulations orthogonales, telles que la modulation par position (PPM) et la modulation par déplacement de fréquence (FSK), atteignent une efficacité énergétique plus élevée en sacrifiant l'efficacité spectrale (SE). Le comportement des modulations orthogonales est ainsi en totale opposition avec celui des modulations linéaires, car l'efficacité énergétique des modulations orthogonales augmente avec la cardinalité de l'alphabet, M, tandis que l'efficacité spectrale décroit, en $\log_2(M)/M$ bit/sec/Hertz. Parmi les modulations orthogonales, la M-aire PPM a été largement étudiée pour les systèmes OWC. Néanmoins, la modulation M-aire PPM est confrontée à de sérieux inconvénients, tels que:

(i) un rapport élevé entre la puissance de crête et la puissance moyenne, alors que la dynamique de modulation des LED est limitée; (ii) des problèmes de synchronisation au niveau du récepteur; et (iii) un fort impact des canaux à trajets multiples sur les performances en taux d'erreur binaire (BER). La modulation M-aire FSK, proposée initialement dans le contexte des communications RF, permet d'atténuer les problèmes qui viennent d'être mentionnés pour la M-aire PPM. Cependant, étant donné que les formes d'onde M-aire FSK originales sont par nature bipolaires (et donc non compatibles IM-DD), de nouvelles modulations M-aire FSK unipolaires et à valeur réelle ont du être introduites dans la littérature, afin de satisfaire aux contraintes IM-DD des systèmes OWC; il s'agit des modulations à courant direct M-aire (DC)-FSK et des modulations unipolaires M-aire (U)-FSK.

Le dictionnaire M-aire DC-FSK, $\mathscr{D}^{\mathrm{DC}}$, est dérivé du dictionnaire conventionnel M-aire FSK, $\mathscr{D}^{\mathrm{FSK}}$, en ajoutant simplement une composante continue ou DC-offset à toutes les formes d'onde FSK afin de les rendre unipolaires. Néanmoins, l'ajout d'un DC-offset aux formes d'onde FSK entraîne un gaspillage d'énergie. D'autre part, le dictionnaire M-aire U-FSK, $\mathscr{D}^{\mathrm{U}}$, est également généré à partir du dictionnaire M-aire FSK classique, $\mathscr{D}^{\mathrm{FSK}}$, en transmettant séquentiellement les échantillons positifs de la forme d'onde FSK dans la première (demi-)période symbole, puis l'opposé des échantillons négatifs dans la seconde (demi-)période symbole. De plus, des récepteurs traditionnels, tels que le récepteur optimal à maximum de vraisemblance (ML) opérant dans le domaine temporel (TD), et le récepteur sous-optimal basé sur la transformée en cosinus discrète (DCT) à 1 coeffecient, ont également été introduits pour les modulations M-aire DC-FSK et M-aire U-FSK par l'équipe communication du Gipsa-lab avant le début de ce travail de thèse. Les résultats de simulation ont confirmé que la M-aire U-FSK présente une meilleure efficacité énergétique que la modulation M-aire DC-FSK et que les modulations linéaires, en particulier lorsqu'un récepteur optimal à maximum de vraisemblance (ML) dans le domaine temporel (TD) est considéré. Les simulations ont également confirmé que le récepteur TD ML optimal permet d'obtenir un gain d'efficacité énergétique important par rapport au récepteur DCT à 1 coefficient pour les modulations M-aire DC-FSK et M-aire U-FSK, mais au prix d'une plus grande complexité de calcul. En effet, la complexité du récepteur TD ML optimal augmente de façon quadratique avec M. Par conséquent, il existe un compromis entre l'efficacité énergétique et la complexité du récepteur.

Dans ce travail de thèse, nous avons proposé de nouvelles modulations FSK efficaces en énergie pour les systèmes OWC, appelées M-aire Asymmetrically Clipped (AC)-FSK et $(M_{\perp}, M_{\phi})$-Asymmetrically Clipped Frequency and Phase Shift Keying (AC- FPSK), qui sont compatibles avec les applications IM-DD. En outre, l'étude spectrale de la M-aire AC-FSK et de la $(M_{\perp}, M_{\phi})$-AC-FPSK nous a permis de proposer un nouveau récepteur harmonique à 2 coefficients dans le domaine des fréquences (FD), qui s'avère être peu complexe. Nous allons brièvement présenter ces 3 contributions à la suite, ainsi qu'un bref résumé des expérimentations menées.

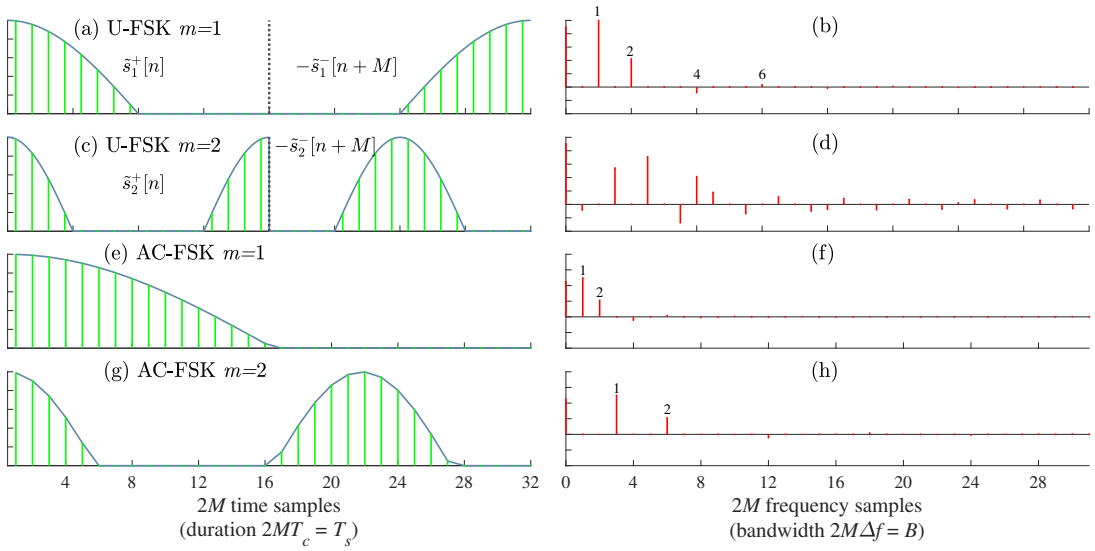

Fig. 1 (a) et (c) représentent les formes d'onde impaires et paires M-aire U-FSK dans le domaine temporel ($m = 1$ et 2, respectivement), tandis que (b) et (d) représentent leurs homologues dans le domaine fréquentiel, en considérant $M = 16$. (e) et (g) représentent les formes d'onde M-aire AC-FSK dans le domaine temporel ($m = 1$ et 2, respectivement), tandis que (f) et (h) représentent leurs homologues dans le domaine fréquentiel, en considérant $M = 16$.

1. Proposition de la modulation M-aire AC-FSK et de son récepteur harmonique à faible complexité

Le dictionnaire M-aire AC-FSK, $\mathscr{D}^{\mathrm{AC}}$, est dérivé du dictionnaire $2M$-aire FSK classique, $\mathscr{D}^{\mathrm{2M-FSK}}$, en éliminant (c'est à dire en forçant à zéro) les parties négatives de chaque forme d'onde FSK impaire. Pour la modulation AC-FSK, seules les formes d'onde FSK écrêtées de fréquence impaire sont considérées pour deux raisons:

- Il existe une propriété dite de symétrie de demi-onde pour les formes d'onde de fréquence impaire. Cela signifie que pour chaque échantillon de la partie des amplitudes positives (d'une forme d'onde de fréquence impaire), il existe un échantillon de même amplitude dans la partie des amplitudes négatives. Ainsi, la partie négative de chaque forme d'onde à fréquence impaire peut être écrêtée sans perte d'information.

- L'écrêtage de la partie négative des formes d'onde bipolaires induit une distorsion harmonique dont les féquences correspondent aux fréquences paires des formes d'ondes. Si seules les formes d'onde de fréquence impaire sont utilisées pour les communications, l'interférence entre les formes d'onde écrêtées peut donc être minimisée.

Les figures 1 (e) et (g) illustrent les formes d'onde de la modulation M-aire AC-FSK dans le domaine temporel pour $m = 1$ et $m = 2$, respectivement, en considérant $M = 16$. On peut voir que la partie négative de chaque forme d'onde est forcée à zéro. La distance euclidienne minimale au carré

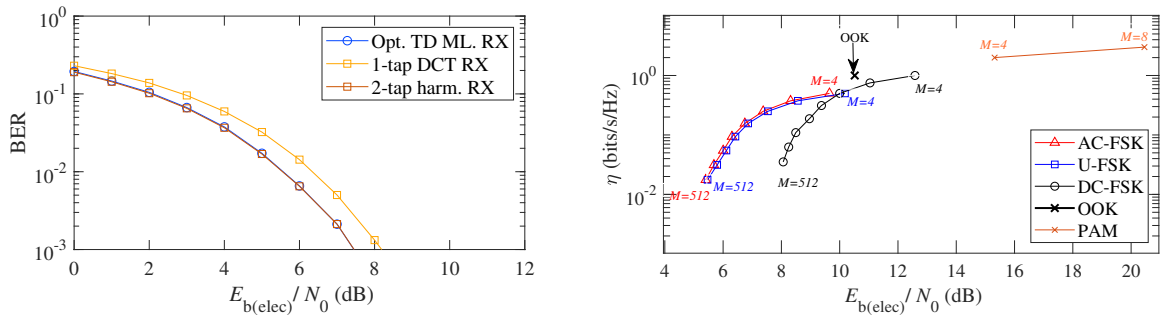

(a) (b)

Fig. 2 (a) Comparaison des courbes de BER versus $E_{b(elec)}/N_0$ pour la modulation M-aire AC-FSK obtenues avec le récepteur harmonique à 2 coefficients proposé, avec le récepteur ML optimal dans le domaine temporel, et avec le récepteur à 1 coefficient. (b) Efficacité spectrale η versus le $E_{b(elec)}/N_0$ nécessaire pour obtenir un BER de 10^{-3} pour les modulations M-aire AC-FSK, M-aire U-FSK, M-aire DC-FSK, OOK et M-aire PAM avec différents ordres de modulation M et en utilisant des récepteurs optimaux (canal AWGN).

entre les paires de formes d'onde a été étudiée et a conduit à la formulation de l'expression théorique de la probabilité d'erreur binaire pour la modulation M-aire AC-FSK, en considérant un canal à Bruit Blanc Additif Gaussien (AWGN) et un récepteur TD ML optimal.

De même, les figures 1 (f) et (h) illustrent les formes d'onde M-aire AC-FSK dans le domaine fréquentiel, pour $m = 1$ et $m = 2$, respectivement, obtenues par DCT. À partir de ces spectres, on peut déduire que la majeure partie de l'énergie du symbole (environ 99%) est distribuée sur 2 coefficients (en ignorant le coefficient DC correspondant à la composante continue), tandis que les autres coefficients ont une énergie très faible et peuvent donc être négligés. Cette observation nous a conduit à la proposition d'un nouveau récepteur pour la modulation M-aire AC-FSK, opérant en fréquence (FD), que l'on a nommé récepteur harmonique à 2 coefficients. Ce récepteur peut atteindre une performance (en BER) presque similaire à celle du récepteur TD ML optimal, mais avec l'avantage d'une réduction importante de complexité.

Le récepteur harmonique à 2 coefficients proposé utilise la DCT d'ordre M_c ainsi que des calculs de corrélation dans le domaine fréquentiel pour identifier les symboles transmis, où $M_c = 2M$ est le nombre de coefficients non-nuls conservés par forme d'onde. Son processus de fonctionnement se déroule en deux étapes: dans la première étape hors ligne, la DCT d'ordre M_c est appliquée à toutes les formes d'onde M-aire AC-FSK pour obtenir des formes d'onde AC-FSK en fréquence (FD). Ensuite, les deux coefficients les plus significatifs (en ignorant le coefficient DC) pour chaque forme d'onde sont sélectionnés et stockés dans une table (LUT). Dans la deuxième étape en ligne, la DCT d'ordre M_c est appliquée à la forme d'onde reçue pour la passer dans le domaine fréquentiel (FD). Enfin, la fréquence transmise est identifiée en cherchant le maximum de corrélation, dans le domaine fréquentiel, entre les formes d'onde de la table (LUT) et la forme d'onde reçue.

La figure 2 (a) illustre les performances en BER versus $E_{b(elec)}/N_0$ de la modulation M-aire AC-FSK obtenues avec le récepteur harmonique à 2 coefficients, en comparaison avec celles obtenues

avec le récepteur TD ML optimal et le récepteur DCT à 1 coefficient. Les résultats de simulation de la figure 2 (a) confirment que le récepteur harmonique à 2 coefficients atteint un BER presque similaire à celui du récepteur TD ML optimal, avec les avantages d'une réduction de la complexité de $98,7\%$ par rapport au récepteur TD ML optimal pour $M = 1024$. De plus, le récepteur harmonique à 2 coefficients pour la modulation M-aire AC-FSK présente de bien meilleures performances en BER que le récepteur à 1 coefficient basé sur DCT.

La figure 2 (b) illustre l'efficacité spectrale η versus $E_{\mathrm{b(elec)}}/N_0$ requis pour obtenir un BER de 10^{-3} à l'aide d'un récepteur TD ML optimal pour la modulation M-aire AC-FSK proposée, par rapport aux modulations basées sur M-aire FSK de l'état de l'art (c'est-à-dire M-aire DC-FSK et M-aire U-FSK), et par rapport aux modulations linéaires (OOK et M-aire PAM). Il ressort de la figure 2 (b) que M-aire AC-FSK montre un gain d'environ 2 dB par rapport à M-aire DC-FSK, en considérant $M \geq 16$, tandis que M-aire AC-FSK montre une performance légèrement meilleure en termes de η versus $E_{\mathrm{b(elec)}}/N_0$ requis, par rapport à la modulation M-aire U-FSK. De plus, les performances d'efficacité énergétique de OOK et de M-aire PAM sont moins bonnes par rapport à celles de la M-aire AC-FSK proposée, d'autant que l'efficacité énergétique de la M-aire PAM est affectée négativement par l'augmentation de M.

2. Récepteur d'Harmonique de L-tap proposé pour la modulation M-aire U-FSK

La même idée du récepteur d'harmonique opérant dans le domaine fréquentiel est également adoptée pour la modulation M-aire U-FSK, mais cette fois, le nombre de coefficients sélectionnés est différent en raison des différences observées entre les formes d'onde impaires et paires. Les figures 1 (a) et (c) illustrent les formes d'onde impaires et paires de la modulation M-aire U-FSK dans le domaine temporel ($m = 1$ et 2, respectivement), tandis que (b) et (d) illustrent leurs homologues dans le domaine fréquentiel, en considérant $M = 16$. On observe que la majeure partie de l'énergie du symbole (plus de 90% de l'énergie du symbole) est distribuée sur deux coefficients fréquentiels pour les formes d'onde impaires (comme $m = 1$ sur la figure 1 (a)). Mais pour les formes d'onde U-FSK paires (comme $m = 2$ sur la figure 1(d), on observe que l'énergie du symbole est distribuée sur davantage de coefficients. Les simulations ont confirmé que deux et douze coefficients fréquentiels sont nécessaires respectivement pour les formes d'onde U-FSK impaires et paires, pour obtenir un BER similaire à celui du récepteur ML optimal opérant dans le domaine temporel.

La figure 3 (a) illustre la courbe d'efficacité spectrale η versus $E_{\mathrm{b(elec)}}/N_0$ requis dans un canal AWGN pour obtenir un BER de 10^{-3} en modulation M-aire U-FSK, en considérant le récepteur harmonique à $(12,2)$ coefficients proposé, en comparaison avec le récepteur TD ML optimal traditionnel et avec le récepteur DCT à 1 coefficient. La figure 3 (a) montre que les performances du récepteur harmonique à $(12,2)$ coefficients proposé sont proches de celles du récepteur TD ML optimal avec une réduction significative de la complexité de $99,1\%$ pour $M = 1024$. L'écart de la valeur requise de

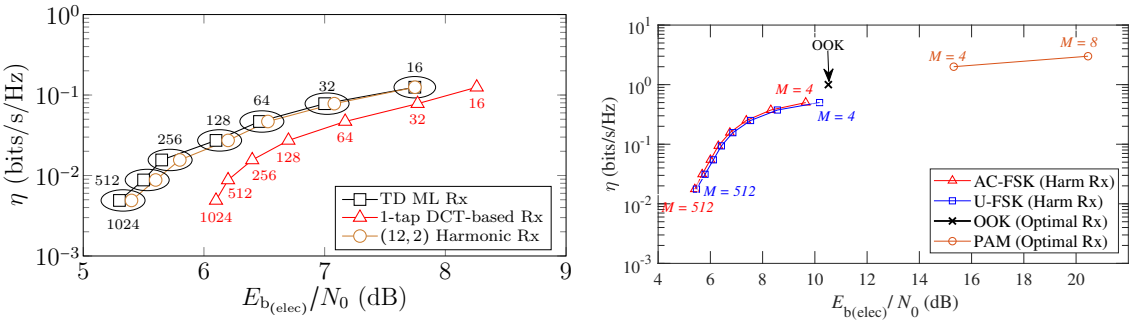

(a) (b)

Fig. 3 (a) Efficacité spectrale η versus $E_{b(elec)}/N_0$ requis pour un BER de 10^{-3} pour la modulation M-aire U-FSK opérant avec le récepteur harmonique à L coefficients proposé, en comparaison avec le récepteur ML optimal dans le domaine temporel et le récepteur à 1 coefficient basé sur la DCT. (b) Efficacité spectrale η versus $E_{b(elec)}/N_0$ requis pour un BER de 10^{-3} pour les modulations M-aire U-FSK, M-aire AC-FSK, OOK et M-aire PAM. Notez que le récepteur harmonique est considéré pour les modulations M-aire U-FSK et M-aire AC-FSK, tandis que le récepteur ML optimal dans le domaine temporel est considéré pour les modulations OOK et M-aire PAM.

$E_{b(elec)}/N_0$ pour le récepteur harmonique à $(12,2)$ coefficient par rapport au récepteur TD ML optimal n'est pas supérieur à 5% pour un BER cible de 10^{-3}. En outre, le récepteur harmonique à $(12,2)$ coefficients proposé pour la modulation M-aire U-FSK présente un gain en énergie par rapport au récepteur à 1 coefficient basé sur la DCT, qui croit avec M.

La figure 3 (b) montre l'efficacité spectrale η versus $E_{b(elec)}/N_0$ requis pour un BER cible de 10^{-3} en canal AWGN, tout en considérant un récepteur harmonique pour les modulations M-aire U-FSK et M-aire AC-FSK, et un récepteur TD ML optimal pour les modulations OOK et M-aire PAM. La figure 3 (b) confirme que les modulations M-aire U-FSK et M-aire AC-FSK présentent des performances approximativement similaires avec un récepteur harmonique, mais la complexité du récepteur harmonique en AC-FSK est inférieure de $41,6\%$ (respectivement $33,3\%$) par rapport à celle du récepteur harmonique en U-FSK pour $M = 16$ (respectivement $M = 128$). Ceci est dû au nombre limité de coefficients sélectionnés dans le cas du récepteur harmonique AC-FSK. En outre, les performances obtenues en modulations OOK et M-aire PAM avec récepteurs TD ML optimaux sont inférieures à celles obtenues en modulations M-aire AC-FSK et M-aire U-FSK avec le récepteur harmonique proposé.

3. Modulation $(M_\perp, M_\phi)$-AC-FPSK proposée

Le dictionnaire de formes d'onde AC-FPSK, $\mathscr{D}^{\mathrm{AC-FPSK}}$, est dérivé du dictionnaire M-aire AC-FSK, $\mathscr{D}^{\mathrm{AC-FSK}}$, en agrégeant la modulation par déplacement de phase (PSK) aux formes d'onde M-aire AC-FSK. Nous considérons $M_\perp$ formes d'onde AC-FSK, et que M_ϕ déphasages (en codage de Gray) sont ajoutés à chaque forme d'onde AC-FSK. Par conséquent, la notation $(M_\perp, M_\phi)$-AC-FPSK est utilisée pour représenter le schéma de modulation proposé, où le nombre total de formes d'onde du dictionnaire $\mathscr{D}^{\mathrm{AC-FPSK}}$ est $M = M_\perp \times M_\phi$.

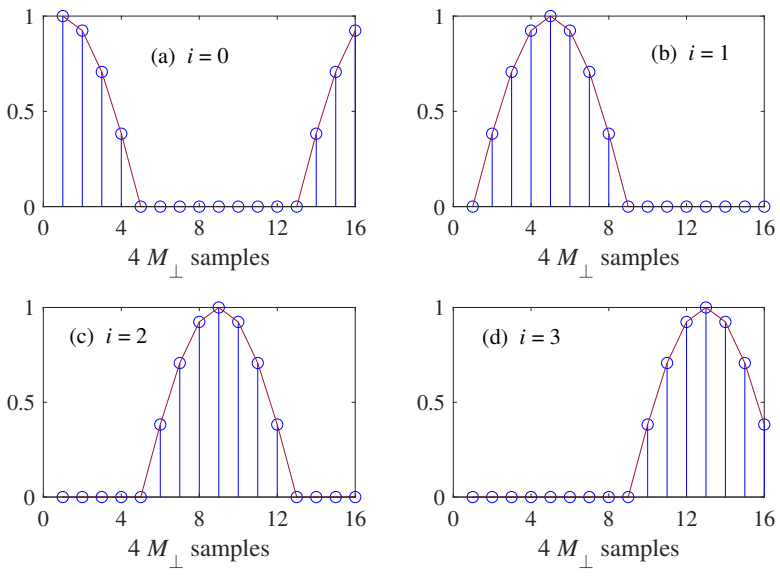

Fig. 4 Représentation du domaine temporel de la forme d'onde $(M_\perp, M_\phi)$-AC-FPSK pour $(M_\perp, M_\phi)$ = (4,4), avec un indice de fréquence $m = 1$. Ici, le nombre de phases ajoutées à chaque forme d'onde AC-FSK à l'aide du codage de Gray est de $M_\phi = 4$, c'est-à-dire que $i \in \{0,1,2,3\}$.

La figure 4 représente les formes d'onde $(M_\perp, M_\phi)$-AC-FPSK dans le domaine temporel pour l'indice de fréquence $m = 1$, en considérant $(M_\perp, M_\phi)$ = (4,4). Ici, quatre phases (c'est-à-dire $i \in \{0,1,2,3\}$) sont ajoutées selon le codage de Gray à une forme d'onde M-aire AC-FSK unique (avec un indice de fréquence $m = 1$), où deux formes d'onde voisines diffèrent par un déphasage de $\phi = \pi/2$.

Les récepteurs traditionnels tels que le récepteur TD ML optimal et le récepteur à transformée de Fourier discrète (DFT) à 1 coefficient sont présentés pour le schéma de modulation $(M_\perp, M_\phi)$-AC-FPSK proposé, tandis que l'analyse spectrale des formes d'onde $(M_\perp, M_\phi)$-AC-FPSK nous permet de proposer un récepteur harmonique (FD) quasi optimal et à faible complexité. Il utilise deux coefficients (harmoniques) avec des amplitudes significatives contenant plus de 90% de l'énergie du symbole. L'analyse de la complexité de $(M_\perp, M_\phi)$-AC-FPSK révèle qu'une réduction significative de la complexité du récepteur est atteinte pour le récepteur harmonique à 2 coefficients par rapport au récepteur TD ML optimal, tout en obtenant une performance en BER similaire. L'analyse de la distance euclidienne entre les paires de formes d'onde $(M_\perp, M_\phi)$-AC-FPSK en $\mathscr{D}^{\text{AC-FPSK}}$ permet d'obtenir des limites inférieures et supérieures analytiques de la probabilité d'erreur binaire théorique pour le récepteur ML avec canal AWGN. Les résultats de simulation ont confirmé que les limites inférieures et supérieures analytiques de la probabilité d'erreur binaire sont des bornes relativement précises. Les modulations M-aire AC-FSK et $(M_\perp, M_\phi)$-DC-FPSK seront utilisées comme références pour apprécier les performances en simulation de la nouvelle modulation $(M_\perp, M_\phi)$-AC-FPSK proposée.

La Fig. 5 (a) illustre l'efficacité spectrale η, en fonction de la valeur requise $E_{\text{b(elec)}}/N_0$ dans un canal AWGN pour obtenir un BER de 10^{-3} pour les méthodes proposées $(M_\perp, M_\phi)$-AC-FPSK,

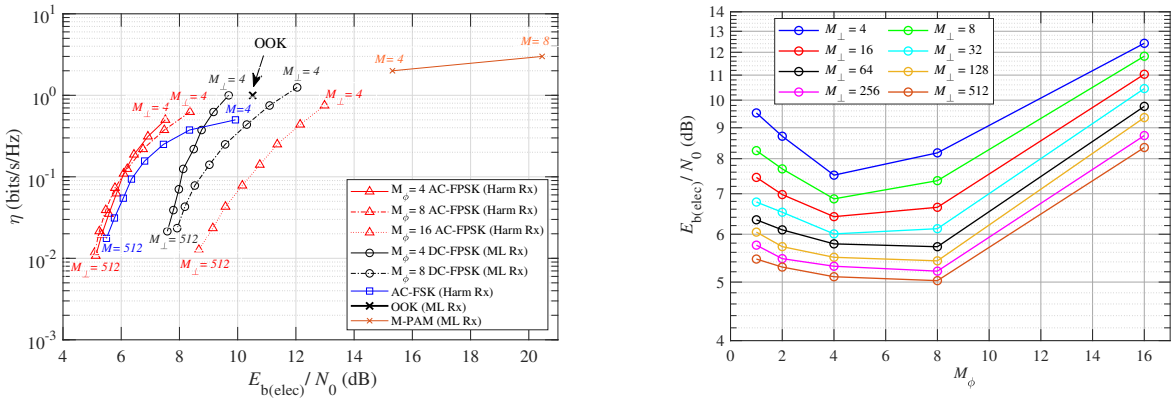

(a) (b)

Fig. 5 (a) Efficacité spectrale η versus $E_{\mathrm{b(elec)}}/N_0$ requis dans un canal AWGN pour obtenir un BER de 10^{-3} en modulations $(M_\perp, M_\phi)$-AC-FPSK, M-aire AC-FSK et $(M_\perp, M_\phi)$-DC-FPSK, en considérant différents $M_\perp$ et M_ϕ, (b) Évaluation de la valeur requise de $E_{\mathrm{b(elec)}}/N_0$ pour obtenir un BER de 10^{-3} pour différents M_ϕ et $M_\perp$, en considérant un récepteur harmonique à 2 coefficients pour $(M_\perp, M_\phi)$-AC-FPSK.

M-aire AC-FSK, $(M_\perp, M_\phi)$-DC-FPSK, OOK et M-aire PAM, en considérant $M_\perp \in \{4, 8, 16, \cdots, 512\}$ et $M_\phi \in \{4, 8, 16\}$. Notez que le récepteur harmonique FD est considéré pour $(M_\perp, M_\phi)$-AC-FPSK et M-aire AC-FSK, tandis que le récepteur ML optimal du domaine temporel est considéré pour $(M_\perp, M_\phi)$-DC-FPSK, OOK et M-aire PAM. La figure 5 (a) confirme que la modulation AC-FPSK présente de meilleures performances que la modulation M-aire AC-FSK pour une valeur de $M_\phi \leq 8$. Cela est dû à l'augmentation de l'efficacité spectrale de la AC-FPSK par rapport à la M-aire AC-FSK ordinaire, tandis que la distance euclidienne minimale au carré entre les paires de formes d'onde AC-FPSK n'est pas fortement affectée lorsque $M_\phi \leq 8$. De plus, la $(M_\perp, M_\phi)$-AC-FPSK permet un gain d'énergie d'environ 2 dB par rapport à la $(M_\perp, M_\phi)$-DC-FPSK pour $M \leq 8$. Pour $M_\phi = 16$, la $(M_\perp, M_\phi)$-AC-FPSK présente des performances dégradées par rapport à la M-aire AC-FSK en raison de la forte réduction de la distance euclidienne minimale au carré entre les paires de formes d'onde AC-FPSK, tandis que l'efficacité spectrale est améliorée avec un gain limité.

La figure 5 (b) illustre l'évaluation de la valeur requise de $E_{\mathrm{b(elec)}}$ pour $(M_\perp, M_\phi)$-AC-FPSK (en utilisant un récepteur harmonique à 2 coefficients) afin d'atteindre un BER ciblé de 10^{-3} pour différents $M_\perp$ et M_ϕ. On constate que le nombre optimal de phases est $M_\phi = 4$ lorsque $M_\perp \leq 32$, et $M_\phi = 8$ lorsque $M_\perp > 32$, ce qui minimise le $E_{\mathrm{b(elec)}}/N_0$ nécessaire pour atteindre un BER cible de 10^{-3}, c'est-à-dire qui maximise l'efficacité énergétique. Un bon choix pour le nombre de phases est $M_\phi = 8$ car il permet d'obtenir le meilleur compromis entre efficacité énergétique et efficacité spectrale, et conduit à la plus faible complexité du récepteur en réduisant $M_\perp$ pour un $M = M_\perp \times M_\phi$ donné, ce qui diminue la taille de la DFT du récepteur.

4. Résultats Expérimentaux pour la modulation M-aire AC-FSK proposée

Une démonstration expérimentale utilisant un prototype OWC interfacé à une plateforme radio logicielle (SDR) est réalisée. La modulation proposée M-aire AC-FSK et son récepteur harmonique associé sont mis en œuvre et les résultats expérimentaux sont comparés aux schémas de modulation FSK les plus récents avec récepteurs traditionnels. Le banc expérimental du prototype OWC est constitué de composants commerciaux disponibles sur le marché (COTS) qui sont interfacés avec les équipements SDR (USRP N210). La LED de l'émetteur est une LED RGBA (LED Engin LZA-00MA00) qui intègre 4 puces (une par couleur, c'est-à-dire rouge, vert, bleu et ambre). Nous avons utilisé la couleur verte de longueur d'onde $\lambda = 525$ nm dans les expériences pour transmettre les signaux de modulation désirés. La LED fonctionne dans une région relativement linéaire de la courbe d'intensité lumineuse (L-I), afin d'éviter les distorsions non linéaires supplémentaires des formes d'onde transmises.

En entrée du récepteur, un filtre optique vert (Thorlabs FD1D) est utilisé pour filtrer les longueurs d'onde indésirables de la lumière ambiante. Il est suivi d'un atténuateur optique accordable (Thorlabs NDC-50C-2M-A), qui est utilisé pour estimer les performances des systèmes OWC en modifiant la puissance optique reçue, en fonction de l'angle de rotation (0° à 360°). Ensuite, une phtotodiode (PD) PIN en silicium (Hamamatsu S10784) est utilisée pour recevoir les signaux optiques modulés en intensité et réalise la conversion directe des signaux optiques reçus en signaux électriques. Enfin, les signaux électriques sont transmis à l'équipement SDR (USRP N210), qui effectue la démodulation. L'équipement SDR (USRP N210) est interfacé avec l'outil logiciel Matlab, qui est utilisé pour effectuer la démodulation en temps réel afin de comparer la performance BER de la modulation M-aire AC-FSK proposée avec les modulations issues de la littérature basées également sur FSK.

L'expression théorique de la probabilité d'erreur binaire, issue de l'analyse de la distance euclidienne entre les formes d'onde de la modulation M-aire AC-FSK proposée, est utilisée pour réaliser une comparaison avec les résultats expérimentaux. Les performances expérimentales du BER en M-aire AC-FSK sont évaluées pour un récepteur TD ML optimal, un récepteur DCT à 1 coefficient et un récepteur harmonique à 2 coefficients. En outre, les résultats expérimentaux du récepteur harmonique pour les modulations M-aire AC-FSK et M-aire U-FSK sont également comparés.

La figure 6 (a) illustre les performances expérimentales du BER en fonction de la puissance optique reçue $P_{\mathrm{r(opt)}}$ pour la modulation M-aire AC-FSK en utilisant un récepteur TD ML optimal, un récepteur DCT à 1 coefficient et un récepteur harmonique à 2 coefficients sur canal optique à visibilité directe, tout en considérant $M = \{16, 128\}$. Il ressort de la figure 6 (a) que la performance en BER pour la M-aire AC-FSK est améliorée en augmentant l'ordre de la modulation en passant de $M = 16$ à 128, comme le prévoient l'étude théorique et les résultats de la simulation. Cela est dû à l'augmentation de la distance euclidienne entre les paires de formes d'onde du dictionnaire M-aire AC-FSK avec M, pour une énergie par bit donnée. En outre, le récepteur harmonique à 2 coefficients proposé présente des performances de BER presque similaires à celles du récepteur ML (domaine temporel) optimal pour $M = 16$ et 128, tandis que la complexité du récepteur harmonique à 2 coefficients par rapport au

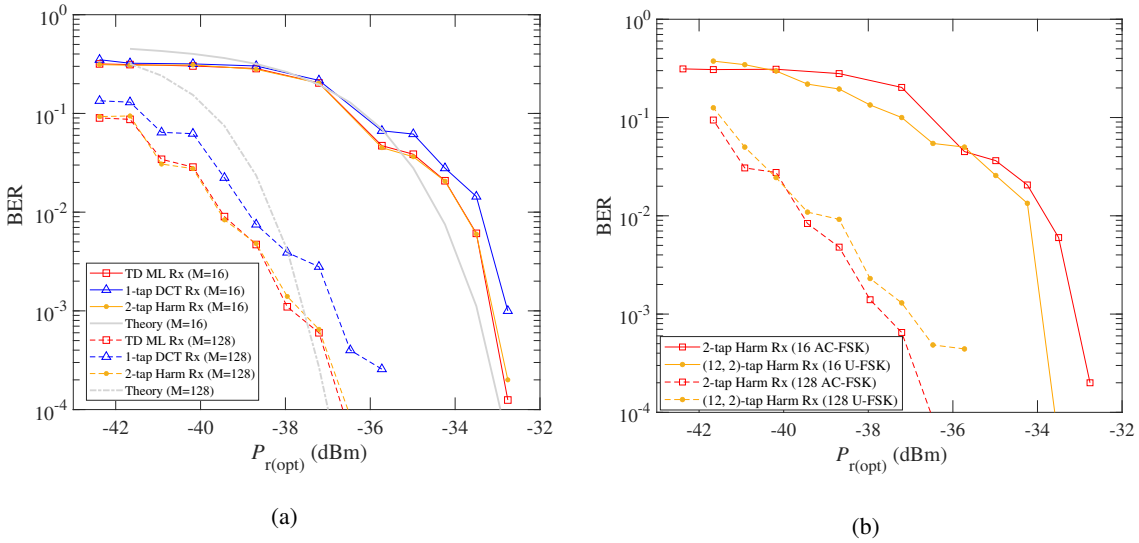

(a) (b)

Fig. 6 (a) Performance expérimentale et théorique (Theory) de la performance en BER versus $P_{r(opt)}$ en modulation M-aire AC-FSK, en considérant $M = \{16, 128\}$, (b) Performance expérimentale en BER versus $P_{r(opt)}$ avec récepteur harmonique à L coefficients (Harm Rx) pour les modulations M-aire AC-FSK et M-aire U-FSK, en considérant $M = \{16, 128\}$.

récepteur ML optimal est réduite de $56,3\%$ (respectivement $92,2\%$) pour $M = 16$ (respectivement $M = 128$). Le récepteur harmonique à 2 coefficients proposé pour la modulation M-aire AC-FSK a un bien meilleur BER à puissance optique $P_{r(opt)}$ donnée que le récepteur basé sur la DCT à 1 coefficient. Notamment, la puissance optique requise $P_{r(opt)}$ afin d'obtenir un BER de 10^{-3}, pour un récepteur harmonique à 2 coefficients, est d'environ 1 dB de moins que celle nécessaire avec le réceteur DCT à 1 coefficient. Il est également confirmé que les résultats expérimentaux sont cohérents avec l'approximation théorique.

La figure 6 (b) illustre le BER expérimental en fonction de la puissance optique reçue $P_{r(opt)}$, comparé pour les modulations M-aire AC-FSK et M-aire U-FSK, en considérant un récepteur harmonique à L coefficients et $M = \{16, 128\}$. Notez que $L = 2$ pour le récepteur harmonique AC-FSK, et $L_e = 12$ et $L_o = 2$ pour le récepteur harmonique U-FSK. Les résultats expérimentaux de la figure 6 (b) montrent que le récepteur harmonique à L coefficients pour les modulations M-aire AC-FSK et M-aire U-FSK a des performances presque similaires pour $M = 16$, tandis que pour $M = 128$, on observe une dégradation des performances en M-aire U-FSK par rapport à M-aire AC-FSK. Cela peut être dû au filtrage passe-bas du récepteur sur les nombreuses harmoniques de la forme d'onde U-FSK. D'autre part, la complexité du récepteur harmonique à L coefficients pour la M-aire AC-FSK est réduite de $41,6\%$ (respectivement $33,3\%$) pour $M = 16$ (respectivement $M = 128$) par rapport au cas M-aire U-FSK. Cela s'explique par le fait que seul un nombre limité de coefficients (c'est-à-dire $L = 2$) est utilisé par le récepteur harmonique de la modulation M-aire AC-FSK, en comparaison au récepteur harmonique de la modulation M-aire U-FSK (c'est-à-dire $L_e = 12$ et $L_o = 2$).

Conclusion: En conclusion, il semble que les schémas que nous avons proposés (c'est-à-dire, les modulations M-aire AC-FSK et $(M_{\perp}, M_{\phi})$-AC-FPSK, ainsi que le récepteur harmonique à faible complexité opérant en fréquence avec L coefficients fréquentiels) sont relativement bons à mettre en œuvre pour les applications OWC à haut rendement énergétique et à bas débit.

Declaration

I declare that the work in this dissertation was carried out in accordance with the requirements of the University's Regulations and Code of Practice for Research Degree Program and that it has not been submitted for any other academic award. Except where indicated by specific reference in the text, the work is the candidate's own work. Work done in collaboration with, or with the assistance of, others, is indicated as such. Any views expressed in the dissertation are those of the author.

June 2023

Table of contents

List of figures

List of tables

List of Acronyms

AC-FSK	Asymmetrically Clipped Frequency Shift Keying
ACO-OFDM	Asymmetrically Clipped Optical-Orthogonal Frequency-Division
ADC	Analog-to-Digital Converter
AP	Access Point
AWGN	Additive White Gaussian Noise
AC-FPSK	Asymmetrically Clipped-Frequency Phase Shift Keying
BER	Bit Error Rate
C2C	Chip-to-Chip
CIR	Channel Impulse Response
CO_2	Carbon Dioxide
D2D	Device-to-Device
DAC	Digital-to-Analog Converter
DC	Direct Current
DC-FSK	Direct Current-Frequency Shift Keying
DCT	Discrete Cosine Transform
DFT	Discrete Fourier Transform
DSP	Digital Signal Processing
ECG	Electrocardiography
EM	Electromagnetic
EMG	Electromyography
EMI	Electromagnetic Interference
FD	Frequency Domain
FFT	Fast Fourier Transform
FoV	Field-of-View
FSK	Frequency Shift Keying
FSO	Free Space Optics
FSOI	Free Space Optics Interconnects
GaS	Gallium Arsenide
GaN	Gallium Nitride
HPF	High Pass Filter
HS	Hermitian Symmetry
IDCT	Inverse Discrete Cosine Transform
IDFT	Inverse Discrete Fourier Transform
IFFT	Inverse Fast Fourier Transform
IF	Intermediate Frequency

IR	Infrared
IM-DD	Intensity Modulation and Direct Detection
IoT	Internet of Things
ISI	Inter-Symbol Interference
LAN	Local Area Network
LB	Lower Bound
LD	Laser-Diode
LED	Light-Emitting Diode
LiFi	Light-Fidelity
LPWAN	Low Power Wide Area Networks
LoS	Line-of-Sight
MA	Multiple Access
MAN	Metropolitan Area Network
MIMO	Multiple-Input Multiple-Output
ML	Maximum Likelihood
mmWave	Millimeter Wave
M2M	Machine-to-Machine
NLOS	Non Line-of-Sight
OC	Optical Communication
OFDM	Orthogonal Frequency-Division Multiple-Access
O-OFDM	Optical-Orthogonal Frequency-Division Multiple-Access
OOK	On-Off Keying
OOK-NRZ	On-Off Keying Non-Return to Zero
OOK-RZ	On-Off Keying Return to Zero
OSR	Over Sampling Ratio
OWC	Optical Wireless Communication
PAM	Pulse Amplitude Modulation
PAN	Personal Area Network
PAPR	Peak to Average Power Ratio
PD	Photo-diode
PMOPR	Peak-to-Mean Optical Power ratio
PPM	Pulse Position Modulation
PSD	Power Spectral Density
PSK	Phase Shift Keying
P/S	Parallel-to-Serial
RF	Radio Frequency
RGBA	Red-Green-Blue-Amber
SDR	Software Defined Radio
SE	Spectral Efficiency

SER	Symbol Error Rate
SNR	Signal to Noise Ratio
S/P	Serial-to-Parallel
TD	Time-Domain
UB	Upper Bound
UE	User Equipment
USRP	Universal Software Radio Peripheral
UV	Ultravoilet
U-FSK	Unipolar-Frequency Shift Keying
VL	Visible Light
VLC	Visible Light Communication
V2V	Vehicle-to-Vehicle
V2I	Vehicle-to-Infrastructure
WBAN	Wireless Body Area Network
WiFi	Wireless-Fidelity
WLAN	Wireless Local Area Network
WPAN	Wireless Personal Area Network

Introduction

With the emergence of the Internet-of-Things (IoT), the number of connected devices are expected to grow up to 30 billions in 2030, as shown in Fig. 7 [1]. In IoT, things or items can exchange information and transmit data to other devices and systems. The information they share can be about objects to which they are attached and the environment they are in (through sensors that come in many shapes for different parameters). Smart devices and machines can also share information about their internal state. Examples of things range from consumer-oriented devices such as wearable and smart home solutions (Consumer IoT) to connected equipment in the enterprise (Enterprise IoT), for instance in a smart office, and industrial assets such as machines, robots, or even workers in smart factories and industrial facilities (Industrial IoT, the essential component of Industry 4.0). In this context, it is worth mentioning that a large set of applications will require relatively low data rates to communicate (typically lower than 1 Mbps) to allow exchange of small amounts of information between sensors and their central node, for example [2]. Generally, IoT technology uses the radio-frequency (RF) spectrum for communication and is expected to require a significant amount of available RF resource to connect IoT devices, while RF spectrum is already saturated. Moreover, RF transceivers are known to exhibit significant power consumption, and billions of RF transceivers in IoT devices may lead to a strong impact on the overall carbon footprint of information and communication technologies (ICT). In this context, optical wireless communication (OWC) is touted as a complementary technology to mitigate the scarcity issue of the RF spectrum. Moreover, OWC communication systems offer considerable interests over RF communications: they can rely on massively deployed low power consumption LED lighting; they allow for secure communications due to the confinement of optical waves into buildings (or vehicles); they do not interfere with currently used RF technologies. However, to implement low power OWC systems for IoT applications, it is necessary to investigate on energy efficient modulation schemes. For a typical OWC system using intensity modulation and direct detection (IM-DD), the modulation signal should be unipolar and positive.

Extensive research has been carried out on high data rate IoT applications, which may be based on the high spectral efficient modulation schemes, such as pulse-amplitude modulation (PAM), optical-orthogonal frequency-division multiplexing (O-OFDM), etc. Only very few studies on low power OWC technologies dedicated to low data-rate IoT communications have been reported in the literature. In this context, frequency shift keying (FSK) raised a substantial interest for OWC applications. As original FSK modulation is not compatible with the IM-DD OWC system due to

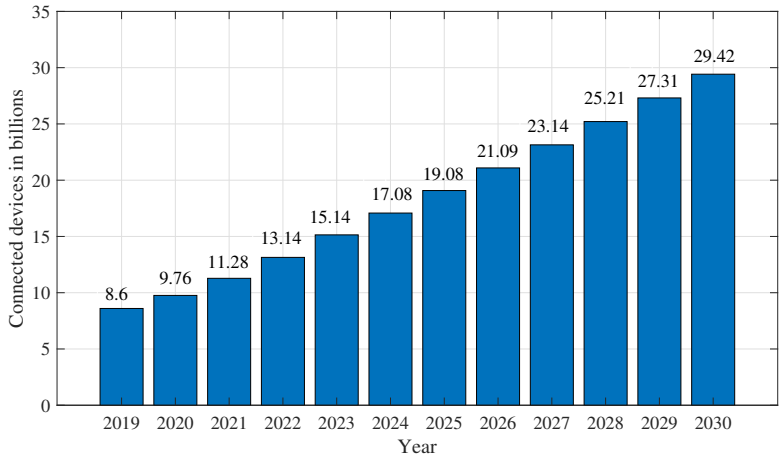

Fig. 7 Number of IoT connected devices worldwide (2019-2022, with forecasts upto 2030) [1].

bipolar nature, therefore, two variants of FSK-based modulations (i.e., direct current (DC)-FSK and unipolar (U)-FSK) have been introduced recently by Gipsa-Lab which are compatible with IM-DD OWC systems.

In this work, we propose a new variant of M-ary FSK called M-ary Asymmetrically Clipped (AC)-FSK which is compatible with IM-DD OWC systems to address the challenge of energy efficient modulation scheme for low data-rate OWC. The spectral analysis of M-ary AC-FSK waveforms allows us to build a low complexity frequency-domain (FD) harmonic receiver, i.e., 2-tap harmonic receiver which has almost the same bit error rate (BER) performance as the optimal ML receiver but with the drastic reduction of receiver complexity. The same approach of harmonic receiver is adopted for the state-of-the-art M-ary U-FSK, leading to the proposition of L-tap harmonic receiver that also reaches the optimal ML receiver performance with a reduce complexity.

Moreover, a new modulation approach (called AC-FPSK) is proposed for OWC systems that is based on the amalgamation of the proposed M-ary AC-FSK and phase-shift keying (PSK). AC-FPSK further improves the energy efficiency versus spectral efficiency trade-off as compared to M-ary AC-FSK. Finally, an experimental demonstration, based on the software defined radio (SDR) is presented for the proposed M-ary AC-FSK and the proposed L-tap harmonic receiver for both M-ary AC-FSK and the state-of-the-art U-FSK. Experimental results are compliant with the simulation results and highlight the interest of the proposed modulation schemes.

Thesis Organization

This thesis is organized as follows:

Chapter 1 is dedicated to the introduction of fundamentals of optical wireless communications (OWC). After a review of the general context of the OWC systems, some of the advantages and

dis-advantages of the OWC systems are introduced. It is followed by the applications of the OWC systems. The basic architecture design of the OWC systems is then introduced which is based on the optical transmitter, the optical wireless channel and the optical receiver. Afterward, a few linear and orthogonal modulation schemes for OWC systems are introduced. Finally, the thesis contribution is presented at the end of the chapter.

Chapter 2 introduces the conventional bipolar M-ary FSK and the two adapted variants of M-ary FSK existing for OWC systems, i.e., M-ary DC-FSK and M-ary U-FSK. Different parameters of M-ary FSK and its variants are also discussed. These modulation schemes are used as the state-of-the-art for our proposed work in the second part of the *Chapter* 2 and also the sub-sequent chapters. Moreover, the chapter also presents the proposed low complexity FD L-tap harmonic receiver for M-ary U-FSK. BER performance of the proposed L-tap harmonic receiver for M-ary U-FSK is also discussed in the simulation results section.

In *Chapter* 3, the proposed M-ary AC-FSK modulation scheme is introduced. Key performance parameters for the proposed M-ary AC-FSK, such as TD and FD waveform analysis, symbol energy, squared Euclidean distance analysis, spectral efficiency, transmitter and different receiver architecture along with the complexity comparison, BER probability analysis are determined. Simulation results of the proposed M-ary AC-FSK are presented, which reveal the superiority in terms of energy efficiency of the proposed M-ary AC-FSK over the state-of-the-art M-ary DC-FSK, M-ary U-FSK, OOK and M-PAM. Moreover, an amalgamation of M-ary AC-FSK and PSK, referred to as AC-FPSK is also introduced in the second part of chapter along with its key parameters. Simulation results are presented at the end of the chapter that reveal the superiority in terms of energy efficiency of the proposed AC-FPSK over the previously proposed M-ary AC-FSK and state-of-the-art DC-FPSK.

In *Chapter* 4, the experimental demonstration for the proposed M-ary AC-FSK is presented which is based on SDR test bench and optical wireless communication prototype based on components off-the-shelf. Experimental results of the proposed M-ary AC-FSK are compared with the ones of M-ary U-FSK. The experimental results are compliant with the simulation results and the theoretical bit error probability.

In the final section, a conclusion is drawn on the interest of the proposed modulation solutions for low power OWC systems and perspectives of this work are discussed.

List of Publications

Journal Publications

J1 : ***M. J. Khan***, A.W. Azim, Y. Le Guennec, G. Maury, and L. Ros, "Theoretical and experimental analysis of asymmetrically clipped-FSK VLC systems", *IEEE Photonics Journal,* 14(3):1-9, 2022.

J2 : A. W. Azim, ***M. J. Khan***, O. D. Wulf, Y. Le Guennec, G. Maury, and L. Ros, "Near-optimal low-complexity harmonic receiver for unipolar-FSK". *IEEE Wireless Communications Letters*, 10(11):2421–2425, 2021.

Conference Publications

International Conferences

C1 : ***M. J. Khan***, A.W. Azim, Y. Le Guennec, G. Maury, and L. Ros, "Asymmetrically clipped-FSK modulation for energy efficient visible light communications". In *2021 IEEE 32nd Annual International Symposium on Personal, Indoor and Mobile Radio Communications (PIMRC)*, pages 458–464. IEEE, 2021.

C2 : P. Miqueu, ***M. J. Khan***, Y. Le Guennec, and L. Ros, "Turbo-DC-FSK: Joint Turbo coding and FSK-based modulation for visible light communications". In *2022 Joint European Conference on Networks and Communications & 6G Summit (EuCNC/6G Summit)*, pages 25–30. IEEE, 2022.

National Conference

C3 : ***M. J. Khan***, Y. Le Guennec, and L. Ros, "Démonstration d'une modulation AC-FSK économe en énergie pour les communications optiques sans-fil". In *Colloque Gretsi, Nancy, France, Sept.2022*, pp. 1-1, 2022.

Communication

COM : Y. Le Guennec, ***M. J. Khan***, A.W. Azim, and L. Ros, "Visible Light Communications for a Greener IoT". In *Webminar GDR Ondes*, March 11th, 2021.

Article to be Submitted in Journal

S1 : ***M. J. Khan***, A.W. Azim, Y. Le Guennec, G. Maury, and L. Ros, "Asymmetrically clipped frequency and phase-shift keying for low energy optical wireless communications". To be submitted in Journal.

Chapter 1

Introduction to Optical Wireless Communications and Thesis Objectives

Contents

This chapter is dedicated to the context of the thesis by presenting general elements and required background about optical wireless communications (OWC). The general context of the OWC is presented in Sec. 1.1. Sec 1.2 is dedicated to the advantages and dis-advantages of OWC, followed by the applications of OWC in Sec. 1.3. The architecture design of the optical wireless transmission is presented in Sec. 1.4, while the information theory compromise between spectral efficiency and energy efficiency is presented in Sec. 1.5. Sec. 1.6 is dedicated for few linear and orthogonal modulation schemes for OWC systems. Thesis contribution is presented at the end of the chapter in Sec. 1.7.

1.1 General Context of the Optical Wireless Communications

Wireless networks have been increasing all over the world for the last twenty-five years. Radio frequency (RF) signals are used to exchange information between end users mobile equipments (ME) and RF access points. For example, if we consider mobile technologies, digital communication technology was first introduced in the form of second generation (2G) for wireless telephony. Initially, voice calling and short text messages were included, that allowed the end users to exchange information. As the time passes, the demands for internet connectivity (for pictures, video and multimedia transmission) increased exponentially, that gave rise to the creation of third and fourth generation (i.e., 3G and 4G, respectively) for the mobile cellular network. Currently, 4G (also known as LTE (long term evolution)) is deployed in almost all over the world, providing high data rate, R_{b}, of upto 1 Giga-bits per second (Gbps). The deployment of fifth generation (5G) is in process and will be available soon for each end user even with higher data rate as compared to the available 4G (LTE). 5G provides the enhanced applications, such as machine to machine (M2M) communications, that can be deployed for Internet-of-Things (IoT). Extensive research is in progress on the future coming sixth generation (6G) technology, that will be available in the near future.

Now-a-days, the internet connectivity and high data rate is the demand of many users and it is growing exponentially with passing time. Many communicating devices use internet for e-mails, watching streaming videos, office and industrial works etc. Fig. 1.1 shows the increase of the number of internet users from 3.9 billions in 2018 to 5.3 billions by 2023 (expected number of internet users), which shows an annual growth rate of 6% [3]. In terms of world population, around 51% of population had access to the internet in 2018, while it is increasing upto 66% of global population by 2023, which is around two-third of the world population [3]. In parallel of the increasing demand for user connectivity, IoT also gains a growing demand for a wide range of connecting devices, such as consumer watches, cars, light, sensors, security and surveillance devices, smart cities equipments, medical devices (in healthcare) to be connected to the internet, etc. These devices need low data rates (100 kbps to 1 Mbps) with a very low power consumption, and rely on simple/low cost hardware. Globally, the number of IoT connected devices are expected to increase to 43 billions by 2023, which is three times increase from 2018 [4].

Most of the wireless technologies in use are based on RF devices and RF systems. The RF spectrum (i.e., from 3kHz to 300 GHz) is a natural resource which is exclusively overseen and controlled by national laws, co-ordinated by International Telecommunication Union (ITU) [5]. RF spectrum is used for a wide set of applications including wireless (fixed or mobile) communications but also TV broadcasting, aerospace applications, radio-navigation, localization etc. In the last few years, with the increasing demand for wireless connectivity, there are difficulties for finding available RF frequencies for IoT, because a tremendous amount of RF spectrum is being consumed, which affirms the RF spectrum scarcity. Different techniques (or methods) can be adapted to alleviate the scarcity issue of RF spectrum, such as;

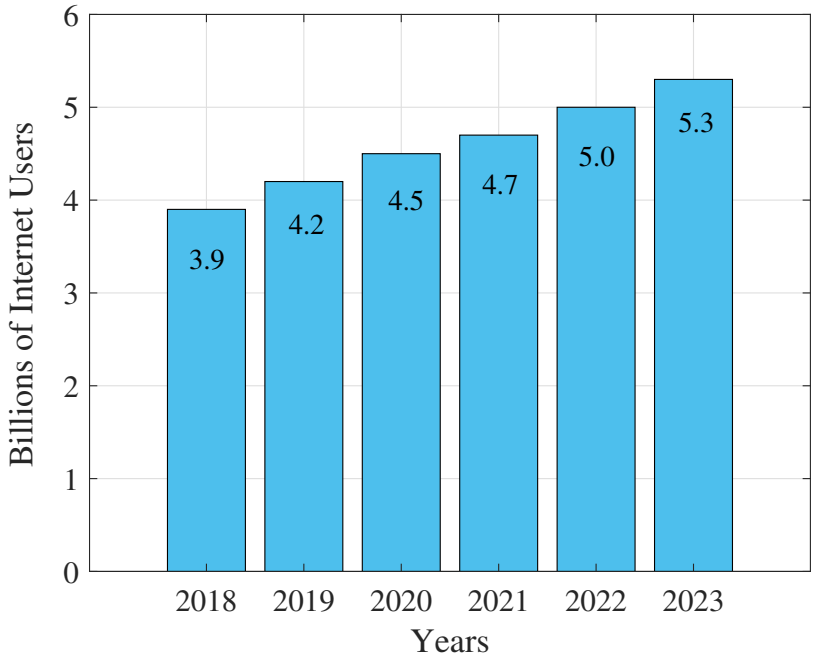

Fig. 1.1 Growth of internet users versus years (from 2018 to 2023) [3].

MIMO Technology: MIMO means multiple-input and multiple-output, which is a technique that uses multiple transmitters and multiple receivers to transmit data simultaneously, which increases the spectral efficiency of the system. However, this solution is coming close to the saturation.

Spectrum Reuse: Second solution is the spectrum reuse or frequency reuse, which increases the coverage area and the capacity of the communication system. The coverage area is basically divided into small clusters of N cells, with each cell consists of a set of frequencies. Since, the adjacent cell must use different set of frequencies, however, the same set of frequencies can be used in another cell which is far away in another cluster. The main aim of the frequency reuse technique is to enhance bits/s/Hz/m^2 [5].

Use of parts of un-used spectrum: Third solution is to use the parts of the spectrum which is not used for RF communications. The millimeter wave (mmWave) communications has gained significant interests in this context [6]. The part of the mmWave spectrum (from 28 GHz to 250 GHz) is used for communication purposes [7]. However, due to the increase of carrier frequency, the mmWave circuits are harder to design and the technology cost is higher than in the RF bands. Terahertz (THz) communication systems offers a large available spectrum from 1000 GHz to 3000 GHz, but the THz transmitter and receiver design is the major issue [6].

Inspite of above three solutions, a good and an appropriate solution can be to use the optical spectrum which consists of infrared (IR), visible light (VL) and ultraviolet light (UV) spectrum. The

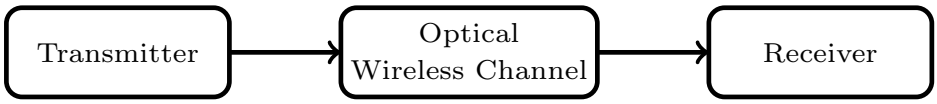

Fig. 1.2 Block diagram of an optical wireless communication (OWC) system.

optical spectrum, ranges from 300 GHz to 30 petahertz, is also a natural resource that can be a best alternate to the RF spectrum, which provides a large un-licensed and un-regulated spectrum for optical wireless communications (OWC) without any interference with the RF spectrum, and which can support high data-rates communication [8]. OWC systems use the un-licensed optical spectrum which is significantly broader than the traditional RF spectrum, but there exists some challenges that has to be in considerations for OWC systems, such as, limited transmitted optical power, diminished reliability towards obstacle, etc [6].

A typical wireless communication (OWC) system is shown in Fig. 1.2, which consists of a transmitter (Tx), the optical wireless channel and a receiver (Rx). The transmitter corresponds to either a laser diode (LD) or a light emitting diode (LED), depending upon the targeted application. Transmitter is followed by an optical wireless channel, line-of-sight (LoS) channel can be the best in terms of achievable required high data-rate and reliable connectivity. Nevertheless, the transmitted waveform usually arises from diffuse components to the optical receiver due to the shadowing or multipath propagation, which leads to high path-loss (PL) and channel dispersion [9]. Finally, the optical wireless channel is followed by a receiver, which uses a photodiode (PD) to detect the received waveform in the form of optical power. In OWC systems based on LEDs, the information is transmitted by intensity-modulation and direct-detection (IM-DD) because of its low cost and low implementation complexity. At the receiver side, the information is photo-detected by PD, which is initially modulated on the envelop of the electromagnetic radiation [7] [10].

1.2 OWC Advantages and Dis-advantages

OWC systems offer some advantages over the RF systems, such as;

Un-licensed Spectrum: The OWC provides a huge un-licensed and un-regulated spectrum unlike the RF spectrum (which is not free and regulated by ITU). Moreover, the RF spectrum is too much congested now due to the large usage by different communication technologies.

High Data Rate: OWC systems offer potential larger data rates as compared to RF technologies because of the ultra-large bandwidth of 400 THz.

Secure Transmission: In the indoor environment, the RF signals can penetrate through the walls, windows and all the obstacles in the buildings, which is not the case for light signals in OWC systems. This makes the OWC technology a safer option for data transmission.

No Interference with RF Signal: The use of light signals in OWC systems show zero interference with RF signals and RF restricted equipment. For this reason, OWC technology is feasible to use instead of RF technology, where the equipment is restricted or sensitive to the RF signals, such as different medical examinations in hospital, aerospace platform, etc [11], [12].

Ease in Implementation: OWC systems offer ease in practical implementations in the indoor applications, as well as in the outdoor applications, due to the use of the off-the-shelf components. For indoor communications, OWC could rely on the massive deployment of LED-based lighting (this technology is known as Visible Light Communications (VLC)).

Energy Efficiency: Now-a-days, LEDs are commonly used for lighting purposes and it can also be used as a transmitter in OWC systems. Moreover, the transmitter in OWC systems (specifically LEDs) are more energy efficient than the other lighting sources and have a significantly lower carbon dioxide (CO_2) footprint, therefore, by using LEDs for lighting instead of other lighting sources, the emission of CO_2 is expected to be reduced by 10 gigatons, which can lead to reduce the oil consumption by 962 million barrels over the decade. This can save around 1.9×10^{20} joules energy over a decade [13], [14], [6].

Human Health Safety: In OWC systems, LEDs follow skin-and-eye safety regulations, which restrict the upper-limit on optical transmit power and hence, it assures the safety of the human health [13].

Low Cost: The OWC technologies use low-cost equipments for communications unlike the RF wireless technologies which use complex and high-cost equipments [15]. Moreover, the components used in OWC systems are more energy efficient which incur low consumption of energy, leading to the low billing.

Spatial Reuse and Beam Forming: In indoor environment, the light signals in the OWC systems cannot penetrate through the walls, ceiling and windows, and hence, the light signals are confined due to reflections inside the room. Therefore, the confined light beam makes it possible to create multiple non-interfering beams, which allow the reuse of modulation bandwidth and avoid the data loss [16], [17], [18], [6].

Integration of OWC with the Existing Systems: The RF communication systems, such as RF/mmWave and THz communication systems require additional complex transceivers which leads to an increase of the integration cost [6]. On the other hand, the integration of OWC systems is quite simple and cheaper due to the deployment of additional low-cost front end components, such as LEDs with related drivers, and PDs with related amplifiers [13], [19].

It is true that OWC systems show a lot of advantages over RF systems, but at the same time, OWC systems face some challenges, that need to be addressed in the practical implementations. Here, we present few most important challenges.

Channel Effect: As the information data is exchanged between the transmitter and receiver through an optical wireless channel in OWC systems, therefore, some channel effects add to the transmitted information, such as obstacle attenuation, noise, multipath propagation, etc. These channel effects have to be taken in consideration, while designing any OWC system, because these issues affect the transmitted information and the system performance.

OWC systems are very sensitive to the obstacles between the transmitter and receiver, specially in case of LoS communication, which can cause transmission blockage. As the PD surface area is much larger than the transmitted optical signal wavelength, λ, therefore, the small-scale fading is usually negligible and can be ignored. However, the signal level fluctuation issue may arise due to the misalignment in point-to-point links or due to the atmospheric turbulence in the outdoor scenarios [9].

Eye Safety: Regulation imposes some standard procedures to use optical transmitter in different indoor and outdoor applications to ensure eyes safety. One of the standard is the use of upper-limit on optical transmit power by optical transmitter (LD or LED), which may restrict us to attain the desired performance for narrow beam and narrow field-of-view (FOV) links [9]. At a very low data rate, the flickering effect may arise and it can restrict the LEDs performance. For the illumination frequency above 80 Hz, the human eye cannot detect the flickering effect of LEDs [20].

Signal Modulation: A suitable modulation scheme must be chosen to deal with the channel effect, the required energy efficiency and spectral efficiency. Energy efficiency is of critical importance when addressing low data rate OWC for IoT. Moreover, the circuit complexity for transmitter and receiver should be minimized.

1.3 Applications of Optical Wireless Communications

OWC has a wide range of applications [21], [22], such as, smart cities and homes, railway stations, airports, data centers, healthcare/hospitals, transportation, production plants, underwater communication, etc. Specifically, OWC can be more promising to use in the RF sensitive or RF restricted environments, such as, healthcare/hospitals, petrochemical plants, etc. Additionally, OWC can also be used for military submarines communications due to the secure exchange of data.

As aforementioned that the transmitter and receiver in an OWC systems communicate to each other through an optical wireless channel. The transmitter and receiver are located at some specific distance from each other, ranging from few millimeters (mm) in case of chip to chip (C2C) communication to thousands of kilometers (km) in case of satellite communication as shown in Fig 1.3 (cf. [23]). Therefore, the OWC applications can be classified on the basis of transmission ranges, such as,

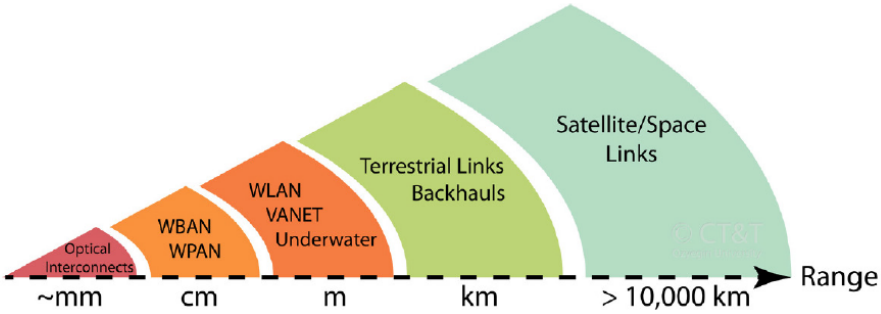

Fig. 1.3 Categorization of OWC applications based on the transmission range [23].

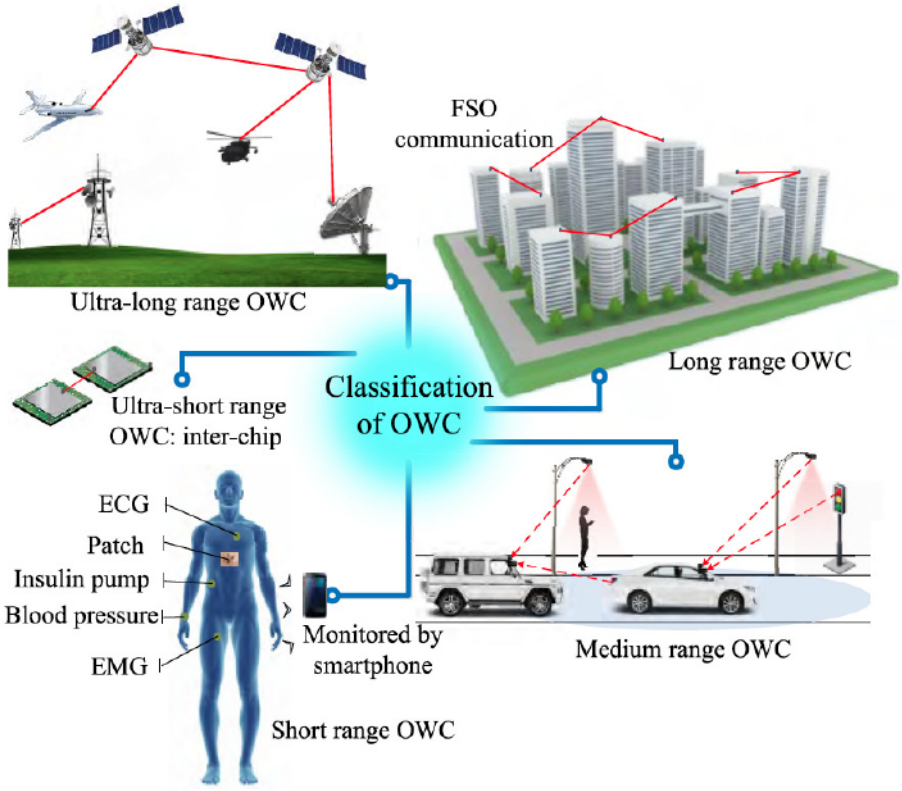

Fig. 1.4 Classification of OWC based on transmission range [21].

ultra-short range, short range, medium range, long range and ultra-long range as shown in Fig. 1.4. Following are few examples:

Ultra-Short Range Applications: The traditional copper-based electrical interconnects are bulky and bandwidth limited, which become the hindrance for system design in ultra-short range OWC [24]. On the other hand, free space optics interconnects (FSOI) are gaining potential importance due to high bandwidth and low latency [25]. FSOI can be used for C2C communications due to high data rate, low latency and high flexibility as compared to the copper-based counterparts.

Short Range Applications: Wireless body area network (WBAN) and wireless personal area network (WPAN) are the typical examples of short range OWC, which support the communications in tens of centimeters [26], [27]. WBAN based on RF is sensitive to the RF restricted equipments in healthcare/hospitals, therefore, WBAN based on OWC can be used in healthcare/hospitals to detect and monitor the health parameters, such as blood pressure, heart rate etc by using the detectors and sensors based on visible light (VL). WPAN uses the short-range wireless connectivity protocols (i.e., Bluetooth) in which all the devices are linked to each other. Internet-of-things (IoT) is the best example of WPAN, which can also be used in healthcare/hospitals [28]. Another example of the short range OWC is optical camera communications (OCC), where a camera is used as an optical receiver to setup machine to machine (M2M) communications [9], [29].

Medium Range Applications: OWC can be deployed to wireless local area network (WLAN) for medium range wireless communications [30], which can support the communications in few meters. Another examples for medium range OWC applications are optical vehicle-to-vehicle (V2V) and vehicle-to-infrastructure (V2I) communications [31], [32] in which the front and back LEDs of the cars are used to communicate with the nearest cars. The targeted communication range of a few meters is typically the scenario for IoT communications supported by OWC [33], [34].

Long Range Applications: Free space optics (FSO) is a typical example of long range application for OWC systems which supports the communication in the range of several hundreds of meters (m) to several kilometers (km). FSO offers a high bandwidth and high data rates (usually in Tbps) and it can be deployed for high speed point-to-point communications. The use of narrow beams laser in FSO link increases the data security and robustness to EMI [22], [9]. Nonetheless, FSO links are sensitive to atmospheric conditions, such as, fog, rain, snowfalls, shadowing etc, which can limit the transmission range and can degrade (or failure) the performance [5]. To mitigate this issue, millimeter wave (mmW) FSO links are used to counter-balance in case of worse atmospheric conditions [35]. Moreover, recent research shows that FSO links can also be deployed for aerospace communications [36].

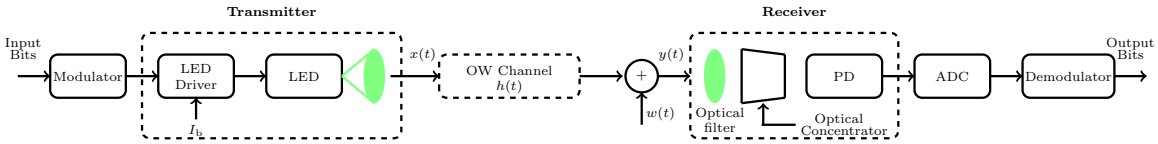

Fig. 1.5 A typical OWC system.

Ultra-Long Range Applications: FSO links can also support ultra-long range OWC applications (thousands of kilometers (km)) and can be employed for ground-to-satellite and satellite-to-satellite communications, hence, benefiting from high spectral efficiency [37], [38]. Some FSO links for satellite-to-satellite communications are presented in [39], [40].

The application context of this PhD work will be on medium range/short range applications to address the issue of energy efficient low data rate IoT communications using OWC systems.

1.4 Architecture of OWC System for Medium Range Communications

Fig. 1.5 illustrates the typical optical wireless communication (OWC) system. The transmitter transmits data to the receiver via an optical wireless channel. The most common example of the down-link communication is the transmission from access point (AP) to the user-equipment [41].

1.4.1 Optical Transmitter

In OWC systems, LDs or LEDs are used as a transmitter (or emitter) which converts the electrical signals into optical signals. LDs are coherent optical devices in which all the transmitted electromagnetic waves travel in a same direction with a same phase [21]. From LDs, the transmitted signals in the form of light travel to the longer distances and deteriorate lesser interferences due to the coherent nature. Furthermore, the modulation bandwidth of the LDs is larger than the LEDs [42], [43], [44]. Note that the radiation power of the LDs have to be controlled to protect the human eyes and to ensure the health safety due to the thermal effects of the LDs radiations [21].

On the other hand, LEDs are commercially used devices for lighting purpose or infra-red (IR) communications. LEDs have few advantages over LDs, such as energy efficiency, lower heat generation, reduced risks for human eyes and health, easy deployment, longer life-span etc [21],[45]. Therefore, LEDs can be a suitable candidates for transmitter front-ends in OWC systems. However, LEDs can be used with multiple colors using the multi-chips LEDs, such as RGBA emitter (red green blue amber LED Engin LZA-00MA00) [46], [47], and Gallium Nitrade emitter (GaN), that provides the efficient transmission for high-speed OWC systems [41]. For our experimental implementations, we used RGBA LED (Engin LZA-00MA00) as an emitter source, that can transmit four different colors (cf. Chapter 4). Note that the LEDs are operated with real-valued and non-negative signals [41].

It should be noticed that the radiation pattern for any optical emitter varies with the distance, therefore, the radiation pattern for such optical emitter can be best modeled by using Lambertian law

[10]. According to Lambertian law, the optical intensity of an optical emitter at a radiant angle of ϕ can be expressed as [10], [41], [6]:

$$P_{(\text{opt})}R(\phi) = P_{(\text{opt})}\frac{(m+1)}{2\pi}\cos^m(\phi) \quad \text{(W/steradian)}, \tag{1.1}$$

where $R(\phi)$ is the radiation profile, $P_{(\text{opt})}$ is the transmitted optical power by the optical emitter (or source) and m represents an order of the Lambertian emission, which depends upon the half power semi-angle, $\phi_{1/2}$, as [41], [6]:

$$m = -\frac{1}{\log_2(\cos[\phi_{1/2}])}. \tag{1.2}$$

Where, the LED light can be approximated as a Lambertian source with $m = 1$, while the half angle in (1.2) is $\phi_{1/2} = 60°$. Note that flat-frequency channel is considered for the theoretical part of this PhD, then no filtering effect of the channel is needed. For such scenario, the delay spread, $\Delta\tau$ (time support of the impulse response, $h(t)$) is approximately 10 ns [48], [49], leading to a coherence bandwidth, $B_{\text{coh}} = 1/\Delta\tau$ of 100 MHz [30]. In such scenario, a flat-frequency channel (or non-selective frequency channel) can be assumed, because the bandwidth of the transmit signal is low as compared to the coherence bandwidth, which leads to a weak inter-symbol-interference (ISI) and weak inter-carrier-interference (ICI) [30].

1.4.2 Optical Channel

An optical wireless communication system is shown in Fig. 1.5, which supports only the intensity-modulation and direct-detection (IM-DD). Input bits are converted into symbols using a digital modulator before digital to analog conversion (DAC). Then, the LED driver combines the analog waveforms with a DC bias to fix the operating current of the LED, generating the modulated waveform, $x(t)$. Hence, the transmitted signal, $x(t)$, modulates only the brightness of the transmitter LED. The transmitted electrical signal, $x(t)$, is transformed into an optical signal by the transmitter as $u(t) = \omega x(t)$, using an electrical-to-optical conversion factor, ω ($Watt/Ampere$). A perfect synchronized transmitter is considered for simplicity [50], [51], that operates in the linear region, i.e., $\omega = 1$ $Watt/Ampere$, therefore, the transmitted signal by the transmitter is $u(t) = x(t)$. The transmitted signal is effected by the optical wireless channel with the channel impulse response (CIR) as $h(t)$.

At the receiver end, the transmitted signal, $u(t)$, is photo-detected by the PD as $r(t) = \upsilon u(t)$, with υ being the responsivity of the PD in $Ampere/Watt$. For simplicity, a lossless and linear behaviour of PD is considered, i.e., $\upsilon = 1$ $Ampere/Watt$, and hence, resulting the received signal by the PD is $r(t) = u(t) = x(t)$. Considering the channel response, $h(t)$, and considering that the transmitted signal is corrupted by noise, $n(t)$, the received signal at the PD output can be expressed as:

$$y(t) = h(t) \otimes x(t) + n(t), \tag{1.3}$$

where $\otimes$ represents the convolution operator and $n(t)$ is the additive white Guassian noise (AWGN) with single-sided power spectral density (PSD) of N_0 [52]. In practical scenario, LED is used as a transmitter in OWC systems which introduces a low-pass filtering response in the channel impulse response (CIR). Furthermore, the received signals may come from multiple paths in the wireless channel, which may introduce the time dispersive response, i.e., the channel may be frequency-selective. Supposing that the impulse response of the photodiode is ideal, the overall channel response can be expressed as [6]:

$$h(t) = h_{\text{chan}}(t) \otimes h_{\text{led}}(t), \tag{1.4}$$

where h_{chan} and h_{led} represent the impulse response added due to the propagation of the transmitted signals (or light) in indoor optical wireless channel and the impulse response due to LED/LED driver combination, respectively. The overall channel impulse response in frequency-domain (FD) can be evaluated by using Fourier Transform as [6], [41]:

$$H(f) = \int_0^\infty h(t) \exp^{-2\pi f t}\, dt = H_{\text{chan}}(f).H_{\text{led}}(f). \tag{1.5}$$

1.4.3 Optical Receiver

The optical receiver is shown at the right side of the Fig. 1.5. The optical concentrator is used to concentrate the received optical power on the photo-detector (PD). Mostly, the optical filter is also used before PD to filter out the un-wanted light from the ambient light source and to confine the spectrum of the light [53]. The photo-detector (PD) converts the received optical signal into an electrical signal before analog-to-digital conversion and digital demodulation to recover the transmitted bits [41], [6]. The receiver performance can be affected by the photo-sensitivity, bandwidth and the aperture area of the PD. The aperture area, A_{PD}, allows the amount of light that can be concentrated by a PD. It means that the larger A_{PD} of the PD increases the received optical power, that increases the photo-sensitivity of the PD and hence, it improves the receiver performance. Somehow, a larger A_{PD} terminates the slow switching speed of the PD which deteriorate the frequency response profile and a smaller A_{PD} leads in low capacitance which results a high bandwidth [6].

As the optical concentrator converges the received optical light signals into the PD from the wide field-of-view (FoV), since the optical concentrator gain is computed as [6],[10],[41]:

$$G_{\text{OC}}(\psi) = \begin{cases} \frac{n_{\text{ref}}^2}{\sin^2(\psi_{\text{FoV}})} & |\psi| \leq \psi_{\text{FoV}} \\ 0 & |\psi| > \psi_{\text{FoV}} \end{cases}, \tag{1.6}$$

where ψ is the incident angle of received optical light to the PD, ψ_{FoV} is the FoV of the receiver PD which is the exceeding incident angle that does not allow any light and n_{ref} is the refractive index. Note that the gain of the optical filter and optical concentrator (i.e., $G_{\text{OF}}(\psi)$ and $G_{\text{OC}}(\psi)$ respectively) are dependent on incident angle, ψ, of the received light to the receiver. Hence, it modifies the effective

area, A_{eff}, of the PD as [10]:

$$A_{\text{eff}}(\psi) = \begin{cases} A_{\text{PD}} G_{\text{OF}}(\psi)\cos(\psi) & |\psi| \leq \psi_{\text{FoV}} \\ 0 & |\psi| > \psi_{\text{FoV}} \end{cases}, \tag{1.7}$$

Several types of photodetector can be used, such as, solar panels [54], image sensors [55], [56] and PIN photodiode [46]. Each photodector has its own advantages and limitations.

1.5 Information Theory Compromise Between Spectral Efficiency and Energy Efficiency

In our work, the main objective is to develop the energy efficient modulation schemes for OWC systems which can be used for low data rate IoT applications. The energy efficiency and the spectral efficiency are related to each other [30]. The goal of this section is to revisit (as in [57], [58], [59](section 5.2.3.2), [30]) the natural trade-off between energy efficiency and spectral efficiency directly imposed by the information theory (Shannon's capacity limit), as well as the existence of a necessary ultimate minimum Energy per bit for reliable communication

Accordingly, the average electrical power, $P_{(\text{elec})}$, of the transmit waveform is considered as $P_{(\text{elec})} = E_{\text{s(elec)}}/T_{\text{s}} = E_{\text{b(elec)}}R_{\text{b}}$, where $E_{\text{s(elec)}}$, $E_{\text{b(elec)}}$, T_{s} and R_{b} represent the average electrical energy per waveform, the average electrical energy per bit, the symbol time and the data rate, respectively. Similarly, the electrical signal-to-noise ratio, $SNR_{(\text{elec})}$, in an AWGN channel (without considering any interference from other users) is expressed as [30]:

$$SNR_{(\text{elec})} \triangleq \frac{P_{(\text{elec})}}{\sigma_n^2} = \frac{E_{\text{b(elec)}}}{N_0}\eta, \tag{1.8}$$

where σ_n^2 is the noise variance (i.e., $\sigma_n^2 = N_0 B$), B is the mono-lateral communication bandwidth (i.e., $B = 1/2T_{\text{s}}$), and η is the spectral efficiency in bps/Hz (i.e., $\eta = R_{\text{b}}/B$). Indeed, the Shannon's capacity limit in [60] defines an upper bound on the data rate that can be achieved theoretically with no errors on bits, considering a given $SNR_{(\text{elec})}$ and a given B in an AWGN channel. It should be noticed that the Shannon's limit can only be achieved by using bipolar modulations [30]. Therefore, for the modulations that are compatible with IM-DD OWC systems, the Shannon's limit cannot be achieved due to the unipolar nature. Hence, Shannon's limit can be used as an upper bound (or extra-upper bound) for IM-DD compatible modulations. The data rate according to the Shannon's theorem with an upper-bound is expressed as [61]:

$$R_{\text{b}} \leq B\log_2(1 + SNR_{(\text{elec})}). \tag{1.9}$$

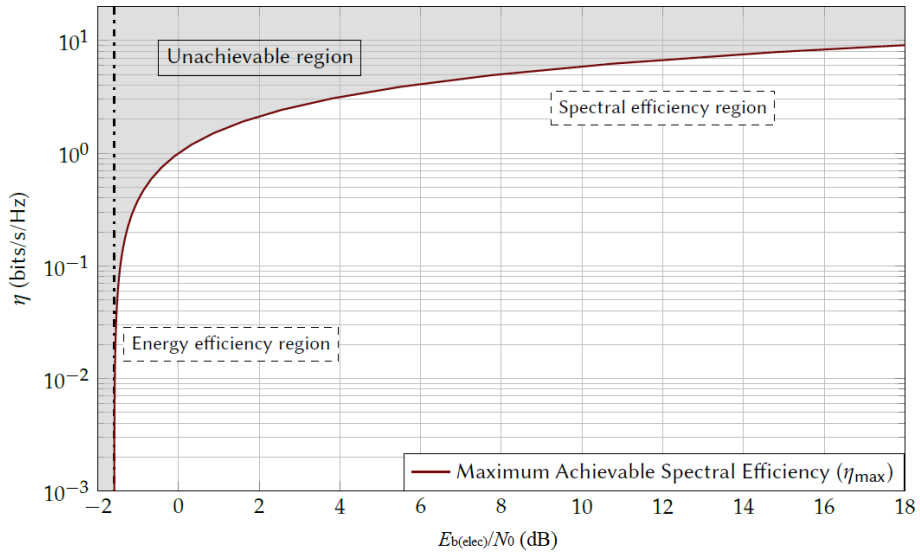

Fig. 1.6 The maximum achievable spectral efficiency versus required $E_{b(elec)}/N_0$. High spectral efficient and energy efficient regions are also shown [58].

Dividing (1.9) by B to attain $R_b/B = \eta$, and using SNR from (1.8) into (1.9), the lower bound on spectral efficiency is obtained as [62], [63]:

$$\eta \leq \log_2\left(1 + \frac{E_{b_{(elec)}}}{N_0}\eta\right). \tag{1.10}$$

To attain $E_{b(elec)}/N_0$ expression for a given η, re-arranging (1.10) as [62], [63]:

$$\frac{E_{b_{(elec)}}}{N_0} \geq \frac{2^\eta - 1}{\eta} = \left(\frac{E_{b_{(elec)}}}{N_0}\right)_{\min}. \tag{1.11}$$

Actually, from (1.11) and from Fig. 1.6, we can see that according to the information theory, the required $(E_{b(elec)}/N_0)_{\min}$ is an increasing function of the spectral efficiency, η. This shows the fundamental trade-off between a good spectral efficiency (that means a high η) and a good energy efficiency (that means a weak $(E_{b(elec)}/N_0)_{\min}$). Also, we see that if we are ready to pay energy (i.e., to have a poor energy efficiency) we may have very good spectral efficiency, η, since we can have η tends to infinity if $(E_{b(elec)}/N_0)$ goes to infinity. This kind of behaviour is exploited in high data rate context. But for our interest in low data-rate/low energy context, we see also from (1.11) and Fig 1.6 that reliable communication is impossible under a lower ultimate limit on $(E_{b(elec)}/N_0)$. Indeed, for bipolar waveforms, the fundamental Shannon's limit is achieved when $\eta \to 0$. Thus, it is leading to a lower bound for$(E_{b(elec)}/N_0)_{\text{lim}} = \ln(2) \approx -1.59$ dB, which expresses the best theoretical compromise in terms of energy efficiency: the ultimate reduction of the required energy per bit can theoretically only be achieved with a very poor spectral efficiency. This information theory lighting will guide the choices retained in this Phd.

For orthogonal modulation schemes which will be the starting point of our proposed schemes), the minimum squared Euclidean distance between the waveforms is expressed as [30]:

$$d^2_{\min} = 2E_{s(\text{elec})} = 2E_{b(\text{elec})}\log_2(M). \tag{1.12}$$

(1.12) implies that $d^2_{\min}$ (that reflects the potential reliability in presence of AWGN) increases by increasing the modulation cardinality M, for a given $E_{b(\text{elec})}/N_0$. It follows that the required $E_{b(\text{elec})}/N_0$ reaches the lower bound of -1.59 dB as M approaches infinity [57], [63]. On the contrary, for linear modulations, the minimum squared Euclidean distance between waveforms decreases with increasing M, leading to an increase in the required $E_{b(\text{elec})}/N_0$ for a given BER [57]. This behaviour is in complete disagreement with the behaviour of orthogonal modulations. The contradictory behaviour of the two families of modulation will be highlighted in the Fig. 1.10.

1.6 Modulation Schemes for Optical Wireless Communications

There exists a significant difference between the modulation techniques used for RF communication and OWC systems. Most often, LED is used as a transmitter device in OWC systems, so the transmitted data are encoded in amplitude to modulate optical field amplitude but not the phase because it will then need coherent detection, since LED is a non-coherent optical source. The digital waveform modulates the optical field amplitude and is demodulated at receiver side after quadratic detection (photodiode), which corresponds to intensity modulation and direct detection (IM-DD). The following conditions have to be satisfied when implementing modulation scheme for an IM-DD OWC system [8];

- The information signal to be transmitted should be real value because it modulates directly the bias current amplitude of the LED.
- The information signal to be transmitted should be unipolar (positive signal) because the transmitter device (LED) can only support positive bias currents.

Considering the above mentioned conditions for IM-DD OWC systems, the available modulation schemes are divided into two groups;

- Linear modulations.
- Orthogonal modulations.

The performance of these modulation schemes can be compared in terms of spectral efficiency versus energy efficiency, and bit error rate (BER). In fact, BER is the number of received bits in error per total number of bits exchanged between the transmitter and receiver during a fixed time interval. The number of bits in error is due to the noise, distortion, interference , synchronization issues or wireless channel effect over a wireless communication channel. BER depends on signal to noise ratio, E_b/N_0, at the input of the receiver. An energy efficient modulation technique is the one for which the necessary E_b/N_0 is minimum for a given BER.

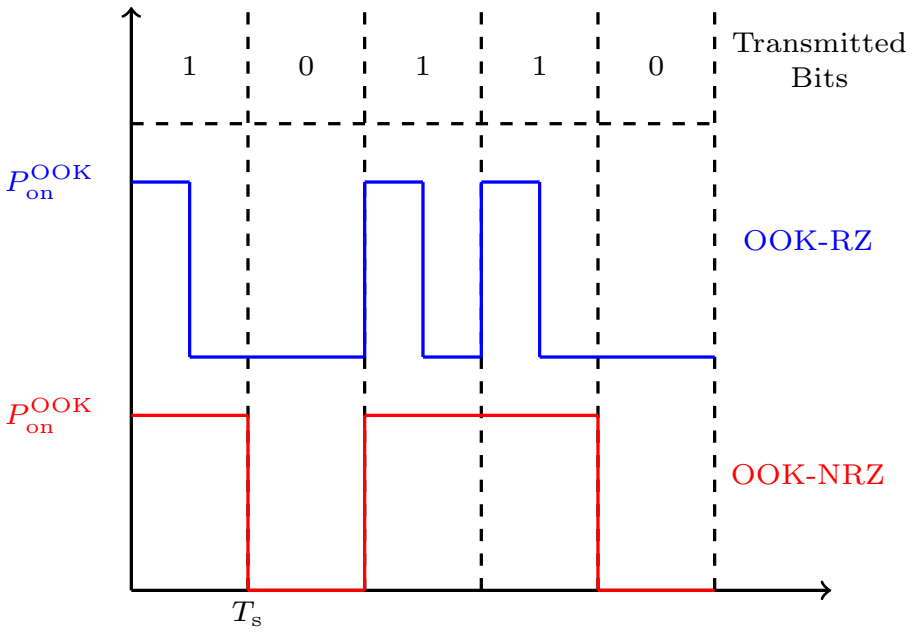

Fig. 1.7 On-Off Keying (OOK) with $P_{\text{off,OOK}}$ is set to zero. OOK-NRZ and OOK-RZ.

In the next subsections, we present few most commonly used linear modulation schemes (i.e., OOK and M-ary PAM) and orthogonal modulation schemes (i.e., M-ary PPM and M-ary FSK).

1.6.1 Linear Modulations

Linear modulation scheme can be defined as the scheme in which the base-band signal is linearly related to the modulated signal, i.e., the modulated signal reflects a continuously variable range of values of the base-band signal [64]. Linear modulation schemes (i.e., On-off Keying (OOK) and M-ary pulse amplitude modulation (PAM)) are extensively studied in the literature for OWC systems [65],[66],[67]. These modulation schemes are straight-forward and easy to implement. Actually, for a M-ary linear modulation, the set of signals (or waveforms) in the dictionary, $\mathscr{D}$, is composed of M waveforms differing only by their amplitudes, but having the same elementary shape [57].

On-Off Keying (OOK)

On-off keying (OOK) is the simplest linear modulation scheme used for OWC systems. It is a binary modulation ($M = 2$). OOK represents a series of logical 0s and 1s for low and high state, respectively. These states are used to send information data by switch on and off the transmitter LED. OOK can be non-return to zero (i.e., OOK-NRZ) and return to zero (i.e., OOK-RZ) as shown in Fig. 1.7. The only difference is in the high state (1s), i.e., the rectangular pulse does not return to zero state during the symbol time, T_{s}, for OOK-NRZ, while it returns to zero during T_{s} for OOK-RZ. The low state (0s) is same for both (OOK-NRZ and OOK-RZ) with null amplitude. Here, we only consider the OOK-NRZ. For OOK-NRZ, two optical power levels, i.e., $P_{\text{on}}^{\text{OOK}}$ and $P_{\text{off}}^{\text{OOK}}$, are assigned to represents the bits 1s

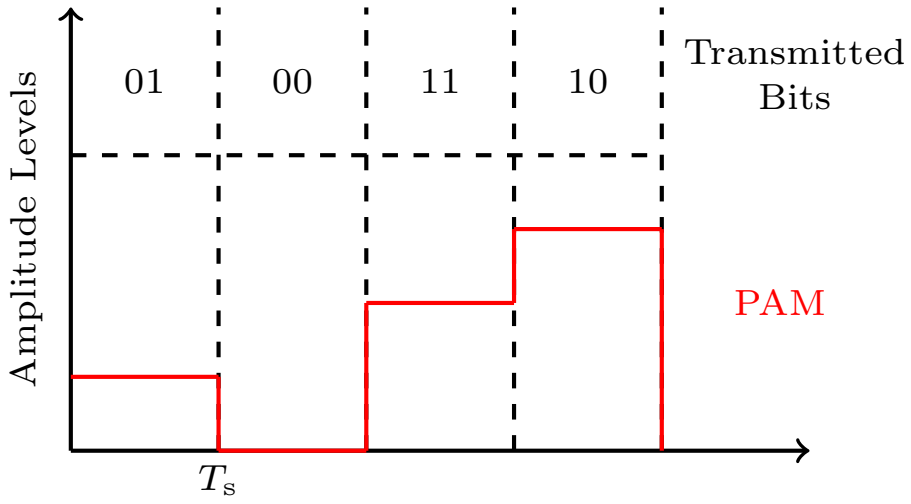

Fig. 1.8 Pulse amplitude modulation (PAM) with $M = 4$.

and 0s, respectively. The average power for OOK-NRZ can be computed as [9]:

$$P_{\text{avg}}^{\text{OOK}} = \frac{P_{\text{on}}^{\text{OOK}} + P_{\text{off}}^{\text{OOK}}}{2}. \tag{1.13}$$

As the bandwidth (containing the main part of energy), B^{OOK}, of the OOK-NRZ is equal to the data rate, $R_{\text{b}}^{\text{OOK}}$, i.e., $B^{\text{OOK}} = R_{\text{b}}^{\text{OOK}}$. Therefore, the spectral efficiency of the OOK-NRZ, η_{OOK}, can be computed as:

$$\eta_{\text{OOK}} = \frac{R_{\text{b}}}{B} = \frac{R_{\text{b}}^{\text{OOK}}}{R_{\text{b}}^{\text{OOK}}} = 1 \text{ bps/Hz}. \tag{1.14}$$

Note that the OOK modulation scheme provides the advantage of high spectral efficiency and low system complexity as compared to the pulse position modulation (PPM) due to linearity, but at the cost of low energy efficiency [13]. Note also that OOK modulation can be regarded as a PAM modulation with only $M = 2$ states (see next section).

Pulse Amplitude Modulation (PAM)

Pulse amplitude modulation is a digital linear multi-level modulation scheme in which the information symbols are encoded using M different levels of amplitude. The number of amplitude levels in M-ary PAM depends upon the modulation (or dictionary) size M. According to [68], the amplitude levels of M-ary PAM can be expressed as:

$$P_m = \frac{2mP_{\text{avg}}}{M-1}, \quad \text{for } m \in \{0, 1, \cdots, M-1\}. \tag{1.15}$$

where P_{avg} is the average optical power of M-ary PAM waveforms. As an example, Fig. 1.8 illustrates the typical M-ary PAM for $M = 4$ levels. In M-ary PAM, the assigned amplitude to each information symbol is controlled by the sampling symbol instantaneous amplitude.

According to [67], the mth transmitted symbol of M-ary PAM, i.e., $s_m^{\text{PAM}}(t)$, can be expressed as:

$$s_m^{\text{PAM}}(t) = A.p(t), \quad \text{for } m \in \{0, 1, \cdots, M-1\}. \tag{1.16}$$

where $p(t)$ is a pulse of symbol duration, T_{s}, and A is a symbol amplitude with discrete values as [67]:

$$A = m, \quad \text{for } m \in \{0, 1, \cdots, M-1\}. \tag{1.17}$$

M-ary PAM can transmit $n = \log_2(M)$ bits per symbol, therefore, M-ary PAM provides a higher bandwidth efficiency than OOK. Since the bandwidth of the transmit signal is mainly due to one of the pulse $p(t)$. The spectral efficiency of M-ary PAM, considering $B^{\text{PAM}} = R_{\text{s}}^{\text{PAM}}$, can be expressed as:

$$\eta_{\text{PAM}} = \frac{R_{\text{b}}}{B} = \frac{R_{\text{b}}^{\text{PAM}}}{R_{\text{s}}^{\text{PAM}}}, \tag{1.18}$$

where $R_{\text{s}}^{\text{PAM}}$ represents the symbol rate of M-ary PAM and $B = R_{\text{s}}^{\text{PAM}} = R_{\text{b}}^{\text{PAM}}/n$, therefore, η_{PAM} from (1.18) can be computed as:

$$\eta_{\text{PAM}} = n = \log_2(M). \tag{1.19}$$

It can be noticed from (1.14) and (1.19) that OOK corresponds to 2-PAM, having the same spectral efficiency of 1 bps/Hz, therefore, OOK can be considered as the special case of M-ary PAM with $M = 2$. Moreover, it can be observed from (1.19) that η_{PAM} can be increased by increasing M, but at the same time, the energy efficiency is penalized, since the minimum distance between two symbols in the original constellation decreases with increasing M [67], [69], which increases the required signal-to-noise ratio (SNR) per bit to attain the targeted BER performance. Therefore, it is impossible for M-ary PAM to reach the Shannon's limit [60], regarding the best possible energy efficiency (or low possible energy per bit, see section. 1.5). Note also that for M-ary PAM modulation, the best possible energy efficiency is obtained for $M = 2$, that means for OOK, with a corresponding spectral efficiency of 1 bps/Hz.

1.6.2 Orthogonal Modulations

Orthogonal modulation scheme is the one for which the set of signals (or waveforms) in the dictionary, $\mathscr{D}$, are orthogonal to each other, i.e., the inner product between the waveform pairs in the dictionary corresponds to zero. The orthogonal modulation schemes such as M-ary pulse position modulation (PPM) and M-ary frequency shift keying (FSK) [61] can approach the Shannon's limit by the cost of low spectral efficiency.

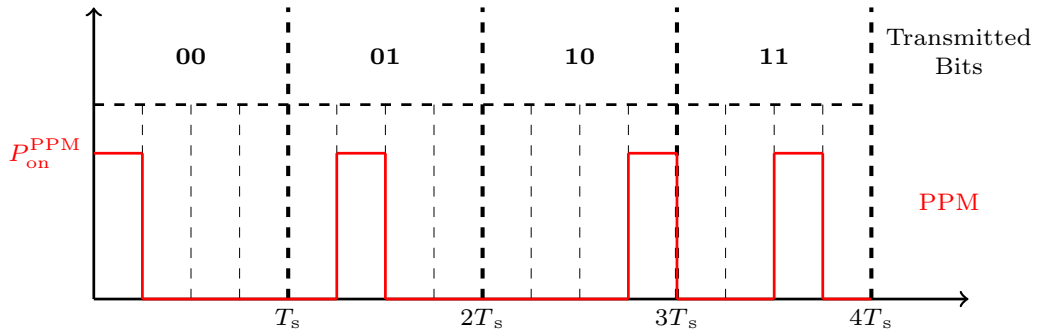

Fig. 1.9 Pulse position modulation (PPM) with $M = 4$, using Gray coding.

Pulse Position Modulation (PPM)

M-ary Pulse position modulation (PPM) is a digital orthogonal (non-linear) scheme in which information data is encoded by simply transmitting a single pulse in one of the 2^n possible required time shifts, where n is the number of bits per symbol [5], [70], [71].

Fig. 1.9 illustrates the M-ary PPM waveforms in different time shifts corresponding to the Gray coding. Each symbol time, T_{s}, is divided into M time slots, in which only one time slot is assigned with the information bits (i.e., that time slot is set to "on" state), while the remaining $M-1$ time slots are set to "off" state. The optical power corresponding to the "on" and "off" states are $P_{\text{on}}^{\text{PPM}}$ and $P_{\text{off}}^{\text{PPM}}$, respectively. Therefore, the average transmit optical power can be computed as [9]:

$$P_{\text{avg}}^{\text{PPM}} = \frac{1}{M}((M-1)P_{\text{off}}^{\text{PPM}} + P_{\text{on}}^{\text{PPM}}). \tag{1.20}$$

The data rate of M-ary PPM is $R_{\text{b}}^{\text{PPM}} = \log_2(M)/T_{\text{s}}$ bps, and the bandwidth (containing the main energy of the transmit signal) of the M-ary PPM is $B^{\text{PPM}} = M/T_{\text{s}}$. Hence, the spectral efficiency of M-ary PPM can be computed as:

$$\eta_{\text{PPM}} = \frac{R_{\text{b}}^{\text{PPM}}}{B^{\text{PPM}}} = \frac{\log_2(M)/T_{\text{s}}}{M/T_{\text{s}}} = \frac{\log_2(M)}{M}. \tag{1.21}$$

From (1.21), it can be observed that η_{PPM} decreases by increasing M. According to [62], [63], the energy efficiency of the orthogonal modulation scheme increases with increasing the alphabet cardinality (or dictionary size), M, at an expense of the decreasing the spectral efficiency, which is in total contradiction with linear modulations. M-ary PPM is widely investigated for OWC in [72]. Although PPM has some advantages over OOK and PAM, such as high energy efficiency, resistant to flat-fading in RF communications etc, but PPM also exhibits some dis-advantages, such as synchronization issue at receiver, sensitivity to multi-path propagation due to the frequency selective channels, high crest factor and high peak-to-mean optical power ratio (PMOPR) [72], [73], [74], [75], [76].

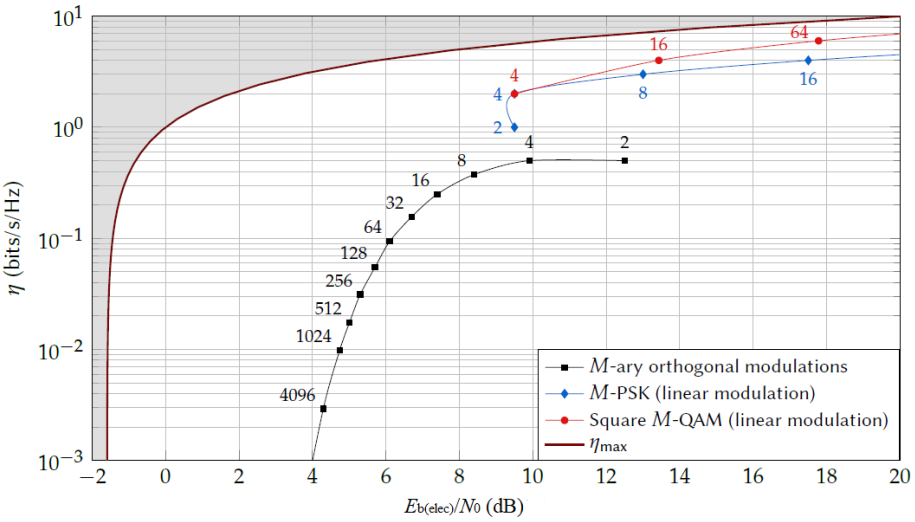

Fig. 1.10 Comparison of the spectral efficiency versus the required $E_{b(elec)}/N_0$ for few linear and orthogonal modulations in an AWGN channel, considering BER = 10^{-5}. Maximum achievable spectral efficiency, η_{max}, according to Shannon's limit is also presented [58].

Frequency Shift Keying (FSK)

Frequency shift keying (FSK) is an orthogonal modulation scheme, which is widely used in RF communications. M-ary FSK based modulations have raised considerable interest for OWC applications in the recent research, because it provides the benefit of high energy efficiency, quasi constant envelop property that overcome the LED non-linearity and easy channel equalization [52]. M-ary FSK also overcome some limitations of M-ary PPM and it can be a possible substitute for low-power wide area network (LPWAN) [62], [63]. Although the conventional M-ary FSK is not compatible with the IM-DD OWC systems due to the bipolar nature [61], but M-ary FSK can be adapted to be compatible with OWC systems. In the next chapter, we will briefly explain the conventional bipolar M-ary FSK and its variants along with the transmitter, different receivers and different parameters, such as symbol energy, spectral efficiency, minimum Euclidean distance, complexity analysis etc.

Fig. 1.10 is taken as an example from [58] (in an RF context) to explain the comparison of the spectral efficiency versus the required $E_{b(elec)}/N_0$ (i.e., energy efficiency) behaviour for linear and orthogonal modulations. Note that an AWGN channel, BER = 10^{-5} and different dictionary sizes for linear and orthogonal modulations are considered for such simulations. The maximum achievable spectral efficiency curve according to Shannon's limit is also presented, while all the modulation schemes lie under Shannon's limit. It can be seen in Fig. 1.10 for the linear modulations (i.e., M-PSK and M-QAM), that the spectral efficiency improves by increasing the dictionary size M, while the required $E_{b(elec)}/N_0$ also increases, leading to poor energy efficiency. On the other hand, for orthogonal modulations, the performance behaviour is different, i.e., the spectral efficiency decreases by increasing the dictionary size M, while the required $E_{b(elec)}/N_0$ also decreases, leading to high

energy efficiency. Additionally, the orthogonal modulations become more and more energy efficient by increasing M, but at an expense of reduction in spectral efficiency. It should be noted that Fig. 1.10 is adapted for RF communications but the same idea can be adapted for OWC systems with the IM-DD compatible modulations.

1.7 Thesis Contribution

As aforementioned, OWC is a most suitable candidate to alleviate the scarcity issue of RF spectrum. Significant research is carried out on high data rate IM-DD OWC systems [8], [77], which is based on high spectral efficient modulations, such as M-ary PAM [67] or optical-orthogonal frequency-division multiplexing (O-OFDM) [78]. These modulation schemes sacrifice the energy efficiency. Nonetheless, the low data rate energy efficient modulations (by sacrificing the spectral efficiency) for OWC systems still need to be analyzed. This thesis presents the work that focuses on energy efficient modulations, consistent with the constraints of the IM-DD for OWC systems.

According to [79], OWC can be used for low data rate energy efficient applications, i.e., 100 kbps to 1 Mbps. In this regard, classical linear modulation schemes, such as M-ary PAM, OOK and O-OFDM are not good choices for energy efficient OWC systems. Although, these modulation schemes are with high spectral efficiency and their spectral efficiencies increases with increasing the modulation cardinallity, but at the same time, these modulation schemes show poor energy efficiency which negatively impacts the autonomy of battery powered terminals [80], [47]. On the contrary, orthogonal modulation schemes can be considered as promising candidates that show improved energy efficiency by sacrificing spectral efficiency, such as M-ary PPM and M-ary FSK. Recent research shows a considerable interest of FSK-based modulations for OWC/VLC applications, due to their high energy efficiency, channel equalization and quasi constant envelop property to deal with the non-linearity of the LED [30]. Indeed, the original FSK modulation is not compatible with the IM-DD constraints of OWC systems due to its bipolar nature. Therefore, Gipsa-Lab has presented two variants of M-ary FSK in [30], i.e., M-ary direct-current (DC)-FSK and M-ary unipolar (U)-FSK. Simulation results reveal that M-ary U-FSK shows better energy efficiency as compared to M-ary DC-FSK and linear modulations, especially when optimal time-domain (TD) maximum likelihood (ML) receiver is considered. Although, optimal TD ML receiver shows better bit-error-rate (BER) performance than sub-optimal reconstruction-based receiver for M-ary U-FSK, but the receiver complexity is high for optimal TD ML receiver relative to the sub-optimal reconstruction-based receiver [30]. Keeping this background in mind, the following contributions have been made:

- A new variant of conventional M-ary FSK is proposed that meets the constraints of the IM-DD OWC systems, i.e., M-ary Asymmetrically Clipped (AC)-FSK. Simulation results reveal that M-ary AC-FSK shows far better BER performance (i.e., better energy efficiency) as compared to M-ary DC-FSK and slightly better BER performance than M-ary U-FSK. Spectral analysis of M-ary AC-FSK waveforms lead to the proposition of frequency-domain (FD) 2-tap harmonic

receiver for M-ary AC-FSK, that achieves a similar BER performance as the optimal TD ML receiver but with the benefit of significant reduction of receiver complexity (cf. Chapter 3).

- Same technique of FD low-complexity L-tap harmonic receiver is proposed for M-ary U-FSK that overcomes the energy efficiency versus receiver complexity trade-off between the optimal TD ML receiver (better BER performance with high receiver complexity) and the sub-optimal DCT-based receiver (poor BER performance with low receiver complexity) for M-ary U-FSK. In L-tap harmonic receiver for M-ary U-FSK, twelve and two taps are selected for even and odd M-ary U-FSK waveforms, respectively, to achieve approximately a similar BER performance as the optimal TD ML receiver. The number of taps selected for even and odd waveforms depend upon the spectral structure of the U-FSK waveforms (cf. Chapter 2, Sec. 2.4).

- A new optical modulation scheme based on amalgamation of M-ary AC-FSK and phase-shift keying (PSK), referred to as AC-FPSK is proposed. It is indicated that the proposed modulation scheme, i.e., AC-FPSK shows better energy and spectral efficiency than M-ary AC-FSK, while it also offers better energy efficiency as compared to the state-of-the-art DC-FPSK (cf. Chapter 3, Sec. 3.5).

- An experimental demonstration on the software defined radio (SDR) test bench of the proposed M-ary AC-FSK (considering both optimal TD ML receiver and harmonic receiver) is presented. Experimental results for M-ary AC-FSK are compared with the state-of-the-art M-ary U-FSK. It is confirmed by experiments that the practical implementation of the proposed M-ary AC-FSK is feasible and it can be a good candidate for low data rate energy efficient OWC applications (cf. Chapter 4).

1.8 Conclusion

For Internet-of-Things (IoT) applications, a large number of wireless connections are expected for a wide range of devices to data hosting platforms via internet, which consumes a significant amount of radio-frequency (RF) spectrum. Thus, it leads to a critical issue of scarcity for RF spectrum. In this context, the integration of optical wireless communication (OWC) with IoT is a possible complementary candidate to alleviate the scarcity issue of RF spectrum. Moreover, OWC also provides some potential advantages, like virtually un-regulated and un-licensed spectrum, security in data transmission, no interference with RF communications etc.

Comprehensive research has been carried out for high data rate IoT applications. On the other hand, recent research confirmed that OWC can also be used for low data rate/high energy efficient IoT applications. In this perspective, orthogonal modulations can be good candidates since their energy efficiency can be increased by increasing the modulation size, contrary to the linear modulations. This is done at the cost of degrading the spectral efficiency, in full agreement with the spectral efficiency and energy efficiency trade-off imposed by information theory. In this regard, M-ary PPM has been studied

for low data rate/high energy efficient IoT applications, but it encounters some serious limitations, such as large PMOPR, synchronization issues at receiver and strong multipath channel impact on BER performance. To alleviate such limitations, M-ary FSK was first proposed for RF communications. Since conventional M-ary FSK is not compatible with IM-DD OWC systems due to its bipolar nature, therefore, unipolar and real-valued FSK-based modulations have been investigated for IM-DD OWC systems, such as M-ary DC-FSK and M-ary U-FSK in the literature (cf. Chapter 2), and we will also propose new schemes in the rest of the manuscript.

Chapter 2

Existing FSK-based modulations for OWC and proposed low complexity receiver for U-FSK

Contents

This chapter is mainly divided into two parts. The first part of the chapter (cf. Sec. 2.1 to Sec. 2.3) is dedicated to the conventional bipolar M-ary FSK and the two state-of the-art adapted variants, that are compatible with the OWC systems i.e., M-ary DC-FSK and M-ary U-FSK. In Sec. 2.1, the conventional bipolar M-ary FSK along with the different parameters are presented. Sec. 2.2 and Sec. 2.3 are dedicated for the FSK-based modulation schemes, i.e., M-ary DC-FSK and M-ary U-FSK, respectively, while their different parameters along with the simulation results are discussed in the appropriate sub-sections. These modulation schemes (i.e., M-ary DC-FSK and M-ary U-FSK) are used as the state-of-the-art for our proposed work presented in Sec. 2.4 and in chapter 3.

In the second part of the chapter (cf. Sec. 2.4), we present (as our first contribution of this Phd manuscript) a new proposed low complexity frequency-domain L-tap harmonic receiver for M-ary U-FSK [81]. We discuss the working principle, the receiver architecture and theoretical BER approximation of the proposed L-tap harmonic receiver for M-ary U-FSK. Simulation results are also present at the end of chapter, that shows the BER performance comparison of the L-tap harmonic receiver for M-ary U-FSK with the other conventional receivers.

2.1 Preliminaries

2.1.1 Conventional and Biorthogonal FSK signaling with base-band bipolar signals

Conventional M-ary FSK specifies a dictionary, $\mathscr{D}^{\text{FSK}}$, of M orthogonal bipolar sinusoidal waveforms, with the frequency of each waveform is identified via index $m \in \{0,1,\cdots,M-1\}$ [57][63]. The size of the FSK dictionary (i.e., cardinality) is denoted $|\mathscr{D}^{\text{FSK}}| = M$. The mth frequency waveform, $\tilde{\boldsymbol{s}}_m$, of the conventional bipolar M-ary FSK in digital time series (i.e., $\tilde{\boldsymbol{s}}_m = [\tilde{s}_m[0], \tilde{s}_m[1], \cdots, \tilde{s}_m[M-1]]^{\text{T}}$) is (considering here unitary amplitude) obtained as [82]:

$$\tilde{\boldsymbol{s}}_m = \boldsymbol{C}^{\text{T}} \boldsymbol{F}_m, \tag{2.1}$$

where $\boldsymbol{F}_m = [0,\cdots,1,\cdots,0]^{\mathrm{T}}$ states the activated frequency tone, i.e., the position of 1 in the vector indicates the activated frequency, and $\boldsymbol{C}$ is the M-order discrete cosine transform (DCT) matrix whose (n_1,n_2)th element is defined as [83]:

$$\boldsymbol{C}_{n_1,n_2} = \begin{cases} \frac{1}{\sqrt{M}} & n_1 = 0 \\ \sqrt{\frac{2}{M}}\cos\left(\frac{\pi(2n_2+1)n_1}{2M}\right) & 1 \le n_1 \le M-1 \end{cases}, \tag{2.2}$$

where $0 \le n_2 \le M-1$. It can be noticed that DCT is used to generate M-ary FSK waveforms instead of discrete Fourier transform (DFT) to obtain directly real-valued waveforms [1]. Since, we are considering real-valued signal, as used for example in wired (electrical) base-band (i.e., without carrier frequency) communication. The analog time-domain (TD) counterpart of M-ary FSK waveforms, $\tilde{s}_m(t)$, is obtained using $t = (n+\frac{1}{2})T_{\mathrm{c}}$ as [30]:

$$\tilde{s}_m(t) = \begin{cases} \frac{A}{\sqrt{2}} & m = 0 \\ A\cos(2\pi m\Delta f t) & 1 \le m \le M-1 \end{cases}, \tag{2.3}$$

where A is the (introduced) amplitude of the waveform and $\Delta f = 1/2\tilde{T}_{\mathrm{s}}$ is the minimal frequency spacing between adjacent waveforms that ensure the orthogonality between waveforms. The chip period is denoted by T_{c} and symbol duration by $\tilde{T}_{\mathrm{s}} = M_{\mathrm{c}}T_{\mathrm{c}}$, where M_{c} represents the number of chips per waveform, i.e., $M_{\mathrm{c}} = M$ for conventional bipolar M-ary FSK.

The orthogonality between the M orthogonal waveforms of $\mathscr{D}^{\mathrm{FSK}}$ is guarantied as the inner product between any pair, $\langle\tilde{s}_i(t),\tilde{s}_j(t)\rangle$, $i \neq j$ is;

$$\langle\tilde{s}_i(t),\tilde{s}_j(t)\rangle \overset{\text{def}}{=} \int_0^{\tilde{T}_{\mathrm{s}}} \tilde{s}_i(t)\tilde{s}_j(t)dt = 0, \quad \text{for} \quad i \neq j. \tag{2.4}$$

It is also possible to extend the dictionary $\mathscr{D}^{\mathrm{FSK}}$ by adding out-of-phase counter-parts of each waveform, still respecting the orthogonality condition (2.4), resulting a new biorthogonal dictionary, $\mathscr{D}_{\mathrm{b}}^{\mathrm{FSK}}$, composed of $2M$ waveforms, i.e., $|\mathscr{D}_{\mathrm{b}}^{\mathrm{FSK}}| = 2M$. The biorthogonal waveforms are denoted by $\tilde{s}_{\tilde{m}(t)}$ with index, $\tilde{m}$, where $\tilde{m} \in \{0,1,\cdots,2M-1\}$. Note that the waveforms corresponding to $M \le \tilde{m} \le 2M-1$ in $\mathscr{D}_{\mathrm{b}}^{\mathrm{FSK}}$ are the out-of-phase versions of the waveforms with indices $0 \le \tilde{m} \le M-1$ in $\mathscr{D}^{\mathrm{FSK}}$, i.e., $\mathscr{D}_b^{\mathrm{FSK}} = \{\mathscr{D}^{\mathrm{FSK}}; -\mathscr{D}^{\mathrm{FSK}}\}$. We define for $M \le \tilde{m} \le 2M-1$ as [30]:

$$\tilde{s}_{\tilde{m}}(t) = -\tilde{s}_{\tilde{m}-M}(t), \tag{2.5}$$

[1] It should be noted that real-valued signal can also be obtanied with DFT, but with the requirement to have some additional manipulations/repetitions in frequency-domain to impose Hermitian symmetry, required to generate real-valued time-domain signal

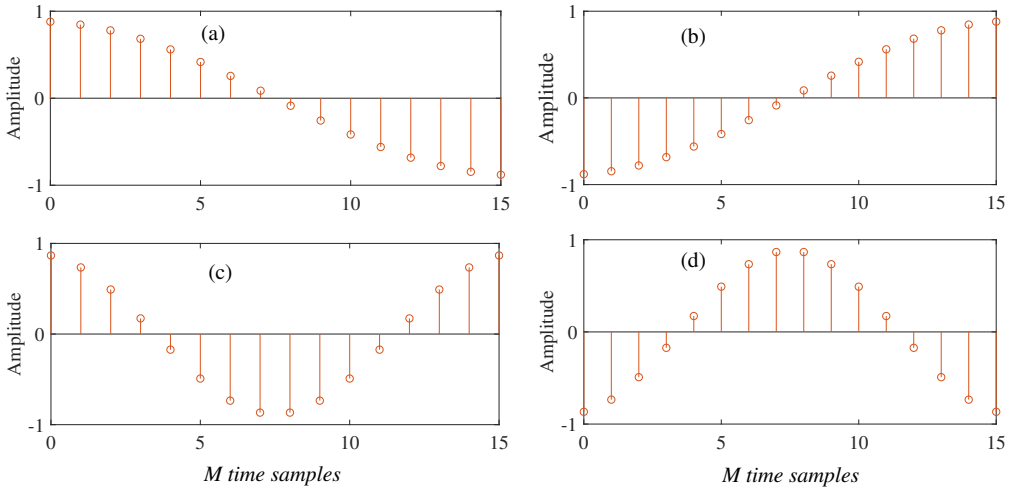

Fig. 2.1 (a) and (c) illustrate the time-domain M-ary FSK orthogonal waveforms, i.e., $\tilde{\mathbf{s}}_m(t) \in \mathscr{D}^{\text{FSK}}$ (for $m = 1$ and $m = 2$, respectively), while (b) and (d) illustrate their bi-orthogonal counterparts, for $M = 16$.

Fig. 2.1 (a) and (c) respectively illustrate the time-domain orthogonal waveforms with frequency indices $m = 1$ and $m = 2$ for M-ary FSK, while Fig. 2.1 (b) and (d) represent their bi-orthogonal counterparts presented in (2.5). It can be seen in Fig. 2.1 that the waveforms in (b) and (d) are exactly the out-of-phase versions of the waveforms in (a) and (c), respectively.

2.1.2 Average M-ary FSK Symbol Energy

The average electrical symbol energy for M-ary FSK, $E^{\text{FSK}}_{\text{s(elec)}}$, is defined from the Euclidean norms of the waveforms, $\|s_i(t)\|^2$, in the dictionary $\mathscr{D}^{\text{FSK}}$, as:

$$E_{\text{s(elec)}} = \frac{1}{M}\sum_{m=0}^{M-1}\|\tilde{s}_m(t)\|^2 = \frac{1}{M}\sum_{m=0}^{M-1}\int_0^{\tilde{T}_s}|\tilde{s}_m(t)|^2\mathrm{d}t, \tag{2.6}$$

As all the M-ary FSK waveforms have equal symbol energy in $\mathscr{D}^{\text{FSK}}$, hence $E^{\text{FSK}}_{\text{s(elec)}}$ can be computed as:

$$\begin{aligned} E^{\text{FSK}}_{\text{s(elec)}} &= \int_0^{\tilde{T}_s}|\tilde{\mathbf{s}}_m(t)|^2\mathrm{d}t, \\ &= \tilde{T}_s\left(\frac{A^2}{2}\right), \quad \text{for} \quad m \in \{0,1,\cdots,M-1\}. \end{aligned} \tag{2.7}$$

where A is the amplitude of M-ary FSK waveforms.

2.1.3 Minimum squared Euclidean Distance between M-ary FSK waveforms

The squared Euclidean distance between waveform pairs, $(s_i(t);s_j(t))$, in any dictionary, $\mathscr{D}$, predicts the performance of the modulation schemes. We evaluate the minimum squared Euclidean distance between symbols, which is related to the bit error probability [57]. The larger the minimum squared Euclidean distance between symbols, the higher robustness of the modulation to noise (assuming optimal receiver in AWGN channel). The squared Euclidean distance, d^2, between any pair of waveforms, $(s_i(t);s_j(t))$, in the dictionary, $\mathscr{D}$, for any modulation scheme can be mathematically computed as [57]:

$$\begin{aligned} d^2 &= \|s_i(t)-s_j(t)\|^2, \\ &= \|s_i(t)\|^2+\|s_j(t)\|^2-2\Re\langle s_i(t),s_j(t)\rangle. \end{aligned} \tag{2.8}$$

where $\Re$ is the real part operator, $\|s_i(t)\|^2$ and $\|s_j(t)\|^2$ represent the symbols energy of ith and jth waveforms, respectively and $\langle s_i(t),s_j(t)\rangle$ represents the inner product between waveforms in $\mathscr{D}$. It can be seen from (2.8) that the squared Euclidean distance, d^2, between any pair of waveforms, $(s_i(t);s_j(t))$, is impacted by the inner product contribution, $\langle s_i(t),s_j(t)\rangle$.

From (2.8), the minimum squared Euclidean distance, $d^2_{\min}$, between waveform pairs, $(s_i(t);s_j(t))$, in dictionary, $\mathscr{D}$, for any real modulation can be computed by introducing the maximum value for $\Re\langle s_i(t),s_j(t)\rangle$, defined as $\Re\langle s_i(t),s_j(t)\rangle_{\max}$ computed from (2.4) as:

$$\begin{aligned} d^2_{\min} &= \min_{i\neq j}\|s_i(t)-s_j(t)\|^2, \\ &= \|s_i(t)\|^2+\|s_j(t)\|^2-2\Re\langle s_i(t),s_j(t)\rangle_{\max}, \end{aligned} \tag{2.9}$$

For the case of conventional bipolar M-ary FSK, all the waveforms in $\mathscr{D}^{\text{FSK}}$ are orthogonal to each other, therefore, the inner product for M-ary FSK is computed as [30]:

$$\langle \tilde{s}_i(t),\tilde{s}_j(t)\rangle = \begin{cases} 0 & \text{for} \quad i\neq j \\ \frac{A^2}{2}\tilde{T}_{\text{s}} = E^{\text{FSK}}_{\text{s(elec)}} & \text{for} \quad i=j \end{cases}, \tag{2.10}$$

Using the orthogonality condition from (2.10) in (2.9), the minimum squared Euclidean distance for M-ary FSK can be computed as:

$$\begin{aligned} d^2_{\text{min,FSK}} &= \|\tilde{s}_i(t)\|^2+\|\tilde{s}_j(t)\|^2 \qquad \text{for} \quad i\neq j, \\ &= 2E^{\text{FSK}}_{\text{s(elec)}}. \end{aligned} \tag{2.11}$$

2.1.4 Spectral Efficiency of M-ary FSK

The spectral efficiency (bit/sec/Hz) of any baseband modulation scheme can be computed as:

$$\eta = \frac{R_{\text{b}}}{B}, \tag{2.12}$$

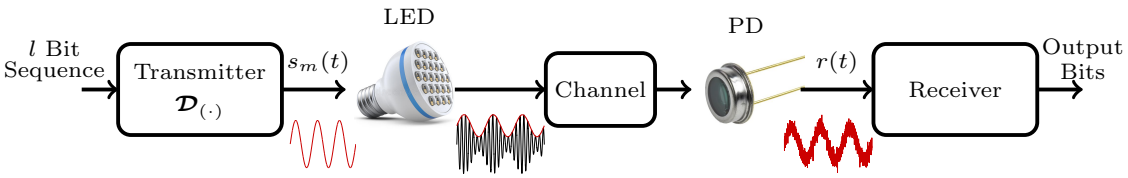

Fig. 2.2 Generalized system model configuration [30].

where R_b is the data rate and B is the baseband occupied bandwidth of the modulation. For the conventional bipolar M-ary FSK modulations, $R_\mathrm{b} = n/\tilde{T}_\mathrm{s}$, where n represents the number of bits per waveform, i,e., $n = \log_2(M)$, and $B \approx M\Delta f$, for sufficiently large M, where $\Delta f = 1/2\tilde{T}_\mathrm{s}$, represents the frequency spacing between adjacent waveforms for M-ary FSK that ensures the orthogonality [84]. Hence, the spectral efficiency of M-ary FSK, η^{FSK}, can be computed as:

$$\eta^{\mathrm{FSK}} = \frac{2\log_2(M)}{M}. \tag{2.13}$$

For biorthogonal $2M$-ary FSK, $R_\mathrm{b} = n_b/\tilde{T}_\mathrm{s}$ with $n_b = \log_2(2M)$, and bandwidth, B, is left unchanged. So, the spectral efficiency of the biorthogonal $2M$-ary FSK, $\eta_\mathrm{b}^{\mathrm{FSK}}$, is greater than the one of M-ary FSK waveform for a given M, and it can be computed as:

$$\eta_\mathrm{b}^{\mathrm{FSK}} = \frac{2\log_2(2M)}{M}. \tag{2.14}$$

2.1.5 System Model for OWC modulation analysis

Fig. 2.2 illustrates the generalized system model configuration. As a general case, the dictionary, $\mathscr{D}^{(.)}$, is considered, where (.) in superscript represents the type of modulations. The mth transmitted waveform is determined via binary to decimal mapping of $l = \log_2(|\mathscr{D}^{(.)}|)$ independent and equiprobable bits, which modulates the intensity of the LED, where $|\mathscr{D}^{(.)}|$ is the cardinality (i.e. size) of the modulation dictionary. For clarity of notation, the sampled version (called symbol) and its vectorial form of the transmitted waveform, $s_m(t)$, is expressed as $s_m[n]$ and $\boldsymbol{s}_m = [s_m[0], s_m[1], \cdots, s_m[M_\mathrm{c}-1]]^\mathrm{T}$, respectively. Each waveform consists of $M_\mathrm{c} = T_\mathrm{s}/T_\mathrm{c}$ chips with the bit rate of $R_\mathrm{b} = \log_2(|\mathscr{D}^{(.)}|)/T_\mathrm{s}$. The LED transforms $s_m(t)$ into an optical intensity waveform, i.e., $u_m(t) = \varepsilon s_m(t)$, where ε (in Watt (W)/Ampere (A)) represents the electrical-to-optical conversion factor. Perfect synchronization is considered at the receiver [50] [51]. The impulse response of the channel is represented by $h(t)$, and after photo-detection, the received waveform is given by $r(t) = \kappa(h(t) \otimes u_m(t))$, where κ (in A/W) is the responsitivity of the photo-diode (PD) [81]. Furthermore, a linear response for LED and PD is adopted [85]. We consider $\varepsilon = 1$ W/A and $\kappa = 1$ A/W to maintain the generality, therefore, $r(t) = h(t) \otimes u_m(t)$, and $u_m(t) = s_m(t)$. The received waveform, $r(t)$, is contaminated by the ambient noise. The digitized received waveform, $\boldsymbol{r}$, is obtained by impinging $r(t)$ on an analog-to-digital converter (ADC) as [81]:

$$\boldsymbol{r} = \boldsymbol{h} \otimes \boldsymbol{s}_m + \boldsymbol{w}, \tag{2.15}$$

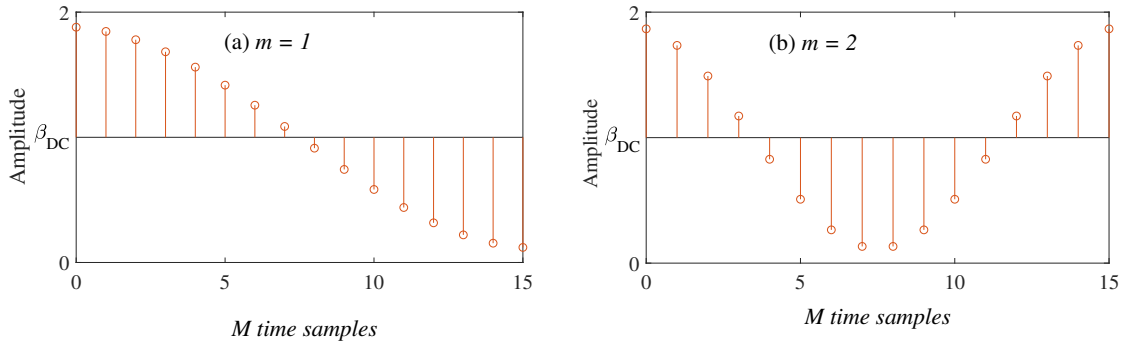

Fig. 2.3 An illustration of M-ary DC-FSK waveforms for (a): $m = 1$ and (b): $m = 2$, i.e., $\boldsymbol{s}_1^{\mathrm{DC}}[n]$ and $\boldsymbol{s}_2^{\mathrm{DC}}[n]$, respectively, considering $M = 16$.

where $\boldsymbol{w}$ is the AWGN having mono-lateral power spectral density (PSD) of N_0, i.e., $\boldsymbol{w} = [w[0], w[1], \cdots, w[M_{\mathrm{c}}-1]]^{\mathrm{T}}$. Similarly, $\boldsymbol{s}_m = [s[0], s[1], \cdots, s[M_{\mathrm{c}}-1]]^{\mathrm{T}}$, $\boldsymbol{h} = [h[0], h[1], \cdots, h[M_{\mathrm{c}}-1]]^{\mathrm{T}}$, and $\boldsymbol{r} = [r[0], r[1], \cdots, r[M_{\mathrm{c}}-1]]^{\mathrm{T}}$. As a first proof-of-concept approach for signalling analysis and simulations, we considered a simple additive white Gaussian noise (AWGN) channel, corresponding to a line-of-sight (LOS) OWC transmission impacted by an AWGN ambient noise, so the impulse response of the channel is $h(t) = \delta(t)$, in (2.15), where $\delta(t)$ represents the Dirac distribution [81].

2.2 M-ary DC-FSK modulation scheme for OWC

2.2.1 M-ary DC FSK signaling

IM-DD OWC systems require a real and unipolar waveform definition to modulate the LED bias current and realize intensity modulation. The easiest way is to add a DC-bias to all the M-ary FSK waveforms in the dictionary, $\mathscr{D}^{\mathrm{FSK}}$, this leads us to the generation of FSK-based modulation, called M-ary DC-FSK modulation which is real and unipolar in nature and is compatible with IM-DD systems.

Fig. 2.3 (a) and (b), respectively illustrate the M-ary DC-FSK waveforms, $\boldsymbol{s}_1^{\mathrm{DC}}$, and $\boldsymbol{s}_2^{\mathrm{DC}}$, for frequency index $m = 1$, and $m = 2$. It can be seen that the required DC-offset, β_{DC}, is added to M-ary FSK waveforms to make them unipolar waveforms, which are compatible with IM-DD OWC systems.

2.2.2 M-ary DC-FSK Transmitter

The transmitter configuration of M-ary DC-FSK is shown in Fig. 2.4, where the mth waveform is chosen from binary-to-decimal conversion of $l = \log_2(M)$, independent and equiprobable bits [30]. Initially, the FSK waveform, $\tilde{s}_m[n]$, is extrapolated from a look-up table (LUT) according to the chosen frequency. Afterwards, a DC-offset, β_{DC}, is added to $\tilde{s}_m[n]$ to achieve a real and unipolar waveform, $\boldsymbol{s}_m^{\mathrm{DC}}$, which defines M-ary DC-FSK waveform. As an example, the illustrations of $\boldsymbol{s}_1^{\mathrm{DC}}$ and $\boldsymbol{s}_2^{\mathrm{DC}}$ are presented in Fig. 2.3 (a) and (b), respectively. Actually, $s_m^{\mathrm{DC}}[n] = \beta_{DC} + \tilde{s}_m[n]$, where the number

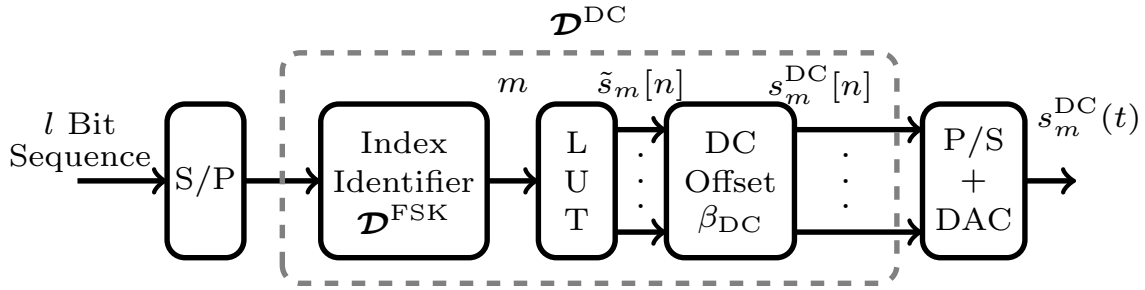

Fig. 2.4 Transmitter configuration of M-ary DC-FSK [30].

of chips per waveform is the same for both M-ary DC-FSK and M-ary FSK, i.e., $M_{\mathrm{c}} = M$. The time-domain (TD) counterpart, $s_m^{\mathrm{DC}}(t)$, of $s_m^{\mathrm{DC}}[n]$ is obtained by impinging $s_m^{\mathrm{DC}}[n]$ on a digital-to-analog converter (DAC), while considering $t = (n+\frac{1}{2})T_{\mathrm{c}}$. The resulting TD mth waveform of M-ary DC-FSK is given as [30]:

$$s_m^{\mathrm{DC}}(t) = \beta_{\mathrm{DC}} + \tilde{s}_m(t), \tag{2.16}$$

where $t \in [0, T_{\mathrm{s}}]$, and symbol time is same for both M-ary DC-FSK and M-ary FSK, i.e., $T_{\mathrm{s}} = \tilde{T}_{\mathrm{s}}$.

2.2.3 Average M-ary DC-FSK Symbol Energy

All the waveforms in M-ary DC-FSK dictionary have the same electrical energy, $E_{\mathrm{s(elec)}}^{\mathrm{DC}}$, except for $s_0^{\mathrm{DC}}(t)$. The average electrical energy per M-ary DC-FSK waveform (for $m \neq 0$) can be computed as [30]:

$$\begin{aligned} E_{\mathrm{s(elec)}}^{\mathrm{DC}} &= \frac{1}{M-1}\sum_{m=1}^{M-1}\int_0^{\tilde{T}_{\mathrm{s}}} |s_m^{\mathrm{DC}}(t)|^2 \mathrm{d}t, \\ &= \tilde{T}_{\mathrm{s}}\left(\frac{A^2}{2} + \beta_{\mathrm{DC}}^2\right). \end{aligned} \tag{2.17}$$

Due the addition of DC-offset, the symbol energy, $E_{\mathrm{s(elec)}}^{\mathrm{DC}}$, for $s_0^{\mathrm{DC}}(t)$ is changed. Therefore, $E_{\mathrm{0,s(elec)}}^{\mathrm{DC}}$ for $s_0^{\mathrm{DC}}(t)$ can be computed as [30]:

$$\begin{aligned} E_{\mathrm{0,s(elec)}}^{\mathrm{DC}} &= \int_0^{\tilde{T}_{\mathrm{s}}} |s_0^{\mathrm{DC}}(t)|^2 \mathrm{d}t, \\ &= E_{\mathrm{s(elec)}}^{\mathrm{DC}} + \sqrt{2}A\beta_{\mathrm{DC}}, \end{aligned} \tag{2.18}$$

Note that the DC waveform, $s_0^{\mathrm{DC}}(t)$, is usually not considered for transmission because of the possible impact of background noise at photo-detection at receiver side.

2.2.4 Minimum squared Euclidean distance between M-ary DC-FSK waveforms

The minimum squared Euclidean distance between waveform pairs, $(s_i^{\mathrm{DC}}(t); s_j^{\mathrm{DC}}(t))$, for M-ary DC-FSK can be computed using (2.9). It can be noticed that the addition of DC-offset affects the

orthogonality between the M-ary DC-FSK waveforms and hence, the inner product, $\langle s_i(t), s_j(t)\rangle$, between the waveform pairs, $(s_i^{\mathrm{DC}}(t); s_j^{\mathrm{DC}}(t))$, is no more equal to zero, i.e., $\langle s_i^{\mathrm{DC}}(t), s_j^{\mathrm{DC}}(t)\rangle \neq 0$. According to [30], the inner product, $\langle s_i^{\mathrm{DC}}(t), s_j^{\mathrm{DC}}(t)\rangle$, for waveform pairs, $(s_i^{\mathrm{DC}}(t); s_j^{\mathrm{DC}}(t)) \in \mathscr{D}^{\mathrm{DC}}$, is given as:

$$\langle s_i^{\mathrm{DC}}(t), s_j^{\mathrm{DC}}(t)\rangle = \int_0^{\tilde{T}_{\mathrm{s}}} s_i^{\mathrm{DC}}(t) s_j^{\mathrm{DC}}(t)\mathrm{d}t = \beta_{\mathrm{DC}}^2 \tilde{T}_{\mathrm{s}} \;\; \forall i \neq j \neq 0. \tag{2.19}$$

To attain the non-negative unipolar transmit waveforms, the minimum value of the DC-offset, β_{DC}, is set to A, that results in $E_{\mathrm{s(elec)}}^{\mathrm{DC}} = 3E_{\mathrm{s(elec)}}^{\mathrm{FSK}}$, for $m \in \{1, 2, \cdots, M-1\}$ (cf. eq (2.17)). Considering $\beta_{\mathrm{DC}} = A$, and integrating (2.19), (2.17) into (2.9), the minimum squared Euclidean distance can be computed as [30]:

$$d_{\mathrm{min,DC}}^2 = 2E_{\mathrm{s}_{(\mathrm{elec})}}^{\mathrm{DC}} \times \gamma^{\mathrm{DC}}. \tag{2.20}$$

where $(i, j) \in \{1, 2, \cdots, M-1\}$, and $\gamma^{\mathrm{DC}} = 1/3$ [30]. γ^{DC} accounts for the penalty coefficient on the minimum squared Euclidean distance for M-ary DC FSK relatively to the minimum squared Euclidean distance for M-ary FSK (2.11). Degradation of the robustness to noise is more important if the penalty coefficient is low (since it decreases d_{min}^2 for a given symbol energy). Penalty coefficient for M-ary FSK being $\gamma^{\mathrm{FSK}} = 1$ used as reference, it can be noticed that $\gamma^{\mathrm{DC}} < \gamma^{\mathrm{FSK}}$ due to the addition of DC-offset, that may alter or decrease the energy efficiency of the M-ary DC-FSK modulation scheme relatively to M-ary FSK. In other words, we have to increase the symbol energy by a factor 3 to ensure a same minimum distance when passing from FSK to DC-FSK.

2.2.5 Spectral Efficiency of M-ary DC-FSK

The spectral efficiency of M-ary DC-FSK can be computed using (2.12), where the signal bandwidth for sufficiently large M is approximately, $B \approx M\Delta f = M/2\tilde{T}_{\mathrm{s}}$, and the data rate, R_{b}, is $\log_2(|\mathscr{D}|)^{\mathrm{DC}}/\tilde{T}_{\mathrm{s}} = \log_2(M)/\tilde{T}_{\mathrm{s}}$, for M-ary DC-FSK. Therefore, the spectral efficiency for M-ary DC-FSK, η^{DC}, is given as:

$$\begin{aligned} \eta^{\mathrm{DC}} &= \frac{R_{\mathrm{b}}}{B} = \frac{\log_2(M)/\tilde{T}_{\mathrm{s}}}{M/2\tilde{T}_{\mathrm{s}}}, \\ &= \frac{2\log_2(M)}{M}. \end{aligned} \tag{2.21}$$

From (2.13) and (2.21), it can be noticed that the spectral efficiency of M-ary DC-FSK, η^{DC}, is same as for conventional M-ary FSK because the addition of DC-offset does not affect the spectral efficiency. Moreover, η^{DC} can be increased by a factor of $\frac{2}{M}$ by introducing biorthogonal extension in the orthogonal dictionary, $\mathscr{D}^{\mathrm{DC}}$ (cf. Sec. 2.1.1).

2.2.6 M-ary DC-FSK Receivers

There are two different types of receivers considered for M-ary DC-FSK, i.e., optimal time-domain (TD) maximum likelihood (ML) receiver and 1-tap DCT-based receiver.

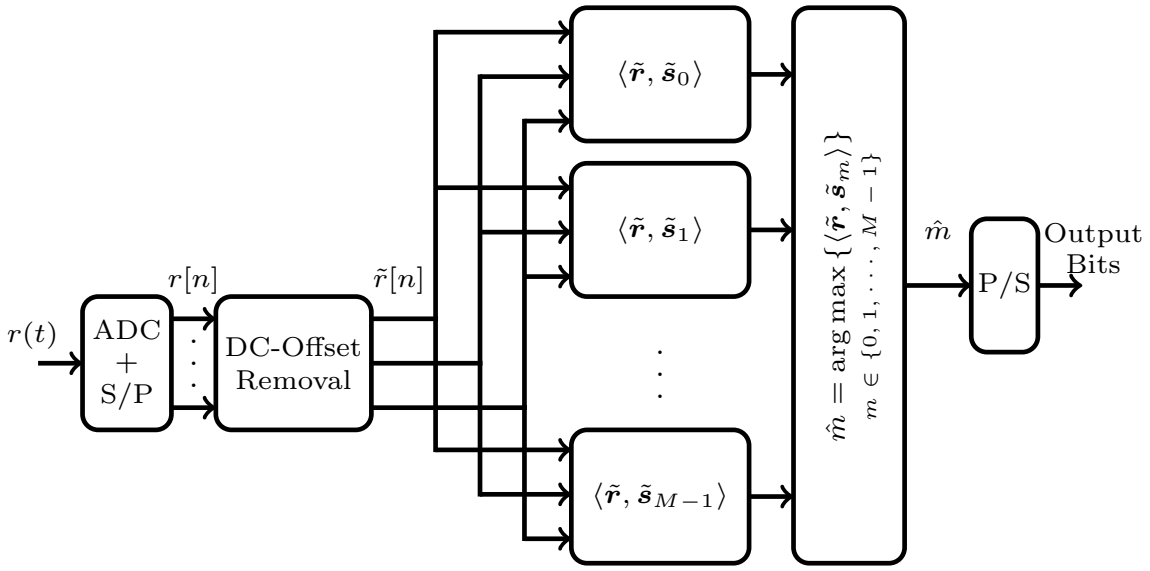

Fig. 2.5 Theoretical time-domain maximum likelihood (ML) receiver architecture for M-ary DC-FSK [30].

Theoretical Maximum Likelihood (ML) Receiver:

It is also known as the optimal time-domain (TD) receiver and its architecture for M-ary DC-FSK is shown in Fig. 2.5. The ML criterion identifies the frequency index m from the received waveform, $\boldsymbol{r}$, in $\mathscr{D}^{\mathrm{DC}}$ by maximum likelihood function, $p(\boldsymbol{r}|\boldsymbol{s}_m^{\mathrm{DC}})$, assuming the equiprobability of the transmit waveforms, i.e., $p(\boldsymbol{s}_m^{\mathrm{DC}}) = 1/M$, where $p(\boldsymbol{r}|\boldsymbol{s}_m^{\mathrm{DC}})$ is the conditional probability of observing $\boldsymbol{r}$ when $\boldsymbol{s}_m^{\mathrm{DC}}$ is sent. Considering an AWGN channel, with a channel noise variance, $\sigma_{ch}^2 = N_0 f_s$, the likelihood function can be computed as [86]:

$$\begin{aligned} p(\boldsymbol{r}|\boldsymbol{s}_m^{\mathrm{DC}}) &= \left(\frac{1}{2\pi\sigma_{ch}^2}\right)^{M_{\mathrm{c}}} \exp\left(-\frac{\|\boldsymbol{r}-\boldsymbol{s}_m^{\mathrm{DC}}\|^2}{2\sigma_{ch}^2}\right) \\ &= \Gamma \exp\left(\frac{\langle \boldsymbol{r}, \boldsymbol{s}_m^{\mathrm{DC}} \rangle}{\sigma_{ch}^2}\right), \end{aligned} \tag{2.22}$$

where $\Gamma = (1/2\pi\sigma_{ch}^2)\exp(-\|\boldsymbol{r}\|^2 - \|\boldsymbol{s}_m^{\mathrm{DC}}\|^2/2\sigma_{ch}^2)$, while $\|\boldsymbol{r}-\boldsymbol{s}_m^{\mathrm{DC}}\|^2 = \|\boldsymbol{r}\|^2 + \|\boldsymbol{s}_m^{\mathrm{DC}}\|^2 - 2\Re\langle \boldsymbol{r}, \boldsymbol{s}_m^{\mathrm{DC}} \rangle$, with $\Re$ being the real operator. For all m, $\|\boldsymbol{s}_m^{\mathrm{DC}}\|^2$ and $\|\boldsymbol{r}\|^2$ are constant, then the estimated frequency index $\hat{m}$ is identified using the ML criterion as:

$$\hat{m} = \arg\max_m p(\boldsymbol{r}|\boldsymbol{s}_m^{\mathrm{DC}}), \;\; m \in \{1, 2, \cdots, M-1\}. \tag{2.23}$$

In practical scenario, (2.23) can be implemented for M-ary DC-FSK by removing the DC-offset, β_{DC}, from $r[n]$ to attained the M-ary FSK waveform, $\tilde{r}[n]$, i.e., $\tilde{r}[n] = r[n] - \beta_{\mathrm{DC}}$. Afterward, the time-domain (TD) cross-correlation is applied between $\tilde{r}[n]$ and $\tilde{s}_m[n] \in \mathscr{D}^{\mathrm{FSK}}$, which provides the

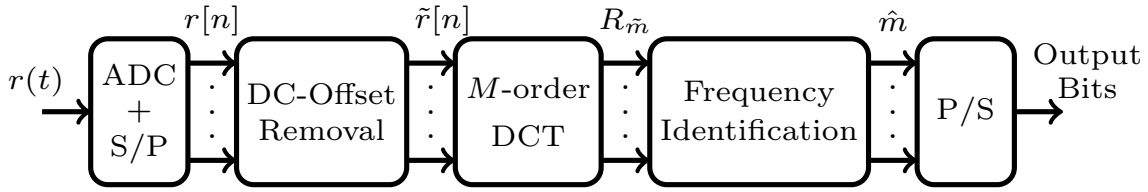

Fig. 2.6 Low-complexity but ML receiver configuration for M-ary DC-FSK, which is based on DCT, also called 1-tap DCT-based receiver [30].

estimated frequency index $\hat{m}$, when considering the highest value of the TD cross-correlation as:

$$\hat{m} = \arg\max_{m} \Big\{ \langle \tilde{\boldsymbol{r}}, \tilde{\boldsymbol{s}}_m \rangle \Big\}, \quad m \in \{1, 2, \cdots, M-1\}. \tag{2.24}$$

(2.24) indicates that ML receiver needs to estimate M TD cross-correlations between $\tilde{\boldsymbol{r}}$ and all the waveforms, $\tilde{\boldsymbol{s}}_m \in \mathscr{D}^{\mathrm{FSK}}$, to identify the frequency index m of the transmitted waveform. It must be noticed that the TD cross-correlator operates TD noise averaging, leading to optimal detection.

Low-complexity ML receiver based on DCT, denoted 1-tap DCT-based Receiver:

1-tap receiver is based on discrete cosine transform (DCT). Fig. 2.6 illustrates the architecture of low-complexity ML receiver based on DCT for M-ary DC-FSK. In the first step, the digitize received waveform, $\boldsymbol{r}$, is attained by impinging the TD received waveform, $r(t)$, into the ADC. Subsequently, the M-ary FSK waveform, $\tilde{\boldsymbol{r}}$, is obtained in the same manner as for the ML receiver by removing the DC-offset, β_{DC}, from $r[n]$. Afterward, the frequency-domain (FD) received waveform, $\boldsymbol{R}$, is obtained by applying the M-order DCT on $\tilde{\boldsymbol{r}}$ using (2.2) as:

$$\boldsymbol{R} = \boldsymbol{C}_{\mathrm{M}} \tilde{\boldsymbol{r}}, \tag{2.25}$$

where $\boldsymbol{R} = [R[0], R[1], \cdots, R[M-1]] \in \Re^{\mathrm{M}}$. It is important to note that the symbol energy is contained by only one tap corresponding to the fundamental harmonic for FD M-ary FSK waveforms, obtained through DCT. Therefore, the decision can be made at a single tap. Finally, the estimated frequency index $\hat{m}$ is identified from (2.25) as:

$$\hat{m} = \arg\max_{m} \Big\{ |R_m| \Big\}, \quad m \in \{1, 2, \cdots, M-1\}. \tag{2.26}$$

2.2.7 Complexity Analysis of M-ary DC-FSK Receivers

The primary contributor to the computational complexity of the receiver is the number of non-zero real multiplications to identify the frequency index, whereas, the number of additions does not lead to

a significant amount of complexity [81]. Hence, only non-zero real multiplications are considered to compute the complexities of the receivers.

As the optimal TD ML receiver for M-ary DC-FSK needs to compute M TD cross-correlations between $\tilde{\boldsymbol{r}}$ and the waveforms from $\mathscr{D}^{\text{FSK}}$, and since the number of chips per waveform is $M_{\text{c}} = M$, therefore, the optimal TD ML receiver for M-ary DC-FSK requires $\mathscr{C}_{\text{TD,ML}} = M_{\text{c}}M = M^2$, non-zero real multiplications [30]. Similarly, the 1-tap DCT-based receiver requires $\mathscr{C}_{1-\text{tap}} = (M/2)\log_2(M)$, non-zero real multiplications due to the M-order DCT operation [87]. Note that the complexity of the 1-tap DCT-based receiver for M-ary DC-FSK relative to the TD ML receiver decreases by 87.5% and 97.2%, considering $M = 16$ and 128, respectively.

2.2.8 DC-FSK with Phase Modulation Extension

A new approach of DC-FSK with phase modulation extension is presented in [88], that amalgamated the conventional DC-FSK with phase-shift keying (FSK), resulting a new hybrid frequency and phase-shift keying modulation. This new modulation is referred as $(M_{\perp}, M_{\phi})$-DC-FPSK, where $M_{\perp}$ represents the number of available frequencies with the m-th activated frequency tone as $m \in \{1, 2, \cdots, M_{\perp}\}$, and M_{ϕ} represents the number of phases added according to Gray coding to each available frequency with the i-th activated phase as $i \in \{0, 1, \cdots, M_{\phi} - 1\}$, while the dictionary size is $M = M_{\perp} \times M_{\phi}$. The spectral efficiency of $(M_{\perp}, M_{\phi})$-DC-FPSK is presented in [88] as:

$$\eta^{\text{DC-FPSK}} = \frac{\log_2(M_{\perp}M_{\phi})}{M_{\perp}} \qquad \text{(bits/s/Hz)}. \tag{2.27}$$

In fact, this approach combines the linear and orthogonal modulation schemes to increase the spectral efficiency of the actual orthogonal modulation. Simulation results in [88] (cf. Fig. 6) confirm that $(M_{\perp}, M_{\phi})$-DC-FPSK shows better performance as compared to DC-FSK in terms of energy efficiency and spectral efficiency trade-off. We will use $(M_{\perp}, M_{\phi})$-DC-FPSK as a state-of-the-art modulation in section 3.5, to compare its performance with the one of our proposed modulation schemes.

2.3 M-ary U-FSK Modulation scheme for OWC

2.3.1 M-ary U-FSK Signaling

An alternative approach, called M-ary U-FSK is also presented in the perspective to decrease the required energy for a given performance regarding the robustness to noise. It is also real and unipolar in nature and is compatible with IM-DD OWC systems [30]. M-ary U-FSK waveform sequentially transmits the positive amplitude samples of M-ary FSK waveform (the negative samples are clipped to zero) in the first symbol period, followed by the polarity reversed negative amplitude samples (the positive samples are clipped to zero) in the second symbol period [30], [52]. Hence, the symbol time, T_{s}, and number of chips per waveform, M_{c}, become doubled, i.e., $T_{\text{s}} = 2\tilde{T}_{\text{s}}$ and $M_{\text{c}} = 2M$, respectively.

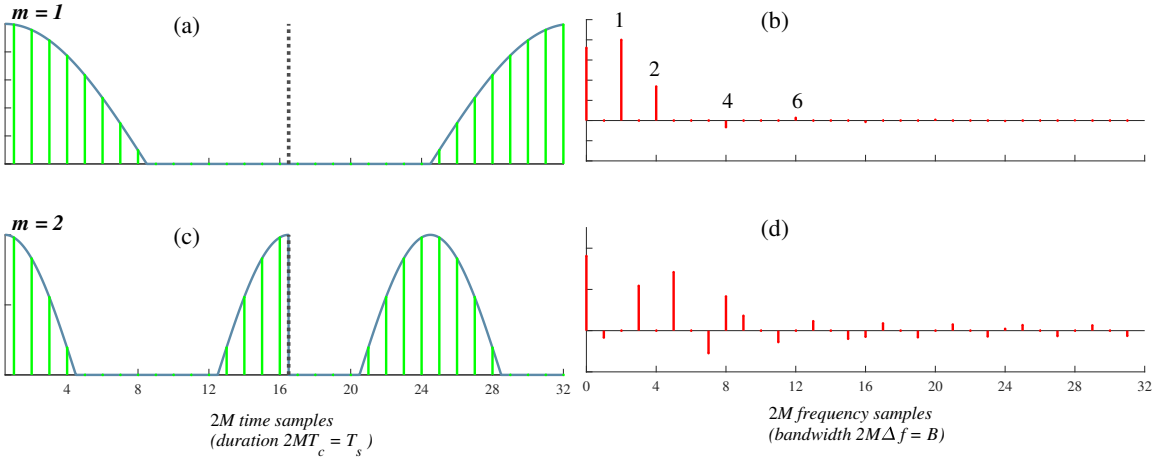

Fig. 2.7 (a) and (c) represent the time-domain M-ary U-FSK odd and even waveforms ($m = 1, 2$ respectively), while (b) and (d) represent their frequency-domain counterpart, considering $M = 16$.

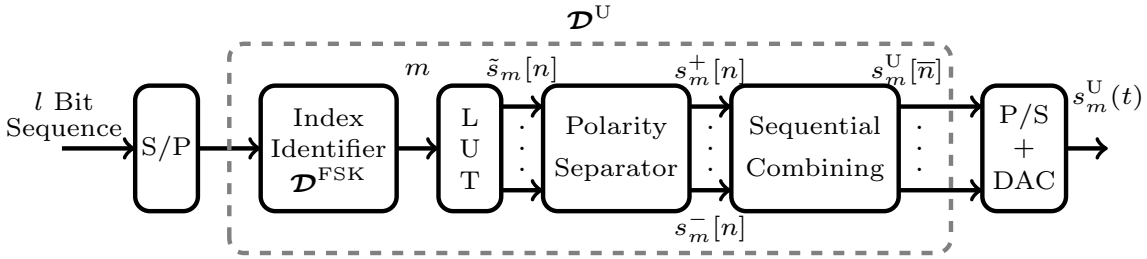

Fig. 2.8 Transmitter configuration for M-ary U-FSK [30].

Fig. 2.7 (a) and (c) respectively illustrates the time-domain odd and even waveform of M-ary U-FSK for frequency index m = 1 and 2, considering $M = 16$ ($M_c = 32$), while their frequency-domain counterparts are obtained through M_c-order DCT and are illustrated in Fig. 2.7 (b) and (d), respectively. It can be generalized that most of the energy (more than 90%) for odd waveforms (as $m = 1$ in Fig. Fig. 2.7 (b)) is distributed only over two harmonics (marked as "1" and "2", ignoring DC component), while other harmonics have smaller amplitudes (marked as "4" and "6"), and can be neglected. For spectra of even waveforms (as $m = 2$ in Fig. 2.7 (d)), it can be observed that the energy is distributed over multiple non-negligible harmonics. Consequently, we have to consider two harmonics for odd waveforms and multiple harmonics for even waveforms (ignoring DC component), irrespective of M.

2.3.2 M-ary U-FSK Transmitter

Fig. 2.8 illustrates the transmitter configuration for M-ary U-FSK, where the M-ary FSK waveform, $\tilde{s}_m[n]$, corresponding to the frequency index m is extrapolated from the LUT. To generate M-ary U-FSK waveforms, the polarity separator splits the M-ary FSK waveform, $\tilde{s}_m[n]$, into positive and negative

amplitude excursions, $\tilde{s}_m^{+}[n]$ and $\tilde{s}_m^{-}[n]$, respectively, as:

$$\tilde{s}_m^{+}[n] = \tilde{s}_m[n], \quad \text{if} \quad \tilde{s}_m[n] \geq 0, \tag{2.28}$$

and

$$\tilde{s}_m^{-}[n] = \tilde{s}_m[n], \quad \text{if} \quad \tilde{s}_m[n] < 0. \tag{2.29}$$

(2.28) and (2.29) can also be computed by:

$$\tilde{s}_m^{+}[n] = \frac{1}{2}\left(\tilde{s}_m[n] + |\tilde{s}_m[n]|\right), \tag{2.30}$$

and

$$\tilde{s}_m^{-}[n] = \frac{1}{2}\left(\tilde{s}_m[n] - |\tilde{s}_m[n]|\right). \tag{2.31}$$

Subsequently, the positive part, $\tilde{s}_m^{+}[n]$, of each conventional bipolar M-ary FSK is transmitted in the first symbol period, while the negative part, $\tilde{s}_m^{-}[n]$, is flipped and transmitted in a consecutive symbol period. This leads to the generation of M-ary U-FSK dictionary, $\mathscr{D}^{\mathrm{U}}$, as:

$$s_m^{\mathrm{U}}[\overline{n}] = \begin{cases} \tilde{s}_m^{+}[\overline{n}] & 0 \leq \overline{n} \leq M-1 \\ -\tilde{s}_m^{-}[\overline{n}-M] & M \leq \overline{n} \leq 2M-1 \end{cases}. \tag{2.32}$$

where $\overline{n}$ represents $2M$ number of chips of M-ary U-FSK waveforms. Considering $t = (\overline{n}+\frac{1}{2})T_{\mathrm{c}}$, the analog domain counterparts, $s_m^{\mathrm{U}}(t)$, are obtained by impinging $s_m^{\mathrm{U}}[\overline{n}]$ on a digital-to-analog converter (DAC). Finally, the TD mth M-ary U-FSK waveforms, $s_m^{\mathrm{U}}(t)$, are obtained as:

$$s_m^{\mathrm{U}}(t) = \begin{cases} \frac{1}{2}\left(\tilde{s}_m(t) + |\tilde{s}_m(t)|\right) & [0, \tilde{T}_{\mathrm{s}}] \\ \frac{1}{2}\left(\tilde{s}_m(t-\tilde{T}_{\mathrm{s}}) - |\tilde{s}_m(t-\tilde{T}_{\mathrm{s}})|\right) & [\tilde{T}_{\mathrm{s}}, 2\tilde{T}_{\mathrm{s}}] \end{cases}, \tag{2.33}$$

which are now compatible with IM-DD systems because of the unipolar nature.

2.3.3 Average M-ary U-FSK Symbol Energy

All the M-ary U-FSK waveforms in the dictionary, $\mathscr{D}^{\mathrm{U}}$, have equal symbol energy, $E_{\mathrm{s(elec)}}^{\mathrm{U}}$, defined as:

$$\begin{aligned} E_{\mathrm{S_{(elec)}}}^{\mathrm{U}} &= \int_0^{T_{\mathrm{s}}} |s_m^{\mathrm{U}}(t)|^2 \mathrm{d}t, \\ &= T_s\left(\frac{A^2}{4}\right) = \tilde{T}_s\left(\frac{A^2}{2}\right). \end{aligned} \tag{2.34}$$

From (2.7) and (2.34), it can be noticed that the symbol energies for M-ary U-FSK and the conventional bipolar M-ary FSK are equal, i.e., $E_{\mathrm{s(elec)}}^{\mathrm{U}} = E_{\mathrm{s(elec)}}^{\mathrm{FSK}}$.

2.3.4 Minimum squared Euclidean distance between M-ary U-FSK waveforms

The minimum squared Euclidean distance between M-ary U-FSK waveform pairs, $(s_i^{\mathrm{U}}(t); s_j^{\mathrm{U}}(t))$, can be computed using (2.9) as:

$$\begin{aligned} d^2_{\min,\mathrm{U}} &= \min_{i\neq j} \|s_i^{\mathrm{U}}(t) - s_j^{\mathrm{U}}(t)\|^2 \\ &= \min_{i\neq j} \left\{ 2E^{\mathrm{U}}_{\mathrm{s(elec)}} - 2\Re\langle s_i^{\mathrm{U}}(t), s_j^{\mathrm{U}}(t)\rangle \right\} \end{aligned} \tag{2.35}$$

Notice that the M-ary U-FSK transformation from the conventional bipolar M-ary FSK affects the orthogonality between the waveform pairs, $(s_i^{\mathrm{U}}(t); s_j^{\mathrm{U}}(t))$, and the inner product between any pair of waveforms, $(s_i^{\mathrm{U}}(t); s_j^{\mathrm{U}}(t))$, in the dictionary, $\mathscr{D}^{\mathrm{U}}$, are not identical. Therefore, it is suitable to find the upper bound on the inner product, $\langle s_i^{\mathrm{U}}(t), s_j^{\mathrm{U}}(t)\rangle$, which defines the lower bound on the minimum squared Euclidean distance in (2.35). From mathematical analysis, it can be seen that the maximum value of $\langle s_i^{\mathrm{U}}(t), s_j^{\mathrm{U}}(t)\rangle_{\max}$ is achieved for $s_0^{\mathrm{U}}(t)$ and $s_j^{\mathrm{U}}(t)$, for $1 \leq j \leq M-1$ resulting in [30]:

$$\langle s_0^{\mathrm{U}}(t), s_{j\neq 0}^{\mathrm{U}}(t)\rangle_{\max} = \frac{A}{\sqrt{2}} \int_0^{\tilde{T}_{\mathrm{s}}} s_{j\neq 0}^{\mathrm{U}}(t)\mathrm{d}t = \frac{\sqrt{2}A^2\tilde{T}_{\mathrm{s}}}{2\pi}. \tag{2.36}$$

The lower bound on the minimum squared Euclidean distance for M-ary U-FSK can be computed using (2.36) in (2.35) as:

$$d^2_{\min,\mathrm{U,lb}} = A^2\tilde{T}_{\mathrm{s}} - \frac{\sqrt{2}A^2\tilde{T}_{\mathrm{s}}}{\pi} = 2E^{\mathrm{FSK}}_{\mathrm{s}_{(\mathrm{elec})}} \times \gamma^{\mathrm{U}}, \tag{2.37}$$

where $\gamma^{\mathrm{U}} = \left(1 - \sqrt{2}/\pi\right) \approx 0.55$. Simulations indicate that the squared Euclidean distance between any waveform pair, $(s_i^{\mathrm{U}}(t); s_j^{\mathrm{U}}(t)) \in \mathscr{D}^{\mathrm{U}}$, does not deviate more than 4.65% from the lower bound, $d^2_{\min,\mathrm{U,lb}}$ [30]. It is important to note that $\gamma^{\mathrm{U}} > \gamma^{\mathrm{DC}}$ (as $\gamma^{\mathrm{DC}} = 1/3$ (cf. Sec. 2.2.4)), therefore, we are expecting better BER performance (i.e., better energy efficiency) for M-ary U-FSK as compared to M-ary DC-FSK.

2.3.5 Spectral Efficiency of M-ary U-FSK

The signal bandwidth for M-ary U-FSK is approximately, $B \approx M\Delta f = M/2\tilde{T}_{\mathrm{s}}$, while considering sufficiently large M. Note that this bandwidth is evaluated by neglecting the out-of-band energy on the harmonics of the clipped waveform [30]. Moreover the data rate, R_{b}, for M-ary U-FSK is $\log_2(|\mathscr{D}|^{\mathrm{U}})/2\tilde{T}_{\mathrm{s}} = \log_2(M)/2\tilde{T}_{\mathrm{s}}$. Therefore, from (2.12), the spectral efficiency for M-ary U-FSK, η^{U}, can be computed as:

$$\begin{aligned} \eta^{\mathrm{U}} &= \frac{R_{\mathrm{b}}}{B} = \frac{\log_2(M)/2\tilde{T}_{\mathrm{s}}}{M/2\tilde{T}_{\mathrm{s}}}, \\ &= \frac{\log_2(M)}{M}. \end{aligned} \tag{2.38}$$

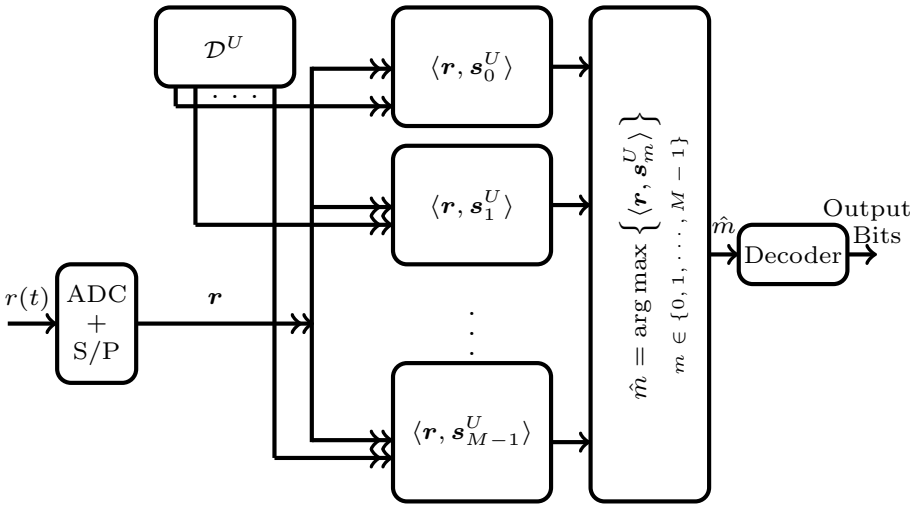

Fig. 2.9 Theoretical time-domain maximum likelihood (ML) receiver architecture for M-ary U-FSK [30].

From (2.21) and (2.38), it can be seen that the spectral efficiency of M-ary U-FSK is half of the spectral efficiency of M-ary DC-FSK, i.e., $\eta^{\mathrm{U}} = \eta^{\mathrm{DC}}/2$. This is because of the symbol time, T_{s}, which is doubled for M-ary U-FSK waveforms. Furthermore, the spectral efficiency, η^{U}, can be increased by a factor of $\frac{1}{M}$ by introducing biorthogonal extension in the orthogonal dictionary, $\mathscr{D}^{\mathrm{U}}$ [30].

2.3.6 M-ary U-FSK Receivers

There are two different types of receivers presented in [30] for M-ary U-FSK, i.e., optimal time-domain (TD) maximum likelihood (ML) receiver and sub-optimal 1-tap DCT-based receiver.

Maximum Likelihood (ML) Receiver

Fig. 2.9 illustrates the theoretical maximum likelihood (ML) receiver, and it is presented in [81] [52]. There is a slight difference in the architecture of ML receiver for M-ary U-FSK as compared to M-ary DC-FSK, i.e., the absence of DC-offset removal and the dictionary, $\mathscr{D}^{\mathrm{U}}$, instead of $\mathscr{D}^{\mathrm{DC}}$. Considering the same symbol energy for all waveforms, $E^{\mathrm{U}}_{\mathrm{s(elec)}}$, and equiprobable symbol transmissions, i.e., $p(\boldsymbol{s}_m^{\mathrm{U}}) = 1/M$, the ML criterion permits to guarantee a minimum error probability. Under such circumstances, the optimal TD ML receiver commits on evaluating the time-domain cross-correlations of the received waveform, $\boldsymbol{r}$, with all the waveforms, $\boldsymbol{s}_m^{\mathrm{U}}$, in the dictionary, $\mathscr{D}^{\mathrm{U}}$. The estimated frequency index $\hat{m}$ is identified as a result of TD cross-correlation as [30]:

$$\hat{m} = \arg\max_{m} \left\{ \langle \boldsymbol{r}, \boldsymbol{s}_m^{\mathrm{U}} \rangle \right\}, \quad m \in \{0, 1, \cdots, M-1\}. \tag{2.39}$$

It is highlighted in [81] that the TD cross-correlation in (2.39) is strictly equal to the FD cross-correlation, but the receiver complexity increases in FD cross-correlation due to the additional step of the M_{c}-order DCT operation.

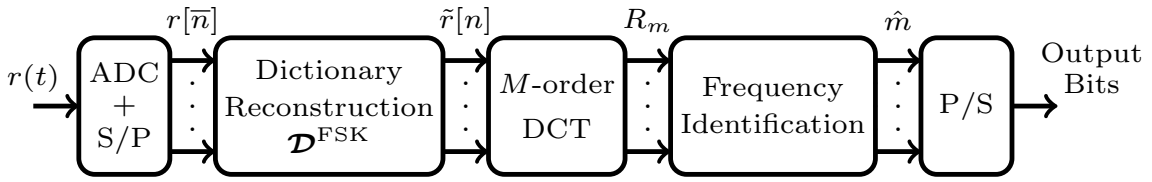

Fig. 2.10 Sub-optimal 1-tap DCT-based receiver for M-ary U-FSK [30].

Sub-optimal 1-tap DCT-based Receiver

The sub-optimal 1-tap DCT-based receiver for M-ary U-FSK can also be known as reconstruction-based receiver, because its process involves the reconstruction of the conventional bipolar M-ary FSK waveforms from the M-ary U-FSK waveforms. Fig. 2.10 illustrates the 1-tap DCT-based receiver architecture for M-ary U-FSK. The waveforms of the orthogonal M-ary FSK dictionary, $\tilde{\boldsymbol{s}}_m \in \mathscr{D}^{\mathrm{FSK}}$, are reconstructed from $\boldsymbol{r}$ as follows:

$$\tilde{r}[n] = r[n] - r[M+n] \qquad \text{for } n = 0, 1, \cdots, M-1, \tag{2.40}$$

Afterward, the M-order DCT is applied on $\tilde{\boldsymbol{r}}$ to attain the frequency-domain received waveform, $\boldsymbol{R}$, as:

$$\boldsymbol{R} = \boldsymbol{C}_{\mathrm{M}}\tilde{\boldsymbol{r}}, \tag{2.41}$$

where $\boldsymbol{R} = [R[0], R[1], \cdots, R[M-1]]^{\mathrm{T}}$. Finally, the transmit waveform is identified using the frequency identification as in (2.26):

$$\hat{m} = \arg\max_{m} \Big\{ |R_m| \Big\}, \quad m \in \{0, 1, \cdots, M-1\}. \tag{2.42}$$

One can think that 1-tap DCT-based receiver may have comparable BER performance as compared to the theoretical ML receiver for M-ary U-FSK because of the use of orthogonal waveforms (after reconstruction) for frequency index m identification. This assumption is incorrect because the positive and the flipped negative parts of the waveforms in the sequential transmission increases the symbol duration to double, i.e., $T_{\mathrm{s}} = 2\tilde{T}_{\mathrm{s}}$. Hence, the symbol reconstruction in (2.40) increases the noise variance by a factor two for the same symbol energy. As a result, the reconstruction-based receiver for M-ary U-FSK is expected to be a sub-optimal receiver [30].

2.3.7 Simulation Results of the Existing FSK-based Modulations

The simulation results for the existing M-ary FSK-based modulations (i.e., M-ary DC-FSK and M-ary U-FSK) are presented in [30]. Here, we quickly review few simulation results to show the performance comparison between M-ary DC-FSK and M-ary U-FSK, that will be used as the state-of-the-art for the subsequent chapters. The following performance parameters are presented here;

- BER performance over AWGN channel for M-ary U-FSK receivers.

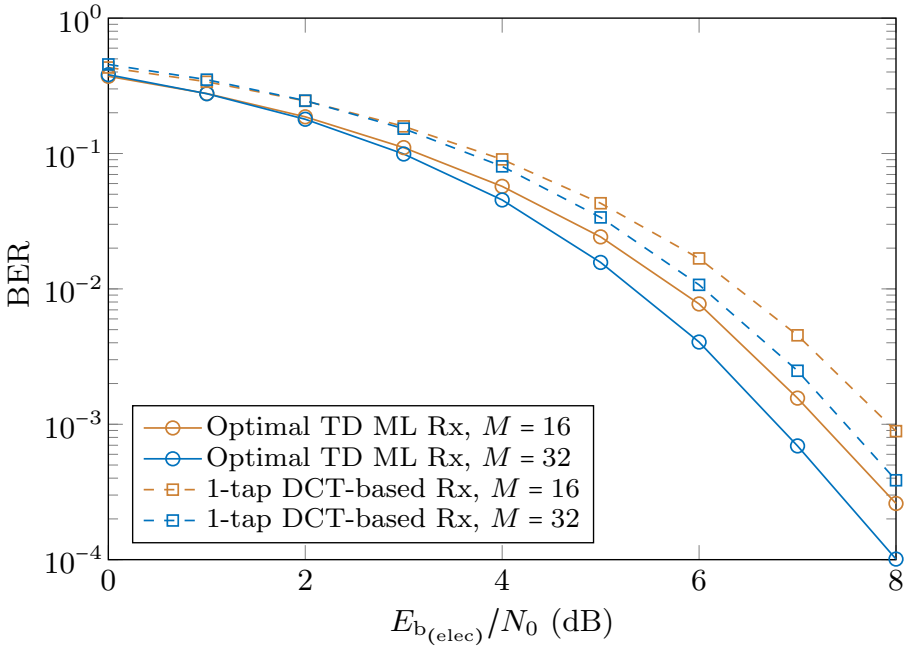

Fig. 2.11 Simulated BER performance comparison for the optimal TD ML receiver vs sub-optimal 1-tap DCT-based receiver of M-ary U-FSK, considering $M = 16$ and 32 [30].

- BER performance comparison for M-ary DC-FSK and M-ary U-FSK using optimal TD ML receiver.
- Energy efficiency vs spectral efficiency comparison for M-ary DC-FSK and M-ary U-FSK.

Note that Monte Carlo simulations have been performed using Matlab over 10^6 runs [52].

BER Performance over AWGN Channel for M-ary U-FSK Receivers

Fig. 2.11 illustrates the BER performance comparison of the optimal TD ML receiver and the sub-optimal 1-tap DCT-based receiver for M-ary U-FSK, considering $M = 16$ and 32. It can be seen that BER performance for the optimal TD ML receiver is better than 1-tap DCT-based receiver for M-ary U-FSK by less than 1 dB for both $M = 16$ and 32. Therefore, the optimal TD ML receiver is used in the subsequent sections for BER comparisons of M-ary DC-FSK and M-ary U-FSK. Furthermore, it can also be seen from Fig. 2.11 that BER vs required $E_{b(elec)}/N_0$ performance improves by increasing M.

BER Performance comparison for M-ary DC-FSK and M-ary U-FSK using optimal TD ML receiver

Fig. 2.12 (a) and (b) illustrate the BER versus required E_b/N_0 comparisons for M-ary DC-FSK and M-ary U-FSK in electrical and optical-domain respectively, considering $M = 16$, i.e., BER vs required

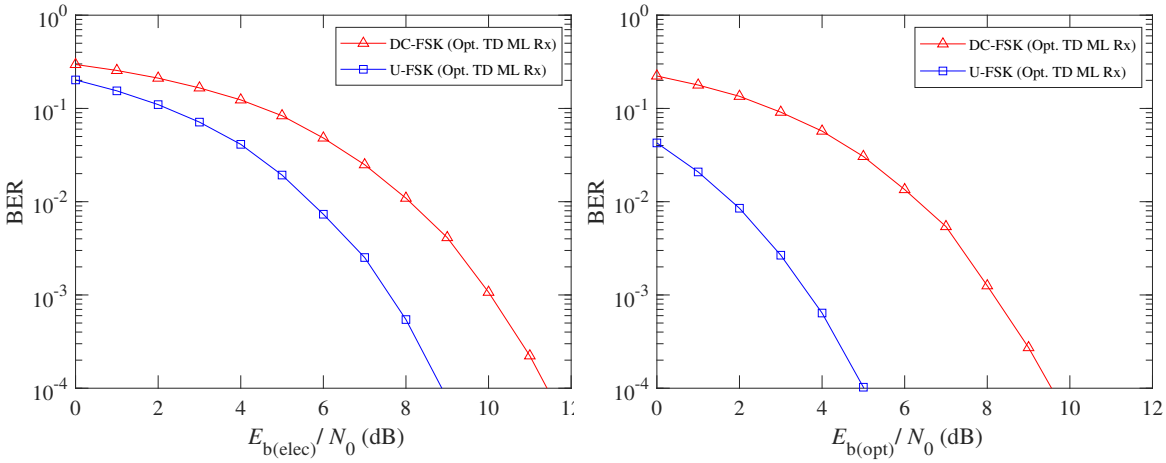

(a) (b)

Fig. 2.12 Simulated BER vs required E_b/N_0 comparison for M-ary DC-FSK and M-ary U-FSK, considering an optimal TD ML receiver and modulation size $M = 16$ in (a) electrical-domain, and (b) optical-domain.

$E_{b(elec)}/N_0$ and BER vs required $E_{b(opt)}/N_0$. Note that an optimal TD ML receiver is considered for Fig. 2.12 , while $P_{opt} = 1W$, is used for Fig. 2.12 (b). It can be seen that M-ary U-FSK shows around 2 dB better BER performance as compared to the M-ary DC-FSK in electrical domain, while around 5 dB better BER performance can be seen for M-ary U-FSK relative to the M-ary DC-FSK in optical domain due to the larger electrical to optical conversion factor for M-ary DC-FSK [30]. This is due to the fact that the M-ary DC-FSK waveforms are negatively affected because of the addition of the DC-offset, which increases the energy requirements [30]. The difference in the energy requirements for M-ary DC-FSK and M-ary U-FSK is compliant with the analytic analysis presented in the previous sections. From (2.20) and (2.37), the required electrical energy for M-ary DC-FSK is expected to be $10\log_{10}(\gamma^U/\gamma^{DC}) \approx 2.2$ dB higher than the required electrical energy for M-ary U-FSK, which is compliant with the simulation results in Fig. 2.12 (a) [30].

Energy Efficiency vs Spectral Efficiency comparison for M-ary DC-FSK and M-ary U-FSK

Fig. 2.13 (a) and (b) illustrate the spectral efficiency η vs required E_b/N_0 performance comparison at a targeted BER = 10^{-3} for M-ary DC-FSK and M-ary U-FSK in electrical and optical-domain respectively, using an optimal TD ML receiver in AWGN channel and considering different dictionary sizes. It is shown that M-ary U-FSK exhibits better BER performance as compared to the M-ary DC-FSK in terms of required $E_{b(elec)}/N_0$ and $E_{b(opt)}/N_0$ over a range of dictionary sizes. This is due to the larger γ^U compared to the γ^{DC}, leading to a better performance for M-ary U-FSK as compared to the M-ary DC-FSK. For larger M, we can achieve 2 dB gain using M-ary U-FSK as compared to the M-ary DC-FSK. At the same time, the spectral efficiency, η, decreases by increasing M as in (2.38), but it can be compatible with the targeted low data rate IoT applications [30]. The performance of M-ary PAM and OOK (special case of M-ary PAM with $M = 2$) are also presented in Fig. 2.13

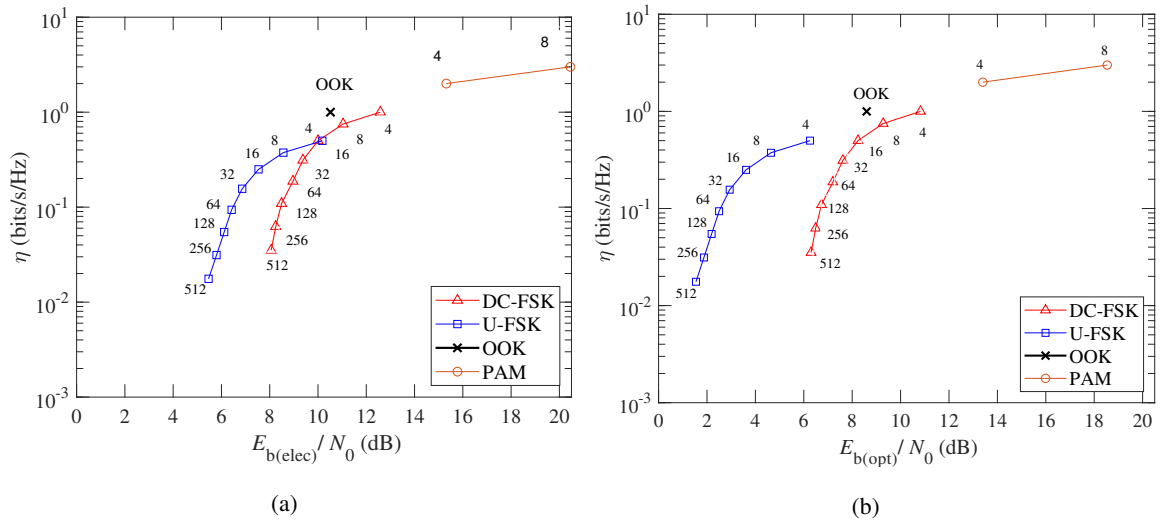

Fig. 2.13 Spectral efficiency η vs required E_b/N_o comparison to target a BER of 10^{-3} for M-ary U-FSK, M-ary DC-FSK, OOK and M-ary PAM using optimal TD ML receiver in (a) electrical-domain (η vs required $E_{b(elec)}/N_0$) , and (b) optical-domain (η vs required $E_{b(opt)}/N_0$).

(a) and (b). From Fig. 2.13 (a) and (b), it can be seen that the performances of M-ary PAM and OOK are worse than both M-ary DC-FSK and M-ary U-FSK. Furthermore, the required $E_{b(elec)}/N_0$ and $E_{b(opt)}/N_0$ for M-ary PAM increases by increasing M, which shows the decrease in the energy efficiency by increasing M.

From simulation results in Sec. 2.3.7, it is confirmed that M-ary U-FSK exhibits better energy efficiency for a given spectral efficiency as compared to the M-ary DC-FSK, therefore, M-ary U-FSK will be used as a reference rather than M-ary DC-FSK in the sequel.

2.4 Proposed Low Complexity Frequency-Domain L-tap harmonic Receiver for M-ary U-FSK

As aforementioned in Sec. 2.3.7 that optimal TD ML receiver shows better BER performance as compared to the 1-tap DCT-based receiver for M-ary U-FSK, but at the same time the computational complexity of the optimal TD ML receiver is larger as compared to the complexity of the 1-tap DCT-based receiver and the complexity of the optimal TD ML receiver increases quadratically with increasing M. Therefore, there exist a trade-off between the complexity and the BER performance for the optimal TD ML receiver and 1-tap DCT-based receiver. It motivates us to adapt a new receiver that shows a similar or comparable BER performance to the optimal TD ML receiver with the benefit of low computational complexity.

The underlying idea of the harmonic receiver is to perform waveforms correlation in the frequency-domain, while considering only the largest energy waveform coefficients (taking advantage of the strong frequency-domain sparsity of the waveform coefficients). It could be noted that chronologically,

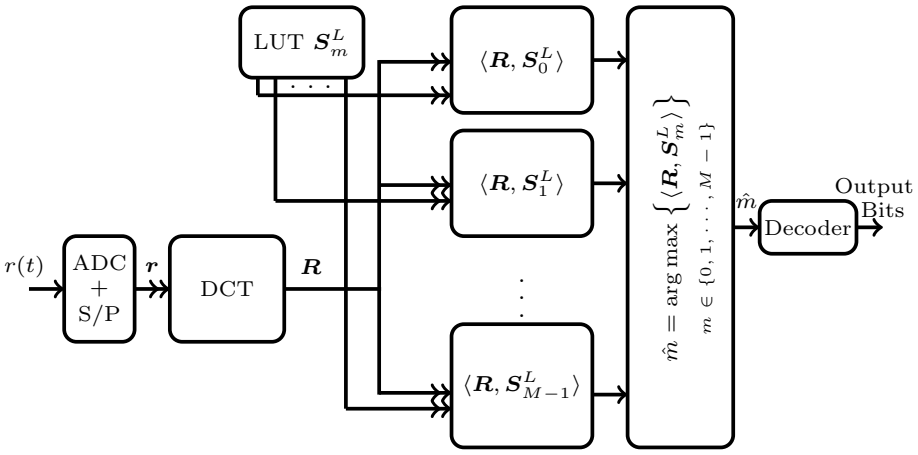

Fig. 2.14 L-tap Harmonic receiver architecture for M-ary U-FSK.

we introduce this idea firstly to simplify the optimal receiver of the new proposed modulation scheme described in the next chapter (namely M-ary AC-FSK), and we secondly decide to apply the same idea for the existing M-ary U-FSK modulation, described in this section. This section/sub-sections correspond to our published contribution [81].

By analyzing the M-ary U-FSK waveforms in FD (cf. Fig. 2.7(b) and (d)) that is obtained through the M_c-order DCT of the $s_m^U(t)$, it is observed that most of the symbol energy (more than 90% of the symbol energy) for M-ary U-FSK odd waveforms (as $m = 1$ in Fig. 2.7(b)) are distributed only over two harmonics (marked as "1" and "2", ignoring DC component), while other harmonics have smaller amplitudes (marked as "4" and "6"), and can be neglected. For spectra of even waveforms (as $m = 2$ in Fig. 2.7(d)), it can be observed that the symbol energy is distributed over multiple non-negligible harmonics (or taps). As a consequence, we have to consider two harmonics for M-ary odd waveforms and multiple harmonics for even waveforms (ignoring DC component) [81]. Note that these consideration is valid for all M.

2.4.1 L-tap Harmonic Receiver for M-ary U-FSK

The main objective of the L-tap harmonic receiver is to simplify the detection process in (2.39) and (2.42), and to attain the BER performance that does not deviate more than 5% of that of optimal TD ML receiver with the benefit of reducing the computational complexity of the receiver by using a minimum number of harmonics [81]. Considering an AWGN channel, the waveforms, $\boldsymbol{s}_m^U$ for $m \in \{1,2\}$ when $M = 16$ ($M_c = 32$) and their frequency-domain counterparts, $\boldsymbol{S}_m$ are depicted in Fig. 2.7. Considering various simulation setups and analyzing the signal structure in frequency-domain (cf. Fig. 2.7 (b) and (d)), we observe that at-least two and twelve harmonics (excluding DC harmonic) are required for odd and even frequency waveforms, respectively to achieve the above mentioned objectives. It should be noticed that this difference in the number of required harmonics in the odd and even frequency waveforms is due to the structure of waveforms. It is observed that the required number harmonics

for odd and even frequency waveforms contain around 90% and 97.8% of the $E^{\mathrm{U}}_{\mathrm{s(elec)}}$ respectively, irrespective of M. For clear understanding, L_{o} and L_{e} are used to denote the number of selected harmonics for odd and even waveforms, respectively.

It is highlighted in [81] that the DCT operation maintains the geometry as any isometric transform (i.e., angles, distance, norms, etc) are preserved. Therefore, the TD cross-correlation in (2.39) is equivalent to the FD cross-correlation. So we can modify (2.39) using FD cross-correlation for frequency index identification as:

$$\hat{m} = \arg\max_{m} \left\{ \langle \boldsymbol{R}, \boldsymbol{S}^{\mathrm{U}}_{m} \rangle \right\}, \quad m \in \{0, 1, \cdots, M-1\}. \tag{2.43}$$

The computation complexity of the FD ML receiver increases due to the M_{c}-order DCT operation together with the required M FD cross-correlations (2.43). It should be noticed that we did not present the FD ML receiver in [81], because of its higher complexity. It is only presented here for the sake of clarification, because it becomes the basis for the proposed L-tap harmonic receiver.

Fig. 2.14 illustrates the necessary operations for L-tap harmonic receiver for M-ary U-FSK. In the first offline step, the frequency-domain waveforms, $\boldsymbol{S}_m$, are obtained by applying M_{c}-order DCT on $s^{\mathrm{U}}_m(t) \in \mathscr{D}^{\mathrm{U}}$. Afterward, L_{o} and L_{e} harmonics are selected for odd and even waveforms, respectively, which are then interpolated in the LUT. Note that the size of the LUT for the L-tap harmonic receiver (defined in-terms of number of non-zero coefficients and their indices to store in memory) is significantly small relatively to the LUT for optimal TD ML receiver, which needs a larger LUT. In the second step, $\boldsymbol{R}$ is obtained by applying M_{c}-order DCT on $\boldsymbol{r}$ as in (2.41). Finally, the transmitted frequency index can be identified by applying the FD cross-correlation between $\boldsymbol{R}$ and $\boldsymbol{S}^{L}_{m}$ as:

$$\hat{m} = \arg\max_{m} \left\{ \langle \boldsymbol{R}, \boldsymbol{S}^{L}_{m} \rangle \right\}, \quad m \in \{0, 1, \cdots, M-1\}. \tag{2.44}$$

Note that the same technique of L-tap harmonic receiver will be adopted for other modulation scheme, such as M-ary AC-FSK (explanation in Chapter 3), while the number of selected harmonics depend upon the spectral structure of the modulation waveforms.

2.4.2 Theoretical BER Probability for M-ary U-FSK

The theoretical BER expression for bipolar conventional M-ary FSK in AWGN channel using ML detection is presented in [57], which depends upon the minimum squared Euclidean distance between waveforms. Similarly, the theoretical BER probability expression for M-ary U-FSK can be derived and can be used as a benchmark in simulations. Recall from Sec. 2.3.4, an approximate minimum squared Euclidean distance, $d^2_{\mathrm{min,U}}$, is presented for M-ary U-FSK, from which, the squared Eulidean distance for all waveform pairs, $((s^{\mathrm{U}}_i(t); s^{\mathrm{U}}_j(t)) \in \mathscr{D}^{\mathrm{U}})$, does not deviate more than 4.65%. By replacing the minimum squared Euclidean distance of the bipolar M-ary FSK with the one evaluated for M-ary U-FSK in the theoretical BER probability expression from [57], a good approximation for the theoretical symbol-error probability, P_{e}, for M-ary U-FSK in an AWGN channel can be achieved as

[81]:

$$P_{\mathrm{e}}^{\mathrm{U}} \approx \frac{1}{\sqrt{2\pi}} \int_{-\infty}^{+\infty} \left[1-(1-Q(x))^{M-1}\right] \times \exp\left(-\frac{1}{2}\left(x-\sqrt{\frac{d_{\min,\mathrm{U}}^2}{N_0}}\right)^2\right) \mathrm{d}x, \tag{2.45}$$

where $Q(\cdot)$ is the Guassian Q-function [57], N_0 is the mono-lateral noise spectral density and $d_{\min,\mathrm{U}}^2$ is presented in Sec. 2.3.4. Finally, from (2.45), the BER probability, P_{b}, in an AWGN channel for M-ary U-FSK can be expressed as [81]:

$$P_{\mathrm{b}} \approx \frac{M}{2(M-1)} P_{\mathrm{e}}. \tag{2.46}$$

2.4.3 Simulation Results of L-tap Harmonic Receiver for M-ary U-FSK

We presented the performance comparison of the proposed L-tap harmonic receiver for M-ary U-FSK with the conventional optimal TD ML receiver and 1-tap DCT-based receiver in terms of the following;

- Complexity analysis for M-ary U-FSK receivers.
- BER vs required $E_{\mathrm{b(elec)}}/N_0$ performance comparison in AWGN channel.
- Spectral efficiency, η, as a function of the required $E_{\mathrm{b(elec)}}/N_0$ performance comparison for L-tap harmonic receiver with the optimal TD ML receiver and 1-tap DCT-based receiver.

For clarity purpose, we use the $(L_{\mathrm{e}}, L_{\mathrm{o}})$-tap nomenclature instead of using L-tap for harmonic receiver to show the number of harmonics selected for even and odd M-ary U-FSK waveforms.

Complexity Analysis for M-ary U-FSK Receivers

It is aforementioned in Sec. 2.2.7 that the primary contributor to the computational complexity of the receiver is the number of non-zero real multiplications. Therefore, the optimal TD ML receiver for M-ary U-FSK requires $\mathscr{C}_{\mathrm{TD,ML}} = MM_{\mathrm{c}} = 2M^2$, non-zero real multiplications, which is increasing quadratically with increasing M. For the optimal FD ML receiver, in addition to the $\mathscr{C}_{\mathrm{TD,ML}}$ multiplications, M_{c}-order DCT is needed to transform TD M-ary U-FSK waveform into the FD waveform. Therefore, the optimal FD ML receiver for M-ary U-FSK requires $\mathscr{C}_{\mathrm{FD,ML}} = M\log_2(2M) + 2M^2$, non-zero real multiplications, which is higher than that of the TD counterpart [81].

For the sub-optimal 1-tap DCT-based receiver, only M-order DCT is needed after reconstruction of waveforms as in (2.40), which requires $\mathscr{C}_{1-\mathrm{tap}} = (M/2)\log_2(M)$, non-zero real multiplications due to the M-order DCT [87], which is much less than the complexity of optimal TD/FD ML receiver. Furthermore, the $(L_{\mathrm{e}}, L_{\mathrm{o}})$-tap harmonic receiver is based on M_{c}-order DCT, followed by $M/2$ FD cross-correlations for the odd frequency waveforms and $M/2$ FD cross-correlations for even frequency waveforms. Therefore, $(M/2)L_{\mathrm{o}} + (M/2)L_{\mathrm{e}}$ multiplications are also needed for FD

Table 2.1 Complexity computations and complexity reduction, β, for (L_e, L_o)-tap harmonic receiver relative to the optimal TD ML receiver for M-ary U-FSK, considering different M.

M	$\mathscr{C}_{\text{TD,ML}}$	$\mathscr{C}_{\text{harm}}$	β (%)
16	512	192	62.5
32	2048	416	79.6
64	8192	896	89.0
128	32768	1920	94.1
256	131072	4096	96.8
512	524288	8704	98.3
1024	2097152	18432	99.1

cross-correlation in addition to the $M\log_2(2M)$ multiplications due to the M_c-order DCT. Hence, $\mathscr{C}_{\text{harm}} = M\log_2(2M) + (M/2)L_o + (M/2)L_e$, non-zero real multiplications are needed for (L_e, L_o)-tap harmonic receiver [81], which is slightly higher than 1-tap DCT-based receiver complexity, but it is much less than the complexity of the optimal TD/FD ML receiver.

For clarity purpose, we introduce a new parameter, β that quantifies the complexity reduction in percentage of the (L_e, L_o)-tap harmonic receiver relative to the optimal TD ML receiver for M-ary U-FSK, considering different dictionary sizes M. The complexity reduction, β, can be defined as [81]:

$$\beta = \left(1 - \frac{\mathscr{C}_{\text{harm}}}{\mathscr{C}_{\text{TD,ML}}}\right) \times 100\%, \tag{2.47}$$

Table 2.1 shows the complexity computations with different modulation sizes M of (L_e, L_o)-tap harmonic receiver and optimal TD ML receiver for M-ary U-FSK, i.e., $\mathscr{C}_{\text{harm}}$ and $\mathscr{C}_{\text{TD,ML}}$, respectively. The complexity reduction, β, is also reported in Table 2.1. It can be seen that the complexity of the (L_e, L_o)-tap harmonic receiver relative to the TD ML receiver reduces by 62.5% and 99.1% for M = 16 and 1024, respectively.

BER Performance Analysis for L-tap Harmonic Receiver

In this sub-section, we present the BER performance comparison of the L-tap harmonic receiver with the conventional optimal TD ML receiver and 1-tap DCT-based receiver for M-ary U-FSK in AWGN channel. Furthermore, it is evident that the BER performance of the optimal ML receiver in FD and TD is strictly equal, we do not provide the simulation results of the optimal ML receiver in FD due to the higher complexity (cf. Sec. 2.3.6).

Fig. 2.15 illustrates the BER vs required $E_{\text{b(elec)}}/N_0$ performance comparison for (L_e, L_o)-tap harmonic receiver with the conventional optimal TD ML receiver and sub-optimal 1-tap DCT-based receiver for M-ary U-FSK, considering an AWGN channel and $M = 16$. Theoretical approximation

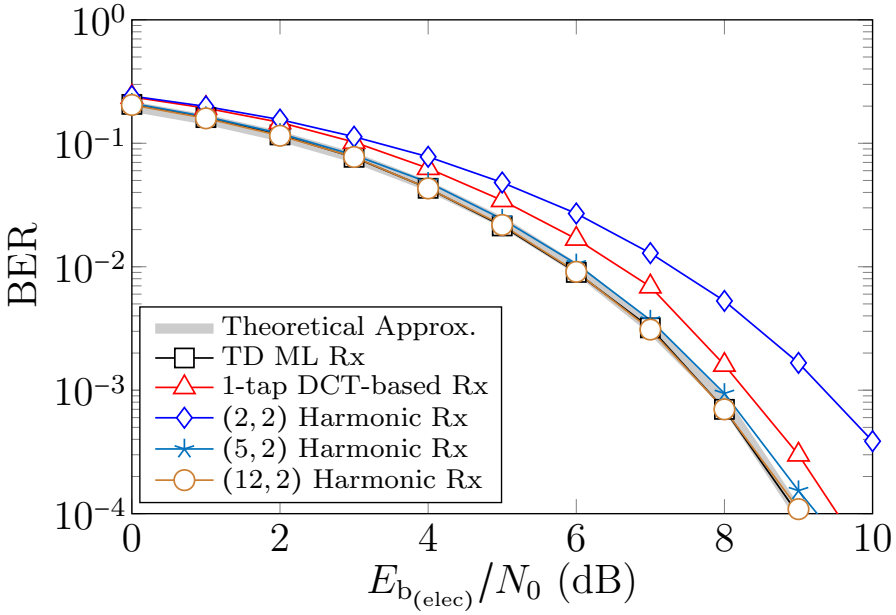

Fig. 2.15 BER performance against required $E_{b(elec)}/N_0$ in AWGN channel of the optimal TD ML receiver, sub-optimal 1-tap DCT-based receiver and proposed L-tap Harmonic receiver, considering $M = 16$ [81].

obtained for ML detection in (2.45) and (2.46) is also presented in the Fig. 2.15. We consider $L_o = 2$ and $L_e = \{2, 5, 12\}$ harmonics for the odd and even frequency waveforms, respectively. We consider different number of harmonics for L_e in order to show the performance improvement with increasing L_e and to find the optimum number of harmonics for L_e, that corresponds to the BER performance equal or comparable to the optimal TD ML receiver. The theoretical approximation curve, optimal TD ML receiver and sub-optimal 1-tap DCT-based receiver are used as the benchmark for the BER performance comparisons.

From Fig. 2.15 it can be seen that the BER performance of the optimal TD ML receiver is in conformity with the theoretical approximation in (2.46). Furthermore, the BER performance of the (L_e, L_o)-tap harmonic receiver improves by increasing L_e and its performance reaches the optimal TD ML receiver for $L_e = 12$, i.e., the deviation is not more than 5% from the optimal TD ML receiver performance. Finally, the $(12, 2)$-tap harmonic receiver achieve the similar BER performance as the optimal TD ML receiver with the benefit of the complexity reduction, $\beta = 62.5\%$, for $M = 16$ (cf. Table 2.1). It can also be observed in Fig. 2.15 that $(12, 2)$-tap harmonic receiver shows approximately 0.6 dB better BER performance as compared to the 1-tap DCT-based receiver at BER $= 10^{-3}$, because the 1-tap DCT-based receiver doubles the noise variance [81].

Energy Efficiency vs Spectral Efficiency Performance Comparison for L-tap Harmonic Receiver

Fig. 2.16 illustrates the spectral efficiency, η, vs required $E_{b(elec)}/N_0$ performance comparison for the proposed $(12, 2)$-tap harmonic receiver with the conventional optimal TD ML receiver and 1-tap DCT-based receiver for a targeted BER of 10^{-3} in AWGN channel. Note that η is varied by changing

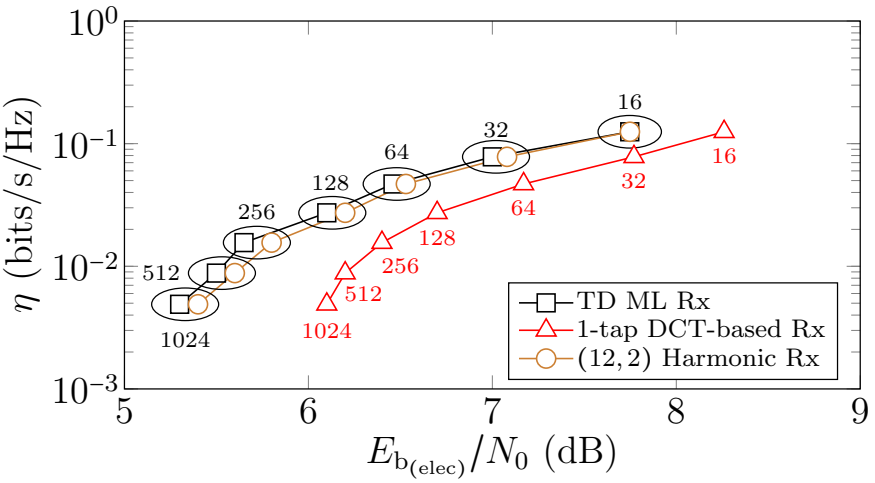

Fig. 2.16 Spectral efficiency vs required $E_{b(elec)}/N_0$ comparison of the optimal TD ML receiver, sub-optimal 1-tap DCT-based receiver and proposed L-tap Harmonic receiver for M-ary U-FSK in AWGN channel [81].

M. Fig. 2.16 demonstrates that the performance of the proposed $(12,2)$-tap harmonic receiver is very close to that of optimal TD ML receiver with the benefit of the drastic reduction of the complexity as reported in Table 2.1. For the BER of 10^{-3}, the required $E_{b(elec)}/N_0$ for the proposed $(12,2)$-tap harmonic receiver does not deviate more than 5% of the optimal TD ML receiver. Furthermore, the proposed $(12,2)$-tap harmonic receiver shows far better performance as compared to the 1-tap DCT-based receiver, and the energy efficiency for $(12,2)$-tap harmonic receiver increases relatively to the 1-tap DCT-based receiver by increasing M [81].

2.5 Conclusion

In this chapter, we presented shortly the M-ary FSK-based modulation schemes (i.e., M-ary DC-FSK and M-ary U-FSK), along with the different parameters. We shortly introduced the Euclidean distance analysis and discussed about the conventional receivers, i.e., optimal TD ML receiver and sub-optimal 1-tap DCT-based receiver. The simulation results confirm that the optimal TD ML receiver shows around 2 dB better BER performance as compared to the 1-tap DCT-based receiver for FSK-based modulations, but the price to be paid is that the computational complexity of the optimal TD ML receiver is higher than the 1-tap DCT-based receiver and its complexity increasing quadratically with increasing M, which makes it less practical. Therefore, there exist a trade-off between the BER performance and the receiver complexity, i.e., the optimal TD ML receiver for M-ary U-FSK shows better performance but with the cost of high complexity.

This observation was our motivation to propose a new FD receiver called, L-tap harmonic receiver, which attains the near-optimal performance with the benefit of reduced complexity to the optimal TD ML receiver. The proposed receiver processes in FD to exploit the spectral features of M-ary U-FSK waveforms by selecting the minimum number of harmonics/taps, that corresponds to the maximum

(more than 90%) of the symbol energy. The simulation results confirm that the proposed L-tap harmonic receiver for M-ary U-FSK exhibits almost similar BER performance to the conventional optimal TD ML receiver, i.e., the deviation is not more than 5% from the optimal TD ML receiver performance, while the computational complexity is reduced upto 99.1% (considering larger M, i.e., $M = 1024$) for L-tap harmonic receiver as compared to the optimal TD ML receiver.

The proposed introduced technique of harmonic receiver will be adapted for the proposed FSK-based modulation technique (i.e., M-ary AC-FSK) in the next chapter to further reduce the global complexity of the transmission scheme.

Chapter 3

Proposed AC-FSK and AC-FPSK Modulation Schemes

Contents

This chapter is divided into two main parts. In the first part, we present our proposed energy efficient modulation scheme in Sec. 3.1 to Sec. 3.4 that is based on conventional bipolar FSK, i.e., M-ary Asymmetrically Clipped (AC)-FSK published in [52]. All the related parameters for M-ary AC-FSK are presented in Sec. 3.1, while the conventional receivers, and the proposed low-complexity FD harmonic receiver along with the complexity analysis are presented in Sec. 3.2. Sec. 3.3 derives a theoretical expression for bit error probability of M-ary AC-FSK considering an AWGN channel and optimal ML receiver, that is used as a benchmark for the performance analysis. Simulation results for M-ary AC-FSK are presented in Sec. 3.4.

In the second part of the chapter, we present an extended version of AC-FSK, i.e. AC-FPSK, which incorporates phase shift keying (PSK) to M-ary AC-FSK (cf. Sec. 3.5 to Sec. 3.8). This increases the energy efficiency as well as spectral efficiency. Sec. 3.5 is dedicated to the different parameters of the proposed AC-FPSK, while different receivers along with complexity analysis are

presented in Sec. 3.6. Bit error probability for AC-FPSK is presented in Sec. 3.7. In the last section (cf. Sec. 3.8), simulation results for AC-FPSK are presented.

3.1 Proposed M-ary AC-FSK Modulation Scheme

3.1.1 M-ary AC-FSK signaling

M-ary AC-FSK is derived from Asymmetrically Clipped Optical - Orthogonal Frequency Division Multiplexing (ACO-OFDM) that has been extensively studied in literature for high data rate visible light communication (VLC) systems [78][89][90][91]. ACO-OFDM exhibits an increased energy efficiency over DC-biased techniques for sufficiently low constellation orders. This is the reason why we try here to couple the asymmetrical clipping with our FSK-based modulation techniques for low data rate OWC. As for ACO-OFDM, the negative part of each symbol of conventional M-ary FSK symbol is clipped to zero as shown in Fig. 3.1, but it can be done without loosing information, since information is already contained in positive samples of each symbol, as it has been demonstrated for ACO-OFDM [78]. In this way the FSK symbols are made real-valued and unipolar and become compatible with OWC systems.

For AC-FSK modulation, only odd waveforms from M-ary FSK dictionary, $\mathscr{D}^{\text{FSK}}$, are selected because of two reasons;

- It exists a so-called half wave symmetry property for odd subcarriers, i.e., for each sample, $x(n)$, in the positive part of odd subcarriers, there exists the same sample amplitude in negative part of odd subcarriers such as [87];

$$x(n) = -x(N-1-n), \qquad 0 \leq n \leq N/2-1. \tag{3.1}$$

  Eq. (3.1) refers to the well known half wave symmetry of odd frequency waveforms [78]. The consequence of this half wave symmetry is that the negative samples of the waveform can be clipped to zero without any loss of information. At the output of AC-FSK transmitter, peak-to-peak waveform amplitudes are half of the original waveforms.

- Clipping of bipolar symbols induces harmonic distortion that falls only into the even subcarriers [78]. Hence, if even subcarriers are not used for data transmission, the interference between clipped symbols is limited.

Fig. 3.1 (a) and (c) illustrate the time-domain conventional bipolar $2M$-ary FSK odd waveforms for $\tilde{m} = 1$ and $\tilde{m} = 3$, respectively, while Fig. 3.1 (b) and (d) illustrate the M-ary AC-FSK waveforms for $m = 1$ and $m = 2$, respectively, that are obtained after clipping the negative parts of the conventional bipolar $2M$-ary FSK waveforms presented in Fig. 3.1 (a) and (c).

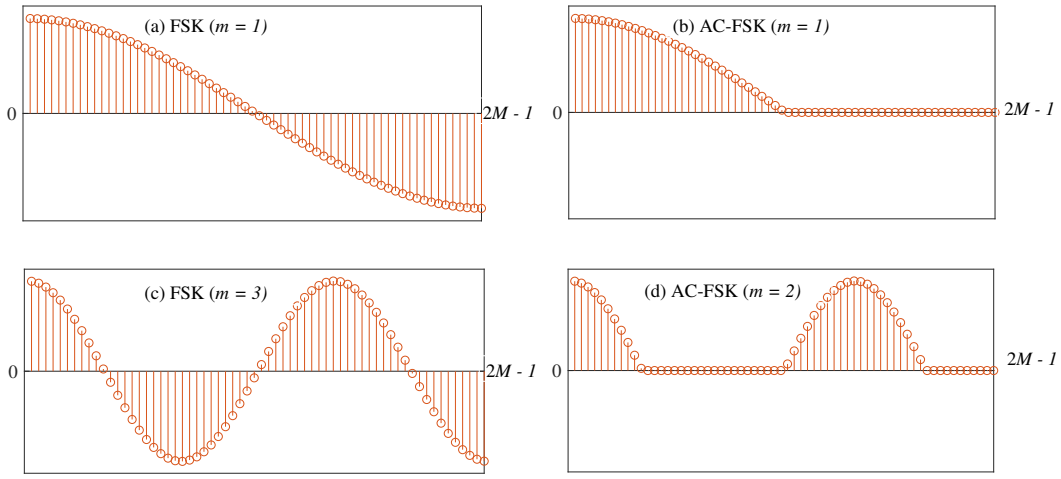

Fig. 3.1 (a) and (c) represent time-domain conventional bipolar $2M$-ary FSK odd waveforms for $\tilde{m} = 1$ and $\tilde{m} = 3$, respectively, while (b) and (d) represent the M-ary AC-FSK waveforms for $m = 1$ and $m = 2$, respectively, that are obtained from conventional bipolar $2M$-ary FSK.

3.1.2 AC-FSK Waveform Analysis

Time-Domain AC-FSK Waveforms

The conventional bipolar M-ary FSK waveforms are presented in Sec. 2.1.1 (cf. eq. (2.3)), from which the M-ary AC-FSK dictionary, $\mathscr{D}^{\text{AC}}$, having cardinality M, is extrapolated from the $2M$-ary FSK dictionary, $\mathscr{D}^{\text{2M-FSK}}$, by considering only odd waveforms and clipping their negative part to zero to comply with the IM-DD constraints [52] [47]. Hence, the mth discrete-time M-ary AC-FSK waveform, $\boldsymbol{s}_m^{\text{AC}}$, can be defined as:

$$s_m^{\text{AC}}[n] = \tilde{s}^{+}_{\tilde{m}_{\text{odd}}}[n] = \begin{cases} \tilde{s}_{\tilde{m}_{\text{odd}}}[n] & \tilde{s}_{\tilde{m}_{\text{odd}}}[n] \geq 0 \\ 0 & \tilde{s}_{\tilde{m}_{\text{odd}}}[n] < 0 \end{cases} \tag{3.2}$$

where $m \in \{1,2,\cdots,M\}$, $n \in \{1,2,\cdots,M_{\text{c}}\}$, M_{c} being the number of chips per waveform and $\tilde{s}^{+}_{\tilde{m}_{\text{odd}}}[n]$ represents the positive part of the odd waveforms for $2M$-ary FSK with $\tilde{m}_{\text{odd}} = 2m-1$, i.e., $\tilde{m}_{\text{odd}} \in \{1,3,\cdots,2M-3,2M-1\}$.

For M-ary AC-FSK, symbol duration T_{s}, being equal to the conventional $2M$-ary FSK symbol duration, $\tilde{T}_{\text{s}}$, i.e. $T_{\text{s}} = \tilde{T}_{\text{s}} = M_{\text{c}}T_{\text{c}}$ with $M_{\text{c}} = 2M$, and T_{c} being the chip time. The analog time-domain counter-parts of $\boldsymbol{s}_m^{\text{AC}}$ in (3.2) is obtained using $t = \left(n + \frac{1}{2}\right)T_{\text{c}}$ as:

$$s_m^{\text{AC}}(t) = \begin{cases} \tilde{s}_{(2m-1)}(t), & if \;\; \tilde{s}_{\tilde{m}_{\text{odd}}}(t) \geq 0 \;\; , \quad \text{for } 1 \leq m \leq M/2 \\ 0 & \text{otherwise} \end{cases} \tag{3.3}$$

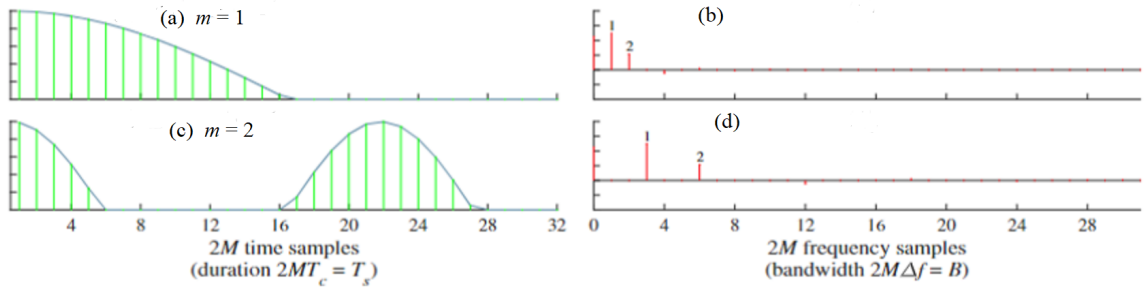

Fig. 3.2 (a) and (c) represent the time-domain M-ary AC-FSK waveforms ($m = 1$ and 2, respectively), while (b) and (d) represent their frequency-domain counter-parts, considering $M = 16$.

As an example, Fig. 3.2 (a) and (c) illustrate the time-domain M-ary AC-FSK waveforms for $m = 1$ and $m = 2$, respectively, considering $M = 16$, i.e., $\boldsymbol{s}_1^{\text{AC}}$ and $\boldsymbol{s}_2^{\text{AC}}$.

Frequency-Domain AC-FSK Waveforms

Frequency-domain (FD) M-ary AC-FSK waveforms, $\boldsymbol{S}_m^{\text{AC}}$, can be obtained by applying $2M$-order DCT on $\boldsymbol{s}_m^{\text{AC}}$ in (3.3) as:

$$\boldsymbol{S}_m^{\text{AC}} = \boldsymbol{C}_{2\text{M}} \boldsymbol{s}_m^{\text{AC}}, \tag{3.4}$$

where $\boldsymbol{C}_{2\text{M}}$ is the $2M$-order DCT matrix presented in (2.2) and $\boldsymbol{S}_m^{\text{AC}}$ in vectorial form is given as $\boldsymbol{S}_m^{\text{AC}} = [S_m^{\text{AC}}[0], S_m^{\text{AC}}[1], \cdots, S_m^{\text{AC}}[2M-1]]^{\text{T}}$ [47].

Consider any M-ary AC-FSK waveforms, $\boldsymbol{s}_m^{\text{AC}} \in \mathscr{D}^{\text{AC}}$, its frequency-domain counter-part (i.e., spectra) shows the following [47]:

- a DC component,
- one harmonic (with amplitude $2A$) to the fundamental frequency with frequency index $2m-1$,
- even order harmonic containing the distortion due to the clipping. The amplitude of the even $2p$th harmonics, S_m^{2p}, can be computed as:

$$S_m^{2p} = \frac{8A}{\pi} \frac{(-1)^p}{1-4p^2}, \tag{3.5}$$

  where $p \in \mathbb{N}^*$. The second harmonic ($p = 1$ in (3.5)) is located at index $4m-2$ for $0 \leq m \leq M/2-1$, i.e., $S_m[4m-2] = 8A/3\pi$, while for $M/2 \leq m \leq M-1$, the second harmonic is aliased at index $4M-4m+2$, i.e., $S_m[4M-4m+2] = -8A/3\pi$ [47].

Fig. 3.2 (b) and (d) respectively illustrate the frequency-domain counter-parts M-ary AC-FSK waveforms for $m = 1$ and $m = 2$, that are obtained through DCT, considering $M = 16$. From spectra in Fig. 3.2 (b) and (d), it can be derived that 99% of the symbol energy is contained in 2 most significant taps (discarding the DC tap), marked as "1" and "2", while the other taps have relatively negligible

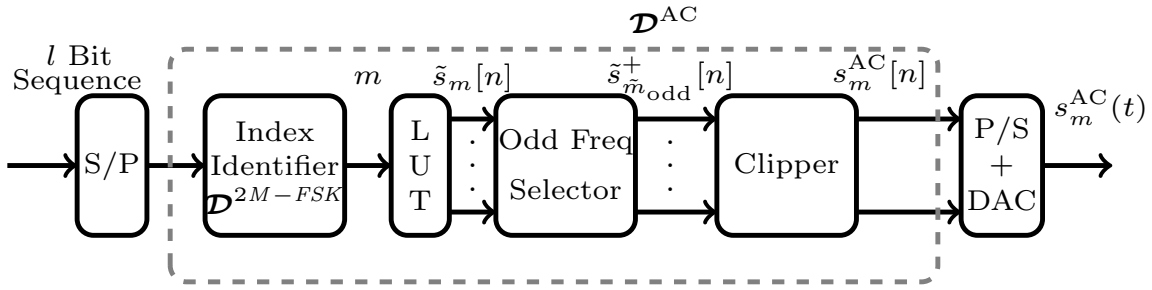

Fig. 3.3 Transmitter architecture of M-ary AC-FSK.

energy and can be neglected. Note that the amplitude of the harmonics illustrated in Fig. 3.2 (b) and (d), which are obtained through DCT, are consistent with (3.5), considering $A = 1$.

3.1.3 M-ary AC-FSK Transmitter

M-ary AC-FSK transmitter architecture is shown in Fig. 3.3. The mth waveform is chosen by binary to decimal conversion of $l = \log_2(M)$ independent and equiprobable bits. The symbol conforming to the chosen frequency m is extrapolated from the LUT (containing conventional bipolar $2M$-ary FSK dictionary, $\mathscr{D}^{\mathrm{2M-FSK}}$), where the number of chips per symbol is $M_{\mathrm{c}} = M$. Then, the odd frequency waveforms, $\tilde{\boldsymbol{s}}_{(2m+1)}$ are selected from the dictionary, $\mathscr{D}^{\mathrm{2M-FSK}}$. Afterward, the mth frequency M-ary AC-FSK waveform, $\boldsymbol{s}_m^{\mathrm{AC}}$, is obtained by clipping the negative samples of $\tilde{\boldsymbol{s}}_{(2m-1)}$ with $1 \leq m \leq M/2$ as [52]:

$$s_m^{\mathrm{AC}}[n] = \tilde{s}^{+}_{\tilde{m}_{\mathrm{odd}}}[n] \tag{3.6}$$

3.1.4 Average M-ary AC-FSK Symbol Energy

For M-ary AC-FSK modulation scheme, the symbol energy, $E^{\mathrm{AC}}_{\mathrm{s(elec)}}$, is directly linked to the average electrical bit energy, $E^{\mathrm{AC}}_{\mathrm{b(elec)}}$, by $E^{\mathrm{AC}}_{\mathrm{s(elec)}} = E^{\mathrm{AC}}_{\mathrm{b(elec)}} \log_2(M)$. All the waveforms in M-ary AC-FSK dictionary, $\mathscr{D}^{\mathrm{AC}}$, have the same symbol energy for any m, therefore, the average symbol energy coincide with the energy of each symbol. The average symbol energy of the mth frequency M-ary AC-FSK waveform can be computed as:

$$E^{\mathrm{AC}}_{\mathrm{s(elec)}} = \|s_m(t)\|^2 = \int_0^{T_s} |s_m^{\mathrm{AC}}(t)|^2 dt \qquad \text{for} \quad 0 \leq m \leq M-1, \tag{3.7}$$

Integrating equation (3.3) into equation (3.7), we can write:

$$E^{\mathrm{AC}}_{\mathrm{s(elec)}} = \frac{E^{\mathrm{FSK}}_{\mathrm{s(elec)}}}{2} = \frac{1}{2}\int_0^{T_s} (A\cos(2\pi m\Delta f t))^2 dt \tag{3.8}$$

$E_{\mathrm{s(elec)}}^{\mathrm{FSK}}$ being the symbol energy for conventional M-ary FSK, which leads to:

$$E_{\mathrm{s(elec)}}^{\mathrm{AC}} = \frac{A^2}{4} T_s \tag{3.9}$$

Hence, from (2.7) and (3.9), we can notice that symbol energy of waveforms before clipping is $E_{\mathrm{s(elec)}}^{\mathrm{FSK}}$ and it becomes half after clipping. i.e., $E_{\mathrm{s(elec)}}^{\mathrm{AC}} = E_{\mathrm{s(elec)}}^{\mathrm{FSK}}/2$. This is because of the clipping of exactly half part (negative part) of the conventional bipolar $2M$-ary FSK waveforms to obtain M-ary AC-FSK waveforms.

Note that for any waveform in the alphabet (except DC carrier), the electrical power is $P_{(\mathrm{elec})} = A^2/2$ before clipping and it is halved after clipping, i.e., $P_{(\mathrm{elec})}^{\mathrm{AC}} = A^2/4$.

3.1.5 Average Optical Power for M-ary AC-FSK

For optical communication systems, average optical power, $P_{(\mathrm{opt})}$, is an important parameter because it quantifies the electrical-to-optical conversion efficiency, depending on the modulation waveform. For M-ary AC-FSK waveforms, the average optical power, $P_{(\mathrm{opt})}^{\mathrm{AC}}$, can be computed as:

$$P_{(\mathrm{opt})}^{\mathrm{AC}} = \frac{1}{T_s} \int_0^{T_s} s_m^{\mathrm{AC}}(t) dt \tag{3.10}$$

M-ary AC-FSK waveforms exhibit a half-wave symmetry, as a consequence average optical power can be derived from optical power evaluation of the first non-DC waveform $(m = 1)$. M-ary AC-FSK waveform for $m = 1$ is illustrated in Fig. 3.2 (a). It can be notice that half of the waveform is clipped to zero, therefore, the integration in (3.10) can be limited from 0 to $T_{\mathrm{s}}/2$ and using $m = 1$ as:

$$P_{(\mathrm{opt})}^{\mathrm{AC}} = \frac{1}{T_{\mathrm{s}}} \int_0^{T_{\mathrm{s}}/2} A\cos(2\pi(1)\Delta f t) dt, \tag{3.11}$$

After simplifying (3.11), it leads to:

$$P_{(\mathrm{opt})}^{\mathrm{AC}} = \frac{A}{\pi} \left[\sin\frac{\pi}{2}\right] = \frac{A}{\pi}. \tag{3.12}$$

3.1.6 Minimum Squared Euclidean Distance between M-ary AC-FSK Waveforms

As aforementioned that minimum squared Euclidean distance between waveform pairs in the dictionary of any modulation is linked with the BER performance. Recall that the M-ary AC-FSK waveforms are derived by clipping the negative parts of the odd frequency $2M$-ary FSK waveforms. The clipping process affects the orthogonality between M-ary AC-FSK waveforms, resulting the inner product $\langle s_i^{\mathrm{AC}}(t), s_j^{\mathrm{AC}}(t)\rangle \neq 0$. The minimum squared Euclidean distance, $d_{\mathrm{min,AC}}^2$, between any waveform pair,

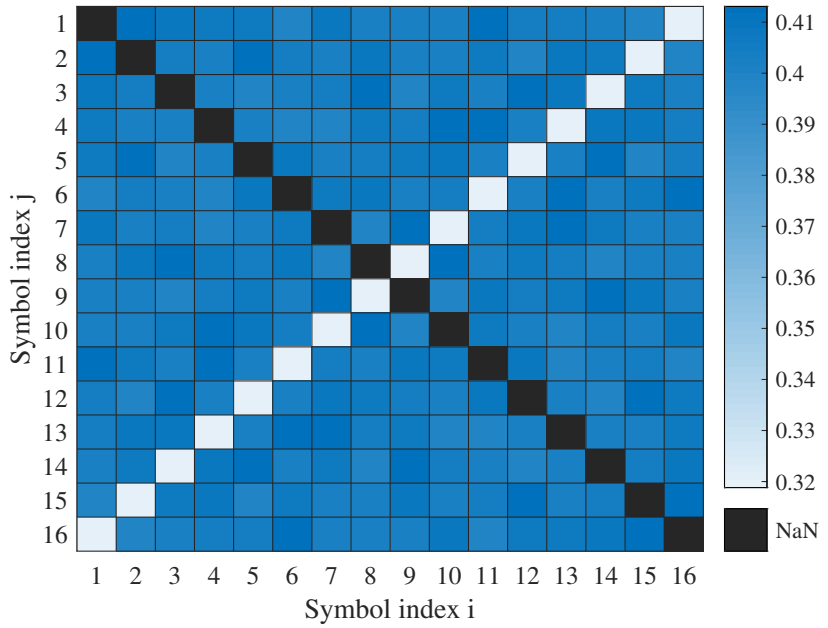

Fig. 3.4 Heatmap of the inner product for M-ary AC-FSK waveform pairs, $(s_i^{\mathrm{AC}}(t);s_j^{\mathrm{AC}}(t))$ for $i \neq j$, considering $M = 16$. NaN: not a number.

$(s_i^{\mathrm{AC}}(t);s_j^{\mathrm{AC}}(t))$, for M-ary AC-FSK can be computed using (2.9) as:

$$\begin{aligned} d^2_{\min,\mathrm{AC}} &= \min_{i\neq j} \|s_i^{\mathrm{AC}}(t) - s_j^{\mathrm{AC}}(t)\|^2 \\ &= \min_{i\neq j} \left\{ 2E^{\mathrm{AC}}_{\mathrm{s(elec)}} - 2\Re\langle s_i^{\mathrm{AC}}(t), s_j^{\mathrm{AC}}(t)\rangle \right\} \\ &= 2E^{\mathrm{AC}}_{\mathrm{s(elec)}} - \max_{i\neq j} \left\{ 2\Re\langle s_i^{\mathrm{AC}}(t), s_j^{\mathrm{AC}}(t)\rangle \right\} \end{aligned} \tag{3.13}$$

It can be seen in (3.13) that the minimum squared Euclidean distance is dependent on the maximum inner product, $\langle s_i^{AC}(t), s_j^{AC}(t)\rangle_{\max}$. Therefore, it is important to identify the pair of waveforms, $(s_i^{\mathrm{AC}}(t);s_j^{\mathrm{AC}}(t))$, for $i \neq j$ in the dictionary, $\mathscr{D}^{\mathrm{AC}}$, for which the inner product is maximum. Recall that the inner product between any pair of real waveforms, $(s_i^{\mathrm{AC}}(t);s_j^{\mathrm{AC}}(t)) \in \mathscr{D}^{\mathrm{AC}}$, can be computed using (2.4).

Simulations of the inner product, $\langle s_i^{\mathrm{AC}}(t), s_j^{\mathrm{AC}}(t)\rangle$, can be seen on the heatmap in Fig. 3.4. The inner products values have been normalized by the symbol energy, $E^{\mathrm{AC}}_{\mathrm{s(elec)}}$. As a consequence, $1/E^{\mathrm{AC}}_{\mathrm{s(elec)}} \cdot \langle s_m^{\mathrm{AC}}(t), s_m^{\mathrm{AC}}(t)\rangle = 1$, for $m \in [0, M-1]$. For $i \neq j$, the maximum value for the inner product, $\langle s_i^{AC}(t), s_j^{AC}(t)\rangle_{\max}$, is obtained for several pairs (i, j). For mathematical computations, we consider the simplest waveform pair, $(i, j) = (1, 2)$, among the waveform pairs, that corresponds to the maximum inner product. Hence, the maximum inner product, $\langle s_i^{AC}(t), s_j^{AC}(t)\rangle_{\max}$, is achieved for the waveform pair,$(i, j) = (1, 2)$, therefore, using $s_1^{\mathrm{AC}}(t)$ and $s_2^{\mathrm{AC}}(t)$ in (2.4), the maximum inner product can be

computed as:

$$\max_{i\neq j}\left\{\langle s_i^{\mathrm{AC}}(t), s_j^{\mathrm{AC}}(t)\rangle\right\} = \langle s_1^{\mathrm{AC}}(t), s_2^{\mathrm{AC}}(t)\rangle,$$
$$= \int_0^{T_\mathrm{s}} A\cos(2\pi\Delta f t).A\cos(2\pi 3\Delta f t)dt, \tag{3.14}$$

Due to previously introduced half-wave symmetry in M-ary AC-FSK waveforms, the integral bounds can be limited from 0 to $T_\mathrm{s}/6$ for the waveforms pair, $(i,j)=(1,2)$, (cf. Fig. 3.1 (b) and (d)), resulting in:

$$\max_{i\neq j}\left\{\langle s_i^{\mathrm{AC}}(t), s_j^{\mathrm{AC}}(t)\rangle\right\} = \int_0^{T_\mathrm{s}/6} A^2\cos(2\pi\Delta f t)\cos(2\pi 3\Delta f t)dt, \tag{3.15}$$

Using trigonometric identity and rearranging (3.15), we can write as:

$$\max_{i\neq j}\left\{\langle s_i^{\mathrm{AC}}(t), s_j^{\mathrm{AC}}(t)\rangle\right\} = \frac{A^2}{2}\int_0^{T_\mathrm{s}/6}\left[\cos(2\pi 3\Delta f t - 2\pi\Delta f t) + \cos(2\pi 3\Delta f t + 2\pi\Delta f t)\right]dt,$$
$$= \frac{A^2}{2}\left[\left[\frac{\sin(2\pi\Delta f t)(2)}{(2\pi\Delta f)(2)}\right]_0^{T_\mathrm{s}/6} + \left[\frac{\sin(2\pi\Delta f t)(4)}{(2\pi\Delta f)(4)}\right]_0^{T_\mathrm{s}/6}\right], \tag{3.16}$$

inserting $\Delta f = 1/2T_\mathrm{s}$ into (3.16), it can be simplified as:

$$\max_{i\neq j}\left\{\langle s_i^{\mathrm{AC}}(t), s_j^{\mathrm{AC}}(t)\rangle\right\} = \frac{A^2 T_\mathrm{s}}{2\pi}\left[\frac{3\sqrt{3}}{8}\right],$$
$$= E_{\mathrm{s(elec)}}^{\mathrm{AC}}\left[\frac{3\sqrt{3}}{4\pi}\right] \tag{3.17}$$

Finally, the minimum squared Euclidean distance for M-ary AC-FSK can be computed by using the maximum inner product from (3.17) into (3.13) as:

$$d_{\mathrm{min,AC}}^2 = 2E_{\mathrm{s(elec)}}^{\mathrm{AC}}\left[1 - \frac{3\sqrt{3}}{4\pi}\right]$$
$$= 2E_{\mathrm{s(elec)}}^{\mathrm{AC}}\gamma^{\mathrm{AC}} \tag{3.18}$$

where $\gamma^{\mathrm{AC}} = \left[1 - \frac{3\sqrt{3}}{4\pi}\right] \simeq 0.586$, is the penalty factor for M-ary AC-FSK modulation scheme, compared to bipolar conventional M-ary FSK for which $\gamma = 1$, while penalty factors for M-ary DC-FSK and M-ary U-FSK are $\gamma^{\mathrm{DC}} = 0.33$, and $\gamma^{\mathrm{U}} = 0.55$, respectively [30]. We can clearly notice that $\gamma^{\mathrm{DC}} < \gamma^{\mathrm{U}} < \gamma^{\mathrm{AC}}$. From this result, we can expect that the energy efficiency for M-ary AC-FSK is improved compared to M-ary U-FSK and M-ary DC-FSK modulation schemes.

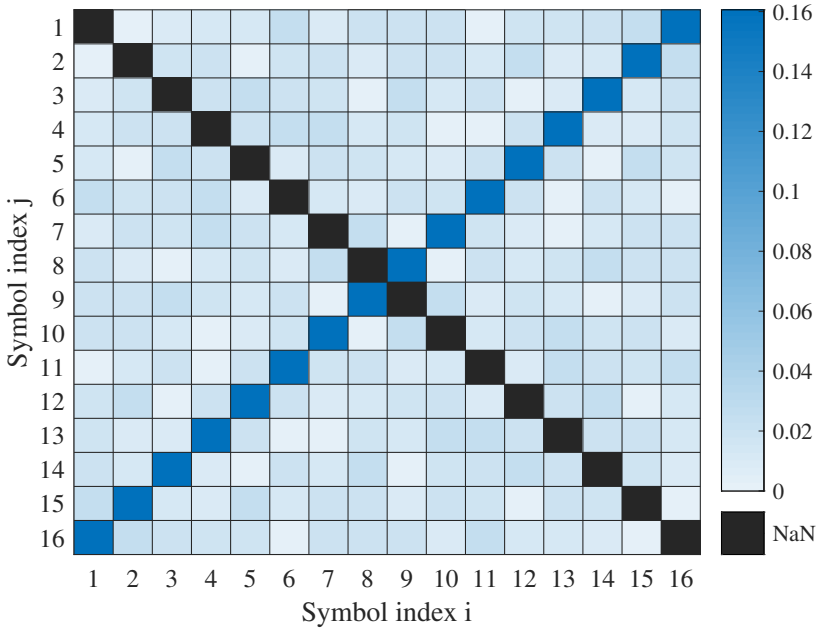

Fig. 3.5 Deviation, Δ of the squared Euclidean distance, $d^2_{i,j}$ between M-ary AC-FSK waveform pairs, relative to the minimum squared Euclidean distance, $d^2_{\text{min,AC}}$. NaN: not a number.

For more clarification, we introduce a new parameter Δ to evaluate the deviation of the squared Euclidean distance, $d^2_{i,j}$ (with $i \neq j$), for all waveform pairs, relative to the minimum squared Euclidean distance, $d^2_{\text{min,AC}}$, as [47]:

$$\Delta = \frac{d^2_{i,j} - d^2_{\text{min,AC}}}{d^2_{\text{min,AC}}}. \tag{3.19}$$

Fig. 3.5 illustrates the heat-map of Δ as a function of all possible M-ary AC-FSK waveform pairs, $(\boldsymbol{s}^{\text{AC}}_i;\boldsymbol{s}^{\text{AC}}_j)$, for $M = 16$. It can be seen that the squared Euclidean distance for any M-ary AC-FSK waveform pair, $(\boldsymbol{s}^{\text{AC}}_i;\boldsymbol{s}^{\text{AC}}_j)$, does not deviate more than 16.06% from $d^2_{\text{min,AC}}$, considering $M = 16$, while the deviation from $d^2_{\text{min,AC}}$ is not more than 16.23% for M-ary AC-FSK, considering higher modulation size, i.e., $M = 1024$ [47].

Fig. 3.6 illustrates the histogram of the normalized squared Euclidean distance, $\tilde{d}^2_{i,j}$, for M-ary FSK waveform pairs, $(\boldsymbol{s}^{\text{AC}}_i;\boldsymbol{s}^{\text{AC}}_j)$, considering $M = 16$, i.e., $\tilde{d}^2_{i,j} = d^2_{i,j}/E^{\text{AC}}_{\text{s(elec)}}$. Note that 15 waveform pairs are considered for a given waveform, $\boldsymbol{s}^{\text{AC}}_i$. It can be seen in Fig. 3.6 that only one waveform, $\boldsymbol{s}^{\text{AC}}_j$, shows a significantly larger squared Euclidean distance related to $d^2_{\text{min,AC}}$, while most of the waveform pairs, $(\boldsymbol{s}^{\text{AC}}_i;\boldsymbol{s}^{\text{AC}}_j)$, have squared Euclidean distance close to $d^2_{\text{min,AC}}$ for which $d^2_{\text{min,AC}}/2E^{\text{AC}}_{\text{s(elec)}} = \gamma^{\text{AC}} \approx 0.59$ [47].

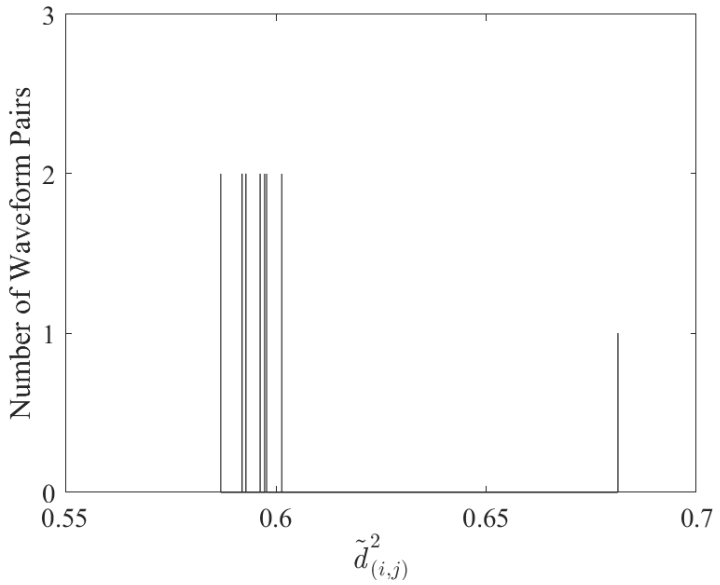

Fig. 3.6 Histogram of the squared normalised distance, $\tilde{d}^2_{i,j}$ for M-ary AC-FSK, considering $M = 16$, i.e., $\tilde{d}^2_{i,j} = d^2_{i,j}/2E_{\mathrm{s(elec)}}$. $\tilde{d}^2_{i,j}$ between one waveform, s_i^{AC} with the whole dictionary, $\mathscr{D}^{\mathrm{AC}}$ is presented.

3.1.7 Spectral Efficiency of M-ary AC-FSK

The spectral efficiency of M-ary AC-FSK, η^{AC}, can be expressed using (2.12) as:

$$\eta^{\mathrm{AC}} = \frac{R_{\mathrm{b}}^{\mathrm{AC}}}{B^{\mathrm{AC}}} \tag{3.20}$$

where $R_{\mathrm{b}}^{\mathrm{AC}}$ is the bit rate and B^{AC} is the bandwidth of M-ary AC-FSK. As the M-ary AC-FSK is derived from $2M$-ary FSK, therefore, the baseband bandwidth (without taking into account the clipping distortion harmonics), is approximated as $B^{\mathrm{AC}} \approx 2M\Delta f = M.\frac{1}{\tilde{T}_{\mathrm{s}}}$. Similarly, the bit rate $R_{\mathrm{b}}^{\mathrm{AC}} = \log_2(M)/\tilde{T}_{\mathrm{s}}$, so the spectral efficiency, η^{AC}, in (3.20) for M-ary AC-FSK can be expressed as:

$$\begin{aligned} \eta^{\mathrm{AC}} &= \frac{\frac{\log_2(M)}{\tilde{T}_{\mathrm{s}}}}{M.\frac{1}{\tilde{T}_{\mathrm{s}}}}, \\ &= \frac{\log_2(M)}{M} \end{aligned} \tag{3.21}$$

Tab. 3.1 shows the quantitative comparison of spectral efficiencies of FSK-based modulation schemes, where M represents the modulation size. It can be seen from Tab. 3.1 that the spectral efficiencies for both M-ary AC-FSK and M-ary U-FSK are equal and it is half of as that of the spectral efficiency of the M-ary DC-FSK and the conventional bipolar M-ary FSK.

Table 3.1 Quantitative comparison of spectral efficiencies of conventional FSK, DC-FSK, U-FSK and AC-FSK

Modulation Scheme	η
FSK	$\frac{2\log_2(M)}{M}$
DC-FSK	$\frac{2\log_2(M)}{M}$
U-FSK	$\frac{\log_2(M)}{M}$
AC-FSK	$\frac{\log_2(M)}{M}$

3.2 M-ary AC-FSK Receivers

The received M-ary AC-FSK waveform is affected by ambient noise that results in receive waveform, $\boldsymbol{r}$. After photodetection, the received waveform, $\boldsymbol{r}$, containing ambient noise is passed through analog-to-digital-converter (ADC), we obtain:

$$\boldsymbol{r} = \boldsymbol{s}_m^{AC} + \boldsymbol{n}, \tag{3.22}$$

where $\boldsymbol{n}$ is additive white Gaussian noise (AWGN) with mono-lateral power spectral density (PSD) of N_o. Explicitly $\boldsymbol{r} = [r[0], r[1], \cdots, r[M_c - 1]]^{\mathrm{T}}$, $\boldsymbol{n} = [n[0], n[1], \cdots, n[M_c - 1]]^{\mathrm{T}}$, and $\boldsymbol{s}_m^{AC}$ is defined in (3.3).

Three types of techniques are used to recover the transmitted bits from received waveform, $\boldsymbol{r}$, for M-ary AC-FSK modulation scheme.

- Optimal TD ML receiver which implements matched filtering.
- Sub-optimal receiver which is based on low-complexity DCT.
- Proposed 2-tap harmonic receiver which is based on the FD cross-correlation.

3.2.1 Optimal TD ML Receiver

Fig. 3.7 (red/black) illustrates the configuration of the optimal TD ML receiver for M-ary AC-FSK. It permits to guarantee a minimum error probability in case of independent and equiprobable bits. Under such condition, the optimal TD ML receiver evaluates the TD cross-correlation of the received waveform, $\boldsymbol{r}$, with all waveforms in $\mathscr{D}^{\mathrm{AC}}$ to identify the frequency index $\hat{m}$ for which the TD cross-correlation is maximum as [52] [47]:

$$\hat{m} = \arg \max_m \langle \boldsymbol{r}, \boldsymbol{s}_m^{AC} \rangle, \quad m \in \{1, 2, ..., M\} \tag{3.23}$$

Finally the identified index $\hat{m}$ is decoded into output bits. The receiver complexity for AC-FSK can be calculated in terms of a total number of required arithmetic operations at the receiver. For M-ary AC-FSK and considering optimal receiver, the receiver complexity is of the order of $\mathscr{O}(M \times M_c)$.

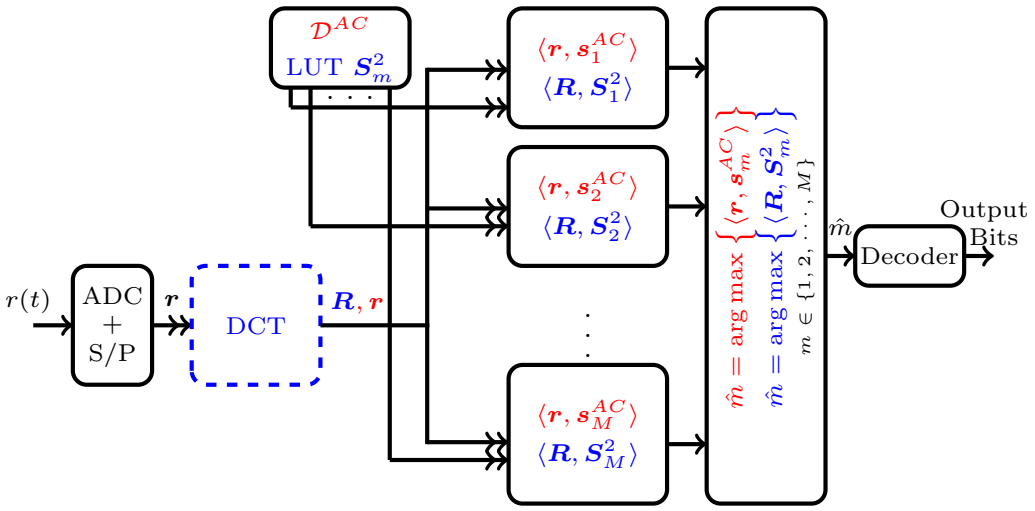

Fig. 3.7 Optimal ML TD receiver (red/black) and 2-tap harmonic receiver (blue/black) architecture for M-ary AC-FSK.

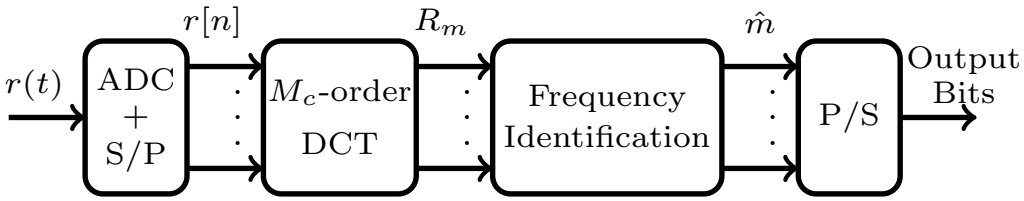

Fig. 3.8 Sub-optimal 1-tap DCT-based receiver architecture for M-ary AC-FSK

3.2.2 1-tap DCT-based Receiver

It is a conventional sub-optimal DCT-based receiver typically used for ACO-FOFDM [87]. Fig. 3.8 illustrates the sub-optimal 1-tap DCT-based receiver for M-ary AC-FSK. In 1-tap DCT-based receiver, M_c-order discrete cosine transform (DCT) is used instead of correlation process to identify the estimated frequency index $\hat{m}$ of the received waveform, $\boldsymbol{r}$. In the first step, M_c-order DCT ($M_c = 2M$) is applied on the digitized received waveform, $r[n]$, where $n = 0, 1, \cdots, 2M-1$, to obtain the FD received waveform, $\boldsymbol{R}$, as [52]:

$$\boldsymbol{R} = \boldsymbol{C}_{2M}\boldsymbol{r}, \tag{3.24}$$

where $\boldsymbol{R} = [R[0], R[1], \cdots, R[2M-1]]^{\mathrm{T}} \in \Re^M$, and $\boldsymbol{C}_{2M}$ is the $2M$-order DCT matrix which is defined in (2.2). Afterward, the estimated frequency index is identified from $\boldsymbol{R}$ as:

$$\hat{m} = \arg\max_{m} \Big\{ |R_m| \Big\}, \quad m \in \{0, 1, \cdots, M-1\}. \tag{3.25}$$

For low complexity sub-optimal receiver for M-ary AC-FSK, the receiver complexity is calculated from the number of operations exists in DCT process. In this way, the receiver complexity for sub-optimal receiver for M-ary AC-FSK is of the order of $\mathcal{O}(M_c/2 \times \log_2(M_c))$.

3.2.3 2-tap Harmonic Receiver

The main idea behind the 2-tap harmonic receiver is to incorporate the harmonic that is induced due to clipping distortion, which was not the case for 1-tap DCT-based receiver, because we considered only one harmonic having maximum amplitude for 1-tap DCT-based receiver. The 2-tap harmonic receiver configuration for M-ary AC-FSK is presented in Fig. 3.7 (blue/black). The transmitted frequency index m is identified using $2M$-order DCT together with the FD cross-correlation [52] [47].

In the first off-line step, $2M$-order DCT is applied to all the M-ary AC-FSK waveforms in $\mathscr{D}^{\mathrm{AC}}$ to get the FD M-ary AC-FSK waveforms, $\boldsymbol{S}_m^{\mathrm{AC}}$, then the two most significant taps are selected to make $\boldsymbol{S}_m^2$ waveforms (ignoring the DC tap) and stored them in the LUT (cf. Fig. 3.2 (b) and (d)). It can be noted that these two selected taps (actually one odd and one even) contains most of the symbol energy for all M-ary AC-FSK waveforms, irrespective of dictionary size, M. In the second on-line step, $2M$-order DCT is applied on the digitized received waveform, $r[n]$, to obtain $\boldsymbol{R}$ as in (3.24). Hence, the on-line front-end processing for both 1-tap DCT-based receiver and 2-tap harmonic receiver is almost the same, but the transmitted frequency index $\hat{m}$ is evaluated by looking for a maximum after 2 taps-based computation using 2-tap harmonic receiver (instead of 1-tap computation in case of 1-tap DCT-based receiver) [52]. Therefore, the transmitted frequency index $\hat{m}$ is identified using the FD cross- correlation of $\boldsymbol{R}$ with all the $\boldsymbol{S}_m^2$ waveforms in the LUT as [52]:

$$\hat{m} = \arg \max_{m} \langle \boldsymbol{R}, \boldsymbol{S}_m^2 \rangle, \quad m \in \{1,2,...,M\}, \tag{3.26}$$

where the factor $\langle \boldsymbol{R}, \boldsymbol{S}_m^2 \rangle$ can be explicitly expressed as:

$$\langle \boldsymbol{R}, \boldsymbol{S}_m^2 \rangle = R[2m-1].S_m[2m-1] + R[k_{2nd}].S_m[k_{2nd}], \tag{3.27}$$

with $(2m-1)$ and k_{2nd}, respectively are the indices of the first harmonic (odd) and second harmonic (even) frequency ($k_{2nd} = 2 \times (2m-1)$ if $m < M/2$, or $2 \times (2M - (2m-1))$ if $m \geq M/2$ (cf. Sec. 3.1.2).

From (3.26) and (3.27), note that the 2-taps computation permits us to approach closely the FD cross-correlation between $\boldsymbol{R}$ and all $\boldsymbol{S}_m^{\mathrm{AC}}$ waveforms, i.e., $\langle \boldsymbol{R}, \boldsymbol{S}_m^{\mathrm{AC}} \rangle$ (frequency formulation), which is the couterpart of the TD inner product $\langle \boldsymbol{r}, \boldsymbol{s}_m \rangle$ (time formulation), appearing in the optimal TD ML receiver (3.23). Therefore, we expect the performance for 2-tap harmonic receiver close to the optimal TD ML receiver.

3.2.4 Complexity Analysis for M-ary AC-FSK Receivers

It is aforementioned in Sec. 2.2.7 that the primary contributor to the receiver complexity is the number of non-zero real multiplications to identify the estimated frequency index $\hat{m}$. As the TD M-ary AC-FSK waveform consists of M_{c} chips and the optimal TD ML receiver is based on the TD cross-correlation of the received waveform, $\boldsymbol{r}$, with all the M-ary AC-FSK waveforms, $\boldsymbol{s}_m^{\mathrm{AC}} \in \mathscr{D}^{\mathrm{AC}}$.

Table 3.2 Complexity computations and complexity reduction, β, for 2-tap harmonic receiver relative to the optimal TD ML receiver, considering different M, for M-ary AC-FSK.

M	$\mathscr{C}_{\text{TD,ML}}$	$\mathscr{C}_{\text{harm}}$	β (%)
16	256	112	56.3
32	1024	256	75.0
64	4096	576	85.9
128	16384	1280	92.2
256	65536	2816	95.7
512	262144	6144	97.7
1024	1048576	13312	98.7

Therefore, the optimal TD ML receiver for M-ary AC-FSK requires $\mathscr{C}_{\text{TD,ML}} = MM_{\text{c}} = M^2$, non-zero real multiplications, because half of the chips of TD M-ary AC-FSK waveforms are clipped to zero. Note that $\mathscr{C}_{\text{TD,ML}}$ increases quadratically with increasing M.

The 1-tap DCT-based receiver for M-ary AC-FSK requires $\mathscr{C}_{1-\text{tap}} = M\log_2(2M)$, non-zero real multiplications due to the $2M$-order DCT operations [87]. Similarly, the 2-tap harmonic receiver for M-ary AC-FSK requires $\mathscr{C}_{\text{harm}} = M\log_2(2M) + 2M$, non-zero real multiplications, which is slightly larger than $\mathscr{C}_{1-\text{tap}}$, but it is still linearitmic with M [47]. Note that the term $(M\log_2(2M))$ in $\mathscr{C}_{\text{harm}}$ is due to the $2M$-order DCT while the additional term $(2M)$ is due the FD cross-correlation of $\boldsymbol{R}$ with $\boldsymbol{S}_m^2$ waveforms in the LUT. Thus, the increase in the computational complexity of 2-tap harmonic receiver relative to the 1-tap DCT-based receiver for M-ary AC-FSK due to the additional FD cross-correlation step (i.e., $2M$) is about 40% and 25% for $M = 16$ and 128, respectively [47].

As the number of non-zero real multiplications is reduced for 2-tap harmonic receiver as compared to the optimal TD ML receiver for M-ary AC-FSK, therefore, we expect a drastic reduction in the complexity of the 2-tap harmonic receiver. For clear understanding, we presented β that evaluates the complexity reduction of the 2-tap harmonic receiver as compared to the optimal TD ML receiver for different M as [47]:

$$\beta = \left(1 - \frac{\mathscr{C}_{\text{harm}}}{\mathscr{C}_{\text{TD,ML}}}\right) \times 100\%, \tag{3.28}$$

In Tab. 3.2 , the computational complexities of optimal TD ML receiver and 2-tap harmonic receiver for M-ary AC-FSK are presented, considering different M, while the complexity reduction, β, for different M are also presented. It can be seen that the complexity reduction, β, for 2-tap harmonic receiver relative to the optimal TD ML receiver for M-ary AC-FSK is about 56.3% and 98.7% for $M = 16$ and 1024, respectively.

Fig. 3.9 illustrates the complexity comparison of the optimal TD ML receiver, sub-optimal 1-tap DCT-based receiver and 2-tap harmonic receiver as a function of the number of bits per symbol

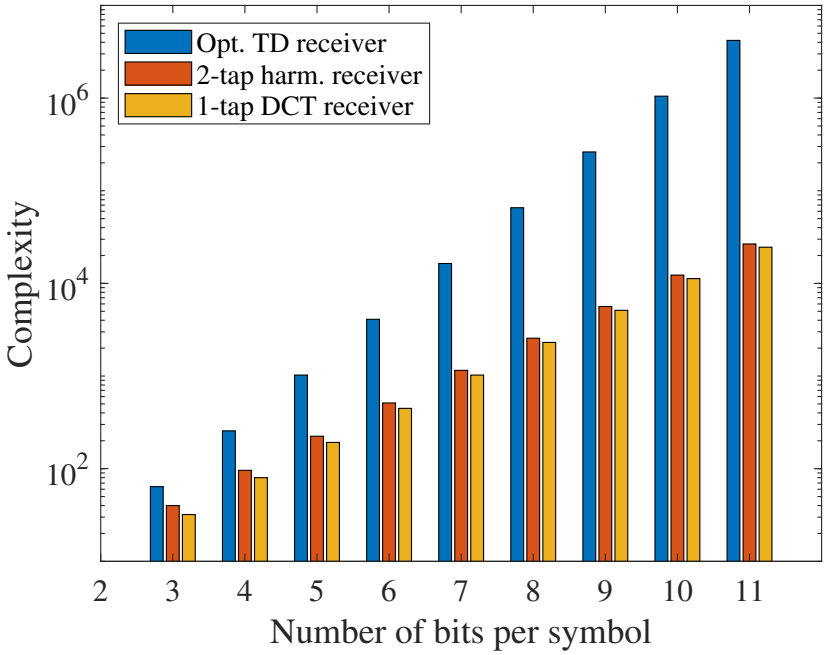

Fig. 3.9 Complexity comparison of optimal time-domain receiver (blue), sub-optimal 1-tap DCT receiver (orange) and 2-tap harmonic receiver (red) as a function of the number of bits per symbol $n = \log_2(M)$ for M-ary AC-FSK.

($n = \log_2(M)$) for M-ary AC-FSK. It can be seen that the optimal TD ML receiver shows a high complexity and its complexity increases quadratically with increasing M. On the other hand, 1-tap DCT-based receiver and 2-tap harmonic receiver show relatively low complexities as compared to the optimal TD ML receiver and their complexities increases linearithmically with increasing M. For large n, i.e., $n \geq 7$, the complexity of the 2-tap harmonic receiver is divided by a factor of 10 as compared to the optimal TD ML receiver. Note that the 2-tap harmonic receiver has slightly high complexity relative to the 1-tap DCT-based receiver [52].

Recall from Sec. 2.4.3 that the complexity of the $(12,2)$-tap harmonic receiver for M-ary U-FSK is $\mathscr{C}^{\mathrm{U}}_{\mathrm{harm}} = M\log_2(2M) + L_{\mathrm{e}}(M/2) + L_{\mathrm{o}}(M/2)$, where $L_{\mathrm{e}} = 12$ and $L_{\mathrm{o}} = 2$ are the number of taps selected for even and odd waveforms, respectively. As we considered only two taps for 2-tap harmonic receiver for M-ary AC-FSK, therefore, we also expect some complexity reduction for 2-tap harmonic receiver for M-ary AC-FSK relative to the $(12,2)$-tap harmonic receiver for M-ary U-FSK. We introduce a new parameter, α, that evaluates the complexity reduction of 2-tap harmonic receiver for M-ary AC-FSK relative to the $(12,2)$-tap harmonic receiver for M-ary U-FSK, considering different M as:

$$\alpha = \left(1 - \frac{\mathscr{C}^{\mathrm{AC}}_{\mathrm{harm}}}{\mathscr{C}^{\mathrm{U}}_{\mathrm{harm}}}\right) \times 100\%, \tag{3.29}$$

Tab. 3.3 shows the complexity computations of the 2-tap harmonic receiver for M-ary AC-FSK and $(12,2)$-tap harmonic receiver for M-ary U-FSK, considering different M, while α is also presented.

Table 3.3 Complexity computations and complexity reduction, α, for 2-tap harmonic receiver for M-ary AC-FSK relative to the $(12,2)$-tap harmonic receiver for M-ary U-FSK, considering different M.

M	$\mathscr{C}_{\text{harm}}^{\text{AC}}$	$\mathscr{C}_{\text{harm}}^{\text{U}}$	α (%)
16	112	192	41.6
32	256	416	38.4
64	576	896	35.7
128	1280	1920	33.3
256	2816	4096	31.2
512	6144	8704	29.4
1024	13312	18432	27.7

It can be seen that the complexity reduction, α, for 2-tap harmonic receiver for M-ary AC-FSK relative to the $(12,2)$-tap harmonic receiver for M-ary U-FSK is about 41.6% and 27.7% for $M = 16$ and 1024, respectively.

3.3 Bit Error Probability for M-ary AC-FSK

3.3.1 Relationship between Average Optical Energy per Bit and $d_{\min}$

Our objective is to express the bit error probability as a function of optical signal-to-noise ratio (SNR) per bit (i.e., $E_{\text{b(opt)}}/N_0$) to compute the theoretical performance of M-ary AC-FSK, that is used as a benchmark for simulation and experimental results [47].

The optical power for M-ary AC-FSK waveforms can be computed as:

$$P_{\text{(opt)}} = \frac{1}{M_{\text{c}}} \sum_{n=0}^{M_{\text{c}}-1} |s_m^{\text{AC}}[n]|. \tag{3.30}$$

The optical energy per bit, $E_{\text{b(opt)}}$, can be defined from P_{opt}, i.e., $E_{\text{b(opt)}} = P_{\text{opt}} T_{\text{b}}$, where T_{b} is the bit time ($T_{\text{b}} = T_{\text{s}}/\log_2(M)$). Bit energy in electrical and optical domain (i.e., $E_{\text{b(elec)}}$ and $E_{\text{b(opt)}}$, respectively) can be expressed using (3.2) as:

$$E_{\text{b(elec)}} = \frac{A^2 T_{\text{b}}}{4} \quad \text{and} \quad E_{\text{b(opt)}} = \frac{A T_{\text{b}}}{\pi}. \tag{3.31}$$

According to (3.18), the minimum squared Euclidean distance for M-ary AC-FSK is $d_{\text{min,AC}}^2 = 2E_{\text{s(elec)}}^{\text{AC}} \gamma^{\text{AC}}$, where $E_{\text{s(elec)}}^{\text{AC}} = E_{\text{b(elec)}}^{\text{AC}} \log_2(M)$. Substituting (3.31) into (3.18), we can obtain $d_{\text{min,AC}}^2$ as [47]:

$$d_{\text{min,AC}}^2 = \Gamma E_{\text{b(opt)}}^2, \tag{3.32}$$

where $\Gamma = \pi^2 \gamma^{\mathrm{AC}} R_{\mathrm{b}} \log_2(M)/2$.

3.3.2 Theoretical Bit Error Probability

As aforementioned in the Sec. 2.4.2 that the expression for theoretical bit error probability for ML detection of conventional bipolar M-ary FSK using AWGN channel is demonstrated in [57]. It is the function of the minimum squared Euclidean distance between M-ary FSK waveforms. As aforementioned in Sec. 3.1.6 that the squared Euclidean distance between any waveform pairs, $(s_i^{\mathrm{AC}}(t); s_j^{\mathrm{AC}}(t))$, for M-ary AC-FSK does not deviate more than 16.06% and 16.23% from $d^2_{\mathrm{min,AC}}$, considering $M = 16$ and 1024, respectively. Therefore, we can obtain a good approximation of the theoretical symbol error probability, P_{e}, for M-ary AC-FSK with ML detection by substituting d_{min} in the M-ary FSK bit error probability expression [57] with $d_{\mathrm{min,AC}}$ from (3.32) as:

$$P_{\mathrm{e}} \approx \frac{M}{2\sqrt{2\pi}(M-1)} \int_{-\infty}^{+\infty} \left[1 - (1 - Q(x))^{M-1}\right] \times e^{\left[-\frac{\left(x - \sqrt{\Gamma \frac{E^2_{\mathrm{b(opt)}}}{N_0}}\right)^2}{2}\right]} \mathrm{d}x, \tag{3.33}$$

where $Q(\cdot)$ is the Gaussian Q-function [57], and $e^{[\cdot]}$ is the exponential function

3.4 Simulation Results for the Proposed M-ary AC-FSK

In this section, we present the simulation results of the proposed M-ary AC-FSK together with the existed M-ary FSK-based modulation schemes, i.e., M-ary DC-FSK and M-ary U-FSK. We present the following performance parameters for the proposed M-ary AC-FSK:

- BER performance comparison between different receivers for M-ary AC-FSK in electrical domain, i.e., BER vs required $E_{\mathrm{b(elec)}}/N_0$.
- BER performance comparison in an AWGN channel for the proposed M-ary AC-FSK with the existed M-ary DC-FSK and M-ary U-FSK using the optimal TD ML receiver in electrical-domain.
- BER performance comparison in an AWGN channel for the proposed M-ary AC-FSK with the existed M-ary DC-FSK and M-ary U-FSK using the optimal TD ML receiver in optical-domain.

Monte Carlo simulations are performed using Matlab over 10^6 runs.

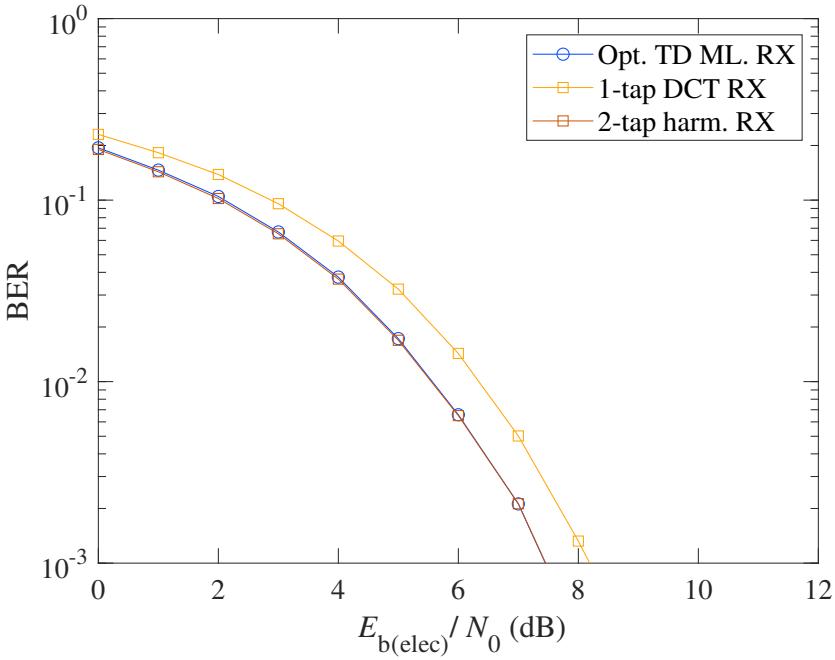

Fig. 3.10 BER vs $E_{b(elec)}/N_0$ comparison between optimal TD ML receiver, 1-tap DCT-based receiver and 2-tap harmonic receiver for M-ary AC-FSK for modulation order $M = 16$.

3.4.1 BER Performance Comparison Between Different Receivers for M-ary AC-FSK in Electrical-Domain

Fig. 3.10 illustrates the BER performance (i.e., BER vs required $E_{b(elec)}/N_0$ comparison) between the optimal TD ML receiver, 1-tap DCT-based receiver and the 2-tap harmonic receiver for M-ary AC-FSK, considering the modulation order $M = 16$. Note that AWGN channel is considered for the simulation in Fig. 3.10. It can be seen that the BER performance for the optimal TD ML receiver is better than the 1-tap DCT-based receiver by less than 1 dB for a BER = 10^{-3}, i.e., the optimal TD ML receiver requires less $E_{b(elec)}/N_0$ as compared to the 1-tap DCT-based receiver for the same BER = 10^{-3}. As expected, the 2-tap harmonic receiver also shows better BER performance than 1-tap DCT-based receiver and almost the same BER performance as the optimal TD ML receiver for M-ary AC-FSK [52].

3.4.2 BER Performance Comparison in Electrical-Domain using Optimal TD ML Receiver for M-ary AC-FSK with the existing M-ary FSK-based Modulations

Fig. 3.11 illustrates the spectral efficiency, η, vs the required $E_{b(elec)}/N_0$ performance comparison for M-ary AC-FSK with respect to the M-ary FSK-based modulation schemes (i.e., M-ary DC-FSK and M-ary U-FSK), OOK and M-ary PAM. Note that the targeted BER $= 10^{-3}$, and an optimal TD ML receiver is considered for all modulation schemes in the Fig. 3.11. As expected, M-ary AC-FSK

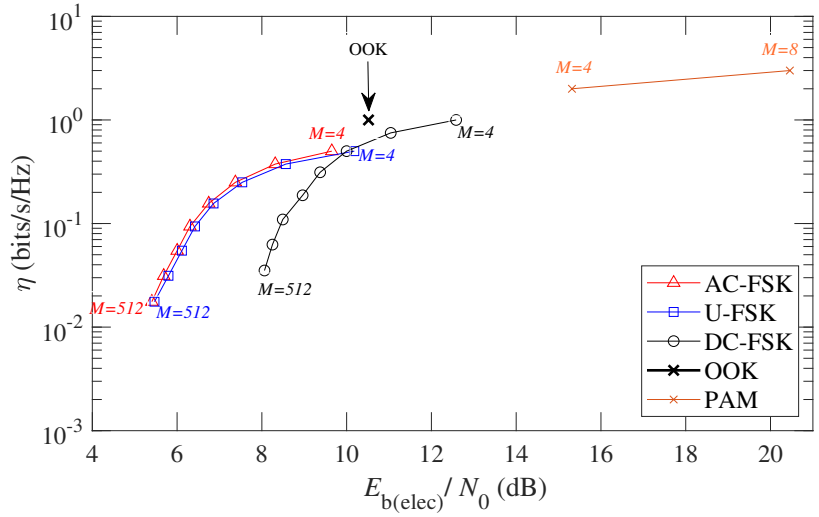

Fig. 3.11 Spectral Efficiency η vs required $E_{\mathrm{b(elec)}}/N_0$ comparison to achieve a BER of 10^{-3} for M-ary AC-FSK, M-ary U-FSK, M-ary DC-FSK, OOK and M-ary PAM for different modulation orders using optimal TD ML receivers.

has far better η vs the required $E_{\mathrm{b(elec)}}/N_0$ performance relative to the M-ary DC-FSK because the waveforms in the dictionary, $\mathscr{D}^{\mathrm{DC}}$, are negatively affected due to the addition of DC-offset [52]. For any targeted η, we need around 2 dB less $E_{\mathrm{b(elec)}}/N_0$ for M-ary AC-FSK as compared to the M-ary DC-FSK, considering $M \geq 16$. Furthermore, M-ary AC-FSK also shows slightly better η vs the required $E_{\mathrm{b(elec)}}/N_0$ performance relative to the M-ary U-FSK. It can be seen in Fig. 3.11 that for any targeted η, we need around 0.1 dB less $E_{\mathrm{b(elec)}}/N_0$ for M-ary AC-FSK relative to the M-ary U-FSK. As an example, for $\eta = 0.1$ bit/s/Hz, M-ary DC-FSK has a penalty of 2 dB relatively to M-ary AC-FSK and M-ary U-FSK. Furthermore, the performance of OOK and M-ary PAM have also been plotted in Fig. 3.11. It is confirmed from Fig. 3.11 that the performance of OOK and M-ary PAM is worse as compared to the proposed M-ary AC-FSK and the energy efficiency of M-ary PAM is degraded with increasing M. This is because the M-ary PAM is a linear modulation and its performance is negatively impacted with increasing the modulation order M [30].

3.4.3 Spectral efficiency vs Energy efficiency in Optical-Domain using Optimal TD ML Receiver for M-ary AC-FSK with the existing M-ary FSK-based modulations

Usually BER vs $E_{\mathrm{b(opt)}}/N_0$ is used to evaluate the performance of any modulation scheme in the optical-domain. E_{b}/N_0 for electrical and optical-domains are specified as follow:

$$\frac{E_{\mathrm{b(elec)}}}{N_0} = \frac{P_{\mathrm{(elec)}}}{\eta B N_0} \quad \text{and} \quad \frac{E_{\mathrm{b(opt)}}}{N_0} = \frac{P_{\mathrm{(opt)}}}{\eta B N_0}. \tag{3.34}$$

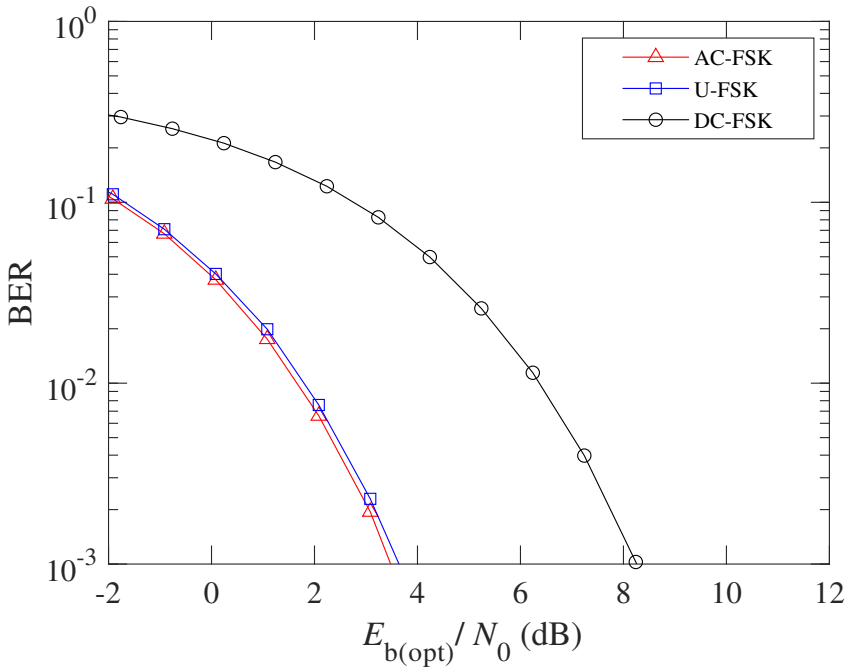

Fig. 3.12 BER vs required $E_{b(opt)}/N_0$ comparison for M-ary AC-FSK, M-ary U-FSK and M-ary DC-FSK using an optimal TD ML receiver, considering $M = 16$.

where $E_{b(opt)}/N_0$ can be represented in terms of $E_{b(elect)}/N_0$ from (3.34) as:

$$\frac{E_{b(opt)}}{N_0} = \frac{P_{(opt)}}{P_{(elec)}} \frac{E_{b(elec)}}{N_0} = \frac{1}{\alpha_{EO}} \frac{E_{b(elec)}}{N_0} \tag{3.35}$$

where α_{EO} represents electrical-to-optical conversion efficiency and it defines that how much electrical power is converted into optical power. From (3.35), it can be seen that any value of $E_{b(opt)}/N_0$ can be achieved from $E_{b(elec)}/N_0$. For a unit reference optical power, $P_{(opt)} = 1W$ [92], it implies from (3.12) that $A = \pi$. Hence resulting $\alpha_{EO} = \pi^2/4$ for M-ary AC-FSK which is similar as the α_{EO} factor for M-ary U-FSK [30].

Fig. 3.12 illustrates simulation results of BER vs required $E_{b(opt)}/N_0$ performance comparison of M-ary AC-FSK with M-ary U-FSK and M-ary DC-FSK using an optimal TD ML receiver, considering $M = 16$. It can be seen in the Fig. 3.12 that M-ary AC-FSK scheme indicates better performance than M-ary DC-FSK scheme and also slightly better performance than M-ary U-FSK scheme in optical-domain in terms of BER vs $E_{b(opt)}/N_0$ which is compliant with the penalty factor analysis. It can be noticed that the difference in performance between, on one side AC-FSK/U-FSK, and on the other side DC-FSK is exacerbated in the optical-domain, due to the fact that $\alpha_{EO(AC)} = \alpha_{EO(U)} > \alpha_{EO(DC)}$ [30]. Electrical to optical power conversion is much more efficient for M-ary AC-FSK and M-ary U-FSK than M-ary DC-FSK.

In conclusion, M-ary AC-FSK is an interesting alternative to M-ary U-FSK since it exhibits slightly better energy efficiency for a given spectral efficiency, but with a reduced complexity into the receiver. In the sequel, we will extend the degrees of freedom of the proposed technique, by incorporating possible phase in the M-ary AC-FSK dictionary.

3.5 Proposed AC-FPSK Modulation Scheme

3.5.1 AC-FPSK Signaling

Time-Domain AC-FPSK Waveforms

AC-FPSK waveforms are derived from AC-FSK waveforms considering different phase shifts for each AC-FSK waveform. As a result, phase shift keying (PSK) is aggregated with AC-FSK to perform AC-FPSK signaling. We consider $M_{\perp}$ orthogonal odd frequency waveforms, and M_{ϕ} Gray coded phases shifts are added to each orthogonal odd frequency waveform. Therefore, we use the notation $(M_{\perp}, M_{\phi})$-AC-FPSK for the proposed modulation scheme, where $M_{\perp}$ and M_{ϕ} represent the number of orthogonal frequencies and phases, respectively. Complex phases are specified as $z_i = \exp(j\phi_i)$ with $\phi_i = 2\pi i/M_{\phi}$, and $i \in \{0, 1, \cdots, M_{\phi}-1\}$. We use Hermitian symmetric FD vector, $\boldsymbol{X}_{m,i}$, to generate the corresponding m-th activated frequency tone with $m \in \{1, 2, \cdots, M_{\perp}-1\}$, and having ϕ_i as the added phase shift. Afterwards, the inverse Discrete Fourier Transform (iDFT) is applied on $\boldsymbol{X}_{m,i}$ to attain a bipolar FPSK waveform. Subsequently, AC-FPSK waveform is obtained by clipping the negative part of the bipolar FPSK waveform. As we use only odd frequency waveforms, therefore, $\boldsymbol{X}_{m,i}$ can be defined as:

$$\boldsymbol{X}_{m,i} = [\underbrace{0}_{\text{DC}}, \underbrace{0, \cdots, 0, z_i, 0, \cdots, 0}_{2M_{\perp}-1}, 0, \underbrace{0, \cdots, 0, \overline{z_i}, 0, \cdots, 0}_{2M_{\perp}-1}]^{\text{T}}, \tag{3.36}$$

where $\overline{(\cdot)}$ denotes complex conjugate. The position of z_i in $\boldsymbol{X}_{m,i}$ is at index $2m-1$, while $\overline{z_i}$ is located at index $4M-2m+1$ to include the Hermitian symmetry. The size of the $\boldsymbol{X}_{m,i}$ vector is $M_{\text{c}} = 4M_{\perp}$. Initially, the bipolar FPSK waveforms are generated from $\boldsymbol{X}_{m,i}$ using iDFT as:

$$\boldsymbol{s}_{m,i}^{\text{FPSK}} = \frac{A}{2}\boldsymbol{F}_{M_{\text{c}}}^{-1}\boldsymbol{X}_{m,i}, \tag{3.37}$$

where A is the amplitude of the bipolar FPSK waveform and $\boldsymbol{F}_{M_{\text{c}}}^{-1}$ is M_{c}-order iDFT matrix [57]. In a vectorial form, the m-th activated frequency and the i-th added phase shift FPSK waveform can be expressed as, $\boldsymbol{s}_{m,i}^{\text{FPSK}} = \left[s_{m,i}^{\text{FPSK}}[1], s_{m,i}^{\text{FPSK}}[2], \cdots, s_{m,i}^{\text{FPSK}}[M_{\text{c}}]\right]^{\text{T}}$. The n-th discrete time sample of $\boldsymbol{s}_{m,i}^{\text{FPSK}}$, i.e., $s_{m,i}^{\text{FPSK}}[n]$, can be expressed as:

$$\begin{aligned} s_{m,i}^{\text{FPSK}}[n] &= A\cos(2\pi(2m-1)\Delta f(n-1)T_{\text{c}} + \phi_i) \\ &\quad n \in \{1, 2, \cdots, M_{\text{c}}\},\ m \in \{1, 2, \cdots, M_{\perp}\},\ i \in \{0, 1, \cdots, M_{\phi}-1\}, \end{aligned} \tag{3.38}$$

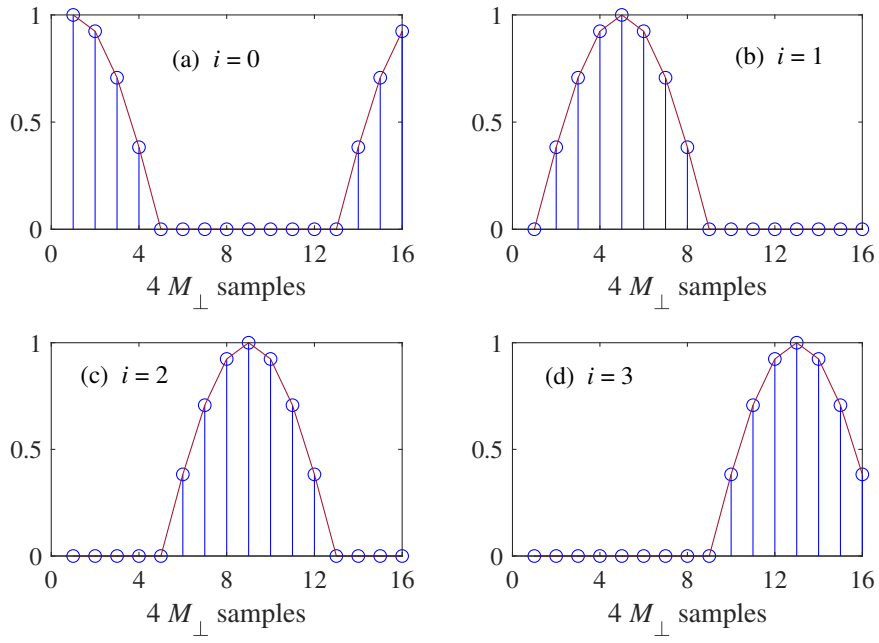

Fig. 3.13 TD representation of the $(M_\perp, M_\phi)$ AC-FPSK waveform for $(M_\perp, M_\phi) = (4,4)$, with $m = 1$ and $i \in \{0,1,2,3\}$.

where $\Delta f = 1/T_s$, is the frequency separation between two adjacent frequency waveforms with T_s being the symbol time, i.e., $T_s = M_c T_c$, while T_c represents the chip time. Finally, the m-th frequency and i-th phase shift AC-FPSK waveform, $\boldsymbol{s}_{m,i}^{\text{AC}-\text{FPSK}}$, is generated by clipping the negative samples of the bipolar FPSK waveform, $\boldsymbol{s}_{m,i}^{\text{FPSK}}$. The n-th discrete time sample of $\boldsymbol{s}_{m,i}^{\text{AC}}$, i.e., $s_{m,i}^{\text{AC}-\text{FPSK}}[n]$, can be expressed as:

$$\boldsymbol{s}_{m,i}^{\text{AC}-\text{FPSK}}[n] = \begin{cases} \boldsymbol{s}_{m,i}^{\text{FPSK}}[n] & \boldsymbol{s}_{m,i}^{\text{FPSK}}[n] \geq 0 \\ 0 & \boldsymbol{s}_{m,i}^{\text{FPSK}}[n] < 0 \end{cases}. \tag{3.39}$$

The size of the $(M_\perp, M_\phi)$-AC-FPSK dictionary, $\mathscr{D}^{\text{AC}-\text{FPSK}}$, is M, i.e., $M = M_\perp \times M_\phi$, while the number of bits per $(M_\perp, M_\phi)$-AC-FPSK waveform is n, i.e., $n = n_\perp + n_\phi$, where $n_\perp = \log_2(M_\perp)$ and $n_\phi = \log_2(M_\phi)$. We use the notation k to represent the frequency index of the unique waveform in $\mathscr{D}^{\text{AC}-\text{FPSK}}$, which depends on m and i as:

$$k = iM_\perp + m, \tag{3.40}$$

with $k \in \{1,2,\cdots,M\}$, $i \in \{0,1,\cdots,M_\phi - 1\}$ and $m = \{1,2,\cdots,M_\perp\}$. In the sequel, we will use the simplified notation $\boldsymbol{s}_k$ for $(M_\perp, M_\phi)$-AC-FPSK waveforms. In vectorial form, $\boldsymbol{s}_k$ can be defined as $\boldsymbol{s}_k = [s_{m,i}[1], s_{m,i}[2], \cdots, s_{m,i}[M_c]]^{\text{T}}$. Fig. 3.13 illustrates the TD $(M_\perp, M_\phi)$-AC-FPSK waveforms for $m = 1$, $(M_\perp = 4, M_\phi = 4)$, and $i = \{0,1,2,3\}$. It can be seen that four phases (i.e., $i = \{0,1,2,3\}$)

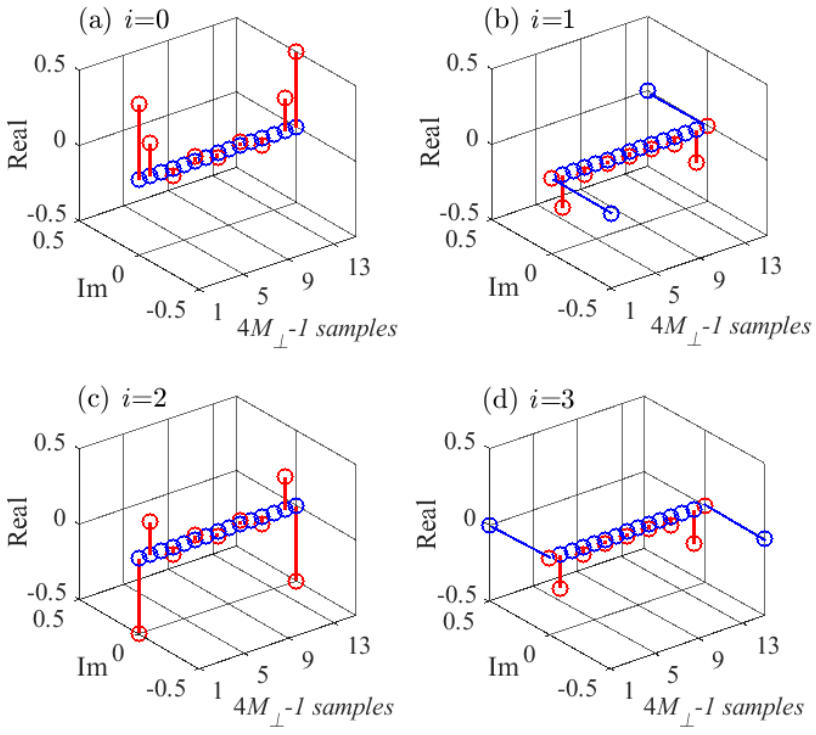

Fig. 3.14 $(M_\perp, M_\phi)$ AC-FPSK waveform spectra for $(M_\perp, M_\phi) = (4,4)$, $m = 1$ and $i \in \{0,1,2,3\}$. Real part of waveform spectrum is represented in red color and Imaginary (Im) part is represented in blue color.

are added to a single M-ary AC-FSK waveform ($m = 1$), according to the Gray coding, where two neighboured are differ by $\phi = 2\pi/4 = \pi/2$.

Frequency-Domain AC-FPSK Waveforms

Frequency-domain (FD) AC-FPSK waveforms, $\boldsymbol{S}_k$, can be obtained by applying M_c-order DFT on $\boldsymbol{s}_k$ as:

$$\boldsymbol{S}_k = \boldsymbol{F}_{M_c} \boldsymbol{s}_k, \tag{3.41}$$

where $\boldsymbol{F}_{M_c}$ denotes the M_c-order DFT matrix, defined in [57]. As we are generating $\boldsymbol{S}_k$ using DFT instead of DCT, there are real and imaginary parts in the spectra. Fig. 3.14 illustrates the real (in red color) and imaginary parts (in blue color) of $(M_\perp, M_\phi)$-AC-FPSK waveform spectra for $m = 1$, considering $(M_\perp = 4, M_\phi = 4)$, and $i \in \{0,1,2,3\}$. Note that the DC component is not considered in the spectra, therefore, $4M_\perp - 1$ samples can be seen for each waveform. Furthermore, we can see that a limited number of real and imaginary spectral lines (i.e., taps) have significant amplitudes, while most of the real and imaginary taps have negligible amplitudes. Intensive spectral study shows that around 99% of the AC-FPSK symbol energy is contained by only 4 taps (excluding DC tap) for

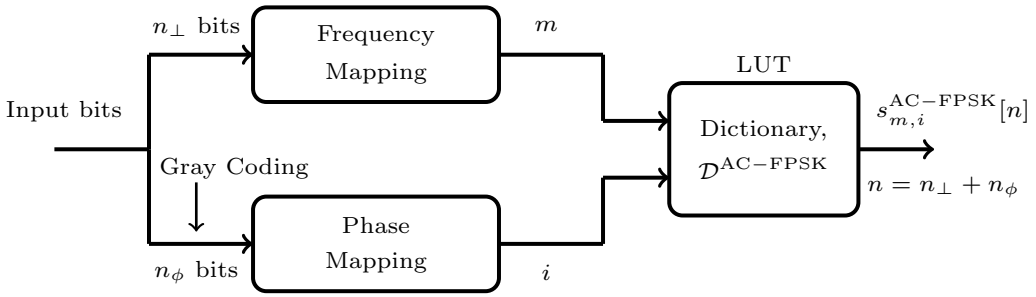

Fig. 3.15 Transmitter architecture of $(M_\perp, M_\phi)$-AC-FPSK.

real and imaginary spectra together. As presented in Sec. 3.1.2, M-ary AC-FSK is attained using inverse discrete cosine transform (iDCT), in which a single phase, $\phi = 0$, is considered. The M-ary AC-FSK spectra in Fig. 3.2 are compliant with the AC-FPSK spectra in Fig. 3.14, because DCT is used for generating FD waveform for M-ary AC-FSK, that is leading to the waveform spectrum without Hermitian symmetry. Thus, around 99% of symbol energy for M-ary AC-FSK FD waveform is contained by only 2 taps (excluding DC tap), while for FD AC-FPSK, 4 taps (2 real and 2 imaginary taps) contain the 99% of the symbol energy.

3.5.2 AC-FPSK Transmitter

Fig. 3.15 predicts the transmitter architecture of $(M_\perp, M_\phi)$-AC-FPSK. The m-th frequency waveform is chosen using $n_\perp$ bits, while the phase shift is added using n_ϕ bits according to the Gray coding. The $(M_\perp, M_\phi)$-AC-FPSK waveforms, $\boldsymbol{s}_{m,i}^{\text{AC-FPSK}} \in \mathscr{D}^{\text{AC-FPSK}}$, are chosen from $n = n_\perp + n_\phi$ input bits and are stored in the LUT. $\{m, i\}$ identifies the waveform, $\boldsymbol{s}_{m,i}^{\text{AC-FPSK}}$, to generate from the LUT.

3.5.3 AC-FPSK Symbol Energy

$(M_\perp, M_\phi)$-AC-FPSK waveforms are generated from conventional bipolar $2M$-FPSK waveforms by clipping negative samples of the odd frequency waveforms. As the negative part of each FPSK waveform (half of each waveform) is clipped to generate $(M_\perp, M_\phi)$-AC-FPSK waveform. All the $(M_\perp, M_\phi)$-AC-FPSK waveforms, $\boldsymbol{s}_k \in \mathscr{D}^{\text{AC-FPSK}}$, have the same electrical symbol energy, $E_{\text{s(elec)}}^{\text{AC-FPSK}}$, which can be computed as:

$$E_{\text{s(elec)}}^{\text{AC-FPSK}} = \|\boldsymbol{s}_k\|^2 = \frac{A^2}{4} T_\text{s}, \tag{3.42}$$

3.5.4 AC-FPSK Spectral Efficiency

The data rate of $(M_\perp, M_\phi)$-AC-FPSK is $R_\text{b}^{\text{AC-FPSK}} = n/T_\text{s}$ with $n = (n_\perp + n_\phi)$ bits per waveform and $T_\text{s} = M_\text{c} T_\text{c} = 4M_\perp T_\text{c}$. Furthermore, the occupied bandwidth, $B^{\text{AC-FPSK}}$, for $(M_\perp, M_\phi)$-AC-FPSK is $B^{\text{AC-FPSK}} \approx 2M_\perp \Delta f = 2M_\perp / T_\text{s}$ (neglecting out-of-band harmonics generated due to clipping [52] [47]). Therefore, the spectral efficiency for $(M_\perp, M_\phi)$-AC-FPSK, $\eta^{\text{AC-FPSK}}$, can be expressed using

(2.12) as:

$$\eta^{\text{AC-FPSK}} = \frac{R_{\text{b}}^{\text{AC-FPSK}}}{B^{\text{AC-FPSK}}} = \frac{M_\phi \log_2(M)}{2M}. \tag{3.43}$$

with $M = M_\perp \times M_\phi$. From (3.43), it can be seen that $\eta^{\text{AC-FPSK}}$ increases by increasing M_ϕ due to the addition of the phases, while keeping $M_\perp$ constant. On the contrary, $\eta^{\text{AC-FPSK}}$ decreases by increasing $M_\perp$, while keeping M_ϕ constant. From (3.21) and (3.43), it can be seen that $\eta^{\text{AC-FPSK}}$ increases by a factor of M_ϕ as compared to $\eta^{\text{AC-FSK}}$ due to the addition of phases, ϕ_i. At the same time, $\eta^{\text{AC-FPSK}}$ decreases by a factor of 2 due to the use of iDFT in the generation of $(M_\perp, M_\phi)$-AC-FPSK waveforms instead of iDCT used for the generation of M-ary AC-FSK waveforms. It should be noticed that using iDFT, the spectral separation between two adjacent frequencies is double as compared to the iDCT to maintain orthogonality between frequency waveforms in the dictionary, i.e., $\Delta f = 1/T_{\text{s}}$ for $(M_\perp, M_\phi)$-AC-FPSK [88], whereas $\Delta f = 1/2T_{\text{s}}$ for M-ary AC-FSK [52].

3.5.5 Minimum Squared Euclidean Distance between $(M_\perp, M_\phi)$-AC-FPSK Waveforms

For $(M_\perp, M_\phi)$-AC-FPSK, the squared Euclidean distance between waveform pairs, $(\boldsymbol{s}_k; \boldsymbol{s}_{k'})$, with $k \neq k'$, can be computed using (2.8) as:

$$\begin{aligned} d_{k,k'}^2 &= \|\boldsymbol{s}_k - \boldsymbol{s}_{k'}\|^2 \\ &= 2E_{\text{s(elec)}}^{\text{AC-FPSK}} - 2\Re\langle \boldsymbol{s}_k, \boldsymbol{s}_{k'} \rangle. \end{aligned} \tag{3.44}$$

From (3.44), the minimum squared Euclidean distance, $d_{\text{min,AC-FPSK}}^2$, between waveform pairs, $(\boldsymbol{s}_k; \boldsymbol{s}_{k'})$, for $(M_\perp, M_\phi)$-AC-FPSK can be computed by determining the maximum inner product, $\langle \boldsymbol{s}_k, \boldsymbol{s}_{k'} \rangle_{\max}$. Note that the clipping process in the generation of $(M_\perp, M_\phi)$-AC-FPSK waveform affects the orthogonality between $(M_\perp, M_\phi)$-AC-FPSK waveform pairs, $(\boldsymbol{s}_k; \boldsymbol{s}_{k'})$, and the inner product, $\langle \boldsymbol{s}_k, \boldsymbol{s}_{k'} \rangle$, is no longer null. Therefore, it is feasible to find an upper bound for the inner product, $\langle \boldsymbol{s}_k, \boldsymbol{s}_{k'} \rangle$, that defines the minimum squared Euclidean distance, $d_{\text{min,AC-FPSK}}^2$, in (3.44). We found in simulations that the maximum inner product, $\langle \boldsymbol{s}_k, \boldsymbol{s}_{k'} \rangle_{\max}$, can be approximated for $k \neq k'$ as:

$$\langle \boldsymbol{s}_k, \boldsymbol{s}_{k'} \rangle_{\max} \approx \begin{cases} 0.5E_{\text{s(elec)}} & \text{for } M_\phi = 2,4 \\ 2E_{\text{s(elec)}} \cos\left(\frac{2\pi}{M_\phi}\right) & \text{for } M_\phi \geq 8 \end{cases}. \tag{3.45}$$

Using (3.45) in (3.44), $d_{\text{min,AC-FPSK}}^2$ can be expressed as:

$$d_{\text{min,AC-FPSK}}^2 \approx \begin{cases} E_{\text{s(elec)}}^{\text{AC-FPSK}} & \text{for } M_\phi = 2,4 \\ 2E_{\text{s(elec)}}^{\text{AC-FPSK}} \left[1 - \cos\left(\frac{2\pi}{M_\phi}\right)\right] & \text{for } M_\phi \geq 8 \end{cases}. \tag{3.46}$$

(3.46) can be simplified by introducing $\gamma^{\text{AC-FPSK}}$ as:

$$d_{\text{min,AC-FPSK}}^2 = 2\gamma^{\text{AC-FPSK}} E_{\text{s(elec)}}^{\text{AC-FPSK}}, \tag{3.47}$$

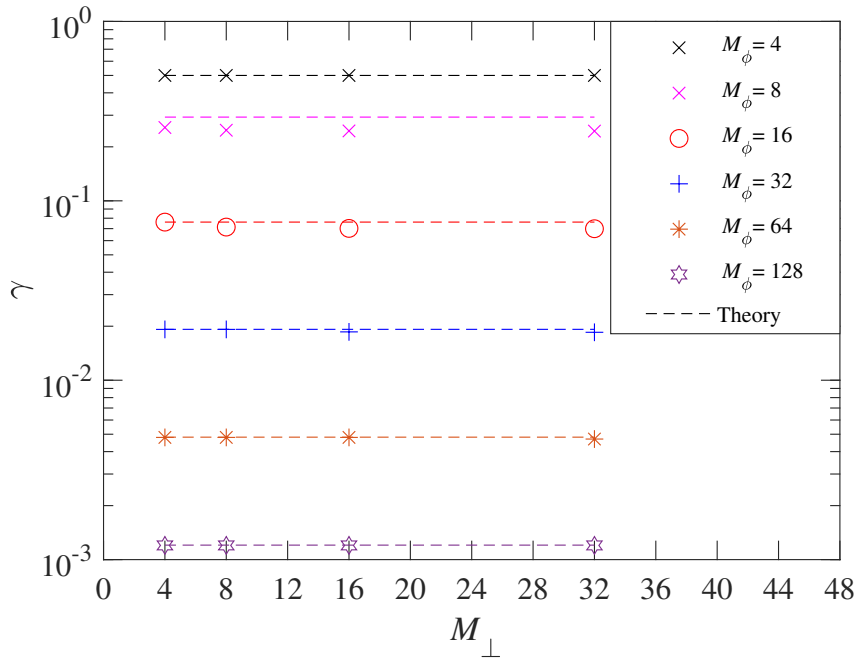

Fig. 3.16 Simulation of $\gamma^{\mathrm{AC-FPSK}}$ with respect to $M_\phi \geq 4$ considering different $M_\perp$ for $(M_\perp, M_\phi)$-AC-FPSK. Theoretical approximation for γ in (3.48) is reported using dash-line for each M_ϕ.

where $\gamma^{\mathrm{AC-FPSK}}$ is the penalty factor on $d^2_{\mathrm{min,AC-FPSK}}$, which is induced due to the loss of orthogonality for $(M_\perp, M_\phi)$-AC-FPSK waveforms. $\gamma^{\mathrm{AC-FPSK}}$ can be expressed as:

$$\gamma^{\mathrm{AC-FPSK}} \approx \begin{cases} 0.5 & \text{for } M_\phi = 2,4 \\ 1-\cos\left(\frac{2\pi}{M_\phi}\right) & \text{for } M_\phi \geq 8 \end{cases}. \tag{3.48}$$

Fig. 3.16 illustrates the simulation result of $\gamma^{\mathrm{AC-FPSK}}$ for $M_\phi \geq 4$ using the maximum inner product, $\langle \boldsymbol{s}_k, \boldsymbol{s}_{k'} \rangle_{\max}$, numerical computation, while theoretical approximation of $\gamma^{\mathrm{AC-FPSK}}$ evaluated in (3.48) is also presented with dash-line for each M_ϕ. From Fig. 3.16, it is confirmed that $\gamma^{\mathrm{AC-FPSK}}$ is independent on $M_\perp$, which is in-line with the $\gamma^{\mathrm{AC-FPSK}}$ theoretical approximation evaluated in (3.48).

Fig. 3.17 represents a heat-map of the normalized squared Euclidean distance, $d^2_{k,k'}/2E^{\mathrm{AC-FPSK}}_{\mathrm{s(elec)}}$, between waveform pairs, $(\boldsymbol{s}_k, \boldsymbol{s}_{k'})$, for $(4,4)$-AC-FPSK. From Fig. 3.17, it is confirmed that $\gamma^{\mathrm{AC-FPSK}} = 0.5$ for $M_\phi = 4$, which is in-line with (3.48). Furthermore, it can also be observed that for any $(4,4)$-AC-FPSK waveform, $\boldsymbol{s}_k$, with $k \in \{1,2,\cdots, M_\perp M\phi\}$, $\gamma^{\mathrm{AC-FPSK}} = d^2_{\mathrm{min,AC-FPSK}}/2E^{\mathrm{AC-FPSK}}_{\mathrm{s(elec)}}$ is reached with 2 other AC-FPSK waveforms (they are not neighboured) (cf. Fig. 3.17, 2 black boxes per column). It means that for any AC-FPSK waveform, $\boldsymbol{s}_k$, only 2 other waveforms are at Euclidean distance corresponding to the minimum Euclidean distance, $d_{\min}$.

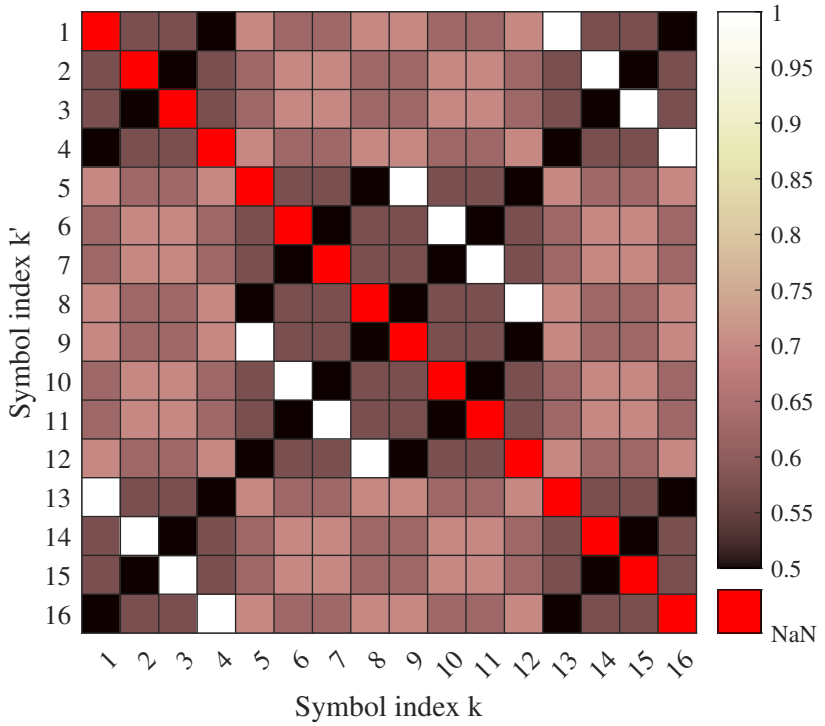

Fig. 3.17 Normalized squared Euclidean distance between $\boldsymbol{s}_k$ and $\boldsymbol{s}_{k'}$, $d_{k,k'}/2E_{\mathrm{s(elec)}}^{\mathrm{AC-FPSK}}$ for $k \neq k'$. NaN: Not a Number.

3.6 $(M_\perp, M_\phi)$-AC-FPSK Receivers

Considering an AWGN channel model, the TD received waveform, $\boldsymbol{r}$, corresponds to the transmitted waveform, ($\boldsymbol{s}_k$ or $\boldsymbol{s}_{m,i}$), contaminated by the ambient noise, $\boldsymbol{n}$, and can be expressed as:

$$\boldsymbol{r} = \boldsymbol{s}_{m,i} + \boldsymbol{n}, \tag{3.49}$$

where $\boldsymbol{n}$ is additive white Gaussian noise (AWGN) having mono-lateral power spectral density (PSD) of N_0. In vectorial form, $\boldsymbol{n}$ and $\boldsymbol{r}$ can be expressed as $\boldsymbol{n} = [n[0], n[1], \cdots, n[M_\mathrm{c}-1]]^\mathrm{T}$ and $\boldsymbol{r} = [r[0], r[1], \cdots, r[M_\mathrm{c}-1]]^\mathrm{T}$, respectively.

We consider three different types of receivers for $(M_\perp, M_\phi)$-AC-FPSK detection process, i.e., optimal TD ML receiver, sub-optimal (1-tap DFT) receiver and 2-tap harmonic receiver.

3.6.1 Optimal TD ML Receiver

Fig. 3.18 in (red/black) illustrates the optimal TD ML receiver architecture for $(M_\perp, M_\phi)$-AC-FPSK. As aforementioned in Sec. 3.5.3, all the $(M_\perp, M_\phi)$-AC-FPSK waveforms, $\boldsymbol{s}_k$, in the dictionary, $\mathscr{D}^{\mathrm{AC-FPSK}}$ have the same electrical symbol energy, $E_{\mathrm{s(elec)}}$, and are equi-probable (i.e., the probability of sending $\boldsymbol{s}_k$ is $p(\boldsymbol{s}_k) = 1/M_\perp M_\phi$). Under these conditions, the ML criterion identifies $\boldsymbol{s}_k$ in $\mathscr{D}^{\mathrm{AC-FPSK}}$ by using the maximum likelihood function, $p(\boldsymbol{r}|\boldsymbol{s}_k)$ [81], [88], where $p(\boldsymbol{r}|\boldsymbol{s}_k)$ is the conditional probability of

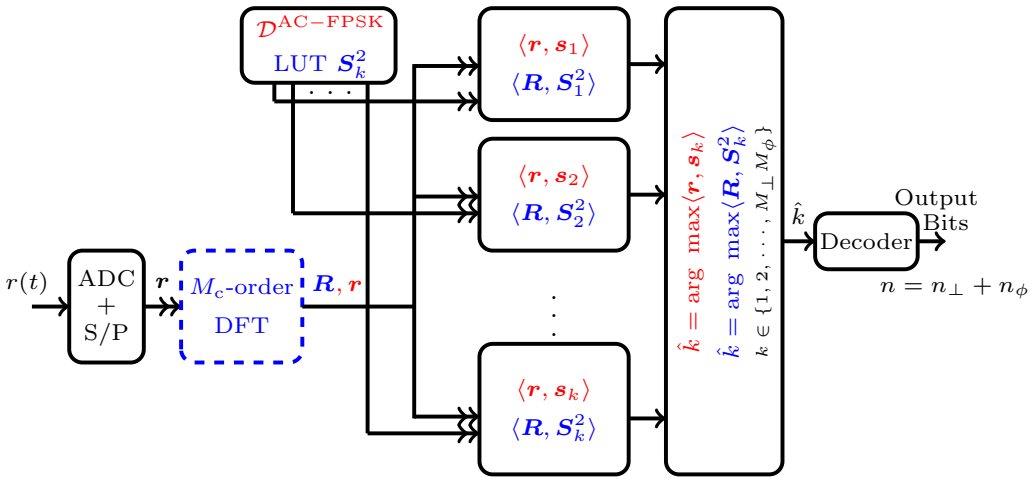

Fig. 3.18 Optimal TD ML receiver (red/black) and 2-tap harmonic receiver (blue/black) architecture for $(M_\perp, M_\phi)$-AC-FPSK.

observing $\boldsymbol{r}$, when $\boldsymbol{s}_k$ is sent. The likelihood function in an AWGN channel with variance, $\sigma^2 = N_0 B$, can be expressed as [86]:

$$\begin{aligned} p(\boldsymbol{r}|\boldsymbol{s}_k) &= \left(\frac{1}{2\pi\sigma^2}\right)^{M_c} \exp\left(-\frac{\|\boldsymbol{r}-\boldsymbol{s}_k\|^2}{2\sigma^2}\right) \\ &= \Gamma \exp\left(\frac{\langle \boldsymbol{r}, \boldsymbol{s}_k \rangle}{\sigma^2}\right), \end{aligned} \tag{3.50}$$

where $\Gamma = (1/2\pi\sigma^2)\exp(-(\|\boldsymbol{r}\|^2 - \|\boldsymbol{s}_k\|^2)/2\sigma^2)$, and $\|\boldsymbol{r}-\boldsymbol{s}_k\|^2 = \|\boldsymbol{r}\|^2 + \|\boldsymbol{s}_k\|^2 - 2\Re\langle \boldsymbol{r}, \boldsymbol{s}_k \rangle$. Here $\|\boldsymbol{r}\|^2$ and $\|\boldsymbol{s}_k\|^2 = E_{s_{(\text{elec})}}^{\text{AC-FPSK}}$, are constant for any k. Therefore, the symbol index k is identified using ML criterion by maximizing the TD cross-correlation between $\boldsymbol{r}$ and $\boldsymbol{s}_k \in \mathscr{D}^{\text{AC-FPSK}}$ as:

$$\hat{k} = \arg\max_k \langle \boldsymbol{r}, \boldsymbol{s}_k \rangle, \quad k \in \{1, 2, \cdots, M_\perp M_\phi\}. \tag{3.51}$$

3.6.2 Sub-optimal (1-tap DFT) Receiver

Fig. 3.19 illustrates the sub-optimal (1-tap DFT) receiver architecture for $(M_\perp, M_\phi)$-AC-FPSK. In the first step, M_c-order DFT is applied on $\boldsymbol{r}$ to attain FD received waveform, $\boldsymbol{R}$, as:

$$\boldsymbol{R} = \boldsymbol{F}_{M_c} \boldsymbol{r}, \tag{3.52}$$

where $\boldsymbol{R}$ in vectorial form is $\boldsymbol{R} = [R[0], R[1], \cdots, R[M_c - 1]]^{\mathrm{T}}$, and $\boldsymbol{F}_{M_c}$ is the M_c-order DFT matrix. Note that $\boldsymbol{R}$ encodes both the frequency and phase of the $(M_\perp, M_\phi)$-AC-FPSK waveform. Since, the estimated frequency index can be identified as:

$$\hat{m} = \arg\max_m \Big\{ |R[2m-1]| \Big\}, \quad m \in \{1, 2, \cdots, M\}, \tag{3.53}$$

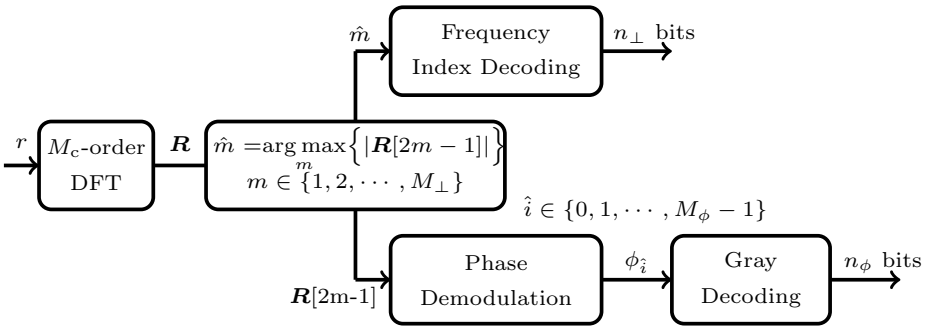

Fig. 3.19 Sub-optimal 1-tap DFT receiver architecture for $(M_\perp, M_\phi)$-AC-FPSK.

where $R[2m-1]$ represents the M_c-order DFT of $\boldsymbol{r}$, that is evaluated only at odd frequency indices $2m-1$. Due to the Hermitian symmetry of $\boldsymbol{R}$, the frequency index identification is realized only on the first $M_c/2$ samples of $\boldsymbol{R}$.

In the second step, the estimated phase index $\hat{i}$ is identified using phase discrimination on $R[2\hat{m}-1]$. Gray decoding is used to retrieve the bits encoded in ϕ_i. Finally, decoding of the estimated frequency index $\hat{m}$ and of the estimated phase $\hat{i}$ are operated to retrieve the transmitted bits.

3.6.3 2-tap Harmonic Receiver

Harmonic receiver evaluates the FD cross-correlation between the FD received waveform, $\boldsymbol{R}$, and all the FD AC-FPSK waveforms in the dictionary, $\mathscr{D}^{\text{AC-FPSK}}$, containing a limited number, L, of the spectral components (i.e., taps) with $L < M_c$ [81], [52]. It is demonstrated in Fig. 3.14 that the $(M_\perp, M_\phi)$-AC-FPSK waveforms spectra exhibit the Hermitian symmetry property. Furthermore, it can also be seen that for each waveform, only 4 taps containing around 99% of the symbol energy. Since, the noise at the receiver input is also a real signal, therefore, the cross-correlation in FD between $\boldsymbol{R}$ and FD AC-FPSK waveforms can be carried out over the first $M_c/2$ chips, without any penalty on signal-to-noise ratio (SNR) at FD correlator output.

The 2-tap harmonic receiver architecture for $(M_\perp, M_\phi)$-AC-FPSK is illustrated in Fig. 3.18, where the necessary operations are indicated in (blue/black). The harmonic receiver process consists of two main steps; in the first off-line step (to do only once), M_c-order DFT is applied on all $(M_\perp, M_\phi)$-AC-FPSK waveforms in $\mathscr{D}^{\text{AC-FPSK}}$ and then selecting the two most significant taps over the first $M_c/2$ chips of AC-FPSK FD waveforms (leaving aside the DC component), while the other samples are forced to zero. This leads to the generation of a new dictionary of M $\boldsymbol{S}_k^2$ frequency-domain waveforms, which are stored in a LUT. In the second online step (to do at symbol rate), FD received waveform, $\boldsymbol{R}$, is obtained by applying M_c-order DFT on $\boldsymbol{r}$ as in (3.52). Finally, the estimated frequency index $\hat{k}$ is identified by applying the FD cross-correlation between $\boldsymbol{R}$ and $\boldsymbol{S}_k^2$ as [52]:

$$\hat{k} = \arg\max_k \langle \boldsymbol{R}, \boldsymbol{S}_k^2 \rangle \quad k \in \{1, 2, \cdots, M_\perp M_\phi\}. \tag{3.54}$$

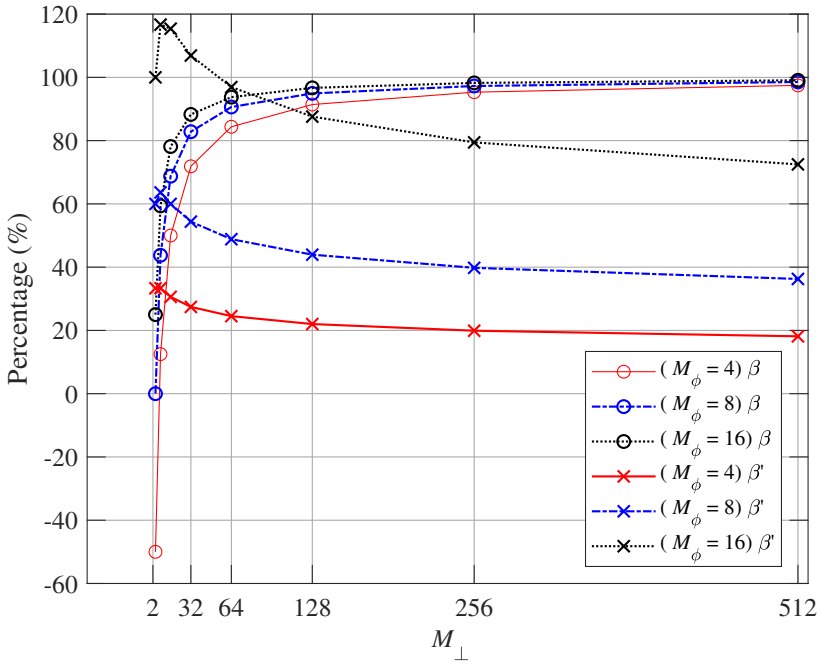

Fig. 3.20 Percentage (%) of complexity reduction, β for 2-tap harmonic receiver relative to the optimal TD ML receiver and percentage of complexity overhead, β' for 2-tap harmonic receiver relative to the 1-tap DFT receiver for $(M_\perp, M_\phi)$-AC-FPSK, considering different $M_\perp$ and M_ϕ.

3.6.4 Complexity Analysis for $(M_\perp, M_\phi)$-AC-FSK Receivers

Recall from Sec. 2.2.7 that the number of non-zero real multiplications consume more bits than the additions, therefore, only the number of non-zero real-multiplication can be considered in the computations of the receiver complexity.

TD ML receiver complexity: There are M waveforms in the dictionary, $\mathscr{D}^{\text{AC-FPSK}}$, i.e., $M = M_\perp \times M_\phi$, and each waveform consists of $M_c = 4M_\perp$ chips with half of the chips clipped to zero. Since optimal TD ML receiver realizes TD cross-correlations between receive signal, $\boldsymbol{r}$, and all the waveforms in the dictionary (i.e., M waveforms), therefore, optimal TD ML receiver requires $\mathscr{C}_{\text{TDML}} = 2M_\perp^2 M_\phi$, non-zero real multiplications.

1-tap DFT receiver complexity: Fast Fourier transform (FFT) algorithm is assumed to be used to implement the 1-tap DFT receiver, which requires $8M_\perp \log_2(4M_\perp)$ real multiplications. After frequency index identification which is based on FFT, phase demodulation is performed, which requires $4M_\phi$ real multiplications. Therefore, 1-tap DFT receiver overall requires $\mathscr{C}_{1-\text{tap}} = 8M_\perp \log_2(4M_\perp) + 4M_\phi$, non-zero real multiplications.

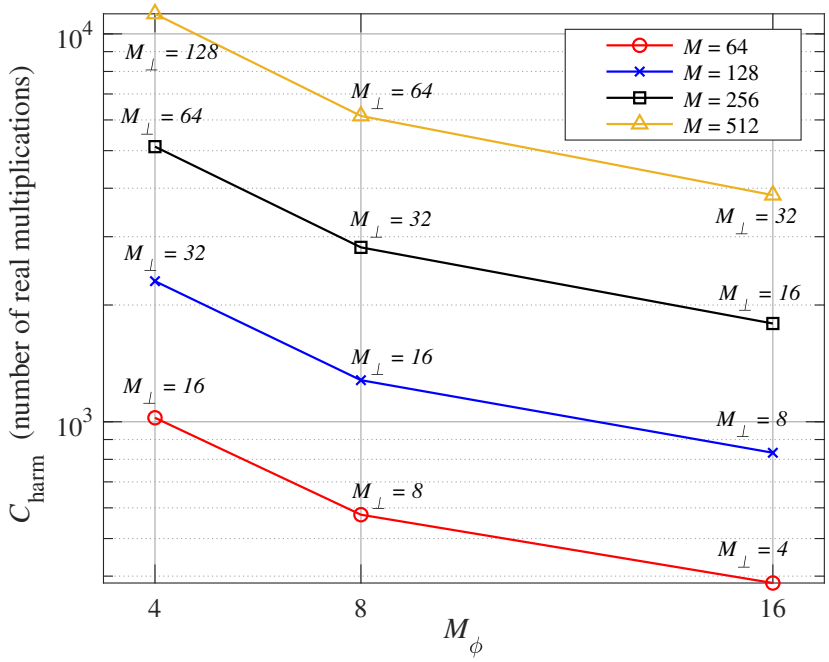

Fig. 3.21 Complexity of 2-tap harmonic receiver for $(M_\perp, M_\phi)$-AC-FPSK, $\mathscr{C}_{\text{harm}}$ for different modulation orders $M = M_\perp \times M_\phi$, varying M_ϕ and $M_\perp$.

2-tap harmonic receiver complexity: As aforementioned in Sec. 3.6.3, 2-tap harmonic receiver is also based on M_c-order DFT (assumed to be based on FFT algorithm) as the first stage, followed by $M = M_\perp \times M_\phi$, FD cross-correlations. For each FD correlation, 2 complex chips from FFT multiply with 2-taps (real or imaginary), which leads to a total of $4M_\perp M_\phi$ multiplications for $M_\perp M_\phi$ FD correlations. Therefore, 2-tap harmonic receiver overall requires $\mathscr{C}_{\text{harm}} = 8M_\perp \log_2(4M_\perp) + 4M_\perp M_\phi$, non-zero real multiplications.

Fig. 3.20 illustrates the complexity reduction, $\beta = (1 - \mathscr{C}_{\text{harm}}/\mathscr{C}_{\text{TDML}}) \times 100\%$, that computes the complexity reduction of 2-tap harmonic receiver as compared to the conventional optimal TD ML receiver, while the complexity overhead, $\beta' = (\mathscr{C}_{\text{harm}}/\mathscr{C}_{1-\text{tap}} - 1) \times 100\%$, that computes the the complexity overhead of 2-tap harmonic receiver relative to the 1-tap DFT receiver, for different $M_\perp$ and M_ϕ. It is confirmed from Fig. 3.20 that the complexity of 2-tap harmonic receiver is significantly reduced relative to the optimal TD ML receiver. This complexity reduction is almost 95% for $M_\perp = 512$, irrespective of M_ϕ. On the other hand, a moderate complexity overhead for 2-tap harmonic receiver relative to the 1-tap DFT receiver can be seen in Fig. 3.20, i.e., not more than 40% complexity overhead for $M_\perp = 512$ and $M_\phi \leq 8$.

Fig. 3.21 illustrates the evolution of 2-tap harmonic receiver complexity for $(M_\perp, M_\phi)$-AC-FPSK, considering different alphabet cardinalities, $M = M_\perp \times M_\phi$, as a function of $M_\perp$ and M_ϕ. From Fig. 3.21, it can be seen that 2-tap harmonic receiver complexity can be reduced by increasing M_ϕ for

a given M. Since $M = M_{\perp} \times M_{\phi}$, $M_{\perp}$ can be reduced by increasing M_{ϕ} while keeping M constant, leading to a reduction of DFT order (and related FFT order). Since FFT computation has the largest contribution in harmonic receiver complexity, increasing M_{ϕ} (while keeping M constant) leads to a decrease of the overall 2-tap harmonic receiver complexity.

3.7 Bit Error Probability for AC-FPSK

The theoretical bit error probability expression for M-ary AC-FSK is presented in Sec. 3.3, which is derived from the theoretical bit error probability expression for ML detection of conventional bipolar M-ary FSK using AWGN channel [57]. The same procedure can be adapted for the derivation of theoretical bit error probability expression for $(M_{\perp}, M_{\phi})$-AC-FPSK.

3.7.1 Upper bound for Theoretical Bit Error Probability

The minimum squared Euclidean distance, $d^2_{\text{min,AC-FPSK}}$, between AC-FPSK waveforms in $\mathscr{D}^{\text{AC-FPSK}}$, is approximated in Sec. 3.5.5 (cf. (3.46)). An upper bound for AC-FPSK theoretical bit error probability, P_{e}^{ub}, can easily be obtained by supposing that the squared Euclidean distance between any AC-FPSK waveform pair is $d^2_{\text{min,AC-FPSK}}$, and then substituting d^2_{min} with $d^2_{\text{min,AC-FPSK}}$ found for AC-FPSK in the conventional M-ary FSK bit error probability expression [57], leading to:

$$\begin{aligned} P_{\text{e}}^{\text{ub}} = & \frac{M}{2\sqrt{2\pi}(M-1)} \int_{-\infty}^{+\infty} \left[1-(1-Q(x))^{M-1}\right] \\ & \times \exp\left(-\frac{1}{2}\left(x-\sqrt{2\frac{E_{\text{s(elec)}}^{\text{AC-FPSK}}}{N_0}\gamma}\right)^2\right) \text{d}x, \end{aligned} \tag{3.55}$$

where $Q(\cdot)$ is the Gaussian Q-function [57], and $E_{\text{s(elec)}}^{\text{AC-FPSK}} = \log_2(M) E_{\text{b(elec)}}^{\text{AC-FPSK}}$. The term $(1-Q(x))^{M-1}$ represents the contribution of the $M-1$ neighboured waveforms into the bit error probability, while it is assumed that all the $M-1$ neighboured waveforms are at a squared Euclidean distance, $d^2_{\text{min,AC-FPSK}}$. As a consequence, (3.55) is an approximated upper bound for AC-FPSK bit error probability since it has been shown in Fig. 3.17 that only a limited number of AC-FPSK waveform pairs show a squared Euclidean distance, d^2, equal to $d^2_{\text{min,AC-FPSK}}$.

3.7.2 Lower bound for Theoretical Bit Error Probability

Fig. 3.17 illustrates that only a limited number, N, of $(M_{\perp}, M_{\phi})$-AC-FPSK waveform pairs show the squared Euclidean distance, $d^2_{\text{min,AC-FPSK}}$. Therefore, a lower bound for theoretical bit error

probability expression for $(M_{\perp}, M_{\phi})$-AC-FPSK can be obtained as:

$$P_{\mathrm{e}}^{\mathrm{lb}} = \frac{M}{2\sqrt{2\pi}(M-1)} \int_{-\infty}^{+\infty} \left[1-(1-Q(x))^{N}\right] \times \exp\left(-\frac{1}{2}\left(x-\sqrt{2\frac{E_{\mathrm{s(elec)}}^{\mathrm{AC-FPSK}}}{N_0}\gamma}\right)^{2}\right)\mathrm{d}x, \tag{3.56}$$

where the term $(1-Q(x))^{N}$ represents the contribution of the N closest AC-FPSK neighboured waveforms at squared Euclidean distance, $d^2_{\mathrm{min,AC-FPSK}}$. As a result, (3.56) is an approximated lower bound for AC-FPSK bit error probability, considering $N = 2$. Note that all the neighbouring AC-FPSK waveforms that are located at a squared Euclidean distance, d^2, which is larger than $d^2_{\mathrm{min,AC-FPSK}}$ are neglected in the bit error probability computation.

3.8 Simulation Results of $(M_{\perp}, M_{\phi})$-AC-FPSK

In this section, we present the simulation results along with the theoretical curves in (3.55) and (3.56) for the proposed $(M_{\perp}, M_{\phi})$-AC-FPSK scheme, and compare the simulation results with the state-of-the-art $(M_{\perp}, M_{\phi})$-DC-FPSK [88], and M-ary AC-FSK [52], OOK and M-ary PAM. We evaluate the following performance parameters:

- BER performance comparison between different receivers for $(M_{\perp}, M_{\phi})$-AC-FPSK in AWGN channel.
- BER performance comparison for $(M_{\perp}, M_{\phi})$-AC-FPSK vs the state-of-the-art $(M_{\perp}, M_{\phi})$-DC-FPSK, M-ary AC-FSK, OOK and M-ary PAM in AWGN channel.

3.8.1 BER Performance Comparison of $(M_{\perp}, M_{\phi})$-AC-FPSK versus $(M_{\perp}, M_{\phi})$-DC-FPSK considering different Receivers

Fig. 3.22 illustrates the BER versus required $E_{\mathrm{b(elec)}}/N_0$ performance comparison of $(M_{\perp}, M_{\phi})$-AC-FPSK versus the state-of-the-art $(M_{\perp}, M_{\phi})$-DC-FPSK [88], using optimal TD ML receiver, 1-tap DFT receiver and 2-tap harmonic receiver (Harm Rx), considering an AWGN channel and $M_{\perp} = 16$, $M_{\phi} = 4$. Note that the theoretical upper and lower bounds, respectively presented in (3.55) and (3.56) for bit error probability are also plotted in Fig. 3.22. It can be observed that both the conventional receivers, i.e., optimal TD ML receiver and 1-tap DFT receiver for $(M_{\perp}, M_{\phi})$-AC-FPSK have around 2 dB better BER vs $E_{\mathrm{b(elec)}}/N_0$ performance than their counter-parts for $(M_{\perp}, M_{\phi})$-DC-FPSK to reach a BER = 10^{-4}. Furthermore, it can also be seen in Fig. 3.22 that the theoretical upper and lower bounds curves for AC-FPSK bit error probability show a relatively accurate range to estimate the bit error probability. For example, the difference in $E_{\mathrm{b(elec)}}/N_0$ for upper and lower bounds is around 1 dB at the BER = 10^{-5}. Moreover, Fig. 3.22 also depicts that BER vs required $E_{\mathrm{b(elec)}}/N_0$ performance

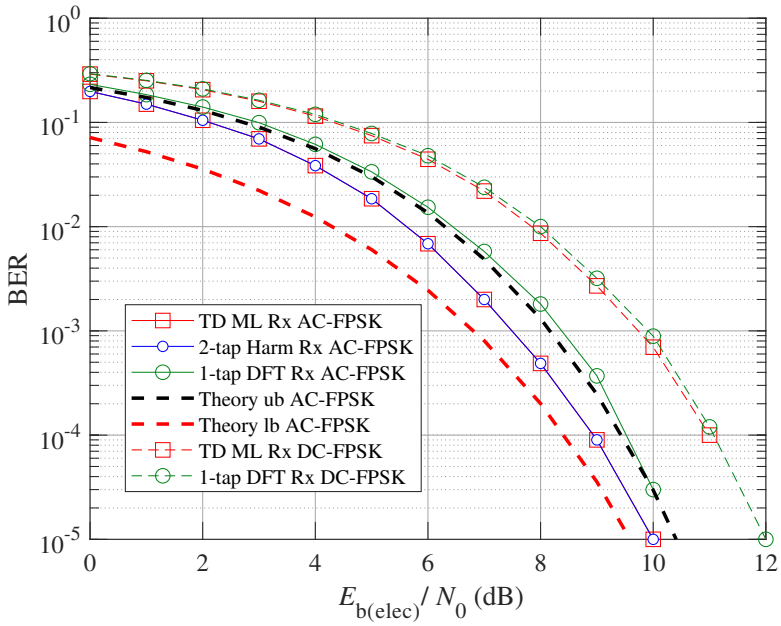

Fig. 3.22 Simulated BER performance against required $E_{b(elec)}/N_o$ for $(M_\perp, M_\phi)$-AC-FPSK versus $(M_\perp, M_\phi)$-DC-FPSK in AWGN channel, considering $M_\perp = 16, M_\phi = 4$. Lower and upper bounds for AC-FPSK theoretical bit error probability have been reported in dashed lines.

of the 2-tap harmonic receiver for $(M_\perp, M_\phi)$-AC-FPSK is exactly similar as the one of conventional optimal TD ML receiver, while the 1-tap DFT receiver for $(M_\perp, M_\phi)$-AC-FPSK shows degraded performance as compared to the 2-tap harmonic receiver by less than 1 dB at BER = 10^{-4}. In the following simulations, we will only consider the 2-tap harmonic receiver for AC-FPSK performance evaluation, because it shows exactly the similar performance as the optimal TD ML receiver with the benefit of reduced complexity.

3.8.2 Evaluation of Optimum M_ϕ for Energy Efficiency

Fig. 3.23 illustrates the simulation results for the required $E_{b(elec)}/N_0$ to target a BER $= 10^{-3}$ of the 2-tap harmonic receiver for $(M_\perp, M_\phi)$-AC-FPSK, considering different $M_\perp$ and M_ϕ. It can be seen from Fig. 3.23 that the optimum number of phases are $M_\phi = 4$ when $M_\perp \leq 32$ and $M_\phi = 8$ when $M_\perp > 32$, which minimizes the required $E_{b(elec)}/N_0$ (i.e., that maximises the energy efficiency) to reach a target BER $= 10^{-3}$. According to (3.43), the number of phases, M_ϕ, impacts the spectral efficiency, $\eta^{\text{AC-FPSK}}$. Therefore, it is important to find out the optimum number of phases, M_ϕ, that can achieve the best trade-off between energy efficiency and spectral efficiency. It is actually the purpose of the next sub-section.

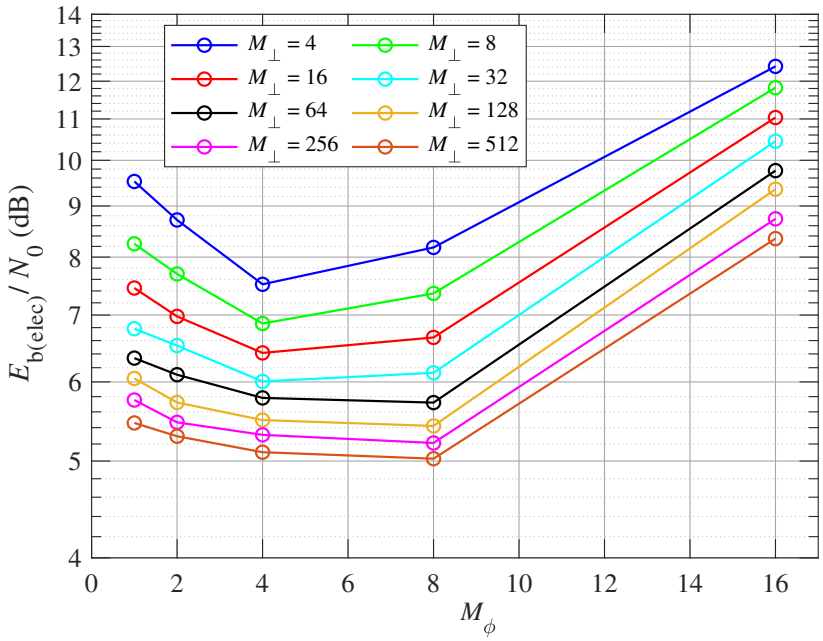

Fig. 3.23 Evaluation of necessary $E_{\mathrm{b(elec)}}/N_0$ to achieve a BER $= 10^{-3}$ for different M_ϕ and $M_\perp$, considering 2-tap harmonic receiver for $(M_\perp, M_\phi)$-AC-FPSK.

3.8.3 Spectral Efficiency versus Energy Efficiency Trade-off

Fig. 3.24 illustrates the spectral efficiency, η, versus the required $E_{\mathrm{b(elec)}}/N_0$ performance to achieve a BER $= 10^{-3}$ for $(M_\perp, M_\phi)$-AC-FPSK, M-ary AC-FSK, $(M_\perp, M_\phi)$-DC-FPSK, OOK and M-ary PAM, considering $M_\phi \in \{4, 8, 16\}$ and $M_\perp \in \{4, 8, 16, \cdots, 512\}$ for $(M_\perp, M_\phi)$-AC-FPSK and $(M_\perp, M_\phi)$-DC-FPSK, while $M \in \{4, 8, \cdots, 512\}$ and $M \in \{4, 8\}$ are considered for M-ary AC-FSK and M-ary PAM, respectively. Note that 2-tap harmonic receiver is used for AC-FPSK and AC-FSK [52], while TD ML receiver is used for DC-FPSK [88], OOK and M-ary PAM [30], [47]. From Fig. 3.24, it can be seen that for a target spectral efficiency $\eta = 10^{-1}$ bits/s/Hz, and considering $M_\phi = 4$, ($M_\perp$, 4)-AC-FPSK requires 2 dB lower $E_{\mathrm{b(elec)}}/N_0$ as compared to ($M_\perp$, 4)-DC-FPSK to reach a BER of 10^{-3}. This is due to the DC offset added in the generation of DC-FPSK waveforms in $\mathscr{D}^{\mathrm{DC-FPSK}}$, that increases the symbol energy requirements without increasing the minimum squared Euclidean distance, $d^2_{\mathrm{min,DC-FPSK}}$, between the waveform pairs [30]. Moreover, it can be observed in Fig. 3.24 that ($M_\perp$, 4)-AC-FPSK and ($M_\perp$, 8)-AC-FPSK have improved performance over conventional M-ary AC-FSK due to the increase of spectral efficiency of AC-FPSK as compared to the conventional M-ary AC-FSK (cf. 3.43), while the minimum squared Euclidean distance, $d^2_{\mathrm{min,AC-FPSK}}$, between AC-FPSK waveforms (cf. (3.46)) is not impacted for $M_\phi \leq 8$. Though, the spectral efficiency for $(M_\perp, M_\phi)$-AC-FPSK can be further increased by considering $M_\phi = 16$, but $(M_\perp, 16)$-AC-FPSK shows significant degradation in performance as compared to M-ary AC-FSK due to the strong reduction of

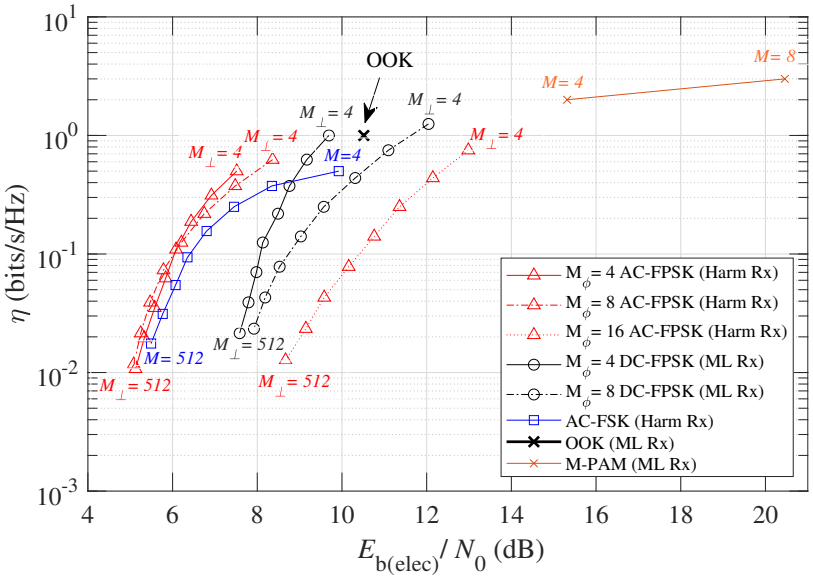

Fig. 3.24 Simulated spectral efficiency η versus required $E_{b(elec)}/N_0$ to achieve a BER $= 10^{-3}$ for $(M_\perp, M_\phi)$-AC-FPSK, M-ary AC-FSK, $(M_\perp, M_\phi)$-DC-FPSK for different M_ϕ and $M_\perp$.Simulation results for OOK and M-ary PAM are also reported.

the minimum squared Euclidean distance between $(M_\perp, 16)$-AC-FPSK waveforms, $d^2_{\min,AC-FPSK}$ (cf. Fig. 3.16). Lastly, it can be concluded from Fig. 3.24 that the optimum number of phases are $M_\phi = 4$ and 8 for $(M_\perp, M_\phi)$-AC-FPSK, depending on $M_\perp$ (i.e., on the target spectral efficiency) to reach the best spectral efficiency versus energy efficiency trade-off. For $M_\phi = 8$, a marginal improvement in terms of spectral efficiency versus energy efficiency trade-off can be achieved over $M_\phi = 4$, and it allows to reduce $M_\perp$ by a factor 2 for a given target $M = M_\perp \times M_\phi$. As aforementioned, $M_\perp$ has more weight than M_ϕ in 2-tap harmonic receiver complexity computation for $(M_\perp, M_\phi)$-AC-FPSK (cf. Fig. 3.21). Therefore, $M_\phi = 8$ is the best choice that reduces $M_\perp$ for a given target $M = M_\perp \times M_\phi$, and minimizes the harmonic receiver complexity and optimizes the spectral efficiency versus energy efficiency trade-off.

The spectral efficiency versus required $E_{b(elec)}/N_0$ performance of the M-ary PAM and OOK (OOK is a special case of M-ary PAM with $M = 2$) using ML receiver have also been reported in Fig. 3.24. From [30], [93], the spectral efficiency of the M-ary PAM is $\log_2(M)$(bits/s/Hz), and it is increasing with M, but the degraded BER performance of OOK and M-ary PAM as compared to $(M_\perp, M_\phi)$-AC-FPSK can be seen in Fig. 3.24.

Considering $M_\phi = 4$ and $M = 512$, complexity of 2-tap harmonic receiver for $(M_\perp, 4)$-AC-FPSK is found to be 83.3% larger than complexity of 2-tap harmonic receiver for M-ary AC-FSK [52], whereas considering $M_\phi = 8$ and for any M value, complexity of 2-tap harmonic receiver for $(M_\perp, 8)$-AC-FPSK is found to be strictly equal to the complexity of 2-tap harmonic receiver for M-ary

AC-FSK. This highlights the interest of AC-FPSK signaling, providing slightly improved performance over AC-FSK (considering large $M_{\perp}$ values), while maintaining an equivalent receiver complexity.

3.9 Conclusion

In the first part of the chapter, we have introduced a new FSK-based modulation scheme, called M-ary AC-FSK for energy efficient low data rate IoT applications. We compared the BER performance of the proposed M-ary AC-FSK with the state-of-the-art FSK-based modulation schemes, i.e., M-ary DC-FSK and M-ary U-FSK. In-fact M-ary AC-FSK is derived from the conventional $2M$-ary FSK by considering only odd frequency waveforms and clipping their negative samples to zero, in order to make them compatible with IM-DD OWC systems. Conventional receivers (i.e., optimal TD ML receiver with high complexity and sub-optimal 1-tap DCT-based receiver with low complexity) for M-ary AC-FSK are also presented. M-ary AC-FSK waveforms spectra reveal that only two harmonics (ignoring the DC tap) have significant amplitudes and contains most of the symbol energy. We highlighted that there exists a trade-off between the energy efficiency of the modulation scheme and conventional receivers complexity for M-ary AC-FSK. To alleviate this trade-off, we proposed a new FD 2-tap harmonic receiver for M-ary AC-FSK, that uses only 2 harmonics having maximum amplitudes, while its complexity is reduced drastically, i.e., the number of real multiplications becomes linearithmic with the dictionary size M, instead of being quadratic for conventional optimal TD ML receiver. Simulation results confirmed that M-ary AC-FSK has far better energy efficiency performance than M-ary DC-FSK in an AWGN channel, and a slight improvement for M-ary AC-FSK energy efficiency performance relative to the M-ary U-FSK is also observed. Furthermore, 2-tap harmonic receiver for M-ary AC-FSK shows the similar energy efficiency performance as the optimal TD ML receiver for M-ary AC-FSK/U-FSK, but with an extremely reduced complexity, comparable to the 1-tap DCT-based receiver.

In the second part of the chapter, we have introduced an extended version of M-ary AC-FSK by incorporating phase shift keying (PSK) into M-ary AC-FSK, resulting a new modulation scheme called $(M_{\perp}, M_{\phi})$-AC-FPSK for energy efficient OWC. We presented three different kinds of receivers for $(M_{\perp}, M_{\phi})$-AC-FPSK; (i) optimal TD ML receiver, (ii) sub-optimal 1-tap DFT receiver, and (iii) 2-tap harmonic receiver. 2-tap harmonic receiver is based on the FD AC-FPSK waveform analysis. Complexity analysis of the receivers for $(M_{\perp}, M_{\phi})$-AC-FPSK is also presented, it reveals that 2-tap harmonic receiver for $(M_{\perp}, M_{\phi})$-AC-FPSK shows a significant reduction in the complexity as compared to the optimal TD ML receiver, while achieving a similar performance. Minimum squared Euclidean distance between $(M_{\perp}, M_{\phi})$-AC-FPSK waveforms is also investigated, and the theoretical approximation for the lower and upper bounds on the bit error probability for ML detection are computed. Simulation results confirmed that the theoretical lower and upper bounds for bit error probability are near to the simulation BER results. Furthermore, the 2-tap harmonic receiver shows a similar BER performance as the optimal TD ML receiver, but with the benefit of a significant reduction of the complexity. Furthermore, the simulation results also confirm that the optimum number of phases

to attain the best energy efficiency vs spectral efficiency trade-off as compared to the state-of-the-art M-ary AC-FSK, and $(M_{\perp}, M_{\phi})$-DC-FPSK are $M_{\phi} = 4$ or 8. A good choice can be $M_{\phi} = 8$, because it leads to the lowest harmonic receiver complexity by reducing $M_{\perp}$ for a given targeted modulation size M, i.e., $M = M_{\perp} \times M_{\phi}$, which decreases the DFT order.

In the next chapter, an experimental demonstration of the proposed M-ary AC-FSK will be presented. The experimental setup using software defined radio (SDR), along with the experimental results for the proposed M-ary AC-FSK will be discussed in the next chapter, which is our published contribution in IEEE Journal [47].

Chapter 4

Experimental Analysis of AC-FSK for OWC System

Contents

This chapter is dedicated to the experimental implementation of the proposed M-ary AC-FSK. The experiments are performed in optical wireless line-of-sight (LOS) channel using a test bench, called Software Defined Radio (SDR). The test bench architecture is presented in Sec. 4.1, followed by the

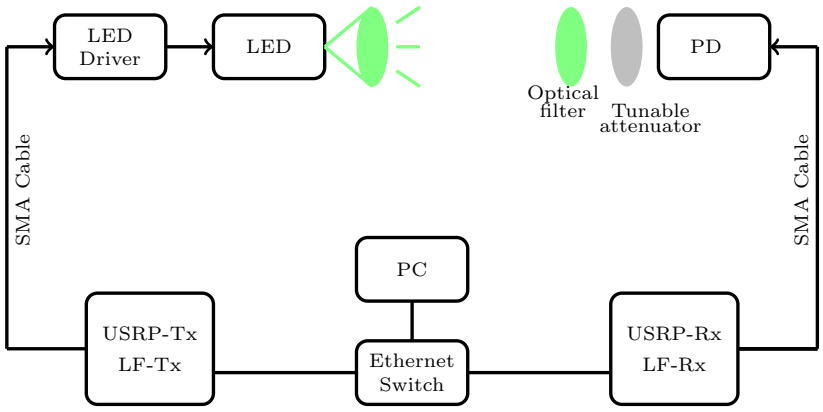

Fig. 4.1 Block diagram of the software defined radio (SDR) test bench architecture.

hardware specifications for the SDR (cf. Sec. 4.2 and Sec. 4.3). In Sec. 4.4, the real experimental test bench based on SDR is presented along with different parameters used in the experiment. Challenges faced in the experimental implementation and their appropriate solutions are discussed in Sec. 4.5. Experimental results for the proposed M-ary AC-FSK are presented in Sec. 4.6. Based on the experimental results, conclusions are rendered in Sec. 4.7.

4.1 Test Bench Architecture

Fig. 4.1 depicts the block diagram of the implementation of the software defined radio (SDR) for OWC systems. The architecture in Fig. 4.1 gives us a general overview of the working principle of the SDR for OWC systems. The test bench has been implemented on the RIESCO (Radio logIcielle pour l'Évaluation des Systèmes Complexes) platform in GIPSA-lab. The transmitter part is shown at the left-hand side, consisting of the LED, LED's driver and the universal software radio peripheral (USRP)-Tx, while the receiver part is shown at the right-hand side, consisting of the photodiode (PD), optical filter and the (USRP)-Rx. Transmitter and receiver parts are connected to each other by a desktop PC through an ethernet switch. Desktop PC is used for the frames generation consisting of the desired modulation waveforms, the demodulation process and the real-time BER computations.

The communication process starts from desktop PC. The baseband waveforms (M-ary orthogonal/biorthognal FSK-based waveforms) are first generated and modulated in a PC by using Matlab software tool. Initially, the information data to be transmitted in frames are created. Preamble symbols are added with the communicating data to allow for frame detection and easy time synchronization at receiver end. The generated frames are then uploaded in the file source block in GNU Radio software to interface with software defined radio (SDR) equipment USRP used as a transmitter (Tx). The frames are transmitted through RIESCO USRP-Tx repeatedly [94]. The LED's driver provides the forward current I_{F} (usually a few hundreds of mA) to the transmitter LED to provide intensity modulation and to avoid the clipping of the waveforms. Frames containing information data and

preamble symbols are send to LED through SMA cable in electrical form, then LED converts this electrical signal into an optical signal that is transmitted through the optical wireless channel.

The optical wireless channel is the optical line-of-sight (LOS) channel and the distance between the transmitter LED and the PD is fixed to 1 meter. The whole setup is fully covered with a box to avoid the unwanted parasitic lights to obtain repeatable measurement results.

At the receiver side, the received optical frames are detected by PD without any multi-path propagation. The PD converts the received optical signal into an electrical signal. The electrical low-pass filter is used to remove the unwanted and out of bandwidth signals from the received optical signal and pass it to the USRP-Rx through SMA cable. Finally, the desired information data is retrieved from the received frames using real-time demodulation with the real-time BER computations in the PC. Ethernet switch, supporting a maximum data rate of 1 Gbps, is used to connect the transmitter and receiver end to the PC.

4.2 Hardware Specifications for SDR

At Gipsa-Lab, the available SDR environment consists of RIESCO USRP-N210 and desktop PCs to perform experimental tests and prototyping.

4.2.1 SDR USRP-N210

Fig. 4.2 shows the universal software radio peripheral (USRP)-N210 used in our experiments. It is a tunable transceiver SDR device for designing, prototyping and deploying radio communication systems. The USRP-N210 provides the advantage of high bandwidth and high dynamic range processing capability. This device includes daughterboards, FPGA, 100 MS/s dual ADC, 400MS/s dual DAC and Gigabit Ethernet connectivity to send and receive data simultaneously from processor.

For N-series USRP, the platform setting process is easy and it is enable by IP Address. This device is widely used in research, industry, academia, wireless communication systems, electronic warfare & signal intelligence (SIGINT), radar etc.

4.2.2 Daughter-boards (Basic-Tx/Rx and LF-Tx/Rx)

Two types of daughter-boards can be used in USRP devices for our baseband OWC applications, i-e, Basix-Tx/Rx and LF-Tx/Rx. Basic-Tx is used in transmitter USRP to transmit signals and it provides transmission capability from 1 to 250 MHz for USRP. This board provides direct access to DAC output of USRP that is matched to 50 Ω SMA cable and to the internal resistance of LED driver [94]. Basic-Rx is used in receiver USRP, which provides direct access to the ADC inputs. The board can accept real-mode signals from 1 to 250 MHz for further processing. Both the Basic-Tx and Basic-Rx daughter-boards have the bandwidth, B, of 100 MHz/channel. The Basic-Tx/Rx daughter-board in USRP acts as a high pass filter (HPF), therefore, the DC and low frequency components (< a few hundreds of kHz) can not be generated by USRP-Tx, nor detected by USRP-Rx. DC signal necessary

Fig. 4.2 Universal Software Radio Peripheral (USRP)-N210 Device

for LED biasing is added externally by LED's driver in the form of I_{F}. The maximum sampling frequency, F_{s}, used is 25 MHz for ADC and DAC of the daughter-boards and over-sampling ratio (OSR) is fixed at the minimum allowable value of $K = 4$ according to the specifications.

For LF-Tx/Rx daughter-boards, LF-Tx is used at transmitter side in the same context as Basic-Tx and it allows transmission from 0 to 30 MHz. Hence, it includes an additional advantage of supporting DC component as well, while LF-Rx daughter-board is used at receiver side in the same context as Basic-Rx, it allows reception from 0 to 30 MHZ by including DC component as well. Both LF-Tx and LF-Rx daughter-boards have four frontends; i.e., Frontends A and B support real signals and Frontends AB and BA support complex signals. LF-Tx/Rx have bandwidth of 33 MHz for Frontends A and B while bandwidth of 66 MHz is available for Frontends AB and BA [94].

We used LF-Tx/Rx daughter-boards in our experimental setup because of additional advantage of supporting DC and low frequency components, which results the reduction in the BER and improving the performance.

4.2.3 Ethernet Switch

For experimental implementation, we used an Ethernet switch (Netgear XS708E) consisting of 8-ports that supports maximum data rate of 1 Gbps. It is used to connect USRP-Tx, USRP-Rx and a PC to provide communication link. Despite the fact that daugther-boards can support sampling frequencies of tens of megahertz, the 1 Gbps Ethernet switch is responsible for a drastic limitation in maximum sampling frequency, due to the encapsulation process of the Ethernet protocol. It has been found that the maximum sampling frequency that can be used by the aforementioned daugther-boards is limited at 25 MHz for ADC and DAC conversions.

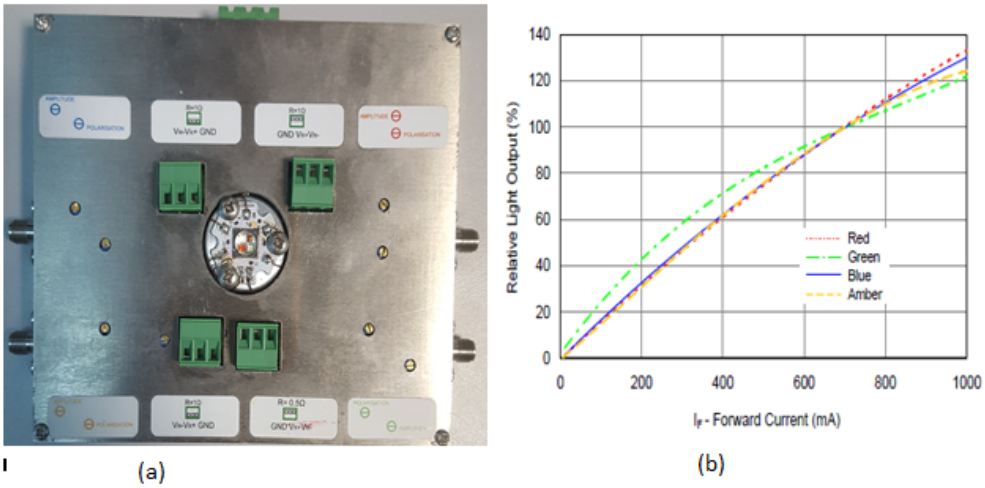

Fig. 4.3 (a) LED (LZA-00MA00) and driver, and (b) Typical light output vs froward current, I_F performance [Appendix A].

4.3 Hardware Specifications for OWC

4.3.1 LED and its Driver

A light-emitting diode (LED) is a semiconductor electrical device that emits incoherent light when electric current flows through it. In early ages LEDs were used only for lightning purpose but advanced research confirmed that LEDs can also be used as a transmitter in OWC systems [80]. The LED driver provides sufficient forward current, I_F, to the LED to set the required output optical power level of LED as depicted in Fig. 4.3 (b). It is preferable to set I_F in the linear region to avoid any kind of clipping of the transmitted waveforms.

For our experiment, we used a Red Green Blue Amber (RGBA) LED (LED Engin LZA-00MA00) as shown in Fig. 4.3 (a), that integrates 4 chips (one per colour), which provides maximum 10W optical power. The usable wavelength, λ, for red, green, blue and amber colours are 618 nm, 525 nm, 457 nm and 590 nm, respectively (cf. data sheet in Appendix A). By using LED driver, the forward current is set to $I_F = 200$ mA using amplitude knob, to operate the LED in a linear region and guarantee the clipped sample amplitude to the zero level optical intensity [47], [95].

4.3.2 Photodiode (PD)

In the SDR experimental setup, we used a Silicon PIN photodiode (PD) (Hamamatsu S10784) as shown in Fig. 4.4 (a), that supports the wavelength range from 190 to 1100 nm. The performance of PD can be better explained by photosensitivity, which can be defined as the ratio of the generated photo-current to the incident light power and it is expressed in A/W. Fig. 4.4 (b) represents the photosensitivity against wavelength, λ, which depicts that for larger wavelength light ($\lambda \leq 750$ nm),

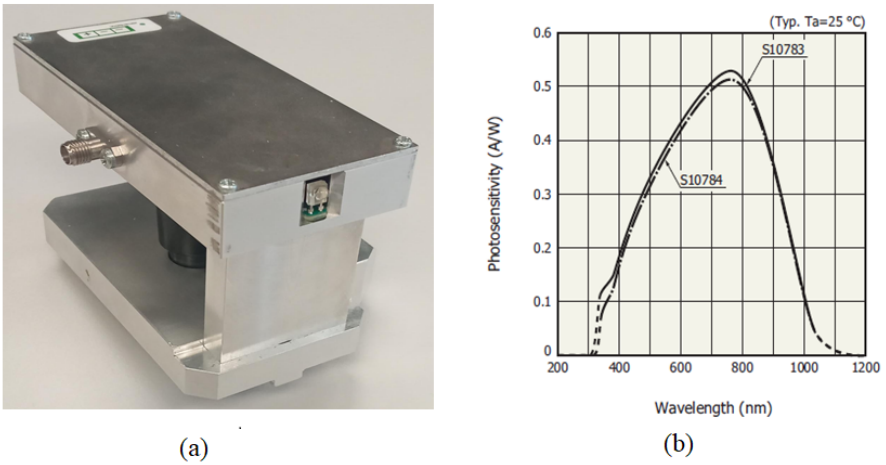

Fig. 4.4 (a) Silicon PIN Photodiode (PD) (Hamamatsu S10784) and (b) photosensitivity vs wavelength performance [Appendix B].

photosensitivity is larger and vice versa (cf. data sheet in Appendix B). The choice of the PD has been made to provide the highest photosensitivity in the visible light spectrum.

4.4 Experimental Test Bench

The experimental test bench for IM-DD OWC system is presented in [47], and it is shown in Fig. 4.5 (a). The test-bench is built from commercial off-the-shelf (COTS) devices [46]. The transmitter LED is shown in Fig. 4.5 (b), which uses a RGBA LED (LED Engin LZA-00MA00), that integrates 4 chips (one per colour). The LED viewing angle is 95° (full opening angle at 50% maximum intensity). We used the green colour in LED with an emitted wavelength, $\lambda = 525$ nm to transmit the desired signals in our experiment. LED driver sets a bias current, $I_F = 200$ mA in a relatively linear region of Light-Intensity (L-I) curve, and modulation depth is adjusted in such a way that guarantee the clipped samples amplitude of M-ary AC-FSK waveforms corresponds to the zero level optical intensity [47] [95]. The emitted surface power density, $\rho_{t(opt)}$, of the LED is evaluated as 1.7mW/cm^2. The transmitter LED and the receiver PD are fixed at a distance of 1 meter, while the line-of-sight (LOS) channel is used between them.

At the receiver end, a green optical filter (Thorlabs FD1D) is used to filter out the unwanted wavelengths from the ambient light. Afterward, a tunable optical attenuator (Thorlabs NDC-50C-2M-A) is used to tune the received optical power, $P_{r(opt)}$, depending on the angle of rotations (from 0° to 360°). It is followed by the silicon PIN photodiode (PD) (Hamamatsu S10784), which integrates a focusing lens, and it realizes direct conversion of the intensity modulation into electrical modulation. The PD effective photosensitive area is 7 mm^2, photosensitivity is approximately 0.35 A/W at $\lambda = 525$ nm and the PD electrical bandwidth is of about 200 MHz [47]. Then, a DC block is used to block any DC offset added due to the parasitic ambient light. Afterward, a low-pass filter (LPF) with a

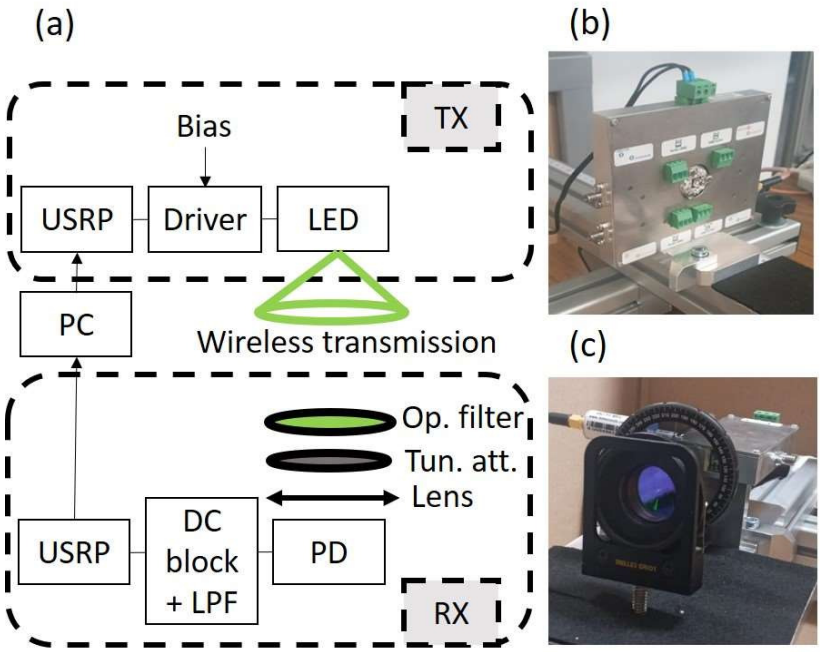

Fig. 4.5 Experimental setup for M-ary AC-FSK OWC system (a), LED transmitter (driver and LED) (b), receiver (c). Op. filter: optical filter, Tun. att.: tunable attenuator.

cut-of-frequency of 12 MHz is used, which act as an anti-aliasing filter to filter out frequencies above $F_s/2$, where F_s is the ADC sampling frequency. Finally, it is followed by SDR equipment (Ettus Research USRP N210), that performs the digital modulation and demodulation. The SDR (USRP N210) is interfaced with MATLAB software tool, that provides the modulator/demodulator signal processing implementation [96]. The real-time demodulation is performed in MATLAB tool to compare the BER performance of the proposed M-ary AC-FSK with the state-of-the-art M-ary U-FSK by implementing different receiver architectures (cf. Sec. 3.2). LF-Tx and LF-Rx daughter-boards are mounted on SDR USRP-N210 for digital-to-analog and analog-to-digital conversions, that can support $(0-30)$ MHz bandwidth.

Tab. 4.1 summarizes details about different parameter values used in the OWC experiment, such as, modulation size (M), USRP sampling frequency (F_s), oversampling ratio (K), modulation signal bandwidth (B), data rate (R_b) and the spectral efficiencies (η) for different M.

4.5 Challenges in SDR OWC Implementation

As the transmitter and the receiver are entirely separate physical devices, they do not share a common time or frequency reference, leading to the channel effect and timing synchronization issues.

Table 4.1 Experimental parameters to evaluate the performance of M-ary AC-FSK and M-ary U-FSK.

	AC-FSK / U-FSK	
Dictionary size, M	16	128
Sampling Frequency, F_s (MHz)	25	25
Oversampling Ratio, K	4	4
Bandwidth, B (MHz)	3.125	3.125
Data Rate, R_b (Mbit/s)	0.78	0.17
Spectral Efficiency, η (bit/s/Hz)	0.25	5.4×10^{-2}

4.5.1 Synchronization

In wireless communication system, information data is exchanged randomly between the transmitter and receiver. Hence, it becomes difficult for the receiver to identify the starting and ending of the information frame, which causes the timing frame synchronization issue. To overcome this issue, a preamble sequence called pseudo-random sequence or m-sequence [97] is added at the beginning of information data, that makes a complete frame to contain m-sequence and information data. At the receiver end, an auto-correlation process is applied between m-sequence and the received frames, and then the time index for the maximum of auto-correlation is identified, that corresponds to the starting of information data.

Pseudo-random sequence or m-sequence is a binary sequence of length $l = 2^m - 1$ with $m \in \{2, 3, \cdots, 8\}$ [97]. Several lengths of m-sequences are possible and used in communication systems, i.e., 3, 7, 15, 31, 63, 127 and 255. Each sequence has its own applications. In our experiments, we have chosen the m-sequence of length = 127 as shown below. The reason behind choosing larger length m-sequence is the accuracy because if the length of the m-sequence is increasing, the auto-correlation value is increasing too. However, increasing to much the m-sequence length induces a longer frame length, which leads to memory issues.

$$m-\text{sequence} = \begin{cases} 0000001000001100001010001111001000101100111010100111110100 \\ 0011100010010011011010110111101100011010010111011100110010 \\ 10101111111 \end{cases}$$

Auto-correlation or Cross-correlation

Auto-correlation or cross-correlation is the measure of the similarity of two sequences or two series of one relative to the other as a function of displacement [97]. It is also called sliding dot product or inner product. It is basically the convolution of two functions or signals (after having temporally reversed one of the two signals) and is mainly used for searching long signal, fault detection, starting

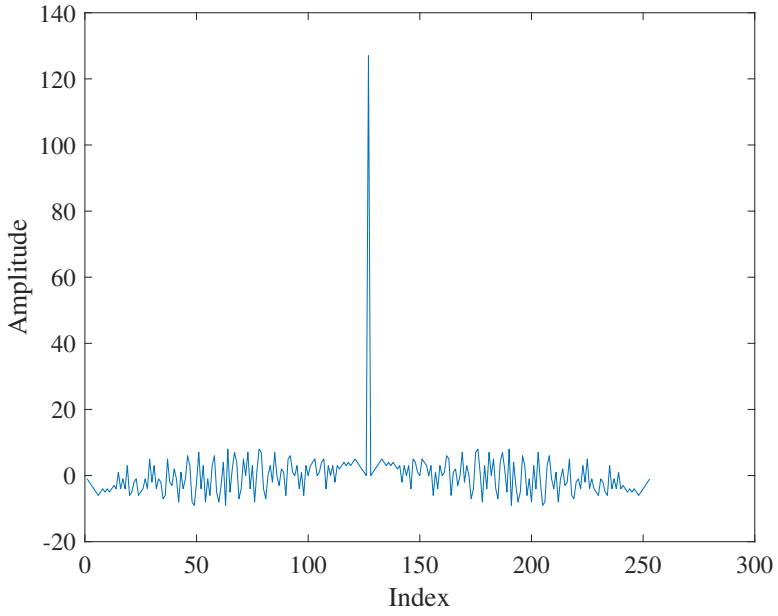

Fig. 4.6 Autocorrelation of m-sequence of length $l = 127$.

index of frame, range etc. Auto-correlation is always applied to the similar signals or sequences, it always results a peak at a lag of zero and its size defines the signal energy.

In SDR OWC experiments, cross-correlation is applied between the m-sequence and the received frames (containing the m-sequence at start of the frames) to identify the starting index of the information data. As an example, Fig. 4.6 depicts the cross-correlation between two m-sequences of length $l = 127$. Hence, the index of the maximum amplitude (cross-correlation amplitude is equal to L), identifies the starting index of the information data.

4.6 Experimental Results

Experiments are performed using the SDR test bench (USRP-N210) shown in Fig. 4.5, with an optical line-of-sight (LOS) channel. The pre-defined modulation is performed at the transmitter side, and real-time demodulation at the receiver side. BER measurements are realized by counting at least 100 bit errors to ensure sufficient BER accuracy [47].

4.6.1 Channel Response

We estimate the channel response of the SDR test bench presented in Fig. 4.5 by considering conventional M-ary FSK waveforms with carrier frequency increasing from $1/2T_s$ to $(M-1)/2T_s$. USRP-N210 (with $F_s = 25$ MHz, and $K = 4$) is used to generate the M-ary FSK waveforms which are sent to the LED driver [47]. As to be compatible with the SDR test bench experiment, the transmitted waveforms should be real and unipolar, therefore, a DC bias is added to M-ary FSK waveforms to

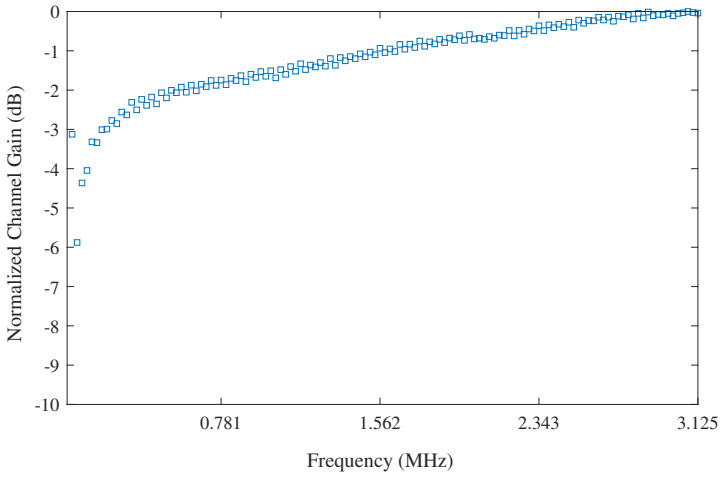

Fig. 4.7 Measured normalized channel gain over bandwidth B = 3.125 MHz.

make them unipolar, while the dictionary size M is set to 128 and the M-ary FSK waveforms occupied bandwidth is $B = 3.125$ MHz, which is same as for both M-ary AC-FSK and M-ary U-FSK (cf. Tab. 4.1). At the receiver end, a DCT is operated on each FSK waveform after photodetection, which gives an estimate of the channel magnitude response, $|H(f)|$ at each FSK waveform frequency.

Fig. 4.7 illustrates the obtained normalized channel gain in Decibel scale (dB), i.e., $20.\log(|H(f)|)$, for the SDR experiment (presented in Fig. 4.5) over the bandwidth B. Note that the channel gain includes LED driver response, wireless channel response and optical receiver response [47]. It is confirmed from the Fig. 4.7 that the channel gain has a high-pass filtering behaviour (in the considered low-pass limited bandwidth B), while a moderate slope (about 6 dB variation in the global bandwidth) can also be seen. It has been identified that this behaviour is mainly induced by the LED driver which includes a bias tee to combine the digitally modulated current with the DC bias current to feed the LED. This bias tee integrates a serial capacitance on its RF port for DC decoupling purpose, which acts as a high pass filter [47].

4.6.2 BER Performance Comparison of different Receivers for M-ary AC-FSK

We provide an overview of the experimental results of the proposed M-ary AC-FSK as compared to the state-of-the-art M-ary U-FSK in this sub-section. Theoretical approximation presented in Chapter 3 (cf. eq (3.33)) is also presented as a benchmark. Experimental BER results for OOK have not been reported as benchmark, because the channel response (cf. Fig. 4.7) strongly affects OOK baseband spectrum due to the high-pass filtering behaviour, which degrades drastically the BER performance of OOK [47].

Fig. 4.8 illustrates the experimental BER performance versus the received optical power, $P_{\mathrm{r(opt)}}$ for M-ary AC-FSK using optimal TD ML receiver, 1-tap DCT-based receiver and 2-tap harmonic receiver over the optical LOS channel, while considering $M = \{16, 128\}$. A clear improvement in the

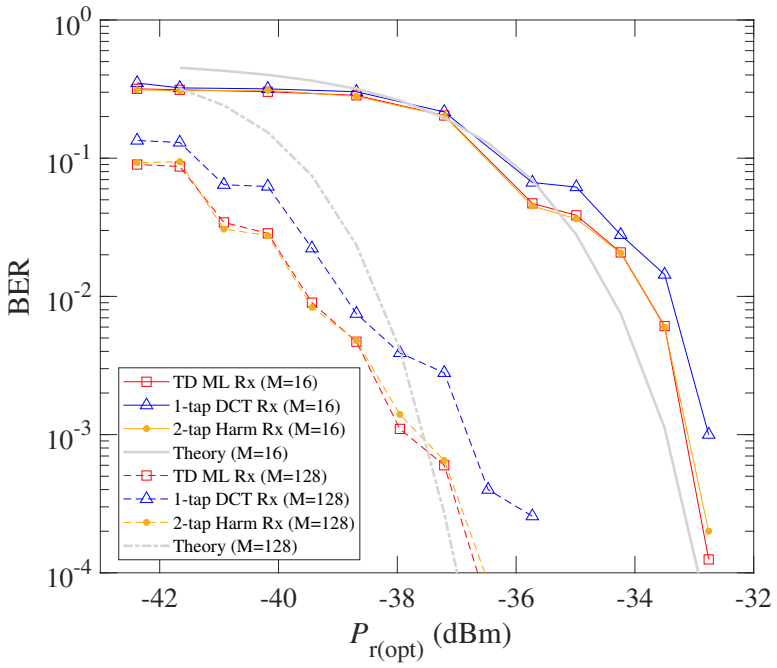

Fig. 4.8 Experimental and theoretical approximation (Theory) for BER performance against $P_{r(opt)}$ for M-ary AC-FSK receivers, considering $M = \{16, 128\}$

.

energy efficiency for M-ary AC-FSK can be seen when increasing the modulation order from $M = 16$ to 128 at an expense of decrease in spectral efficiency (cf. Tab. 4.1). This is due to the minimum distance between M-ary AC-FSK waveform pairs, which is increasing by increasing dictionary size M, while $d^2_{\min,AC}$ is proportional to the symbol energy, $E^{AC}_{s(elec)}$, with a proportionality constant, γ^{AC}, which is independent on M (cf. (3.18)). As a result, for a given $E_{s(elec)}/N_0$ ratio, BER is identical for any dictionary size M. Hence, the electrical bit energy is $E_{b(elec)} = E_{s(elec)}/n$, with $n = \log_2(M)$ is the number of bits per symbol, so by increasing n, the BER as a function of the required $E_{b(elec)}/N_0$ is improved [47]. This result is counter-intuitive when considering linear modulations, but it is a common behavior when considering (orthogonal) non-linear modulations, as also discussed in the chapter 1 of this manuscript [47], [62], [63], [57], [58].

It can be seen in Fig. 4.8 that the optimal TD ML receiver for M-ary AC-FSK has far better BER versus the required optical power $P_{r(opt)}$ performance than 1-tap DCT-based receiver, i.e., the required received optical power $P_{r(opt)}$ for TD ML receiver to achieve a BER of 10^{-3} is around 1 dB less than the required $P_{r(opt)}$ to achieve the same BER value for 1-tap DCT-based receiver. Moreover, the proposed 2-tap harmonic receiver for M-ary AC-FSK shows approximately similar BER versus required optical power $P_{r(opt)}$ performance as the optimal TD ML receiver for both dictionary sizes $M = \{16, 128\}$, while the receiver complexity for 2-tap harmonic receiver as compared to the TD ML receiver is reduced by 56.3% (respectively 92.2%) for $M = 16$ (respectively $M = 128$) (cf. Table 3.2). These results are compliant with the simulation results presented in Chapter 3 (cf. Fig. 3.10),

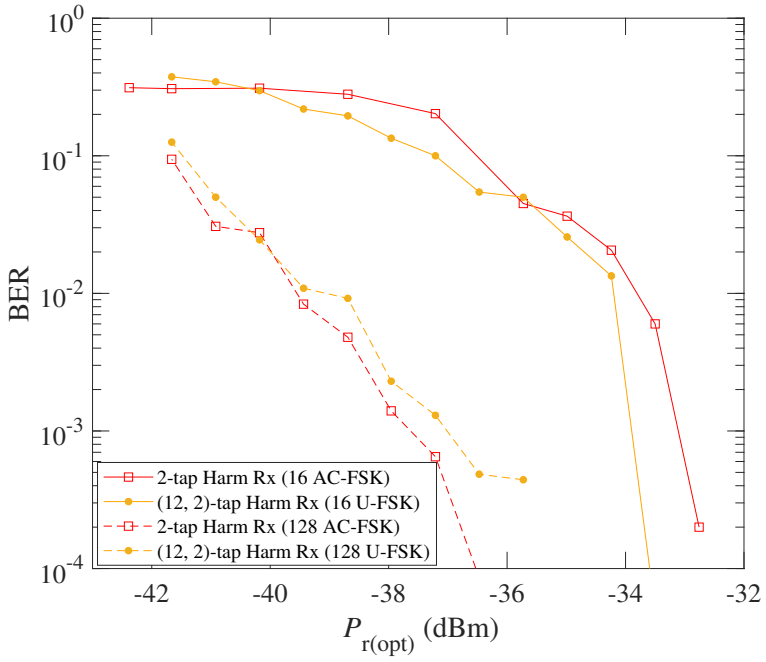

Fig. 4.9 Experimental BER performance against $P_{r(opt)}$ of the L-tap harmonic receiver (Harm Rx) for M-ary AC-FSK and M-ary U-FSK, considering $M = 16$ & 128.

considering that the noise power spectrum density, N_0, is supposed to be independent from $P_{r(opt)}$ (N_0 is mainly induced by thermal noise, ambient noise and receiver circuit noise figure [47]). Theoretical approximation computed in Sec. 3.3.2 (cf. eq (3.33) has been reported on Fig. 4.8. For calibrating $E_{b(opt)}/N_0$ in the theoretical bit error probability (3.33) relatively to $P_{r(opt)}$, $E_{b(opt)}$ and $P_{r(opt)}$ are related using $E_{b(opt)} = P_{r(opt)} T_b$. $T_b = 1/R_b$ is extracted from Tab. 4.1 and is used also to explicit Γ parameter definition (see (3.32)) used in (3.33). Then, a N_0 value of -160 dBm/Hz is found so that the bit error probability reaches a value of 10^{-3} for the optical power $P_{r(opt)} = -36.7$ dBm for $M = 16$, in order to fit approximately the experimental BER result of Fig. 4.8. In the following step, maintaining the same value $N_0 = -160$ dBm/Hz, the theoretical bit error probability is computed for $M = 128$ as a function of $P_{r(opt)}$ using (3.33). Theoretical bit error probabilities for $M = \{16, 128\}$ plotted in Fig. 4.8 match approximately with TD ML and harmonic receivers experimental results. A slight difference can be seen between the theoretical bit error probability curves and the BER measurements curves of the optimal TD ML receiver and the 2-tap harmonic receiver, due to the channel frequency response, which is not perfectly flat, as shown on Fig. 4.7.

4.6.3 BER Performance Comparison of L-tap Harmonic Receiver for M-ary AC-FSK and M-ary U-FSK

Fig. 4.9 shows the experimental result for the BER versus received optical power $P_{\mathrm{r(opt)}}$ performance comparison between M-ary AC-FSK and M-ary U-FSK [81], considering only L-tap harmonic receiver and for modulation orders $M = \{16, 128\}$. Recall that only $L = 2$ taps are considered for M-ary AC-FSK harmonic receiver [52], while $L_{\mathrm{e}} = 12$ and $L_{\mathrm{o}} = 2$ taps are considered for M-ary U-FSK [81]. It can be seen in Fig. 4.9 that the experimental BER performance of L-tap harmonic receiver for M-ary AC-FSK is similar as the one of M-ary U-FSK for $M = 16$, while a slightly degraded BER performance of L-tap harmonic receiver can be depicted for M-ary U-FSK relatively to the M-ary AC-FSK for $M = 128$, which may come from the impact of the receiver low pass filtering behaviour (cf Fig. 4.5) on the numerous U-FSK waveform harmonics [47]. Furthermore, the L-tap harmonic receiver complexity for M-ary AC-FSK is reduced as compared to the M-ary U-FSK by 41.6% (respectively 33.3%) for $M = 16$ (respectively $M = 128$) (cf. Table 3.3). These reductions in the complexity are achieved due to the use of limited number of taps for M-ary AC-FSK harmonic receiver as compared to the M-ary U-FSK harmonic receiver [47],[52],[95].

4.7 Conclusion

In this chapter, an experimental demonstration on SDR for the proposed M-ary AC-FSK is presented. The experimental test bench, composed of COTS devices is presented, which is interfaced with the SDR equipment (USRP-N210), and OWC channel gain is measured. Different challenges faced in the experimental implementations are also presented. Experimental results for the proposed M-ary AC-FSK confirmed the similar results as the theoretical results presented in Chapter 3. Experimental BER measurement comparison between 3 different receivers for M-ary AC-FSK confirm that 2-tap harmonic receiver shows far better BER performance as compared to the 1-tap DCT-based receiver, while 2-tap harmonic receiver shows approximately similar BER performance as the conventional optimal TD ML receiver, but with the benefit of drastic reduction in the receiver complexity for L-tap harmonic receiver. Furthermore, experimental BER performance comparison between M-ary AC-FSK and state-of-the-art M-ary U-FSK considering L-tap harmonic receiver, is presented, which confirms that both modulation schemes reach similar BER, whereas, AC-FSK harmonic receiver shows significantly low computational complexity as compared to U-FSK harmonic receiver. This is because of the limited number of taps in frequency-domain AC-FSK waveforms. In conclusion, it seems that our proposed scheme (i.e., AC-FSK modulation + low-complexity 2-tap harmonic receiver) is a relevant scheme to be implemented in practice for low energy communication applications.

Providing additional experimental results on $(M_{\perp}, M_{\phi})$-AC-FPSK would be an interesting extension of this practical work, to compare the performances of $(M_{\perp}, M_{\phi})$-AC-FPSK with M-ary AC-FSK.

Conclusion and Perspectives

There is a growing interest in IoT with an expectation of 30 billions of connected devices by 2030. Many connected devices will have to transmit small amount of data with limited data rates (up to 1 Mbps). RF spectrum is saturated and the excessive use of the RF spectrum gives rise to co-channel interference issues. As RF spectrum is saturated, OWC systems may constitute a viable alternative to address the issue of low power communication system for low data rate IoT communications. Moreover, OWC has gained excessive interest due to the use of incoherent light emitting diodes (LEDs) and high sensitive photo-detectors (PDs). Furthermore, OWC also benefits from license free (un-regulated) virtually unlimited optical bandwidth, high security in data transmission and no interference with RF communications. However, to build a low power OWC system for low data rate applications, a challenging point is to define a suitable energy efficient modulation scheme compatible with the intensity modulation and direct detection (IM-DD) constraint. This is precisely the objective of this PhD work.

According to recent research, frequency shift keying (FSK)-based modulations gain a substantial interest for low data rate and high energy efficiency for IM-DD OWC systems. A new energy efficient modulation based on FSK is proposed in this work (cf. Chapter 3) for low data rate IoT applications, i.e., M-ary Asymmetrically Clipped (AC)-FSK and its bit-error-rate (BER) performance is compared with the state-of-the-art M-ary DC-FSK and M-ary U-FSK modulations. In-fact M-ary AC-FSK is derived from the conventional bipolar $2M$-ary FSK by considering only the odd frequency waveforms and clipping their negative parts to zero in order to be compatible with the IM-DD OWC systems. Conventional receivers for M-ary AC-FSK are also presented, i.e., optimal time-domain (TD) maximum likelihood (ML) receiver and the sub-optimal 1-tap discrete cosine transform (DCT)-based receiver. Although the optimal TD ML receiver shows better BER performance (energy efficiency) relative to the 1-tap DCT-based receiver for M-ary AC-FSK, its receiver shows high computational complexity. We have demonstrated that there exists a trade-off between energy efficiency of the modulation scheme and the receivers computational complexity for M-ary AC-FSK. To mitigate this trade-off, spectral analysis of M-ary AC-FSK waveforms allow us to propose a new frequency-domain (FD) 2-tap harmonic receiver. Only two harmonics/taps (leaving aside DC component) have significant amplitudes and contain around 99% of the symbol energy, and are selected for each waveform. This leads to a drastic reduction in the complexity of the proposed 2-tap harmonic receiver for M-ary AC-FSK, i.e., the number of multiplications become linearithmic with the size of the alphabet

instead of being quadratic for optimal TD ML receiver. Simulation results reveal that the proposed M-ary AC-FSK exhibits far better energy efficiency than M-ary DC-FSK and a slightly better energy efficiency than M-ary U-FSK. Moreover, the proposed 2-tap harmonic receiver for M-ary AC-FSK shows approximately similar BER performance (or energy efficiency) as the traditional optimal TD ML receiver, but a drastic reduction in the receiver computational complexity is achieved, i.e., a complexity reduction of 92.2% (respectively 98.7%) is achieved for $M = 128$ (respectively $M = 1024$) as compared to the optimal TD ML receiver.

The same idea of low complexity harmonic receiver is also adopted for the state-of-the-art M-ary U-FSK, leading to the proposition of the L-tap harmonic receiver for M-ary U-FSK (cf. Chapter 2, Sec. 2.4) which attains a similar BER performance as the optimal TD ML receiver with the benefit of reduced receiver complexity. This time, the number of harmonics/taps selected for M-ary U-FSK waveforms are different. Spectral analysis of M-ary U-FSK waveforms suggests that at least twelve and two harmonics/taps are necessary for even and odd U-FSK waveforms to attain the desired BER performance. Simulation results reveal that the proposed L-tap harmonic receiver for M-ary U-FSK shows almost similar BER performance as of the optimal TD ML receiver with the benefit of a complexity reduction of 94.1% (respectively 99.1%) for $M = 128$ (respectively $M = 1024$). Since only 2 harmonics/taps are selected for all AC-FSK waveforms, therefore, further reduction in the complexity of 2-tap harmonic receiver for M-ary AC-FSK is obtained as compared to the L-tap harmonic receiver for M-ary U-FSK. In this regard, the complexity reduction of 2-tap harmonic receiver for M-ary AC-FSK as compared to the L-tap harmonic receiver for M-ary U-FSK is about 33.3% (respectively 27.7%) for $M = 128$ (respectively $M = 1024$).

Moreover, we proposed a new energy efficient modulation scheme, called $(M_\perp, M_\phi)$-AC-FPSK for OWC systems (cf. Chapter 3, Sec. 3.5), which is an extended version of M-ary AC-FSK by incorporating phase shift keying (PSK) into the M-ary AC-FSK. Here, $M_\perp$ and M_ϕ represent the number of orthogonal frequency waveforms and the number of phases added to each orthogonal waveform, respectively. We presented two kinds of traditional receivers for $(M_\perp, M_\phi)$-AC-FPSK, i.e., optimal TD ML receiver and 1-tap discrete Fourier transform (DFT) receiver, while 2-tap harmonic receiver is also adapted for the proposed $(M_\perp, M_\phi)$-AC-FPSK. The theoretical lower and upper bounds approximation for the bit error probability using ML detection are also computed. Simulation results confirmed that the 2-tap harmonic receiver for $(M_\perp, M_\phi)$-AC-FPSK achieves similar BER performance as the optimal TD ML receiver with the benefit of a reduction in the receiver complexity and the simulated BER curve for 2-tap harmonic receiver lies in between the theoretical lower and upper bound curves. Note that there also exists a trade-off between energy efficiency and spectral efficiency for $(M_\perp, M_\phi)$-AC-FPSK which depends upon the number of phases, M_ϕ. Theory and simulations confirmed that the optimum number of phases can be $M_\phi = 4$ or 8, to achieve the best energy efficiency versus spectral efficiency trade-off relative to the state-of-the-art M-ary AC-FSK and $(M_\perp, M_\phi)$-DC-FPSK. To reduce the receiver complexity, the best choice for the number of phases is $M_\phi = 8$, because it leads to the decrease of $M_\perp$ for a given targeted modulation size M, i.e., $M = M_\perp \times M_\phi$, which decreases the DFT order in the receiver, decreasing the receiver complexity.

Finally, an experimental demonstration of the proposed M-ary AC-FSK and the proposed 2-tap harmonic receiver (respectively L-tap harmonic receiver) for M-ary AC-FSK (respectively state-of-the-art M-ary U-FSK) are presented (cf. Chapter 4) which is based on a software defined radio (SDR) test bench and OWC prototype. The OWC prototype is built from commercial off-the-shelf (COTS) devices and it is interfaced with the SDR equipments (USRP-N210). The OWC channel gain is measured by transmitting DC-FSK waveforms. Experimental results confirmed that the BER performance of the proposed M-ary AC-FSK is compliant with the simulation results. Furthermore, the experimental BER measurement also confirmed that the proposed 2-tap harmonic receiver for M-ary AC-FSK shows approximately similar BER performance as of the conventional optimal TD ML receiver and far better BER performance than 1-tap DCT-based receiver. Moreover, the experimental BER performance comparison between the 2-tap harmonic receiver for M-ary AC-FSK and the L-tap harmonic for the state-of-the-art M-ary U-FSK, is also presented. This comparison confirms that both modulation schemes reach similar BER performance using 2-tap (or L-tap) harmonic receiver, while 2-tap harmonic receiver for M-ray AC-FSK depicts significantly low complexity relative to the L-tap harmonic receiver for M-ary U-FSK. This is due to the limited number of taps (only 2 taps) in the FD M-ary AC-FSK waveforms.

In short, it is confirmed that our proposed modulation schemes, i.e., M-ary AC-FSK and $(M_{\perp}, M_{\phi})$-AC-FPSK, and the proposed low complexity 2-tap harmonic receiver are relatively good choices to be implemented for high energy efficient and low data rate OWC applications.

Prospects of Future Work

Channel or Component Impairments

Techniques developed in this thesis could be tested in presence of more difficult conditions that could be encountered in practice. For example, difficulties could be:

- Frequency selective OWS channel, because of an increase in delay spread due to more important transmission distances and reflection issues.
- Material impairments like frequency drift or jitter/phase noise affecting clocks, or non-linearities in the TX or RX optic of electrical components.

Also techniques to compensate or take more into account this difficulties could be addressed, like equalizer, advanced synchronizer, digital signal processing mitigation/corrections.

Coding Techniques and their Experimental Implementations

In this work, new modulation approaches with high energy efficiency, such as M-ary AC-FSK and $(M_{\perp}, M_{\phi})$-AC-FPSK along with the FD low-complexity harmonic receiver have been presented for IM-DD OWC systems. In future, an idea of combining coding and energy efficient modulations (such

as Turbo-FSK principle used in RF [62], [86], [98]) can be a logical extension of this work to further improve the energy efficiency. For example, a joint turbo coding with M-ary DC-FSK, leading to a Turbo-DC-FSK can achieve around 4 dB energy gain over conventional M-ary DC-FSK for the same spectral efficiency, while considering a BER of 10^{-4} [99]. The same idea of joint turbo coding could be adapted in future work for M-ary AC-FSK and $(M_{\perp}, M_{\phi})$-AC-FPSK to further improve the energy efficiency for IM-DD OWC systems.

Another possible extension of this work could be the experimental implementations of the propose joint turbo techniques on the software defined radio test bench. The idea will be to experimentally validate the propose joint turbo techniques for IM-DD OWC applications.

Index Modulation

It has been established recently in RF literature that coupling OFDM with index modulation (IM) can add flexibility in terms of spectral efficiency and energy efficiency [100], [101]. As FSK modulation can be viewed as a special case of OFDM-IM scheme for which only one index is on (one frequency among the M possible, whereas several indices (frequencies) could be on at the same time in the general system), the extension of our work could be used in order to increase the flexibility. The index modulation concept with some adaptation to be compatible with the intensity-modulation and direct detection constraint has already been applied for OWC system [87] [102], [103], [104], but the study could be continued with the new FSK-based alphabet introduced in this thesis.

References

[1] *Statista Website visited in November 2022 on internet, website: https://www.statista.com/statistics/1183457/iot-connected-devices-worldwide/.*

[2] *Scoop Website visited in November 2022 on internet, website: https://www.i-scoop.eu/internet-of-things-iot/.*

[3] *Cisco Annual Internet Report (2018-2023), visited in September 2022 on internet, website: https://www.cisco.com/c/en/us/solutions/collateral/executive-perspectives/annual-internet-report/white-paper-c11-741490.html.*

[4] *McKinsey and Company Report (2018-2023), visited in November 2022 on internet, website: https://www.mckinsey.com/industries/private-equity-and-principal-investors/our-insights/growing-opportunities-in-the-internet-of-things.*

[5] *Wikipedia website, visited in September 2022 on internet, website: https://en.wikipedia.org/wiki/Radio-spectrum.*

[6] Ali Waqar Azim. *Signal processing techniques for optical wireless communication systems*. PhD thesis, Université Grenoble Alpes (ComUE), 2018.

[7] Lajos Hanzo, Harald Haas, Sándor Imre, Dominic O'Brien, Markus Rupp, and Laszlo Gyongyosi. Wireless myths, realities, and futures: from 3G/4G to optical and quantum wireless. *Proceedings of the IEEE*, 100(Special Centennial Issue):1853–1888, 2012.

[8] Harald Haas, Liang Yin, Yunlu Wang, and Cheng Chen. What is LiFi? *Journal of Lightwave Technology*, 34(6):1533–1544, 2015.

[9] Oussama Haddad. *Modélisation du canal et solutions d'accés multiple pour les réseaux corporels basés sur la technologie d'optique sans-fil dans un milieu hospitalier*. PhD thesis, Ecole centrale de Marseille, 2021.

[10] Joseph M Kahn and John R Barry. Wireless infrared communications. *Proceedings of the IEEE*, 85(2):265–298, 1997.

[11] Shuze Zhao, Jiale Xu, and Olivier Trescases. A dimmable LED driver for visible light communication (VLC) based on LLC resonant DC-DC converter operating in burst mode. In *2013 Twenty-Eighth Annual IEEE Applied Power Electronics Conference and Exposition (APEC)*, pages 2144–2150. IEEE, 2013.

[12] Hao Ma, Lutz Lampe, and Steve Hranilovic. Integration of indoor visible light and power line communication systems. In *2013 IEEE 17th International Symposium on Power Line Communications and Its Applications*, pages 291–296. IEEE, 2013.

[13] Dilukshan Karunatilaka, Fahad Zafar, Vineetha Kalavally, and Rajendran Parthiban. LED based indoor visible light communications: State of the art. *IEEE Communications Surveys & Tutorials*, 17(3):1649–1678, 2015.

[14] Jong Kyu Kim and E Fred Schubert. Transcending the replacement paradigm of solid-state lighting. *Optics Express*, 16(26):21835–21842, 2008.

[15] Bilal A Ranjha. *OFDM based RF and optical wireless systems*. The Pennsylvania State University, 2014.

[16] Mauro Biagi, Tarik Borogovac, and Thomas DC Little. Adaptive receiver for indoor visible light communications. *Journal of Lightwave Technology*, 31(23):3676–3686, 2013.

[17] Chi-Wai Chow, CH Yeh, YF Liu, PY Huang, and Y Liu. Adaptive scheme for maintaining the performance of the in-home white-LED visible light wireless communications using OFDM. *Optics Communications*, 292:49–52, 2013.

[18] Yuanquan Wang, Yiguang Wang, Nan Chi, Jianjun Yu, and Huiliang Shang. Demonstration of 575-Mb/s downlink and 225-Mb/s uplink bi-directional SCM-WDM visible light communication using RGB LED and phosphor-based LED. *Optics Express*, 21(1):1203–1208, 2013.

[19] Aleksandar Jovicic, Junyi Li, and Tom Richardson. Visible light communication: opportunities, challenges and the path to market. *IEEE Communications Magazine*, 51(12):26–32, 2013.

[20] *Electronics Tutorials, visited in November 2022 on internet, website: https://911electronic.com/flickering-led-lights-effect/.*

[21] Mostafa Zaman Chowdhury, Md Tanvir Hossan, Amirul Islam, and Yeong Min Jang. A comparative study of optical wireless technologies: Architectures and applications. *IEEE Access*, 6:9819–9840, 2018.

[22] Mohammad Ali Khalighi and Murat Uysal. Survey on free space optical communication: A communication theory perspective. *IEEE Communications Surveys & Tutorials*, 16(4):2231–2258, 2014.

[23] Murat Uysal and Hatef Nouri. Optical wireless communications—An emerging technology. In *2014 16th International Conference on Transparent Optical Networks (ICTON)*, pages 1–7. IEEE, 2014.

[24] Christoforos Kachris, Keren Bergman, and Ioannis Tomkos. *Optical interconnects for future data center networks*. Springer Science & Business Media, 2012.

[25] Yunfeng Lu and Huaxi Gu. Flexible and scalable optical interconnects for data centers: Trends and challenges. *IEEE Communications Magazine*, 57(10):27–33, 2019.

[26] Pascal Toumieux, Ludovic Chevalier, Stéphanie Sahuguède, and Anne Julien-Vergonjanne. Optical wireless connected objects for healthcare. *Healthcare Technology Letters*, 2(5):118–122, 2015.

[27] Ludovic Chevalier, Stephanie Sahuguede, and Anne Julien-Vergonjanne. Optical wireless links as an alternative to radio-frequency for medical body area networks. *IEEE Journal on Selected Areas in Communications*, 33(9):2002–2010, 2015.

[28] Phillip A Laplante, Mohamad Kassab, Nancy L Laplante, and Jeffrey M Voas. Building caring healthcare systems in the internet of things. *IEEE Systems Journal*, 12(3):3030–3037, 2017.

[29] Trang Nguyen, Amirul Islam, Tanvir Hossan, and Yeong Min Jang. Current status and performance analysis of optical camera communication technologies for 5G networks. *IEEE Access*, 5:4574–4594, 2017.

[30] Ali Waqar Azim, Antoine Rullier, Yannis Le Guennec, Laurent Ros, and Ghislaine Maury. Energy efficient M-ary frequency-shift keying-based modulation techniques for visible light communication. *IEEE Transactions on Cognitive Communications and Networking*, 5(4):1244–1256, 2019.

[31] Murat Uysal, Zabih Ghassemlooy, Abdelmoula Bekkali, Abdullah Kadri, and Hamid Menouar. Visible light communication for vehicular networking: Performance study of a V2V system using a measured headlamp beam pattern model. *IEEE Vehicular Technology Magazine*, 10(4):45–53, 2015.

[32] Murat Uysal. Visible light communications: from theory to industrial standardization. In *2019 Optical Fiber Communications Conference and Exhibition (OFC)*, pages 1–3. IEEE, 2019.

[33] Yong Hyeon Kim, Willy Anugrah Cahyadi, and Yeon Ho Chung. Experimental demonstration of VLC-based vehicle-to-vehicle communications under fog conditions. *IEEE Photonics Journal*, 7(6):1–9, 2015.

[34] Vima Gupta and Rahul Singhal. Performance analysis of a visible light vehicle-to-vehicle wireless communication system. In *2019 TEQIP III Sponsored International Conference on Microwave Integrated Circuits, Photonics and Wireless Networks (IMICPW)*, pages 521–523. IEEE, 2019.

[35] Farukh Nadeem, Vaclav Kvicera, Muhammad Saleem Awan, Erich Leitgeb, Sajid Sheikh Muhammad, and Gorazd Kandus. Weather effects on hybrid FSO/RF communication link. *IEEE Journal on Selected Areas in Communications*, 27(9):1687–1697, 2009.

[36] Hubertus Haan, Martin Gerken, and M Tausendfreund. Long-range laser communication terminals: Technically interesting, commercially incalculable. In *2012 8th International Symposium on Communication Systems, Networks & Digital Signal Processing (CSNDSP)*, pages 1–4. IEEE, 2012.

[37] Juraj Poliak, Dirk Giggenbach, Florian Moll, Fabian Rein, Christian Fuchs, and Ramon Mata Calvo. Terabit-throughput GEO satellite optical feeder link testbed. In *2015 13th International Conference on Telecommunications (ConTEL)*, pages 1–5. IEEE, 2015.

[38] Hemani Kaushal and Georges Kaddoum. Optical communication in space: Challenges and mitigation techniques. *IEEE Communications Surveys & Tutorials*, 19(1):57–96, 2016.

[39] Toni Tolker-Nielsen and Gotthard Oppenhauser. In-orbit test result of an operational optical intersatellite link between artemis and spot4, silex. In *Free-Space Laser Communication Technologies XIV*, volume 4635, pages 1–15. SPIE, 2002.

[40] Berry Smutny, Hartmut Kaempfner, Gerd Muehlnikel, Uwe Sterr, Bernhard Wandernoth, Frank Heine, Ulrich Hildebrand, Daniel Dallmann, Martin Reinhardt, Axel Freier, et al. 5.6 Gbps optical intersatellite communication link. In *Free-Space Laser Communication Technologies XXI*, volume 7199, pages 38–45. SPIE, 2009.

[41] Harald Haas, Cheng Chen, and Dominic O'Brien. A guide to wireless networking by light. *Progress in Quantum Electronics*, 55:88–111, 2017.

[42] Chandrajit Basu, Merve Meinhardt-Wollweber, and Bernhard Roth. Lighting with laser diodes. *Advanced Optical Technologies*, 2(4):313–321, 2013.

[43] Richard J Fitzgerald. Lighting with laser diodes. *Physics Today*, 66(9):18, 2013.

[44] Alexander Neumann, JJ Wierer, Wendy Davis, Yoshi Ohno, SRJ Brueck, and JY Tsao. Four-color laser white illuminant demonstrating high color-rendering quality. *Optics Express*, 19(104):A982–A990, 2011.

[45] Parth H Pathak, Xiaotao Feng, Pengfei Hu, and Prasant Mohapatra. Visible light communication, networking, and sensing: A survey, potential and challenges. *IEEE Communications Surveys & Tutorials*, 17(4):2047–2077, 2015.

[46] FM Wu, Chun-Ting Lin, CC Wei, CW Chen, ZY Chen, HT Huang, and Sien Chi. Performance comparison of OFDM signal and CAP signal over high capacity RGB-LED-based WDM visible light communication. *IEEE Photonics Journal*, 5(4):7901507–7901507, 2013.

[47] Muhammad Jehangir Khan, Ali W Azim, Yannis Le Guennec, Ghislaine Maury, and Laurent Ros. Theoretical and experimental analysis of Asymmetrically Clipped-FSK VLC system. *IEEE Photonics Journal*, 14(3):1–9, 2022.

[48] Kwonhyung Lee, Hyuncheol Park, and John R Barry. Indoor channel characteristics for visible light communications. *IEEE Communications Letters*, 15(2):217–219, 2011.

[49] Murat Uysal, Farshad Miramirkhani, Omer Narmanlioglu, Tuncer Baykas, and Erdal Panayirci. IEEE 802.15. 7r1 reference channel models for visible light communications. *IEEE Communications Magazine*, 55(1):212–217, 2017.

[50] Ali W Azim, Yannis Le Guennec, and Ghislaine Maury. Decision-directed iterative methods for PAPR reduction in optical wireless OFDM systems. *Optics Communications*, 389:318–330, 2017.

[51] Amir Weiss, Arie Yeredor, and Mark Shtaif. Iterative symbol recovery for power-efficient DC-biased optical OFDM systems. *Journal of Lightwave Technology*, 34(9):2331–2338, 2016.

[52] Muhammad Jehangir Khan, Ali Waqar Azim, Yannis Le Guennec, Ghislaine Maury, and Laurent Ros. Asymmetrically Clipped-FSK modulation for energy efficient visible light communications. In *2021 IEEE 32nd Annual International Symposium on Personal, Indoor and Mobile Radio Communications (PIMRC)*, pages 458–464. IEEE, 2021.

[53] Jean Armstrong, Roger J Green, and Matthew D Higgins. Comparison of three receiver designs for optical wireless communications using white LEDs. *IEEE Communications Letters*, 16(5):748–751, 2012.

[54] Zixiong Wang, Dobroslav Tsonev, Stefan Videv, and Harald Haas. Towards self-powered solar panel receiver for optical wireless communication. In *2014 IEEE International Conference on Communications (ICC)*, pages 3348–3353. IEEE, 2014.

[55] Jiang Liu, Wasinee Noonpakdee, Hiroshi Takano, and Shigeru Shimamoto. Foundational analysis of spatial optical wireless communication utilizing image sensor. In *2011 IEEE International Conference on Imaging Systems and Techniques*, pages 205–209. IEEE, 2011.

[56] Chen Chen, Wen-De Zhong, and Dehao Wu. Non-hermitian symmetry orthogonal frequency division multiplexing for multiple-input multiple-output visible light communications. *Journal of Optical Communications and Networking*, 9(1):36–44, 2017.

[57] John G. Proakis and Masoud Salehi. *Digital communications*. McGraw-Hill., 2008.

[58] Yoann Roth. *The physical layer for low power wide area networks: a study of combined modulation and coding associated with an iterative receiver*. PhD thesis, 2017.

[59] Laurent Ros. *Traitement du signal pour les communications numériques au travers de canaux radio-mobiles*. PhD thesis, Université de Grenoble, Ecole doctorale EEATS, spécialité Signal, Image, Parole et Télécommunications , 2016.

[60] Claude Elwood Shannon. A mathematical theory of communication. *The Bell System Technical Journal*, 27(3):379–423, 1948.

[61] Kazuro Kikuchi and Masayuki Osaki. Highly-sensitive coherent optical detection of M-ary frequency-shift keying signal. *Optics Express*, 19(26):B32–B39, 2011.

[62] Yoann Roth, Jean-Baptiste Doré, Laurent Ros, and Vincent Berg. Turbo-FSK, a physical layer for low-power wide-area networks: Analysis and optimization. *Comptes Rendus Physique*, 18(2):178–188, 2017.

[63] Yoann Roth, Jean-Baptiste Doré, Laurent Ros, and Vincent Berg. *The Physical Layer of Low Power Wide Area Networks: Strategies, Information Theory's Limit and Existing Solutions*. Advances in Signal Processing: Reviews, vol. 1, Book Series, 2018.

[64] Robert C Moore. Satellite RF communications and onboard processing. 2003.

[65] Mohamed Sufyan Islim and Harald Haas. Modulation techniques for LiFi. *ZTE Communications*, 14(2):29–40, 2019.

[66] Marcin Jarzyna and Konrad Banaszek. Efficiency of optimized pulse position modulation with noisy direct detection. In *2017 IEEE International Conference on Space Optical Systems and Applications (ICSOS)*, pages 166–171. IEEE, 2017.

[67] Asanka Nuwanpriya, Siu-Wai Ho, Jian Andrew Zhang, Alex J Grant, and Lin Luo. PAM-SCFDE for optical wireless communications. *Journal of Lightwave Technology*, 33(14):2938–2949, 2015.

[68] Shihe Long. *Indoor channel modeling and high data-rate Transmission for visible-light communication systems*. PhD thesis, Ecole Centrale Marseille (ECM), 2016.

[69] Steve Hranilovic. *Wireless optical communication systems*. Springer Science & Business Media, 2006.

[70] Kainam Thomas Wong. Narrowband PPM semi-'blind'spatial-rake receiver & co-channel interference suppression. *European Transactions on Telecommunications*, 18(2):193–197, 2007.

[71] Angga Pradana, Nur Ahmadi, Trio Adiono, Willy Anugrah Cahyadi, and Yeon-Ho Chung. VLC physical layer design based on pulse position modulation (PPM) for stable illumination. In *2015 International Symposium on Intelligent Signal Processing and Communication Systems (ISPACS)*, pages 368–373. IEEE, 2015.

[72] Hyuncheol Park and John R Barry. Trellis-coded multiple-pulse-position modulation for wireless infrared communications. *IEEE Transactions on Communications*, 52(4):643–651, 2004.

[73] Shlomi Arnon. The effect of clock jitter in visible light communication applications. *Journal of Lightwave Technology*, 30(21):3434–3439, 2012.

[74] Hyung-Joon Jang, Joon-Ho Choi, Zabih Ghassemlooy, and Chung Ghiu Lee. PWM-based PPM format for dimming control in visible light communication system. In *2012 8th International Symposium on Communication Systems, Networks & Digital Signal Processing (CSNDSP)*, pages 1–5. IEEE, 2012.

[75] Shengyang He, Guanghui Ren, Zhi Zhong, and Yaqin Zhao. M-ary variable period modulation for indoor visible light communication system. *IEEE Communications Letters*, 17(7):1325–1328, 2013.

[76] CT Manimegalai, Sabitha Gauni, Nikita Raghavan, and T Rama Rao. Investigations on suitable modulation techniques for visible light communications. In *2017 International Conference on Wireless Communications, Signal Processing and Networking (WiSPNET)*, pages 1818–1822. IEEE, 2017.

[77] Dushyantha A Basnayaka and Harald Haas. Hybrid RF and VLC systems: Improving user data rate performance of VLC systems. In *2015 IEEE 81st Vehicular Technology Conference (VTC Spring)*, pages 1–5. IEEE, 2015.

[78] Sarangi Devasmitha Dissanayake and Jean Armstrong. Comparison of ACO-OFDM, DCO-OFDM and ADO-OFDM in IM/DD systems. *Journal of Lightwave Technology*, 31(7):1063–1072, 2013.

[79] Bastien Béchadergue, Luc Chassagne, and Hongyu Guan. Suitability of visible light communication for platooning applications: An experimental study. In *2018 Global LiFi Congress (GLC)*, pages 1–6. IEEE, 2018.

[80] Stefan Schmid, Benjamin von Deschwanden, Stefan Mangold, and Thomas R Gross. Adaptive software-defined visible light communication networks. In *2017 IEEE/ACM Second International Conference on Internet-of-Things Design and Implementation (IoTDI)*, pages 109–120. IEEE, 2017.

[81] Ali Waqar Azim, Muhammad Jehangir Khan, O De Wulf, Yannis Le Guennec, Ghislaine Maury, and Laurent Ros. Near-optimal low-complexity harmonic receiver for Unipolar-FSK. *IEEE Wireless Communications Letters*, 10(11):2421–2425, 2021.

[82] K Ramamohan Rao and Ping Yip. *Discrete cosine transform: Algorithms, Advantages, Applications*. Academic press, 2014.

[83] Nasir Ahmed, T Natarajan, and Kamisetty R Rao. Discrete cosine transform. *IEEE Transactions on Computers*, 100(1):90–93, 1974.

[84] John G Proakis. *Digital signal processing: principles algorithms and applications*. Pearson Education India, 2001.

[85] Hany Elgala, Raed Mesleh, and Harald Haas. Non-linearity effects and predistortion in optical OFDM wireless transmission using LEDs. *International Journal of Ultra Wideband Communications and Systems*, 1(2):143–150, 2009.

[86] Yoann Roth, Jean-Baptiste Doré, Laurent Ros, and Vincent Berg. Coplanar Turbo-FSK: A flexible and power efficient modulation for the Internet-of-Things. *Wireless Communications and Mobile Computing*, 2018.

[87] Ji Zhou, Yaojun Qiao, Tiantian Zhang, Erkun Sun, Mengqi Guo, Zhenshan Zhang, Xizi Tang, and Fei Xu. FOFDM based on discrete cosine transform for intensity-modulated and direct-detected systems. *Journal of Lightwave Technology*, 34(16):3717–3725, 2016.

[88] Ali Waqar Azim, Yannis Le Guennec, and Laurent Ros. Hybrid frequency and phase-shift keying modulation for energy efficient optical wireless systems. *IEEE Wireless Communications Letters*, 9(4):429–432, 2019.

[89] Fang Yang, Junnan Gao, and Sicong Liu. Novel visible light communication approach based on hybrid OOK and ACO-OFDM. *IEEE Photonics Technology Letters*, 28(14):1585–1588, 2016.

[90] Haozhe Chen, Shizhe Hu, Junjie Ding, Shihang Bian, Hao Wu, Peiyi Hua, Shanhong You, Xiang Li, Qi Yang, and Ming Luo. Performance comparison of visible light communication systems based on ACO-OFDM, DCO-OFDM and ADO-OFDM. In *2017 16th International Conference on Optical Communications and Networks (ICOCN)*, pages 1–3, 2017.

[91] Cuiwei He, Thomas Q. Wang, and Jean Armstrong. Performance of optical receivers using photodetectors with different fields of view in a MIMO ACO-OFDM system. *Journal of Lightwave Technology*, 33(23):4957–4967, 2015.

[92] Jean Armstrong and Brendon JC Schmidt. Comparison of asymmetrically clipped optical OFDM and DC-biased optical OFDM in AWGN. *IEEE Communications Letters*, 12(5):343–345, 2008.

[93] Zabih Ghassemlooy, Wasiu Popoola, and Sujan Rajbhandari. *Optical wireless communications: system and channel modelling with Matlab®*. CRC Press, 2019.

[94] *ETTUS Website, visited in September 2022 on internet, website: www.ettus.com.*

[95] Muhammad Jehangir Khan, Yannis Le Guennec, and Laurent Ros. Démonstration d'une modulation AC-FSK économe en énergie pour les communications optiques sans-fil. In *Gretsi-2022, XXVIIIème Colloque Francophone de Traitement du Signal et des Images*, Nancy, France, September 2022.

[96] Jorge Baranda, Pol Henarejos, and Ciprian G Gavrincea. An SDR implementation of a visible light communication system based on the IEEE 802.15.7 standard. In *ICT 2013*, pages 1–5. IEEE, 2013.

[97] F Jessie MacWilliams and Neil JA Sloane. Pseudo-random sequences and arrays. *Proceedings of the IEEE*, 64(12):1715–1729, 1976.

[98] Yoann Roth, Jean-Baptiste Doré, Laurent Ros, and Vincent Berg. Turbo-FSK: A new uplink scheme for low power wide area networks. In *2015 IEEE 16th International Workshop on Signal Processing Advances in Wireless Communications (SPAWC)*, pages 81–85. IEEE, 2015.

[99] Paul Miqueu, Muhammad Jehangir Khan, Yannis Le Guennec, and Laurent Ros. Turbo-DC-FSK: Joint Turbo coding and FSK-based modulation for visible light communications. In *2022 Joint European Conference on Networks and Communications & 6G Summit (EuCNC/6G Summit)*, pages 25–30. IEEE, 2022.

[100] Ertugrul Basar, Miaowen Wen, Raed Mesleh, Marco Di Renzo, Yue Xiao, and Harald Haas. Index modulation techniques for next-generation wireless networks. *IEEE Access*, 5:16693–16746, 2017.

[101] Tianqi Mao, Qi Wang, Zhaocheng Wang, and Sheng Chen. Novel index modulation techniques: A survey. *IEEE Communications Surveys & Tutorials*, 21(1):315–348, 2018.

[102] Ali Waqar Azim, Marwa Chafii, Yannis Le Guennec, and Laurent Ros. Spectral and energy efficient fast-OFDM with index modulation for optical wireless systems. *IEEE Communications Letters*, 24(8):1771–1774, 2020.

[103] Ali Waqar Azim, Yannis Le Guennec, Marwa Chafii, and Laurent Ros. Filtered asymmetrically clipped optical-OFDM with index modulation for optical wireless systems. *IEEE Communications Letters*, 25(5):1592–1595, 2021.

[104] Ali Waqar Azim, Yannis Le Guennec, Marwa Chafii, and Laurent Ros. Enhanced optical-OFDM with index and dual-mode modulation for optical wireless systems. *IEEE Access*, 8:128646–128664, 2020.

Appendix A

Data Sheet of RGBA LED Emitter

You can find below the data sheet of the RGBA LED emitter (LZA-00MA00), that is used in the experimental setup.

High Luminous Efficacy
RGBA LED Emitter

LZ4-00MA00

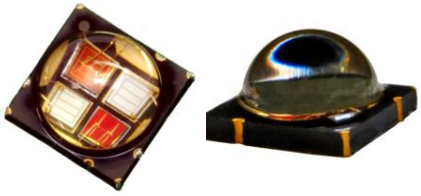

Key Features

- High Luminous Efficacy 10W RGBA LED
- Individually addressable Red, Green, Blue and Amber die
- White point tunable to any CCT or hue with enhanced CRI
- Ultra-small foot print – 7.0mm x 7.0mm
- Surface mount ceramic package with integrated glass lens
- Very low Thermal Resistance (1.1°C/W)
- Very high Luminous Flux density
- JEDEC Level 1 for Moisture Sensitivity Level
- Autoclave compliant (JEDEC JESD22-A102-C)
- Lead (Pb) free and RoHS compliant
- Reflow solderable (up to 6 cycles)
- Emitter available on Standard MCPCB (optional)

Typical Applications

- Architectural Lighting
- Retail Spot and Display Lighting
- Stage and Studio Lighting
- Hospitality Lighting
- Museum Lighting
- Dental and Medical Illumination
- Microscope Illumination
- Video Walls and Full Color Displays

Description

The LZ4-00MA00 RGBA LED emitter contains one red, green, blue and amber LED die which provides 10W power in an extremely small package. With a 7.0mm x 7.0mm ultra-small footprint, this package provides exceptional luminous flux density. LED Engin's RGBA LED offers ultimate design flexibility with individually addressable die. The LZ4-00MA00 is capable of producing any white color temperature with CRI values on the order of 90+ and millions of colors. The patent-pending design has unparalleled thermal and optical performance. The high quality materials used in the package are chosen to optimize light output and minimize stresses which results in monumental reliability and lumen maintenance. The robust product design thrives in outdoor applications with high ambient temperatures and high humidity.

LED Engin | 651 River Oaks Parkway | San Jose, CA 95134 USA | **ph** +1 408 922 7200 | **fax** +1 408 922 0158 | **em** sales@ledengin.com | www.ledengin.com

Part number options

Base part number

Part number	Description
LZ4-00MA00-xxxx	LZ4 emitter
LZ4-20MA00-xxxx	LZ4 emitter on 4 channel Standard Star MCPCB

Bin kit option codes

MA, Red-Green-Blue-Amber (RGBA)			
Kit number suffix	**Min flux Bin**	**Color Bin Range**	**Description**
0000	09R	R2 – R2	Red full distribution flux; full distribution wavelength
	12G	G2 – G3	Green full distribution flux; full distribution wavelength
	01B	B01– B02	Blue full distribution flux; full distribution wavelength
	01A	A9 – A9	Amber full distribution flux; full distribution wavelength

Notes:
1. Default bin kit option is -0000

LED Engin | 651 River Oaks Parkway | San Jose, CA 95134 USA | **ph** +1 408 922 7200 | **fax** +1 408 922 0158 | **em** sales@ledengin.com | www.ledengin.com

Luminous Flux Bins

Table 1:

Bin Code	Minimum Luminous Flux (Φ_V) @ I_F = 700mA[1,2] (lm)				Maximum Luminous Flux (Φ_V) @ I_F = 700mA[1,2] (lm)			
	Red	Green	Blue	Amber	Red	Green	Blue	Amber
09R	90				140			
12G		125				195		
01B			17				27	
02B			27				43	
01A				60				95

Notes for Table 1:
1. Luminous flux performance guaranteed within published operating conditions. LED Engin maintains a tolerance of ±10% on flux measurements.
2. Future products will have even higher levels of radiant flux performance. Contact LED Engin Sales for updated information.

Dominant Wavelength Bins

Table 2:

Bin Code	Minimum Dominant Wavelength (λ_D) @ I_F = 700mA[1,2] (nm)				Maximum Dominant Wavelength (λ_D) @ I_F = 700mA[1,2] (nm)			
	Red	Green[2]	Blue	Amber	Red	Green[2]	Blue	Amber
R2	618				630			
G2		520				525		
G3		525				530		
B01			452				457	
B02			457				462	
A9				590				595

Notes for Table 2:
1. LED Engin maintains a tolerance of ± 1.0nm on dominant wavelength measurements.
2. Green LEDs are binned for dominant wavelength @ I_F = 350mA. Refer to Figure 6 for typical dominant wavelength shift over forward current.

Forward Voltage Bin

Table 3:

Bin Code	Minimum Forward Voltage (V_F) @ I_F = 700mA[1] (V)				Maximum Forward Voltage (V_F) @ I_F = 700mA[1] (V)			
	Red	Green	Blue	Amber	Red	Green	Blue	Amber
0	2.00	3.20	3.20	2.24	2.96	4.40	4.48	3.44

Notes for Table 3:
1. LED Engin maintains a tolerance of ± 0.04V on forward voltage measurements.

Mechanical Dimensions (mm)

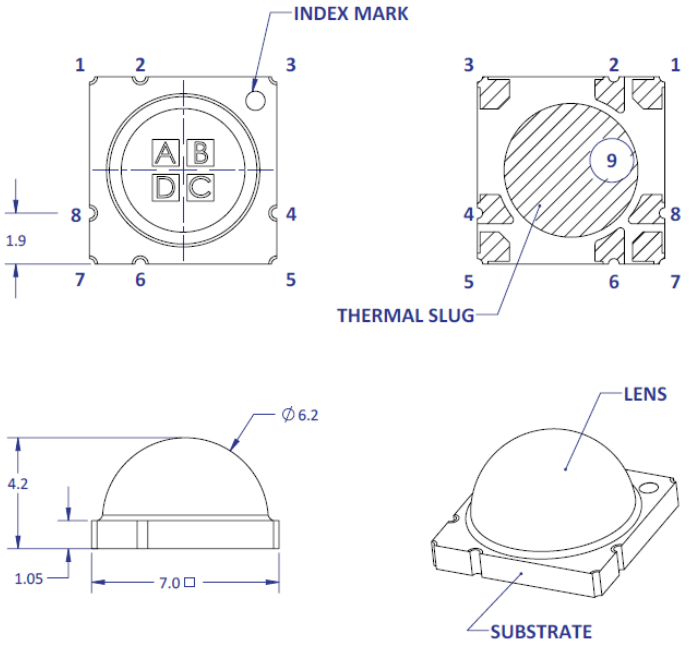

Pin Out			
Pad	Die	Color	Function
1	A	Blue	Anode
2	A	Blue	Cathode
3	B	Red	Anode
4	B	Red	Cathode
5	C	Green	Anode
6	C	Green	Cathode
7	D	Amber	Anode
8	D	Amber	Cathode
9 [2]	n/a	n/a	Thermal

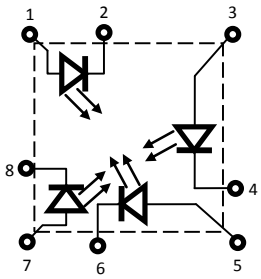

Figure 1: Package Outline Drawing.

Notes for Figure 1:
1. Unless otherwise noted, the tolerance = ± 0.20 mm.
2. Thermal contact, Pad 9, is electrically neutral.

Recommended Solder Pad Layout (mm)

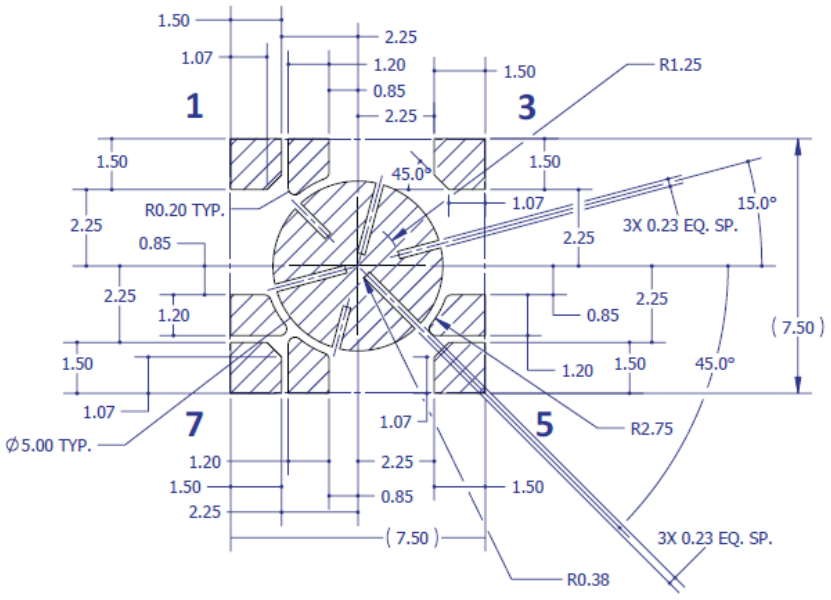

Figure 2a: Recommended solder pad layout for anode, cathode, and thermal pad.

Note for Figure 2a:
1. Unless otherwise noted, the tolerance = ± 0.20 mm.
2. This pad layout is “patent pending”.

Typical Relative Light Output

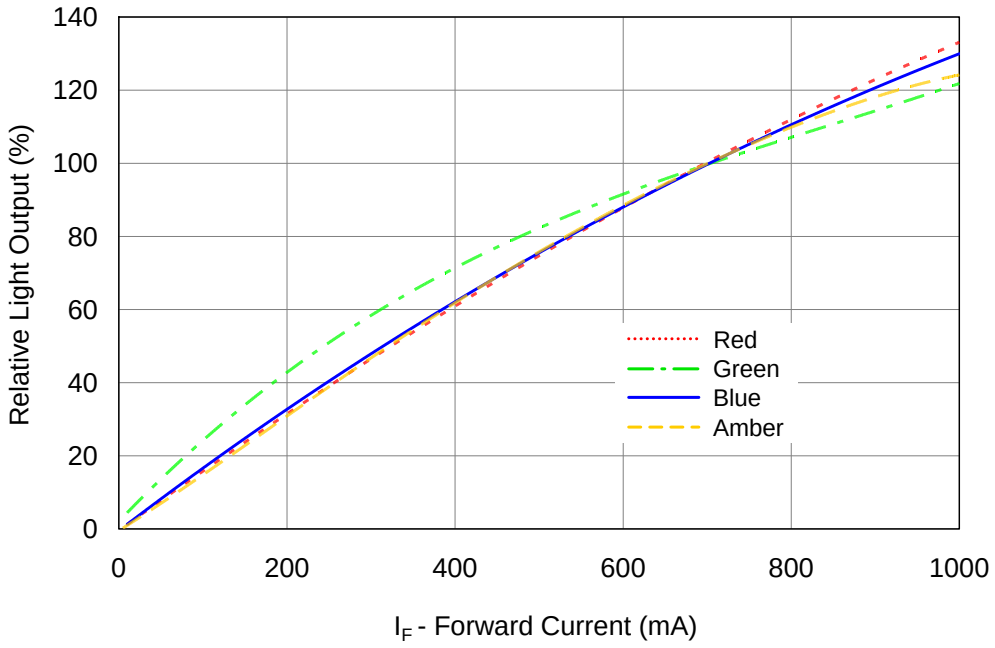

Figure 8: Typical relative light output vs. forward current @ T_C = 25°C.

Typical Relative Light Output over Temperature

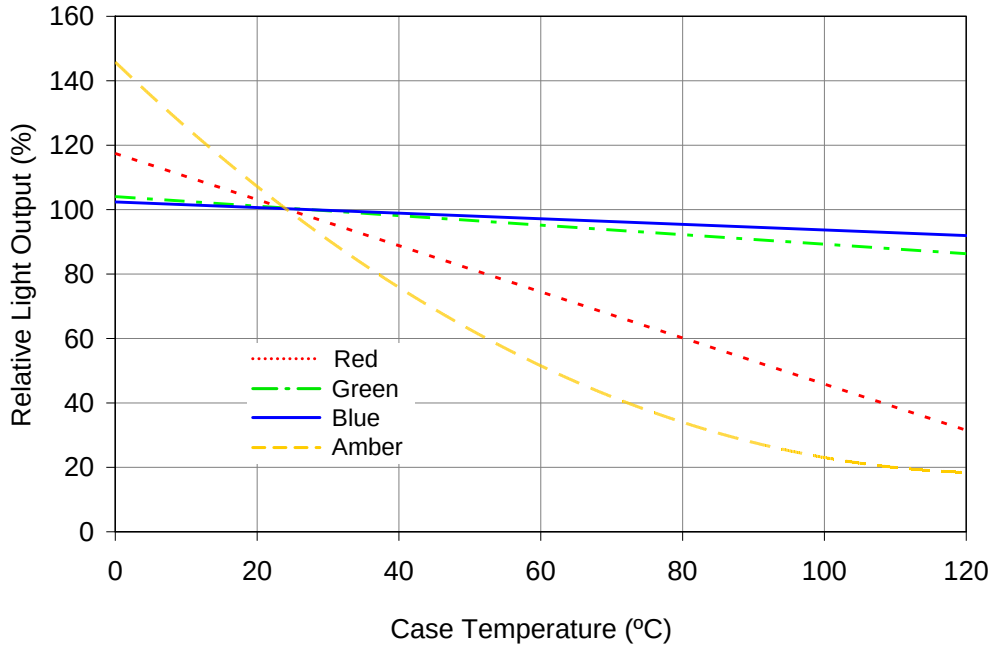

Figure 9: Typical relative light output vs. case temperature.

Appendix B

Data Sheet of Si PIN Photodiode

You can find below the data sheet of the HAMAMATSU Si PIN photodiode (S10783)/(S10784), that is used in the experimental setup.

HAMAMATSU
PHOTON IS OUR BUSINESS

Si PIN photodiodes

S10783 S10784

High-speed detectors with plastic package

The S10783 and S10784 are high-speed APC (auto power control) detectors developed for monitoring laser diodes with a peak wavelength of 660 nm or 780 nm. The S10783 is designed for surface mount and the S10784 is a plastic package with ϕ3 mm lens.

Features

- **High-speed response**
  300 MHz typ. (λ=650 nm, VR=2.5 V)
  250 MHz typ. (λ=780 nm, VR=2.5 V)
- **High sensitivity**
  S10783: 0.46 A/W typ. (λ=650 nm)
  S10784: 0.45 A/W typ. (λ=650 nm)

Applications

- **Laser diode monitors of optical disk unit (high-speed APC)**
- **Sensors for red laser diode**

Structure

Parameter	Symbol	S10783	S10784	Unit
Photosensitive area size	-	ϕ0.8	ϕ3.0	mm
Effective photosensitive area	-	0.5	7.0	mm^2
Package	-	Surface mount type plastic	Plastic with lens	-

Absolute maximum ratings

Parameter	Symbol	S10783	S10784	Unit
Reverse voltage	VR max	20		V
Power dissipation	P	50		mW
Operating temperature	Topr	-25 to +85		°C
Storage temperature	Tstg	-40 to +100		°C

Note: Exceeding the absolute maximum ratings even momentarily may cause a drop in product quality. Always be sure to use the product within the absolute maximum ratings.

This product does not support lead-free soldering. For details on reflow soldering conditions for surface-mount conponents, please contact our sales office.

Electrical and optical characteristics (Ta=25 °C)

Parameter	Symbol	Condition	S10783			S10784			Unit
			Min.	Typ.	Max.	Min.	Typ.	Max.	
Spectral response range	λ		330 to 1040			340 to 1040			nm
Peak sensitivity wavelength	λp		-	760	-	-	760	-	nm
Photosensitivity	S	λ=660 nm	0.41	0.46	-	0.40	0.45	-	A/W
		λ=780 nm	0.47	0.52	-	0.46	0.51	-	
Dark current	ID	VR=2.5 V	-	0.01	1.0	-	0.01	1.0	nA
Temperature coefficient of ID	TCID		-	1.15	-	-	1.15	-	times/°C
Cutoff frequency	fc	VR=2.5 V, λ=660 nm	150	300	-	150	300	-	MHz
		RL=50 Ω, λ=780 nm	125	250	-	125	250	-	
Terminal capacitance	Ct	VR=2.5 V, f=1 MHz	-	4.5	9	-	4.5	9	pF
Noise equivalent power	NEP	VR=2.5 V	-	3.5×10^{-15}	-	-	3.5×10^{-15}	-	$W/Hz^{1/2}$

Spectral response

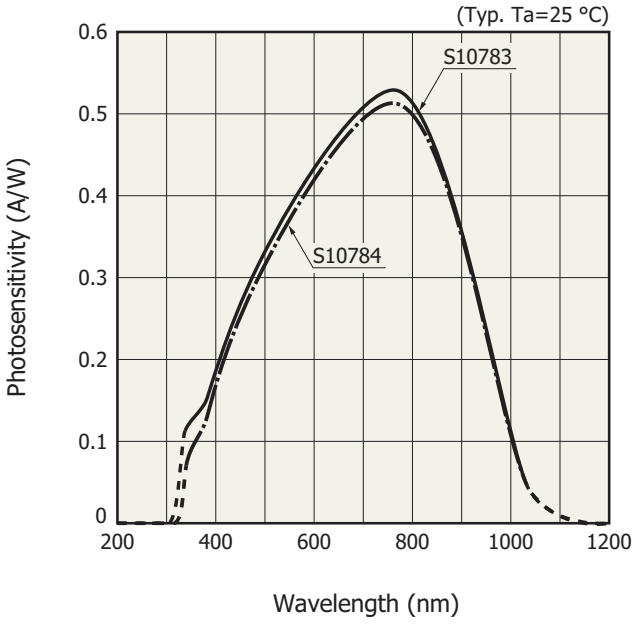

Linearity

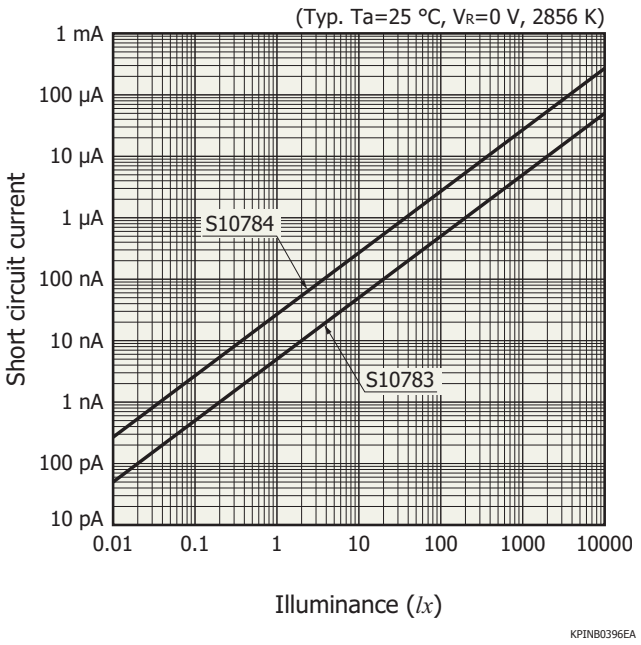

Dark current vs. reverse voltage

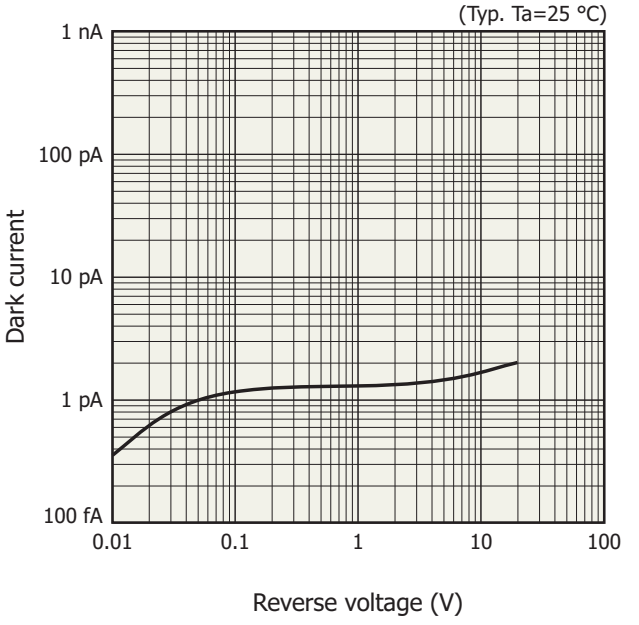

Photosensitivity temperature characteristics

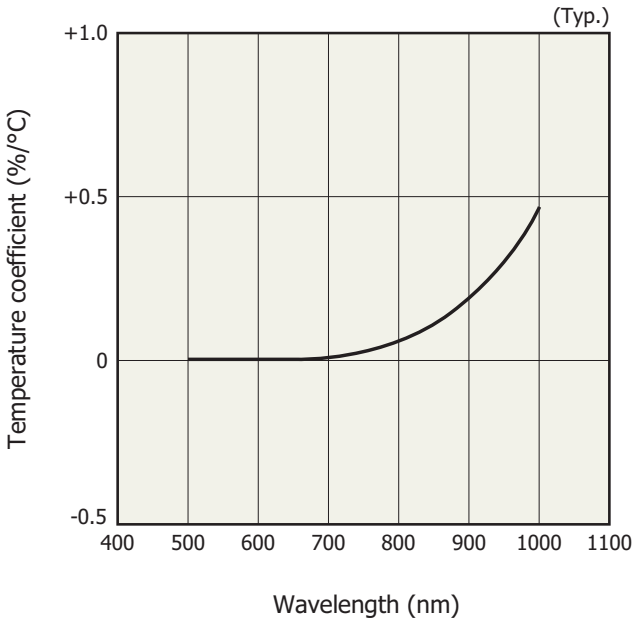

Dark current vs. ambient temperature

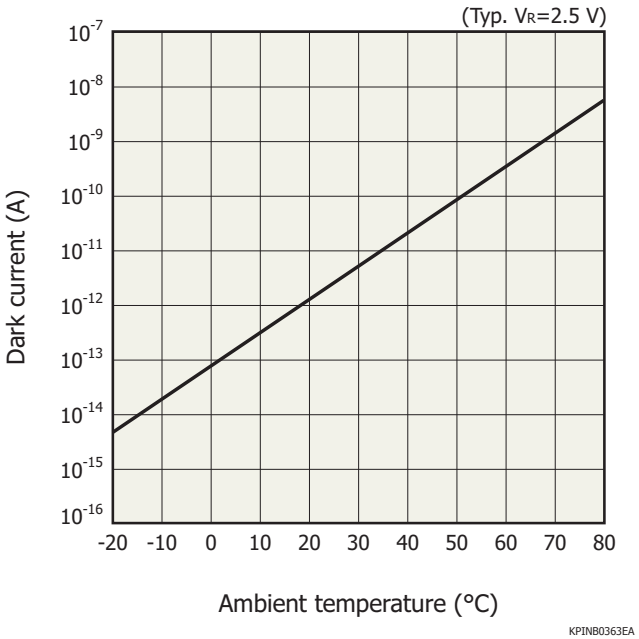

Terminal capacitance vs. reverse voltage

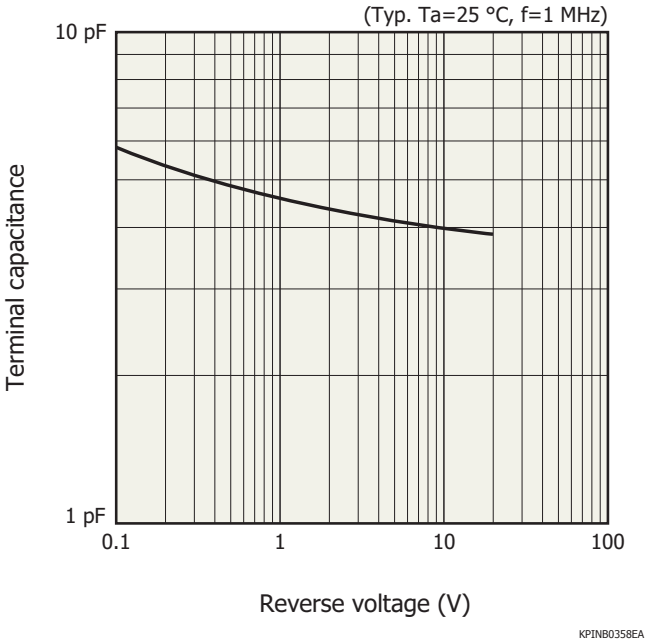

Directivity

S10783

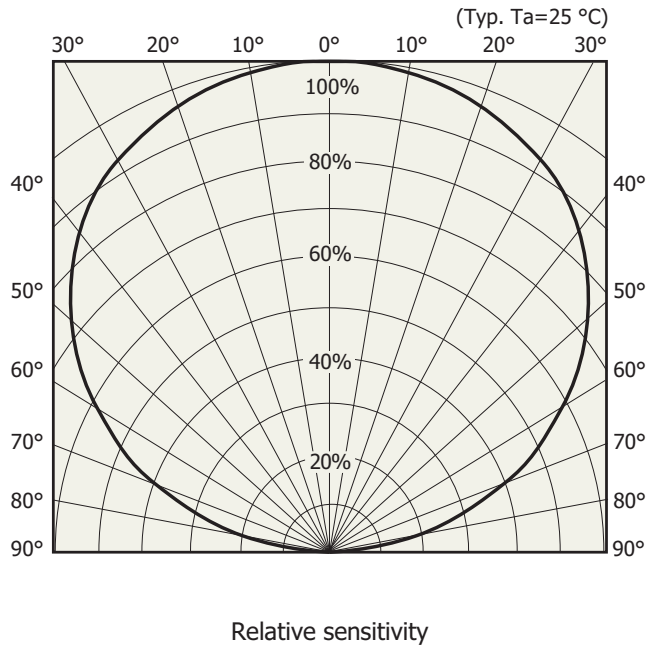

KPINB0362EA

S10784

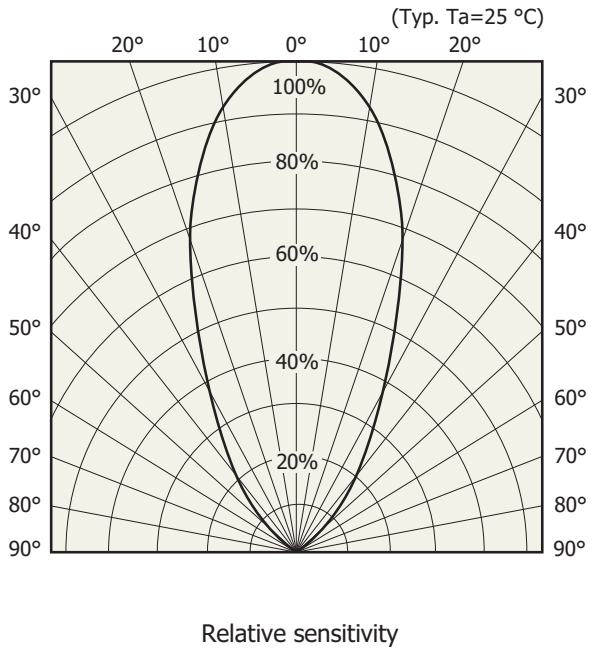

KPINB0359EA

Frequency characteristics

λ=660 nm

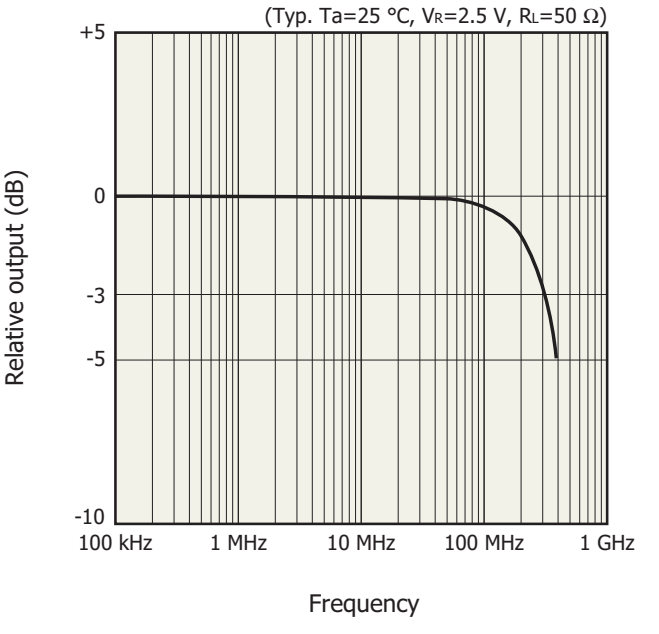

KPINB0360EA

λ=780 nm

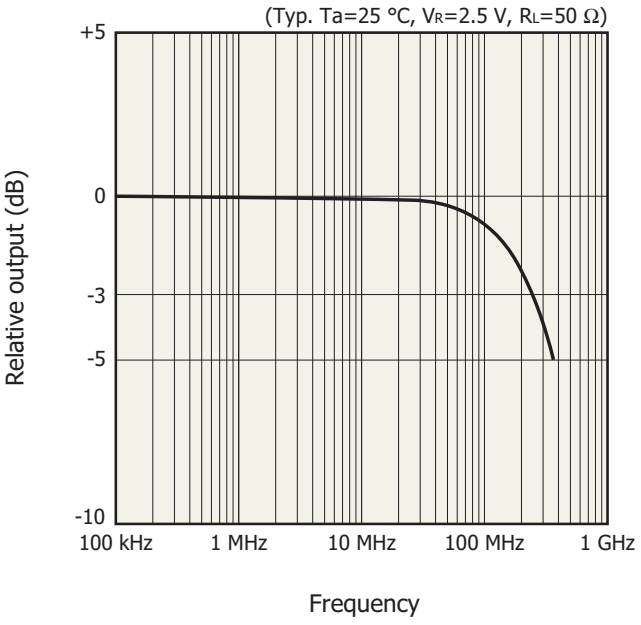

KPINB0361EA

Dimensional outlines (unit: mm)

S10783

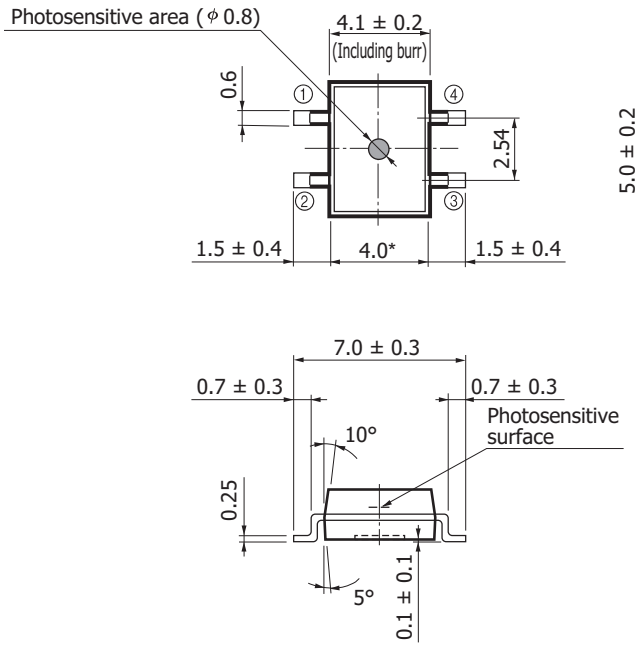

① NC
② Cathode
③ Anode
④ Cathode

Tolerance unless otherwise noted: ±0.1
Position accuracy of photosensitive area center with respect to the package dimensions marked *
X, Y≤±0.2
θ≤±2°
Lead surface finish: silver plating
Standard packing: stick (50 pcs/stick)

KPINA0105EB

S10784

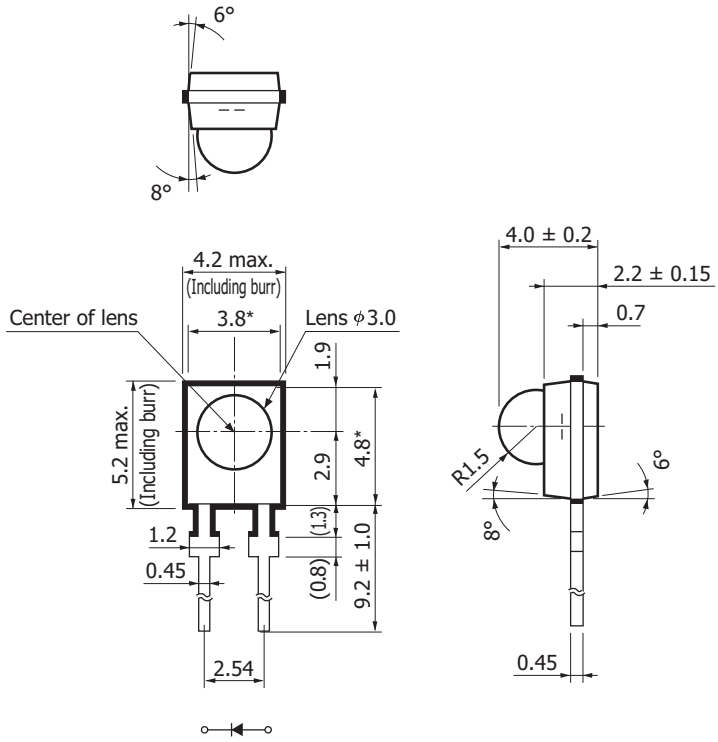

Tolerance unless otherwise noted: ±0.1
Position accuracy of photosensitive area center with respect to the package dimensions marked *
X, Y≤±0.2
θ≤±2°
Lead surface finish: silver plating
Standard packing: polyethylene pack [anti-static type] (500 pcs/pack)

KPINA0032EC

ENERGY EFFICIENT OPTICAL WIRELESS COMMUNICATIONS BASED ON FREQUENCY-SHIFT KEYING MODULATIONS

Abstract: **-** Optical wireless communications (OWC) is an appropriate technology to alleviate the scarcity issue of the radio-frequency (RF) spectrum. For OWC technology, the transmitted signals should be real-valued and unipolar to satisfy the constraints of the intensity modulation and direct detection (IM-DD). OWC have been extensively investigated for pervasive applications in high data rate communications which is based on pulse-amplitude modulation (PAM), optical-orthogonal frequency-division multiplexing (O-OFDM), etc. Recent research has confirmed the interest of OWC low data rate (100 kbps to 1 Mbps) applications, requiring high energy efficiency. In this context, frequency-shift keying (FSK) raised considerable interest for OWC technology. For IM-DD OWC systems, the conventional *M*-ary FSK is not compatible because of the bipolar nature of the FSK waveforms, but two compatible variants of FSK modulation have been introduced in the literature for OWC systems, i.e., direct current (DC)-FSK and unipolar (U)-FSK.

The current PhD work focuses on high energy-efficient modulation approaches for OWC, which are based on extensions/adaptations of the conventional *M*-ary FSK modulations. After the review of the state-of-the-art, a new modulation scheme called *M*-ary asymmetrically clipped (AC)-FSK is presented for high energy-efficient/low data rate OWC, which is based on the conventional bipolar *M*-ary FSK. Traditional receivers such as optimal time-domain (TD) receiver (based on maximum likelihood (ML) detection), and sub-optimal receiver (based on 1-tap DCT-based detection) exhibit the trade-off between the energy efficiency and the receiver complexity. A new frequency-domain (FD) low complexity receiver called *L*-tap harmonic receiver is proposed for the proposed *M*-ary AC-FSK and state-of-the-art *M*-ary U-FSK that alleviates the energy-efficiency and the receiver complexity trade-off. Simulation results confirm that the bit error rate (BER) performance of the proposed *M*-ary AC-FSK is far better than the state-of-the-art *M*-ary DC-FSK, and its BER performance is slightly improved as compared to the state-of-the-art *M*-ary U-FSK. Moreover, simulation results also confirm that the proposed *L*-tap harmonic receiver for both *M*-ary AC-FSK and *M*-ary U-FSK approaches the optimal TD ML receiver performance with a benefit of the drastic reduction in the receiver complexity.

Secondly, a new modulation approach, i.e., Asymmetrically Clipped Frequency and Phase Shift Keying (AC-FPSK) is proposed for IM-DD OWC applications that is based on the amalgamation of *M*-ary AC-FSK and phase-shift keying (PSK). It is highlighted that AC-FPSK shows improved energy efficiency and spectral efficiency as compared to *M*-ary AC-FSK.

Finally, an experimental demonstration of the proposed *M*-ary AC-FSK and the proposed *L*-tap harmonic receiver is presented and compared with the state-of-the-art FSK-based modulations. The experimental setup is based on commercial off-the-shelf components and a software defined radio (SDR) test bench. The experimental results confirm the validity of the proposed schemes in the thesis.

GRENOBLE IMAGES PAROLE SIGNAL AUTOMATIQUE
UNIVERSITÉ GRENOBLE ALPES